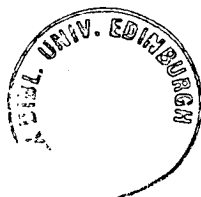# Polydimethylsiloxane (PDMS) monolayers: morphology, nanostructure, adhesive and frictional properties.

Frédéric Madani

A thesis submitted to the University of Edinburgh
for the Degree of Doctor of Philosophy

School of Engineering & Electronics *and* Centre for Materials Science &
Engineering

September 2005

A mes parents

Declaration

I declare that this thesis has been composed by myself and is all my own work except where otherwise stated.

<div align="right">

Frédéric Madani

September 2005

</div>

Acknowledgments

«...Maintenant toutes les disciplines sont restituées, les langues instaurées, le grec sans lequel il est honteux qu'une personne se dise savante, l'hébreu, le chaldéen, le latin. Des impressions fort élégantes et correctes sont utilisées partout, qui ont été été inventées à mon époque par inspiration divine, comme inversement l'artillerie l'a été par suggestion du diable. Tout le monde est plein de gens savants, de précepteurs très doctes, de librairies très amples, tant et si bien que je crois que ni à l'époque de Platon, de Cicéron ou de Papinien, il n'y avait de telle commodité d'étude qu'il s'en rencontre aujourd'hui. Pour cette raison, mon fils, je te conjure d'employer ta jeunesse à bien profiter dans tes études et dans la vertu. Tu es à Paris, tu as ton précepteur Epistémon qui, d'une part par ses leçons vivantes, d'autre part par ses louables exemples, peut bien d'éduquer. Je veux que tu apprennes les langues parfaitement. Premièrement le grec, comme le veut Quintilien. Deuxièmement le latin. Et puis l'hébreu pour les lettres saintes, et le chaldéen et l'arabe pareillement. Qu'il n'y ait aucune histoire que tu n'aies en mémoire, ce à quoi t'aidera la cosmographie de ceux qui en ont écrit. Des arts libéraux, la géométrie, l'arithmétique et la musique, je t'ai donné un avant-goût quand tu étais encore petit, âgé de cinq à six ans : poursuis le reste et deviens savant dans tous les domaines de l'astronomie mais laisse-moi de côté l'astrologie divinatrice, et l'art de Lulle comme des excès et des inutilités. Du droit civil, je veux que tu saches par coeur tous les beaux textes, et que tu puisses en parler avec philosophie. Et quant à la connaissance des faits de la nature, je veux que tu t'y adonnes avec curiosité, qu'il n'y ait ni mer, ni rivière, ni fontaine dont tu ne connaisses les poissons, tous les oiseaux de l'air, tous les arbres, arbustes et fruits des forêts, toutes les herbes de la terre, tous les métaux cachés dans le ventre des abîmes, les pierreries de tout l'Orient et du midi. Que rien ne te soit inconnu. »

«...En somme, que je voie un abîme de science : car avant de devenir un homme et d'être grand, il te faudra sortir de cette tranquillité et du repos de l'étude et apprendre la chevalerie et les armes pour défendre ma maison et secourir nos amis dans toutes leurs affaires contre les assauts des malfaisants. Et je veux que rapidement tu mettes en application ce dont tu as profité, ce que tu ne pourras mieux faire qu'en discutant publiquement avec tous et contre tous les gens de savoir en fréquentant les gens lettrés, qui sont tant à Paris qu'ailleurs. »

«...Mais parce que selon le sage Salomon la sagesse n'entre jamais dans les âmes mauvaises, et **science sans conscience n'est que ruine de l'âme**, il te faudra servir, aimer et craindre Dieu, et en Lui mettre toutes tes pensées et tout ton espoir, et par foi formée de charité être joint à Lui, si fort que jamais le péché ne t'en sépare. Prends garde des tromperies du monde, ne laisse pas la vanité entrer dans ton coeur car cette vie est passagère, mais la parole de Dieu demeure éternellement. Sois serviable envers tous tes prochains, et aime-les comme toi-même. Respecte tes précepteurs, fuis la compagnie des gens à qui tu ne veux pas ressembler, et ne gaspille pas les grâces que Dieu t'a données. Et quand tu t'apercevras que tu disposes de tout le savoir que tu peux acquérir là-bas, reviens vers moi, afin que je te voie une dernière fois et que je te donne ma bénédiction avant de mourir. Mon fils, que la paix et la grâce de notre Seigneur soient avec toi. Amen.

D'Utopie, le dix-septième jour du mois de mars.
Ton père, Gargantua. »

François Rabelais
Pantagruel, Chapitre 8
« Lettre de Gargantua à Pantagruel », 1532.

Abstract

Anchored polymer chains to silica substrates have many technological applications such as lubrication, adhesion and colloid stabilisation. Over the past ten years many studies, whether experimental or theoretical, have striven to highlight the physical phenomena responsible for those properties that gave rise to technological applications. However most of the techniques used to probe the properties of those systems provide average values of a particular physical property. It is then difficult to relate a measurement to the behaviour of a single or a few chains, which are yet believed to be at the origin of a monolayer's properties. In this work polymer and other organic films deposited on silica substrates were studied. Special attention was given to adsorbed polydimethylsiloxane (PDMS) monolayers.

Scanning White Light Interferometry (SWLI) is shown to provide direct three-dimensional imaging of thin films with a thickness higher than ≈ 0.5 nm. The thickness values are precise (± 0.1 nm) if the system is covered with a metal layer of thickness ≈ 80 nm. The lateral resolution is in the sub-micrometre range. This makes SWLI a credible alternative to imaging ellipsometry, the standard technique for global imaging of thin and ultra-thin films. SWLI has also been used to establish the irreversible nature of adsorption of PDMS on silica. It has also been to judge whether or not a film is a true monolayer through height measurement across the layer. A leap in lateral resolution of two or three orders of magnitude is obtained by using Intermittent Contact Scanning Force Microscopy (IC-SFM). A dense dry PDMS monolayer consists of a bimodal system: a smooth layer made of chains with a flat conformation topped by upright chain segments of poorly adsorbed chains that aggregate to form large spots. The presence of the smooth base layer was verified by means of an SFM tip used as a 'nanodigger'.

X-ray photoelectron spectroscopy (XPS) in combination with Contact angle goniometry (CAG) was used to try and identify the nature of the adsorption between PDMS chains and silica substrates. The weak basicity of PDMS (H-bond acceptor) has been highlighted as well as the key role played by OH-groups at the end of PDMS chains. However condensation of depolymerised PDMS segments to silanol sites cannot be ruled out (chemisorption).

Pull-off force experiments carried out in bad solvent conditions between an SFM-tip and a PDMS monolayer (contact area ≈ 10 nm) have shown two main energy dissipation mechanisms: chain or chain segment stretching, long range adhesive plateaus. The length of these plateaus is related to chain size and the type medium surrounding the two interacting media (air, water, and octane). Their height is related to the surface energy of PDMS that was estimated through contact angle goniometry. This phenomenon has been interpreted as the elongation of a collapse chain going from a globule to coil state. Denser areas of monolayers show a curvature of the force-separation curve where a straight line is expected. This effect is believed to be an effect due to the compliance of PDMS monolayers. Friction force microscopy at the nanoscale shows that PDMS monolayers have frictional properties that depend on the normal force applied to them. At low load PDMS behaves as a lubricant, medium loads correspond to instabilities associated to the penetration of the SFM tip into the monolayer. At higher loads the high measured friction coefficient is characteristic of a tip-silica contact.

Contents

1. Introduction

This work is concerned with the study of ultrathin polymer films deposited on solid substrates, mainly glass, silica and oxidised silicon. These oxides are models of metal surfaces. After a concise presentation of the importance of polymers at surfaces to industry and an introduction of the fundamental and experimental work being done to develop knowledge of these systems, we will justify our own approach of the subject and the areas where we tried to contribute to research. Finally we will give an outline of this thesis.

Polymer chains anchored at surfaces play a key role in many a technological area, to name a few: adhesion [Lee, 1980], lubrication, chromatography, colloidal stabilisation [Napper, 1983] [Gast & Leibler, 1986], microelectronics and biocompatibility of artificial organs in medicine [Ruckenstein & Chang, 1988]. Nowadays the understanding of the behaviour of these polymer-modified surfaces has made progress, in particular monolayers referred to as *brushes* through theoretical studies [Guiselin, 1992] [Aubouy *et al.*, 1996] and experimental investigations. A great variety of techniques have been used. Amongst those, we can mention neutron reflectivity and x-ray reflectivity for their ability to give information about the structure and dimensions of such films; the surface force apparatus (SFA), the Johnson-Kendall-Roberts (JKR) technique and shear force measurements respectively for adhesion and friction studies [Milner, 1991] [Déruelle *et al.*, 1995] [Piau *et al.*, 2005] [Kim *et al.*, 1997].

A major drawback of these techniques is that they probe large surface areas (from some hundreds of squared microns to some squared centimetres) so that the quantity being measured is at best an average and any meaningful lateral variation of that quantity cannot be detected. The fast coming of age of a family of techniques called Scanning Probe Microscopies (SPMs), born barely two decades ago [Binnig & Rohrer, 1983], allows unprecedented lateral resolution (nanometre range) for mapping as well as measuring adhesion and friction forces. So far authors have focussed on isolated single polymer chains and started to investigate their conformation depending on whether they are covalently bonded to a substrate by one or two ends of the chain (end-grafted) [Ortiz & Hadziioannou, 1999] or physically adsorbed [Conti *et al.*, 2001] [Kiriy *et al.*, 2002]. They have started to study the energy dissipation mechanisms between an imaging SPM probe and single

polymer chains [Conti *et al.*, 2001]. More densely packed chains and in particular polymer layers of height equal to the size of one macromolecule (monolayers) have not received as much attention whether end-grafted or not [Anczykowski *et al.*, 1995] [Schonherr *et al.*, 1998].

We propose to map and measure the adhesive and frictional properties of monolayers and sub-monolayers of polydimethylsiloxane (PDMS), with a lateral resolution of some nanometres using Scanning Force Microscopy (SFM) as well as use nano-manipulation techniques to investigate the structure of these ultrathin films. SFM images being limited in size (some tens of squared micrometres), we also propose to use optical imaging techniques to ensure uniformity at the microscale. The established technique in that regard is imaging ellipsometry [Jin *et al.*, 1996]. However, since it is model-dependent, the results it provides can be doubtful when, for instance, the optical constants of the sample being measured are not uniform throughout the surface or when they are uniform but almost identical to those of the substrate (observed in particular with mica) [Richter *et al.*, 2001] [Vallant *et al.*, 1998]. This uncertainty is even more relevant to situations where the film has a complex structure that cannot be modelled in terms of laterally homogeneous layers [Beyerlein *et al.*, 2002]. Some groups are trying to develop instruments using white-light interferometry as an alternative to imaging ellipsometry for thin film characterisation, as it is a direct height, hence thickness-measuring technique. Following pioneering work by Mohanty *et al.* [1986], Kim and Kim [1999], Leizerson and Lipson [2003] have developed a prototypical three-beam interference setup with which they investigated the presence of thin and thicker water films on mica (films down to 30 Å). We chose a different route and exploited the unsuspected capabilities of a commercial optical profilometer (New View 100, Zygo Corp) designed to deal with 'old-days engineering issues' such as estimating quantitatively wear in cutting tools [Devillez *et al.*, 2004]. Hariharan and Roy [1996] pointed out that transparent films could change significantly the spectral reflectance of a surface and therefore bring about height artefacts in surface profiles. Solving that problem we were able to obtain reliable quantitative measurements.

We are also interested in finding out experimentally the type of interactions that occur between silica and PDMS chains. The surface of silica is said to be acidic due to its silanol (OH) sites as is the case for other oxides like alumina [Layman & Hemminger, 2004]. PDMS adsorption onto silica in the form of powder has been studied by Litvinov *et al.*

[2002] using solid-state NMR with special emphasis on two nuclei ^{1}H and ^{29}Si. Vibrational spectroscopies capable of measuring a frequency shift in the O-H stretch are obviously the type of techniques to turn to but few of them are surface-specific. For non-metals, Reflection-Absorption Infrared Spectroscopy (RAIRS) is not suitable. High Resolution Electron Loss Spectroscopy (HREELS), often considered as the electron-analogue of Raman Spectroscopy, has been used with success to detect acid-base interactions [Layman & Hemminger, 2004] [Yates, 2004]. In the field of thin polymer film, an interesting study by De Koven and Mitchell [1991] shows the potential of this technique. We suggest a combination of x-ray photoelectron spectroscopy (XPS) and contact angle goniometry (CAG) with application of semi-empirical models to propose the likeliest interactions between PDMS chains and silica.

In Chapter 2 we present the latest theories being used to determine the physical interactions between two bodies in vacuum or a medium. We also give some information about polymer physics when chains are in a liquid solvent or at the surface of solids.

In Chapter 3 we present the various experimental techniques employed during this work with some emphasis on Scanning White Light Interferometry (SWLI), XPS and Scanning Force Microscopy (SFM). This first technique is probably the most unknown to surface scientists.

In Chapter 4 the results of a feasibility study regarding the capabilities of SWLI to characterise ultra-thin films (thickness, homogeneity) are reported. We also make a first step into the study of the structure of PDMS monolayers and other Self Assembled Monolayers (SAMs) that currently receive a lot of attention such as micro-patterned silanes.

In Chapter 5 SFM, XPS, CAG and Force Spectroscopy join forces to provide: a detailed picture of the optimum conditions of preparation of a PDMS monolayer, surface tension component values of PDMS monolayers and silica, some information about the energy dissipation mechanisms involved in adhesion and friction within a PDMS monolayer.

1.1. References

Anczykowski, B; Chi, L.F; Fuchs, H. (1995) *Atomic force microscopy investigations on polymer latex films*, Surface and Interface Analysis. **23**(6), 416-425.

Aubouy, M; Guiselin, O; Raphael, E. (1996) *Scaling description of polymer interfaces: flat layers*, Macromolecules. **29**(22), 7261-7268.

Beyerlein, D; Kratzmüller, T; Eichhorn, K.J. (2002) *Study of novel polymer architectures on solid surfaces by variable angle spectroscopic and imaging ellipsometry*, Vibrational Spectroscopy. **29**(1-2), 223-227

Binnig, G; Rohrer, H. (1983) *Surface imaging by scanning tunneling microscopy*, Ultramicroscopy. **11**(2-3), 157-160.

Conti, M; Bustanji, Y; Falini, G; Ferruti, P; Stefoni, S; Samori, B. (2001) *The desorption process of macromolecules adsorbed on interfaces: the force spectroscopy approach*, Chemphyschem. **2**(10), 610-613.

De Koven, B.M; Mitchell, G.E. (1991) *HREELS, XPS and in-situ friction studies of thin polyphenyl ether films on steel surfaces*, Applied Surface Science. **52**(3), 215-226.

Déruelle, M; Léger, L; Tirrell, M. (1995) *Adhesion at the solid-elastomer interface: influence of the interfacial chains*, Macromolecules. **28**(22), 7419-7428.

Devillez, A; Lesko, S; Mozer, W. (2004) *Cutting tool crater wear measurement with white light interferometry*, Wear. **256**(1-2), 56-65.

Gast, A; Leibler, L. (1986) *Interactions of sterically stabilized particles suspended in a polymer solution*, Macromolecules. **19**(3), 686-691.

Guiselin, O. (1992) *Irreversible adsorption of a concentrated polymer solution*, Europhysics Letters. **17**(3), 225-230.

Hariharan, P; Roy, M. (1996) *Interferometric surface profiling with white light: effects of surface films*, Journal of Modern Optics. **43**(9), 1797-1800.

Jin, G; Jansson, R; Arwin, H. (1996) *Imaging ellipsometry revisited: developments for visualization of thin transparent layers on silicon substrates*, Review of Scientific Instruments. **67**(8), 2930-2936.

Kim, S; Choi, G.Y; Nezaj, J; Ulman, A; Fleischer, C. (1997) *Effect of chemical functionality on adhesion hysteresis: a study using the JKR method*, Proceedings of The Materials Research Society Symposiums - Morphological Control in Multiphase Polymer Mixtures. **461**, 81-86.

Kim, S-W; Kim, G-H. (1999) *Thickness-profile measurement of transparent thin-film layers by white-light scanning interferometry*, Applied Optics. **38**(28), 5968-5973.

Kiriy, A; Gorodyska, G; Minko, S; Jaeger, W; Stepanek, P; Stamm, M. (2002) *Cascade of coil-globule conformational transitions of single flexible polyelectrolyte molecules in poor solvent*, Journal of the American Chemical Society. **124**(45), 13454-13462.

Layman, K.A; Hemminger, J.C. (2004) *Determination of surface OH acidity from the formation of acid/base complexes on ultrathin films of γ-Al$_2$O$_3$ on NiAl(100)*, Journal of Catalysis. **222**(1), 207-213.

Lee, L-H. (1980) *Adhesion and adsorption of polymers*, Plenum Press, New York, USA.

Leizerson, I; Lipson, S.G. (2003) *Three-beam interference method for measuring very thin films*, Applied Physics Letters. **83**(2), 260-262.

Litvinov, V.M; Barthel, H; Weis, J. (2002) *Structure of a PDMS layer grafted onto a silica surface studied by means of DSC and solid-state NMR*, Macromolecules. **35**(11), 4356-4364.

Luengo, G; Schmitt, F-J; Hill, R; Israelachvili, J. (1997) *Thin film rheology and tribology of confined polymer melts: contrasts with bulk properties*, Macromolecules. **30**(8), 2482-2494.

Milner, S.T. (1991) *Polymer brushes*, Science. **251**(4996), 905-914.

Mohanty, P.K; Puntambekar, P.N; Sen, D. (1987) *Film thickness measurement with white light fringes*, Optics and Laser Technology. **19**(3), 149-152.

Napper, D. (1983) *Polymeric stabilization of colloidal dispersions*, Academic Press, London, UK.

Ortiz, C; Hadziioannou, G. (1999) *Entropic elasticity of single polymer chains of poly(methacrylic acid) measured by atomic force microscopy*, Macromolecules. **32**(3), 780-787.

Piau, J-M; Ravilly, C; Verdier, C. (2005*) Peeling of polydimethylsiloxane adhesives at low velocities: cohesive failure*, Journal of Polymer Science Part B: Polymer Physics. **43**(2), 146-157.

Richter, A; Guico, R; Wang, J. (2001) *Calibrating an ellipsometer using x-ray reflectivity*, Review of Scientific Instruments. **72**(7), 3004-3007.

Ruckenstein, E; Chung, D.B. (1988) *Surface modification by a two-liquid process deposition of A–B block copolymers*, Journal of Colloid and Interface Science. **123**(1), 170-185.

Schonherr, H; Hruska, Z; Vancso, G.J. (1998) *Surface characterization of oxyfluorinated isotactic polypropylene films: scanning force microscopy with chemically modified probes and contact angle measurements*, Macromolecules. **31**(11), 3679-3685.

Vallant, T; Brunner, H; Mayer, U; Hoffmann, H; Leitner, T; Resch, R; Friedbacher, G. (1998) *Formation of self-assembled octadecylsiloxane monolayers on mica and silicon surfaces studied by atomic force microscopy and infrared spectroscopy*, Journal of Physical Chemistry B. **102**(37), 7190-7197.

Yates, J.T. (2004) *Water interactions with silica surfaces: A big role for surface structure*, Surface Science. **565**(2-3), 103-106.

2. Theoretical background and bibliographical review

In this chapter we will list and describe the type of attractive and sometimes repulsive forces that act between two bodies in vacuum (or air) as well as in a liquid medium. In an attempt to treat this issue in a general manner, we will not only focus on polymeric, generally insulating materials but also on oxides, semi-conducting or conducting solids as well as liquids. We will stress the importance of van der Waals forces and introduce a quantity called the Hamaker constant: a convenient means of merging all these forces into one quantitative energetic parameter. We will then show that shorter-range forces such as Lewis acid/base interactions (generally H-bonds) are sometimes needed to more fully account for adhesion between different substances or even cohesion.

The concept of surface tension or surface free energy and particularly the various surface tension component theories being used in the field of surface energetics will be presented. They offer relatively simple semi-empirical quantitative methods for predicting interactions between bodies.

The last sections of this chapter will be dedicated to presenting and discussing some aspects of polymer physics, mainly in the context of chains adsorbed or anchored to a substrate.

2.1. Some elements on intermolecular forces

2.1.1. Long range forces and Hamaker constant

-Interactions involving ions or elemental (simple) charges:

Interaction between substances is often of electrostatic origin. In the simple case of two ions, where each one creates its own electric field, the expression of this force is given by Coulomb's law:

$$F(r) = \frac{1}{4\pi\varepsilon_0\varepsilon_r} \frac{q_1 q_2}{r^2} \qquad (2.1),$$

where ε_0 is the electric permittivity of vacuum, ε_r is the dielectric constant of the medium that contains the ions if there is one, r is the intermolecular distance, q_1 is the charge of ion 1 and q_2 is the charge of ion 2. The corresponding potential energy $U(r)$ is obtained by

integration of $F(r)$ and therefore varies as $U(r) \propto 1/r$. Coulomb's forces are important in systems like solutions of polyelectrolytes [Gaboriaud, 1996].

Aside from ions, some neutral molecules with an electric dipole moment can create electric fields or electric dipole fields [Halliday *et al.*, 2001]. This happens when these molecules are made up of atoms having different electronegativities, which produces a pair of 'charges' of opposite sign, that is a dipole. A good example is water: the oxygen atom attracts electrons while the hydrogen atom is depleted and gains a pseudo positive charge. Some dipoles appear at the surface of solid surfaces where there are localised charges; they are referred to as fixed dipoles. Their interaction with ions gives rise to forces that vary as $F(r) \propto 1/r^3$. While mobile dipoles such as most solvents and in particular water can be involved in solvation processes, the corresponding force varies as $F(r) \propto 1/r^5$ [Gaboriaud, 1996]. All these interactions can occur during Scanning Force Microscopy (SFM) experiments, a technique that we describe in details in § 3.1.3. For the present we will only say that it lies on short-range interactions between an SFM probe tip and the surface to be mapped. Long-range electrostatic interactions involving charges are (when possible) to be avoided as they only deteriorate the resolution, make the control of the probe more difficult or even prevent from imaging the surface altogether. Meyer *et al.* [2004] give a list of such interactions:

- insulating tip and insulating sample with localised charges;
- conducting tip and insulating sample with localised or 'uniform' charges like mica and vice-versa;
- tip with a dipolar apex and conducting surface and vice-versa;
- a conducting tip and conducting sample at different potential make a capacitor.

The range of electrostatic forces is virtually unlimited. In terms of SFM work their influence can be felt over hundreds of nanometres.

-Dipole-dipole interactions:

These common interactions are usually referred to as **van der Waals** forces. Prior to defining the main members of this family, we can mention briefly the so-called *wall effects*. They originate from interactions between permanent fixed dipoles located at the surface of solids and (mobile) liquids with permanent dipole moments, in other words polar liquids. Such forces vary as $F(r) \propto 1/r^4$. Keesom studied and highlighted the importance of interactions between polar molecules (permanent mobile dipoles). They are often referred to

as *orientation forces*. They vary as $F(r) \propto 1/r^7$. Debye found out that a polar molecule passing by a polar or non-polar molecule induced a dipole moment in the other molecule. The dipole field deforms the 'electron cloud' of the molecule target so that the centre of gravity of positive charges no longer matches with that of the negative charges, therefore a dipole is created. The ability of a molecule or atom to acquire an induced dipole depends on its *polarisability*. This is a physical quantity with tabulated values. Interactions between permanent dipoles and induced dipoles are also called *induction forces*. They too vary as $F(r) \propto 1/r^7$. As for London, his efforts have permitted to define the *dispersion forces* responsible for cohesion in condensed phases with no dipole moment such as carbon tetrachloride (CCl_4) or alkanes. In non-polar molecules and especially in symmetrical molecules like CCl_4, the dipole moment is only naught in average over time. At a given time such a molecule can possess an instantaneous dipole moment [Gaboriaud, 1996]. These dipoles vary or oscillate rapidly with time and produce a field that is electromagnetic in nature. A molecule with such a varying dipole can polarise a neighbouring molecule and induce a similar dipole in phase with the first one. This induced oscillating dipole will in turn, interact with the one that gave birth to it. These dispersion forces present in all atoms and molecules vary like Keesom's and Debye's forces as $F(r) \propto 1/r^7$. London's theory was later modified to take into account a phenomenon called *retardation*. At distances beyond 10 nm, it takes an electromagnetic wave a finite time to reach its molecule target, which can correspond to a situation where the configuration of the electron cloud is less favourable to attraction so that the corresponding forces vary as $F(r) \propto 1/r^8$ [Lee, 1991]. For a more exhaustive list of intermolecular forces along with complete formulations of associated potential energies, the reader is referred to an authoritative treatise by Israelachvili [1992]. Van der Waals forces can be effective from interatomic distances, that is 0.2 nm up to large distances of order or greater than 10 nm. Like other electrostatic forces, dipole-dipole attractive interactions are a nuisance in SFM imaging experiments and therefore should be avoided.

-Hamaker constant:

In order to be able to quantitatively estimate the magnitude of van der Waals forces, Hamaker proposed equations assuming the additivity of dispersion forces [Hamaker, 1937]. This theory was later modified to include the other van der Waals forces. The pairwise additivity approach was however proved to be valid only in rarefied media. In condensed phases neighbouring atoms participate in the polarisation process. The instantaneous dipole

field from atom1 polarises atom2 as well as neighbouring atom3. The induced field in atom3 or reflected field affects atom2 in the same way as the field produced by atom1. The Lifshitz theory solves the problem because it no longer considers the atomic structure and regards large interacting bodies as continuous media [Israelachvili, 1992]. The interaction forces are then derived from bulk dielectric constants ε_r and refractive indices. For two bodies (1, 2) interacting across a medium (3) that can be vacuum (air) or a liquid, the Hamaker constant is given by:

$$A_{123} = \frac{3}{2}kT\sum_{n=0}^{\infty}{}' \sum_{j=1}^{\infty} \left\{ \left[\frac{\varepsilon_1(iv_n) - \varepsilon_3(iv_n)}{\varepsilon_1(iv_n) + \varepsilon_3(iv_n)} \right] \left[\frac{\varepsilon_2(iv_n) - \varepsilon_3(iv_n)}{\varepsilon_2(iv_n) + \varepsilon_3(iv_n)} \right] \right\}^j \left(1/j^3 \right) \text{ (2.2),}$$

where k is Boltzmann's constant, T is the temperature (K), $\varepsilon(iv_n)$ are the dielectric permittivities at imaginary frequencies, $v_n = (2\pi kT/h)n = 4.10^{13} n$ Hz at 300 K with h being Planck's constant and Σ' means that the zero frequency $n = 0$ term is multiplied by 0.5.

Israelachvili [1992] proposed to simplify equation (2.2) by considering that the calculation of the term for which j = 1 is sufficient to obtain a good estimate, substituting an integration over n for the discrete sum because the frequencies are close together in the UV region, and neglecting the molecular rotational relaxation phenomena that take place at microwave frequencies (MW) $v_{rot} < 10^{12}$ Hz.

The change in frequency of a medium's dielectric permittivity is usually expressed in terms of typical absorption regions, namely MW, IR and UV as in the case of that put forward by Ninham and Parsegian [1970]. Israelachvili assumes that only electronic absorption occurring in the UV typically at $v_e = 3.10^{15}$ Hz is important, therefore the dielectric permittivity reduces to:

$$\varepsilon(iv) = 1 + \frac{\left(n^2 - 1\right)}{\left(1 + v^2/v_e^2\right)} \tag{2.3},$$

where n is the refractive index of the medium in the visible.

This and the assumption that the absorption frequencies are the same for all three media, leads to a simplified expression of the Hamaker constant valid for non-conducting materials:

$$A_{123} \approx \underbrace{\frac{3}{4}kT\left(\frac{\varepsilon_{r1} - \varepsilon_{r3}}{\varepsilon_{r1} + \varepsilon_{r3}} \right)\left(\frac{\varepsilon_{r2} - \varepsilon_{r3}}{\varepsilon_{r2} + \varepsilon_{r3}} \right)}_{A_{v=0}} + \underbrace{\frac{3hv_e}{8\sqrt{2}} \frac{\left(n_1^2 - n_3^2\right)\left(n_2^2 - n_3^2\right)}{\left(n_1^2 + n_3^2\right)^{1/2}\left(n_2^2 + n_3^2\right)^{1/2}\left\{\left(n_1^2 + n_3^2\right)^{1/2} + \left(n_2^2 + n_3^2\right)^{1/2}\right\}}}_{A_{v>0}} \tag{2.4}$$

The first term in equation (2.4) is the zero-frequency contribution $A_{v=0}$, it depends only on static dielectric constants ε_r. The second term is the dispersion contribution term $A_{v>0}$, it depends on refractive indices n, that is dielectric permittivities in the visible.

For conducting materials such as metals, the dielectric constants are expected to be infinite, so that equation (2.3) does not apply. The following approximation can be used:

$$\varepsilon(iv) = 1 + \frac{v_p^2}{v^2}, \quad \varepsilon(0) = \infty.$$ v_p is the plasma frequency of the free electron gas. The

Hamaker constant for two metals interacting across vacuum is then:

$$A_{12} \approx \frac{3\sqrt{2}}{16} h v_e \tag{2.5}$$

It ranges from 25×10^{-20} J to 40×10^{-20} J.

Some authors like Parsegian and Weiss [1981] have obtained exact solutions to equation (2.2) but such a computation is demanding and cannot be as easily implemented as Israelachvili's approximated equation. A slightly different route to the calculation of the Hamaker constant was employed by Krupp [1967]. Using another formulation of equation (2.2), he obtained the following expression of A_{12}:

$$A_{12} = \frac{3\hbar\overline{\omega}}{4\pi}, \text{ where } \overline{\omega} = \int_0^\infty \left(\frac{\varepsilon_1(i\xi)-1}{\varepsilon_1(i\xi)+1} \right) \left(\frac{\varepsilon_2(i\xi)-1}{\varepsilon_2(i\xi)+1} \right) d\xi \tag{2.6},$$

This route has been used to calculate the Hamaker constant of semi-conductors and in particular silicon Si(111), a crystalline material and a face of special interest to us [Böhme *et al.*, 1973] [van den Tempel, 1972].

Combining relations can be handy to calculate the Hamaker constant for two dissimilar materials across a medium or vacuum when one of these is either a metal or a semi-conductor and the other is a dielectric. Although Israelachvili [1992] highlighted the fact that the relevance of combining relations is questionable, we are reduced to using them to estimate the magnitude of van der Waals forces between semi-conductors and dielectric. The non-retarded Hamaker constant for media 1 and 2 interacting across vacuum is estimated as:

$$A_{12} \approx \sqrt{A_{11}A_{22}} \tag{2.7},$$

while the Hamaker constant for the same two media interacting across medium 3 is:

$$A_{132} \approx \left(\sqrt{A_{11}} - \sqrt{A_{33}} \right) \left(\sqrt{A_{22}} - \sqrt{A_{33}} \right) \tag{2.8}.$$

We now calculate the Hamaker constant both in vacuum and in a medium for several relevant molecules in the spirit of predicting experimental problems that may occur in SFM as well as adhesion between a solid substrate and polymer chains.

Medium	Dielectric constant ε_r	Refractive Index n	Absorption frequency v_e (10^{15} Hz)	Hamaker constant A_{11} (10^{-20} J)	Method or reference
Water	78.41	1.33	2.9	3.6	Eq (2.4)
Octane	1.94	1.39	3.0	4.5	Eq (2.4)
Decane	1.98	1.41	3.0	5	Eq (2.4)
Dodecane	2.01	1.41	3.0	5	Eq (2.4)
Hexadecane	2.04	1.42	2.9	5.2	Eq (2.4)
Cyclohexane	2.02	1.43	2.9	5.2	Eq (2.4)
Toluene	2.37	1.50	2.1 est	5	Eq (2.4)
Benzene	2.28	1.50	2.1	5	Eq (2.4)
CCl_4	2.23	1.46	2.7	5.5	Eq (2.4)
PS	2.55	1.56	2.3	6.5	Eq (2.4)
PVC	3.20	1.53	2.9	7.5	Eq (2.4)
PMMA	2.50	1.50	3.0	6.7	Eq (2.4)
PTFE	2.10	1.36	2.9	3.8	Eq (2.4)
PDMS	2.60	1.40	3.0 est	4.8	Eq (2.4)
SiO_2	3.80	1.45	3.2	6.3	Eq (2.4)
Mica	5.40	1.57	3.0	9	Eq (2.4)
Si_3N_4	6.34	1.99	3.0 est	20.9	Eq (2.4)
Si	11.80	3.86	-	24.8	A
Si+13nm SiO_2	-	-	-	20.2	A
Al_2O_3	11,60	1,75	3.0 est	13.9	Eq (2.4)
Fe_3O_4	-	1.97	3.0 est	20.6	Eq (2.4)
Rutile, TiO_2	-	2.61	3.0 est	41.1	Eq (2.4)
Au, Ag, Cu	∞	-	3.0 to 5.0	25 to 40	Eq (2.5)
Hg	∞	-	-	33	B

Table 2.1 Non-retarded Hamaker constants for two identical media interacting across vacuum at 25°C. Dielectric constant and refractive index values were taken from [Israelachvili, 1992], [Lide, 2001], [Hutter & Bechhoefer, 1993], [Palik, 1985]. Absorption frequencies values were obtained from [Israelachvili, 1985] and [van Oss et al., 1988]. When necessary the value was only estimated (est) by Israelachvili [1985]. A: [van den Tempel, 1972]. B: [Chaudhury, 1987].

The data in Table 2.1 as well as equations (2.4), (2.7) and (2.8) enable us to study the influence of a medium on the magnitude of the Hamaker constant between identical or dissimilar materials. We propose to study a few systems relevant to SFM of silicates and PDMS: Si, Si + 13 nm of oxide and Si_3N_4 with Si, Si + 13 nm of oxide, mica, fused quartz and PDMS across air, water and octane.
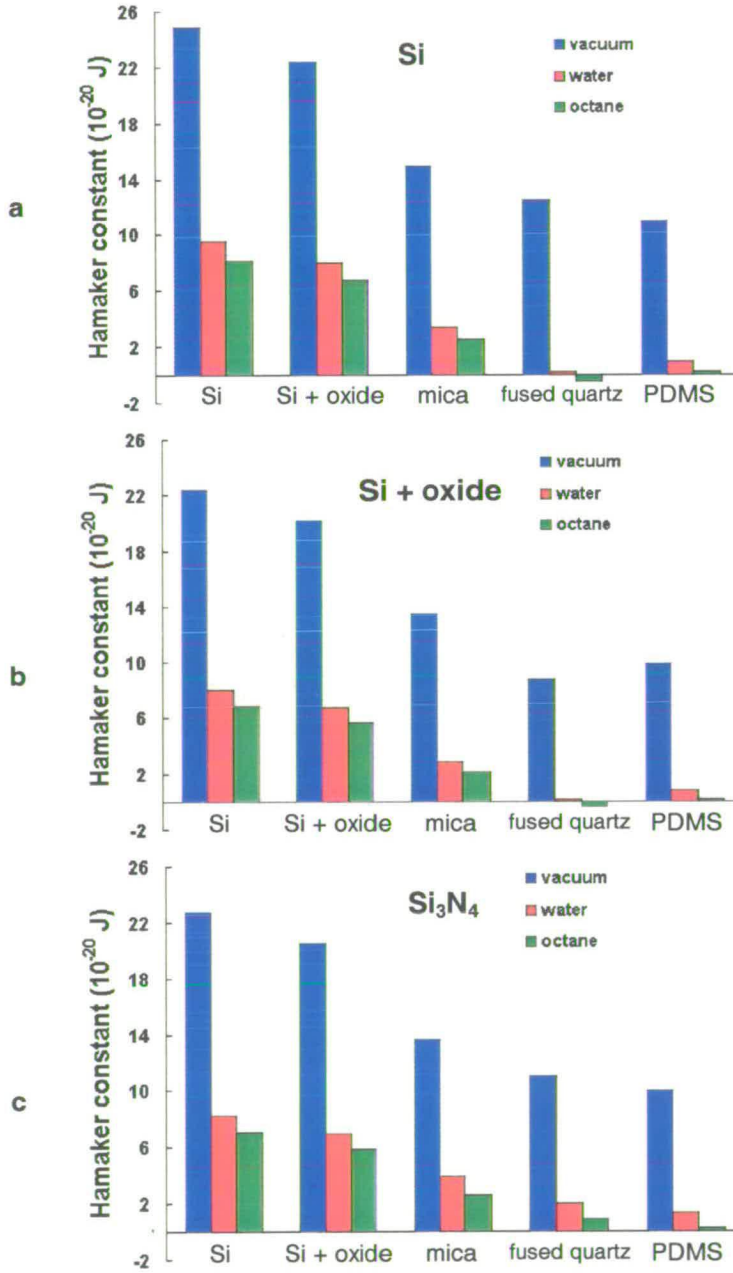
Fig. 2.1. Hamaker constants for several pairs of media across vacuum, water and octane. a: pure silicon interacts with five media. b: silicon covered in a 13 nm thick oxide layer interacts with the same five media. c: silicon nitride, idem.

Even though the absolute values of the Hamaker constant for the various materials studied may be different from our coarse calculations, Fig. 2.1 shows clearly that a liquid medium placed in between two interacting media does reduce van der Waals forces by a significant amount. They can even be repulsive if the liquid is an alkane. It is therefore beneficial to perform SFM imaging in liquid where these long-range forces are smaller. Another benefit of imaging in liquid is the elimination of shorter-range capillary forces. These forces come about because atmospheric water vapour finds in micro-contacts favourable condensation sites especially with hydrophilic silicon and many silicates. Capillary forces can be one or two orders of magnitude higher than van der Waals forces [Meyer *et al.*, 2004]. They would mask most of the materials-related adhesive phenomena in relevant measurement techniques such as force spectroscopy (see § 3.1.4).

If pure liquids do not result in a large enough decrease of van der Waals forces, it is possible to use salt solutions. The effect of having free charges is to screen the electrostatic fields potentially created by the interacting solid media. Only Keesom and Debye forces are concerned by this effect. The general expression of the Hamaker constant (see equation (2.4)) becomes:

$$A = A_{v=0}(2\kappa D)e^{-2\kappa D} + A_{v>0} \qquad (2.9),$$

where κ is the Debye screening length and D is the separation between the two interacting media [Israelachvili, 1992].

We also calculate the Hamaker constant for a series of systems that will be studied in the experimental sections of this thesis (Chapters 4 and 5) in order to estimate quantitatively the potential influence of a liquid on the interaction between some polymers and some solids.
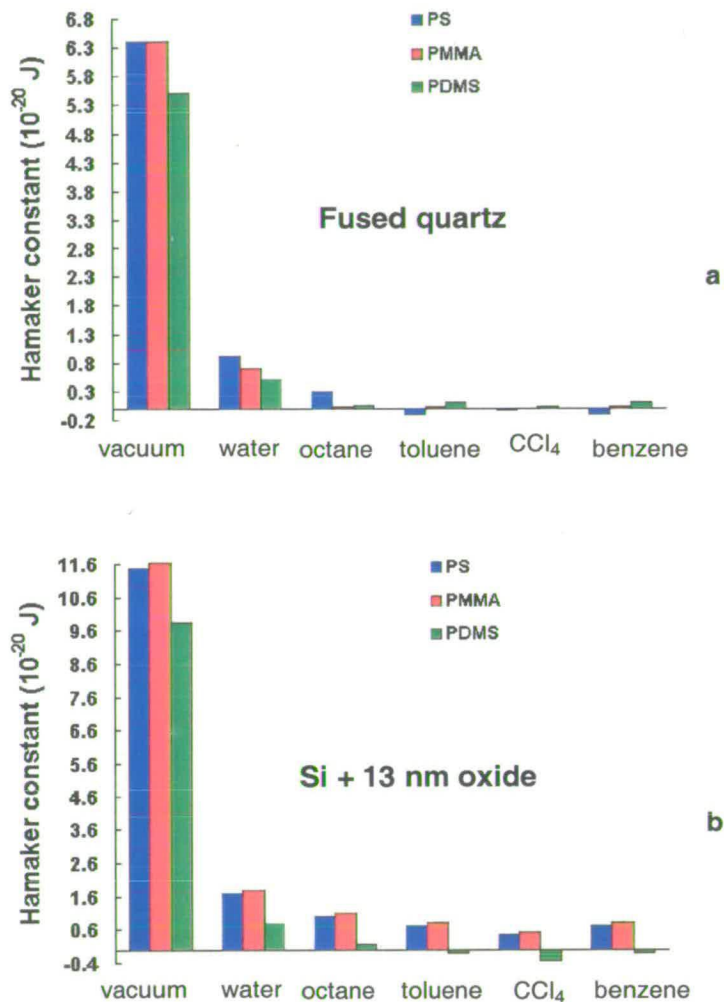
Fig. 2.2. Hamaker constant of polystyrene (PS), polymethylmethacrylate (PMMA) and polydimethylsiloxane (PDMS) interacting with solid substrates across six media: vacuum, water, octane, toluene, carbon tetrachloride (CCl_4) and benzene. a: the substrate is fused quartz. b: the substrate is silicon with a 13 nm thick oxide layer.

Much like Fig. 2.1, Fig. 2.2 shows mainly that any liquid has the effect of decreasing the Hamaker constant, that is the magnitude of the van der Waals forces. Organic liquids being more effective than water in that respect. If these forces are the only ones involved in adsorption processes then it is best to work with pure substances in air as opposed to in a solvent to obtain good adsorption of polymers onto silica substrates.

2.1.2. Interface acid-base interactions

To begin with let us just recall some basic aspects of acid-base reactions or interactions before we expand into acid-base interactions at interfaces.

In the famous Brønsted-Lowry theory, an acid is a proton donor while a base is a proton acceptor. If we consider NH_4^+ as our acid, the equilibrium with its conjugated base is as follows:

$$H^+ \; + \; \begin{matrix} H \\ | \\ :N-H \\ | \\ H \end{matrix} \; \rightleftharpoons \; \left(\begin{matrix} H \\ | \\ H-N-H \\ | \\ H \end{matrix} \right)^+ \tag{2.10}$$
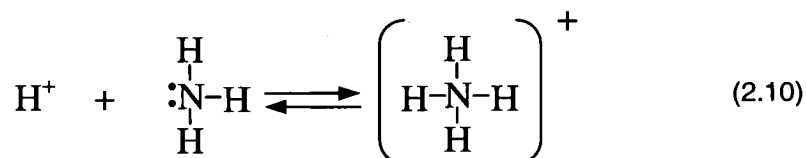
Another way to look at the reaction is to say that the base NH_3 has donated an electron pair (:) to H^+. This is the definition of a Lewis base. A Brønsted-Lowry base is also a Lewis base. Obviously a Lewis acid is an electron-pair acceptor. An important property is that Lewis bases can donate their electron-pair to acids other than H. A good example of this is the following reaction:

$$\begin{matrix} H \\ | \\ H-N: \\ | \\ H \end{matrix} \; + \; \begin{matrix} F \\ | \\ B-F \\ | \\ F \end{matrix} \; \rightleftharpoons \; \begin{matrix} H \; F \\ | \; | \\ H-N-B-F \\ | \; | \\ H \; F \end{matrix} \tag{2.11}$$
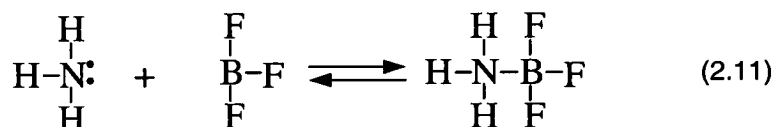
There is no hydrogen involved and yet NH_3 behaves as a base. The result of this interaction is the formation of an *adduct* or complex [Jensen, 1980].

Hydrogen bond (H-bonds) are often regarded as a sub-class of Lewis acid-base interactions. A hydrogen bond occurs between two electronegative atoms, one of which is covalently bonded to a hydrogen atom prior to the establishment of the H-bond. Practically, atoms such as fluorine (F), oxygen (O), nitrogen (N) or chlorine (Cl) make good targets for an H-bond, with H...F being the strongest bond. In a chemistry-like manner the following equilibrium describes the nature of a H-bond [Gutowski, 1991]:

$$A\text{---}H\cdot \cdots \cdot B \rightleftharpoons A^- H^+\text{---}B \tag{2.12}$$

Although it always involves hydrogen atoms, it is a phenomenon closer to Lewis acid-base interaction than it is to Brønsted-Lowry acid-base interaction. It is believed to be of fundamental importance to many interface phenomena, in particular adhesion [Good *et al.*, 1991]. X-ray measurements performed recently on ice showed that hydrogen bonds in this material were of covalent nature to an extent of 10%, the other 90% being ionic [Isaacs *et al.*, 1999]. The range of the corresponding forces is said to vary widely depending on the

system being considered. They sometimes act over some Angstroms like covalent or metallic bonds [Gutowski, 1991] and in other situations over a couple of nanometres and can be effective over large distances (from $\approx$ 100 nm to $\approx$ 2 μm) in much the same way as electrostatic forces do [Rabinovich & Derjaguin, 1988] [Christenson, 1988].

About 30 years ago Drago *et al.* [1971] [1977] undertook a systematic study of interactions between many organic liquids as well as water. Through computer simulation and spectroscopic (infrared) and calorimetric measurements they established a database of acid-base parameters and came up with a thermodynamic quantity: the enthalpy of adduct formation or heat of mixing. This quantity is predictable as Lewis acid-base interactions between electron donors and electron acceptors. In this sense a Lewis acid becomes a substance capable of accepting electron density rather than a real pair of electrons. Many of these interactions involve H-bonds but not all. The enthalpy of adduct formation is given by:

$$- \Delta H = E_A E_B + C_A C_B \qquad (2.13),$$

where Es and Cs are empirically determined parameters. E_A is the electrostatic (ionic) contribution to A's interaction with bases while C_A represents the covalent contribution to its acidity. They make up the database mentioned above. In this framework H-bonds are proper acid-base interactions as we have mentioned that they have a dual electrostatic and covalent nature.

Shortly after that, building on the results already available, Fowkes and co-authors [1984] [1985] performed experiments (microcalorimetry) to measure the amount of polymer adsorbed onto solid oxides in the form of powder with the purpose of interpreting these data in terms of the enthalpy of adduct formation, that is in terms of acid-base interactions [Fowkes & Mostafa, 1978] [Fowkes *et al.*, 1984] [Fowkes & Joslin, 1985]. They gave special emphasis to the case of PMMA solutions deposited on acidic surfaces such as silica. Here they refer probably to Brønsted-Lowry acidity. The acidity and basicity of a solid surface is, in this context, expressed by the isoelectric point I_s, that is the pH of a suspension of solid particles at which the zeta potential equals zero (the number of positive charges equals that of negative charges). Bolger and Michaels [1968] give for silicon dioxide values of isoelectric points ranging from 1.8 to 2.2. The surface sites of silica responsible for acidity are referred to as silanol sites (Si-OH). This point of view seems to have been shared by all the surface scientists for at least 30 years [Fowkes & Mostafa, 1978] [Villette *et al.*, 1996] [Layman & Hemminger, 2004]. The expected basicity of PMMA lies on the presence

of numerous oxygen atoms (electron-pair donors) along its backbone, many of which are not cluttered up with methyl groups: $-(C(CH_3)_2-COOCH_3)-_n$. Fowkes and Mostafa [1978] note that the coverage of PMMA on silica depends strongly on the solvent being used. It is maximum when the solvent is neither an acid nor a base, for instance carbon tetrachloride. Acidic solvents like chloroform tend to inhibit PMMA from adsorbing because of their acidity being higher than that of silica. Some basic solvents also inhibit adhesion by competing with PMMA for silica's silanol sites. The most basic solvents are up to three times as effective as acidic solvents as regards inhibiting PMMA adsorption. By comparing these data with Drago's database, we have estimated the acid-base parameters of some solvents, PMMA and silica and calculated the enthalpy or heat of mixing.(see Table 2.2).

solvents	E_B (kJ/mol)$^{1/2}$	C_B (kJ/mol)$^{1/2}$	E_A (kJ/mol)$^{1/2}$	C_A (kJ/mol)$^{1/2}$	Lewis basicity $-\Delta H$ vs SiOH (kJ/mol)	Lewis acidity $-\Delta H$ vs PMMA (kJ/mol)
Benzene	0.22	2.86			8.8	
Dimethyl sulfoxide	2.74	5.83			37.9	
Tetrahydrofuran	2.0	8.73			38.3	
Carbon tetrachloride	0	0			0	
Octane	0	0			0	
Hexadecane	0	0			0	
PMMA	1.39	1.9			16.7	
Chloroform			6.77	0.31		10.0
Dichloromethane			3.40	0.02		4.8
Water			5.01	0.68		8.2
Silica (SiOH)			8.80	2.37		16.7

Table 2.2 Acid-base interactions between some organic solvents or non-solvents (water), silica and PMMA. These results were obtained from calculations based on Drago's and Fowkes's data [Drago et al., 1971] [Drago et al., 1977] [Fowkes & Mostafa, 1978] [Fowkes et al., 1984] [Fowkes & Joslin, 1985].

The comments made above are in accordance with the data in Table 2.2, apart from the heat of mixing values for chloroform that should be higher than that for silica. Acid-base interactions are thus key factors to the adsorption of polymers onto solid substrates, to the extent that predictions based on estimations of van der Waals forces (Hamaker constant) are misleading. Fig. 2.2 shows that benzene reduces less the magnitude of van der Waals forces

between PMMA and silica than do octane or carbon tetrachloride (CCl$_4$). Experiments and analysis done taking into account acid-base interactions show the exact opposite: benzene inhibits PMMA adsorption onto silica while octane and CCl$_4$ do not. It is clear that any predicting theory of interactions in binary or ternary systems must include acid-base interactions. These conclusions apply to other systems where the substrate is a relatively acidic oxide, namely rutile (TiO$_2$) and ferric oxides (α-Fe$_2$O$_3$) [Fowkes & Joslin, 1985].

2.1.3. Surface tension components theories

Basic equations:

A quantity that has received a lot of attention by experts in the field of physical chemistry of surfaces is undoubtedly the surface tension. If G^S is the Gibbs surface free energy of a substance, the part of this free energy that is necessary to modify the surface area A is γ, the surface tension. The process of increasing or decreasing the surface area is being done at constant temperature T, pressure P and composition n^S within a thin layer of material regarded as being the 'surface'. The mathematical expression of the surface tension is then:

$$\gamma = \left(\frac{\partial G^S}{\partial A} \right)_{T,P,n} \tag{2.14}.$$

The total free energy is given by:

$$G^S = \sum_i n_i^S \mu_i + A\gamma \tag{2.15},$$

where μ_i is the chemical potential of the species making up the substance and n_i^S is the number of moles of each species at the surface [Douillard *et al.*, 2002].

It is experimentally easier to measure surface tensions than it is to measure heats of interaction (enthalpies), at least for liquids. A simple distorting drop hanging on a needle is sufficient. Solids do not deform so easily, therefore an indirect method has to be employed to determine their surface tension. The measurement of the contact angle that a liquid makes on a flat, chemically homogeneous and smooth (ideally at the atomic scale) solid surface is usually the main step in the estimation of the surface tension of a solid.

Historically, Thomas Young [1805] was the first to study in depth contact angles and to this day his equation has not been replaced by a better one.

The mathematical expression of Young's equation as written in a modern form is as follows:

$$\gamma_{SV} = \gamma_{SL} + \gamma_{LV}\cos\theta_Y \qquad (2.16),$$

where γ_{SV} is the solid-vapour interface tension, γ_{SL} is the solid-liquid interface tension, γ_{LV} is the liquid-vapour interface tension with the liquid in contact with the solid and θ_Y is Young's contact angle (see Fig. 2.3). The thermodynamic meaning of this angle and the question of whether common experimental conditions can lead to its measurement are still under discussion [Andrieu et al., 1994] [Della Volpe et al., 2002]. For the present we will consider it to be a macroscopic angle that corresponds to a situation where the liquid drop is in equilibrium (absolute minimum of energy or metastable state) with some vapour and a solid whose surface is chemically homogeneous, flat and smooth.
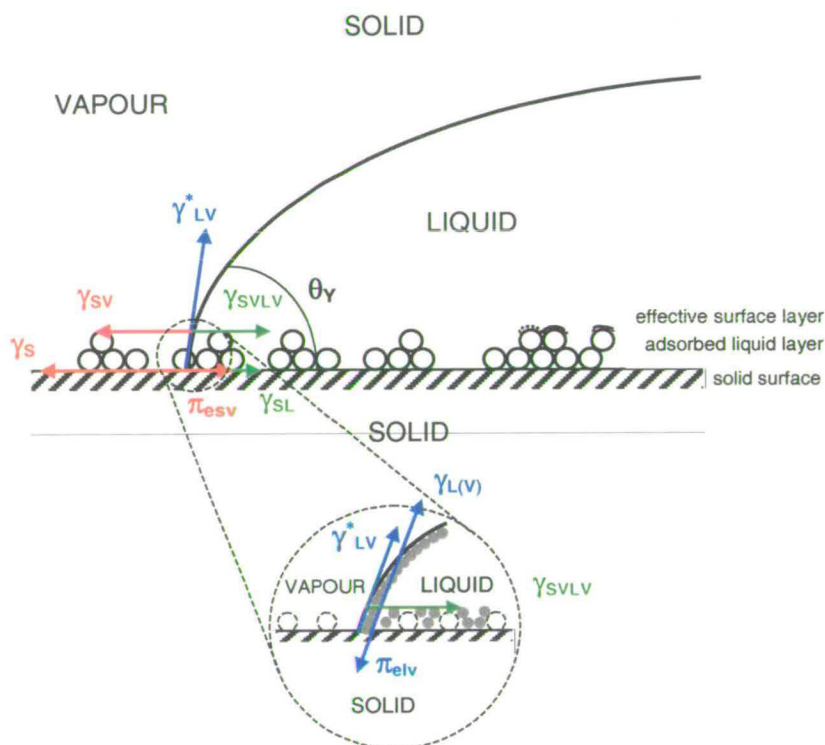
Fig. 2.3. Schematic of a liquid drop in contact with a solid in presence of vapour (this illustrates the situation described by Young's equation). Effect of film pressure due to adsorbed vapour both on the solid and liquid surface. This vapour comes from the liquid probe, any vapour present in the atmosphere prior to depositing the drop and possibly the solid [Good, 1993]. Note the insert where the liquid and/or atmospheric vapour is marked by 'big' dashed circles while particles and/or molecules coming from the solid phase are marked by smaller solid grey circles. This drawing is inspired by Busscher et al. [1983].

Generally, experiments take place in air with some humidity (RH $\neq$ 0) so that adsorption onto the solid is bound to occur. Adsorbate can come from the probe liquid (it probes the surface tension of the solid being studied), from ambient air (water vapour, possibly hydrocarbons etc.) or even from the solid as illustrated by Fig. 2.3, which makes the classical form of Young's equation (see equation (2.16)) too coarse. Some corrections are therefore needed. Often, authors use the liquid-vapour interface tension γ_{LV} in the sense that the liquid is in equilibrium with its own vapour. According to Good [1993], this is not the quantity that should be used in Young's equation. Even if the solubility of the solid in the liquid is low, equilibrium adsorption can be large enough to decrease the liquid-vapour interface tension because the solute's activity matters more than its concentration. Also diffusion of matter across the solid-liquid interface is not to be ruled out and can affect the contact angle [Good, 1993]. On the ground of these comments we can write the following equation:

$$\gamma^{*}_{LV} = \gamma_{L(V)} - \pi_{elv} \qquad (2.17),$$

where γ^{*}_{LV} is the interface tension of the liquid in contact and in equilibrium with the solid and any other vapour present in the vicinity[1]; $\gamma_{L(V)}$ is the real surface tension of the liquid, that is in equilibrium with its own vapour; finally π_{elv} is the film pressure associated with any vapour chemically different from that of the liquid, that is the solid's own vapour or even particles of impurities as well as atmospheric vapour.

The solid-liquid interface can also be subject to mutual adsorption but in a binary system at equilibrium the corresponding film pressure equals zero. Note that in presence of atmospheric vapour this statement might be false. For now we consider that $\gamma_{SVLV} = \gamma_{SL}$ (see Fig. 2.3). The solid is in equilibrium with at least the liquid vapour and possibly atmospheric vapour, the relationship between the true solid surface tension (in equilibrium with its own vapour) and the solid-vapour interface tension is given by:

$$\gamma_{S} = \gamma_{SV} + \pi_{esv} \qquad (2.18),$$

where π_{esv} is the film pressure associated with any vapour adsorbed onto the solid surface. Young's equation then becomes:

$$\gamma_{SV} = \gamma_{SL} + \gamma^{*}_{LV} \cos\theta_{Y} \qquad (2.19)$$

---

[1] Good [1993] does not envisage the effect of atmospheric vapour other than that of the liquid.

γ^*_{LV} is measured experimentally by axisymmetric drop shape analysis profile (ADSA-P), the liquid drop being sessile on the solid surface of interest [Kwok *et al.*, 1998] [Gutowski, 1991]. $\gamma_{L(V)}$ can be measured in a similar manner by the so-called pendant drop method if the environment is controlled or obtained from literature at a particular temperature [Jasper, 1972]. The difference between these two values gives the film pressure π_{elv} according to equation (2.17).

The film pressure on the solid π_{esv} is accessible experimentally by measuring adsorption isotherms in controlled environment (cleanliness, vapour pressure, temperature). Gibbs equation relates the film pressure to the amount of vapour adsorbed [Adamson, 1990]:

$$\pi_{esv} = RT \int_0^{P_{sat}} \Gamma(P) d \ln P \qquad (2.20),$$

where T is the temperature, R is the molar gas constant, P is the pressure and Γ is the amount of vapour adsorbed onto the surface per unit area.

For solids in powdery form, volumetric techniques in vacuum are generally used to get adsorption isotherms [Douillard *et al.*, 2002] and there is a relatively abundant literature on this subject, especially for silicate minerals and other high surface tension materials. The Montpellier school is particularly active in this field [Douillard *et al.*, 1995] [Malandrini *et al.*, 1997] [Médout-Marère *et al.*, 1998] [Douillard *et al.*, 2002] [Médout-Marère *et al.*, 2003]. Adsorption isotherms on plane surfaces can be obtained by ellipsometry [Good, 1993]. Only few and relatively old (1970s, 1980s) data is available in the literature, some of which concerns polymers. We can cite work by Busscher *et al.* [1986] as well as work by Tadros *et al.* [1974] and Hu and Adamson [1977]. Another interesting method was developed more recently. It is based on the measurement of the contact angle that a mercury droplet makes on a solid [Bellon-Fontaine & Cerf, 1990]. Because of the low vapour pressure of mercury ($P_{sat}^{Hg} \cong 0.002$ mm Hg whereas $P_{sat}^{water} \cong 17$ mm Hg) and of its high surface tension ($\gamma^{Hg} \cong 490$ mJ.m^{-2} whereas $\gamma^{water} \cong 73$ mJ.m^{-2}), mercury is supposed not to leave any adsorbed film on the solid. That is why a simple comparison between the contact angle that mercury makes on a solid with that of other probe liquids gives an estimate of the film pressure for any solid-liquid pair (for a more detailed presentation of the mercury drop method see § 5.1.1). This method is said to give results comparable to those obtained by ellipsometry [Lee, 2001].

The second fundamental equation to the quantitative estimation of adhesive properties in materials is that of Dupré [1869]. We owe him the concepts of work of cohesion W^c and work of adhesion W^a. The work necessary to separate a body into two portions in a reversible way is the work of cohesion. It is twice the surface tension of the body in equilibrium with its own vapour. For two dissimilar materials this work is called work of adhesion. If instead of works we use more modern and relevant to thermodynamics quantities like the variation of surface energy ΔG, Dupré's equations can be written [van Oss *et al.*, 1988]:

$$\Delta G_{ii}^c = -2\gamma_{i(V)} = -W_{ii}^c \qquad (2.21),$$

where $\Delta G^c{}_{ii}$ is the free energy change due to cohesion, that is the energy needed to bring from infinity (in a vacuum) into contact two like materials (*i*) reversibly. In the process two interfaces disappear hence the negative sign.

$$\Delta G_{ij}^a = \gamma_{ij} - \gamma_{i(V)} - \gamma_{j(V)} = -W_{ij}^a \qquad (2.22)$$

where $\Delta G^a{}_{ij}$ is the free energy change due to adhesion, that is the energy needed to bring from infinity (in a vacuum) into contact material (*i*) and material (*j*) reversibly. In the process two interfaces disappear and one is created hence the positive sign and the two negative signs. From now onwards we will identify $\gamma_{i(V)}$ to γ_i as a condensed phase's own vapour does not modify its surface tension.

The combination of the corrected Young's equation with Dupré's equation gives rise to the...Young-Dupré equation. After some basic algebra and considering a liquid *L* interacting with a solid *S* its mathematical expression is:

$$\Delta G_{SL}^a = -\gamma_{LV}^* \cos\theta - \gamma_L - \pi_{esv} \qquad (2.23)$$

or,

$$\Delta G_{SL}^a = -\gamma_{LV}^* (1 + \cos\theta) - (\pi_{esv} + \pi_{elv}) \qquad (2.24),$$

These two expressions are equivalent but the second will be preferred as in non-controlled environment, measurements of γ_{LV}^* by the sessile drop method are more likely to be physically meaningful than measurements of γ_L by the pendant drop method. Moreover the 'mercury drop method' is appropriate in estimating the total film pressure $\pi_{esv} + \pi_{elv}$. It is therefore possible to calculate the free energy change related to adhesion or work of adhesion for any liquid-solid pairs from simple macroscopic measurements. Some extra

equations must be combined with equation (2.24) to relate the change in free energy due to adhesion to individual surface tensions and particularly that of the solid being studied. The estimation of the contributions of van der Waals forces, acid-base interactions or others would also be desirable.

Critical surface tension:

Some authors have tried to characterise solid surfaces in terms of quantities that are not surface tensions *sensu stricto* but are related to them to some degree. Notably Shafrin and Zisman [1960], Zisman [1964] measured the contact angle between several homologous series of liquids and polymer surfaces like PTFE. A homologous series of liquids is made of liquids with similar physicochemical properties and surface tensions that vary monotonically from one liquid to the next in the series. They observed that $cos\theta$ varies linearly with the surface tension of the liquid γ_{LV}. They even proposed the following function:

$$\cos\theta_{SLV} = 1 - \beta(\gamma_{LV} - \gamma_c)$$ (2.25),

where θ_{SLV} is the advancing contact angle at the three-phase line. It is obtained by pumping out fluid and filming the expanding droplet. It may or may not be the same as Young's contact angle. β is the slope of the function and γ_c is the critical surface tension. The first liquid belongs to a series that wets the surface ($cos\theta = 1$) and gives the critical surface tension its value. For solids like PTFE that develop only dispersive interactions (London forces) with other materials γ_c seems to be close to the true surface tension [Chaudhury, 1996].

Attempts to provide a thermodynamically sound and direct relationship between solid surface tension and contact angle were made by Neumann *et al.* [1974]. The outcome was the thermodynamic sounding 'equation of state for interfacial tensions of solid-liquid systems'. It was later revised [Li & Neumann, 1990] [Li & Neumann, 1992]. Combining this so-called equation of state with Young's leads to:

$$\cos\theta = -1 + 2\sqrt{\frac{\gamma_{SV}}{\gamma_{LV}}} \exp\left[-\beta(\gamma_{LV} - \gamma_{SV})^2\right]$$ (2.26),

where $\beta = 0.0001247(m^2/mJ)^2$, θ is the contact angle, γ_{LV} is the liquid surface tension in equilibrium with a vapour (the nature and origin of this vapour is not specified) and γ_{SV} is

the solid surface tension in equilibrium with a vapour that could be that of the liquid probe. Besides Li and Neumann [1991] minimise the importance of film pressure on the estimation of solid surface tensions. In a study of talc's surface energetics both in powder and plane sheet form by means of techniques such as immersion microcalorimetry, adsorption isotherm and contact angle measurements, Douillard *et al.* [2002] claim that Li and Neumann's equation of state (EOS) does not estimate the solid surface tension. It is nevertheless useful in that it allows for the calculation of a scaling parameter, which is in fact Zisman's critical surface tension. In other words $\gamma^{EOS}_{SV} = \gamma_c$. Li's and Neumann's EOS can therefore be used to predict wettability behaviours of solids as long as a few contact angle measurements corresponding to probe liquids of different surface tension are available to make a good fit of the function $cos\ \theta = f(\gamma_{L(V)})$. The coefficient β can also be allowed to vary to get a better fit (see equation (2.26)).

Surface Tension Component theories (STC):

They are all based on the idea that free energy changes due to adhesion between two bodies (a liquid and a solid for instance); ΔG^a_{SL} can be expressed in terms of the surface tensions of the interacting bodies. This free energy change is related to experimentally measurable quantities (see equations (2.23) and (2.24)). Girifalco and Good [1957] proposed a geometric mean law:

$$\Delta G^a_{ij} = -2\Phi\left(\gamma_i\gamma_j\right)^{1/2} \qquad (2.27),$$

where Φ is a parameter that depends on the molar volumes of the two liquids [Adamson, 1990]. Fowkes [1963], whom we have mentioned lengthily in § 2.1.2 for his contributions to the study of Lewis acid-base interactions and particularly H-bonds, suggested that, for interactions through dispersive forces only (e.g. one substance is H-bonding and the other is not), equation (2.27) should be modified:

$$\Delta G^a_{ij} = -2\left(\gamma^d_i\gamma^d_j\right)^{1/2} \qquad (2.28),$$

where γ^d_i is the dispersive component of the surface tension of substance *i*. Coefficient Φ has disappeared in the process. Dupré's equation (2.22) finds therefore a new expression:

$$\gamma_{ij} = \gamma_i + \gamma_j - 2\left(\gamma^d_i\gamma^d_j\right)^{1/2} \qquad (2.29).$$

This enables us to get around the problem that there is no experimental way of measuring γ_{SL}, a quantity that is yet fundamental to adhesion studies. The combination of equation (2.29) with Young's equation in its classical, simplified form for a solid-liquid pair yields:

$$\cos\theta = -1 + \frac{2\left(\gamma_S^d \gamma_L^d\right)^{1/2}}{\gamma_L} \tag{2.30}.$$

This is the Girifalco-Good-Fowkes-Young equation (GGFY), the first of a series of semi-empirical models being used nowadays [Adamson, 1990].

Fowkes [1980] proposed to generalise equation (2.28) and (2.29) to take into account acid-base phenomena that he studied experimentally with methods other than contact angle goniometry (see § 2.1.2). To him the total change in free energy due to adhesion should be:

$$\Delta G_{ij}^a = \Delta G_{ij}^d + \Delta G_{ij}^p + \Delta G_{ij}^h \tag{2.31},$$

where ΔG_{ij}^d is the change in free energy related to dispersive interactions, ΔG_{ij}^p is the change in free energy related to dipole interactions (Keesom and Debye forces) and ΔG_{ij}^h is the change in free energy related to H-bond (acid-base) interactions.

Van Oss $et\ al.$ [1988] further developed this idea. Their main contribution concerns the definition of ΔG_{ij}^h. They denote it ΔG_{ij}^{ab} for acid-base interaction. An H-bond donor or electron pair acceptor, that is an acid cannot interact with another acid but necessarily with a base. Equation (2.28) then becomes:

$$\Delta G_{ij}^{ab} = -2\left(\gamma_i^+ \gamma_j^-\right)^{1/2} - 2\left(\gamma_i^- \gamma_j^+\right)^{1/2} \tag{2.32},$$

where γ_i^+ is the acidic or H-bond donating component of the surface tension of substance i, and γ_i^- is the basic or H-bond accepting component of the surface tension of substance i. In this definition substances can be either monopolar: γ_i^+ or $\gamma_i^- = 0$, bipolar : γ_i^+ and $\gamma_i^- \neq 0$ or non-polar: γ_i^+ and $\gamma_i^- = 0$. They also consider the dipole contributions ΔG_{ij}^p to the total change in free energy to be small with respect to both dispersive and acid-base interactions, therefore they combine dipole and dispersive interactions into one quantity that represents all of the electrodynamic Lifshitz-van der Waals interactions, ΔG_{ij}^{LW}. Equations (2.24) and (2.29) can then be completed:

$$-2\left(\gamma_i^{LW} \gamma_j^{LW}\right)^{1/2} - 2\left(\gamma_i^+ \gamma_j^-\right)^{1/2} - 2\left(\gamma_i^- \gamma_j^+\right)^{1/2} = -\gamma_{LV}^*\left(1 + \cos\theta\right) - \left(\pi_{esv} + \pi_{elv}\right) \tag{2.33}$$

$$\gamma_{ij} = \gamma_i + \gamma_j - 2\left(\gamma_i^{LW}\gamma_j^{LW}\right)^{1/2} - 2\left(\gamma_i^+\gamma_j^-\right)^{1/2} - 2\left(\gamma_i^-\gamma_j^+\right)^{1/2} \qquad (2.34),$$

or using squared roots and the formulation of Good *et al.* [1991]:

$$\gamma_{ij} = \left(\sqrt{\gamma_i^{LW}} - \sqrt{\gamma_j^{LW}}\right)^2 + 2\left(\sqrt{\gamma_i^+} - \sqrt{\gamma_j^+}\right)\left(\sqrt{\gamma_i^-} - \sqrt{\gamma_j^-}\right) \qquad (2.34 \text{ bis})$$

Usually equation (2.33) is used in an oversimplified form where film pressure parameters are (wrongly) neglected [Douillard *et al.*, 2002] and liquid surface tension values are taken either from the literature or measured as a pendant drop not in contact with the solid are substituted (wrongly) for γ_{LV}^*.

The additivity assumption made for changes in free energy (see equation (2.31)) has also been made for interface and surface tensions, therefore:

$$\gamma = \gamma^{LW} + \gamma^{ab} \qquad (2.35),$$

where $\gamma^{LW} = \gamma^d + \gamma^i + \gamma^p$: the Lifshitz-van der Waals electrodynamic term combines all three van der Waals types of interaction, namely dispersion, induction and polarisation.

It is noteworthy that there is a relation between the Hamaker constant defined in § 2.1.1 and the Lifshitz-van der Waals component of a surface tension. For substance i interacting with itself through vacuum, one can write:

$$\frac{A_{ii}}{\gamma_i^{LW}} \cong (1.88 \pm 0.19) \times 10^{-18} \, m^2 \qquad (2.36),$$

where γ_i^{LW} is expressed in mJ.m^{-2} and A_{ii} in J [van Oss *et al.*, 1988]. Israelachvili [1992] proposes a slightly larger ratio:

$$\frac{A_{ii}}{\gamma_i^{LW}} \cong 2.1 \times 10^{-18} \, m^2 \qquad (2.37)$$

From equations (2.21), and (2.32) the acid-base component of the surface tension of a substance i can be calculated:

$$\gamma_i^{ab} = 2\left(\gamma_i^+\gamma_i^-\right)^{1/2} \qquad (2.38)$$

Good *et al.*, [1991] have proposed a scale for the acidic and basic components of a substance's surface tension with water as an arbitrary zero. In the Brønsted-Lowry framework water's pH equals 7 so that it is neither a base nor an acid or both. In the Lewis framework, water is both an acid and a base due to its H-bonding nature. They then decided of their own accord that $\gamma_W^+ = \gamma_W^-$. They determined the LW surface tension component of some liquids including water experimentally by depositing a drop of liquid on a purely dispersive (non-polar) material PTFE of known surface tension and measuring the corresponding contact angle. The simplified form of equation (2.33) (see comments accompanying equations (2.33) and (2.34)) then reduces to one unknown.

Acidic components of the same liquids were obtained in a similar manner but with a monopolar basic solid surface: PMMA. The LW component of PMMA's surface tension was determined by using dispersive liquids of high surface tension relative that of common polymers, that is diiodomethane or α-bromonaphthalene. Basic components were determined through equation (2.38). A small set of well-characterised liquids from the surface tension point of view are at the disposal of users to work out the surface tension components of a solid surface (see Table 2.3). In theory the contact angle between three different liquids (ideally one non-polar liquid, one acid and one base) and the solid of interest are enough to obtain the three components of the solid surface tension. This model is often referred to as the vOCG model. We have to bear in mind though that in this semi-empirical model many approximations have been made, in particular film pressures have been neglected.

Liquid	γ	γ^{LW}	γ^{ab}	γ^+	γ^-
Water	72.8	21.8	51	25.5	25.5
Glycerol	64	34	30	3.92	57.4
Formamide	58	39	19	2.28	39.6
Diiodomethane	50.8	50.8	≈ 0	0	0
Ethylene glycol	48	29	19	1.92	47
α-bromonaphthalene	44.4	43.5	≈ 0	0	0
Dimethyl sulfoxide	44	36	8	0.5	32
Hexadecane	27.5	27.5	0	0	0

Table 2.3 Surface tension components for probe liquids in mJ.m^{-2} at 20°C [van Oss *et al.*, 1989].

As can be seen from the table, liquids are systematically basic and even substances whose acidic nature is agreed upon like formamide appear basic. This problem was recognized by the authors themselves [Good *et al.*, 1991] as well as other contributors in the field [Lee, 1996] [Della Volpe *et al.* - 1, 2003]. Using these values without corrections for polymer surface characterisation lead to strange results. For instance PVC would be a base [Good *et al.*, 1991] while it is chemically a Lewis acid [McCafferty, 2003]. The equality of water's acidic and basic components has been questioned by Lee [1996] [2001] and Della Volpe *et al.* [1 - 2003]. Claiming that there is a correlation between acid-base components and spectroscopically determined solvatochromic parameters by Marcus [1993], Lee [1996] proposed that pure water's acid to base component ratio should be 1.8 at 20°C, that is more acidic than basic. Della Volpe *et al.* [1 - 2003] proposed an even higher ratio: 4.3. The 'corrected' liquid surface tension components are presented in Table 2.4 and Table 2.5.

Liquid	γ	γ^{LW}	γ^{ab}	γ^{+}	γ^{-}
Water	72.8	26.2	46.4	48.1	11.2
Glycerol	64	34	28.5	27.8	7.33
Formamide	58	35.5	22.6	11.3	11.3
Diiodomethane	50.8	50.8	≈ 0	0	0
Ethylene glycol	48	33.9	14.1	0.966	51.6
α-bromonaphthalene	44.4	44.4	≈ 0	0	0
Dimethyl sulfoxide	44	32.3	10.7	0.0373	763
Hexadecane	27.6	27.6	0	0	0

Table 2.4 Surface tension components for probe liquids in mJ.m^{-2} at 20°C [Della Volpe *et al.* - 1, 2003].

Liquid	γ	γ^{LW}	γ^{ab}	γ^{+}	γ^{-}
Water	72.8	21.8	51	34.2	19
Glycerol	64	34	30	5.3	42.5
Formamide	58	39	19	3.1	29.1
Diiodomethane	50.8	50.8	≈ 0	0	0
Ethylene glycol	48	29	19	2.6	34.8
α-bromonaphthalene	44.4	43.5	≈ 0	0	0
Dimethyl sulfoxide	44	36	8	0.7	23.8
Hexadecane	*27.5*	*27.5*	*0*	*0*	*0*

Table 2.5 Surface tension components for probe liquids in mJ.m^{-2} at 20°C [Lee, 1996]. Hexadecane was not originally in Lee's table but being a true dispersive liquid we have included it (italics).

The effect of Lee's corrections is not as spectacular as Della Volpe's. Dimethyl sulfoxide (DMSO) got more basic and the acids appear less basic but overall the problem has not been solved. It is worth noticing that in a recently published study by Della Volpe *et al.* [2 - 2003] the characterisation of PVC surfaces using their corrected scale (see Table 2.5) did not give rise to the expected acidity: $\gamma^+_{PVC} = 0.95$ and $\gamma^-_{PVC} = 1.14$. Lee [2001] reckoned that the problem could lie in the fact that neglecting the importance of film pressure due to adsorbed vapour on even low surface tension solids, like polymers is wrong. He developed a semi-empirical model based on the vOCG one but substituted the dispersion component originally introduced by Fowkes [1980] for the Lifshitz-van der Waals component. He also suggested that the film pressure is related to induction and polarisation effects, so that the other two vdW forces are not left out but are still included in the equations. Finally he regards the acid-base interactions that his model can treat as H-bonds only. Rather than making his own measurements, he used published data in order to recalculate the components of the liquid surface tensions free of atmospheric vapour.

Lee [2001] started off with equation (2.33) but for some reason he used a plus sign in front of the film pressure terms, as did Good [1993] earlier. At this stage we do not have an explanation to this strange initiative all the more so since either author did not justify this choice. Repeatedly, work published by the Montpellier school as well as other authors confirms the formulation we propose in equation (2.33) [Malandrini *et al.*, 1997] [Douillard *et al.*, 2002] [Xu *et al.*, 1995].

Lee [2001] uses dispersive and basic polymeric surfaces to recalculate the liquid surface tensions with water as a reference (see Table 2.5). Combining equation (2.33) for water on PMMA with equation (2.33) for another liquid L on the same surface, he obtains an expression where the only unknown is γ^+_L:

$$\frac{\gamma^+_W}{\gamma^+_L} = \left[\frac{\gamma_W \left(1 + \cos\theta^{PMMA}_W\right) - \pi^{PMMA}_{ewv} - 2\left(\gamma^d_W \gamma^d_{PMMA}\right)^{1/2}}{\gamma_L \left(1 + \cos\theta^{PMMA}_L\right) - \pi^{PMMA}_{elv} - 2\left(\gamma^d_L \gamma^d_{PMMA}\right)^{1/2}} \right]^2 \qquad (2.39).$$

The result of this computation is a series of so-called initial surface tension components [Lee, 2001]. These values fill Table 2.6, a table established in the same spirit as Table 2.4 and Table 2.5.

Liquid	γ	γ^d	γ^h	γ^+	γ^-
Water	72.8	21.8	51	34.2	19
Glycerol	64	34	30	17.4	12.9
Formamide	58	28	30	22.4	10.1
Diiodomethane	50.8	50.8	≈ 0	0	0
Ethylene glycol	_48_	_29_	_19_	_15.1_	_6_
α-bromonaphthalene	44.4	43.5	≈ 0	0	0
Dimethyl sulfoxide	44	29	15	2	28
Hexadecane	*27.5*	*27.5*	*0*	*0*	*0*

Table 2.6 Initial (vapour free) tension components for probe liquids in mJ.m^{-2} at 20°C [Lee, 2001]. Values for ethylene glycol are underlined because they result from extrapolations. Hexadecane was not originally in Lee's table but being a true purely dispersive liquid, we have included it (italics).

Lee [2001] applied his set of values to PVC surfaces and obtained the following H-bond donating (acidic) and H-bond accepting (basic) values: $\gamma_{PVC}^+ = 7.3$ mJ.m^{-2} and $\gamma_{PVC}^- = 2.0$ mJ.m^{-2}. The acidic nature of PVC considered in terms of H-bond is clear. However the uncertainties as regards equation (2.39) due to the correct use, in equation (2.33), of the film pressure terms are still present.

The case of two bodies (solid or not) interacting in a medium, often water or even organic liquids is a common situation. The treatment of van Oss *et al.* [1988] applies in a similar way as it does for two bodies interacting through vacuum. The change is surface free energy due to adhesion between substances *i* and *j* through medium *k* is obviously:

$$\Delta G_{ikj}^a = \Delta G_{ikj}^{LW} + \Delta G_{ikj}^{ab} \qquad (2.40)$$

The Lifshitz van der Waals component is:

$$\Delta G_{ikj}^{LW} = \gamma_{ij}^{LW} - \gamma_{ik}^{LW} - \gamma_{jk}^{LW} = 2\left(\sqrt{\gamma_i^{LW}} - \sqrt{\gamma_k^{LW}}\right)\left(\sqrt{\gamma_k^{LW}} - \sqrt{\gamma_j^{LW}}\right) \qquad (2.41),$$

while the acid/base (H-bond donor/H-bond acceptor) component is:

$$\Delta G_{ikj}^{ab} = 2\left[\sqrt{\gamma_k^+}\left(\sqrt{\gamma_i^-} + \sqrt{\gamma_j^-} - \sqrt{\gamma_k^-}\right) + \sqrt{\gamma_k^-}\left(\sqrt{\gamma_i^+} + \sqrt{\gamma_j^+} - \sqrt{\gamma_k^+}\right) - \sqrt{\gamma_i^+\gamma_j^-} - \sqrt{\gamma_i^-\gamma_j^+}\right]$$

$$(2.42)$$

One-liquid model:

The three previous models are multi-liquid models. It is not always possible to have three liquids with a high enough surface tension not to wet completely the solid surface to be characterised. We have presented the GGFY model as being the first one-liquid model, unfortunately it is limited mainly to dispersive and low surface tension materials. A one-liquid model suitable for high energy materials usually quite strongly acidic or basic would be of value. A group based in Argentina and interested in clay minerals, recently proposed such a model which they applied to the determination of montmorillonite's surface tension [Helmy *et al.*, 2003]. They combine Young's equation in its proper form (film pressure included) with a general relation for binary systems, close to the equation (2.29)-type:

$$\gamma_S + \gamma_L - k\gamma_{SL} = 0 \qquad (2.43)$$

Isolating k, they calculate its value for a number of possible values of γ_S within a sensible range. The resulting curve can be fitted by a polynomial with appropriate coefficients. Finally they eliminate k and solve the equation for γ_S. This only provides the total surface tension without any information about the physicochemical properties of a material's surface but it is useful nonetheless.

Some uncertainties in STC and contact angle measurements:

Many groups have studied the validity of the acid-base vOCG model[2]; we can cite Della Volpe and Siboni [1997], Gindl *et al.* [2001] and more recently Shalel-Levanon and Marmur [2003]. They all conclude that sensible results are usually obtained when the three probe liquids represent each major type of interaction, namely LW, H-bond acceptor and H-bond donor. It is even worth measuring the contact angle of five or more probe liquids and solve an overdetermined set of equations by minimisation methods to avoid getting negative acidic surface tension components [Gindl *et al.*, 2001] [Della Volpe & Siboni, 1997]. The latter have even developed an online program that implements this multi-liquid approach (three or more liquids). Criticisms regarding the thermodynamic foundations of these models have been made recently by Douillard [1997] and other members of the 'Montpellier school' [Médout-Marère, 2000]. They criticise the fact that the interactions between substances are treated in terms of surface tension, that is from a thermodynamic viewpoint,

---

[2] Lee's model can be considered a variation of the vOCG model.

surface free enthalpy, and not energy or enthalpy. In the bulk, internal energy and enthalpy differ by the product of pressure by volume. At the surface volume effects are negligible so that internal energy and enthalpy are almost identical. Surface enthalpy is therefore the relevant quantity to treat interaction between condensed phases. Equations of the type of equation (2.34) should therefore apply to surface enthalpies and not surface tensions:

$$H_{ij}^S = H_i^S + H_j^S - f\left(H_1^S, H_2^S\right) \qquad (2.44)$$

How does the surface free enthalpy relate to the surface enthalpy? At chemical equilibrium between two insoluble phases:

$$dH^S = TdS^S - Ad\gamma \text{ and } dG^S = -Ad\gamma \qquad (2.45),$$

where dH^S is the differential of the surface enthalpy, dS^S is the differential of the surface entropy, dG^S is the differential of the surface free enthalpy, A is the surface area and γ is the surface tension.

It is clear that the knowledge of the surface enthalpy is not sufficient to obtain information on the surface free enthalpy, hence of the surface tension. Surface entropy is needed too [Douillard, 1997]. At least are dH^S and dG^S proportional? In equation (2.45) we can eliminate the surface tension term and switch from differentials to variations:

$$\Delta G^S = f\Delta H^S \text{ with } f = 1 - T\frac{\Delta S^S}{\Delta H^S} \qquad (2.46),$$

f is not constant, it depends on the temperature. Even if experiments are being performed at a given temperature, can the entropy be considered constant? Douillard observes that for many solids and liquids of interest, whose melting point and boiling point are far from ambient temperature and pressure, the variations of entropy must be similar. He adds that this is the reason why surface tension component models give usually satisfactory results: the value of f is not known but there is proportionality so that any change in surface enthalpy brings about a proportional change in surface free enthalpy and therefore in surface tension. Polymers whose glass transition temperature T_g is close to ambient conditions may exhibit non-linearity in surface tension change.

2.2. Elements of polymer physics: solutions and thin films

2.2.1. Polymer chains in a solvent

When polymer chains are 'few', they rarely interact with each other; they are said to be in *dilute regime*. They form coils whose size or radius of gyration is: $R_F \cong aN^{3/5}$, with N being the number of monomers in a chain and a is Kuhn's length, a quantity that is not very different from the size of one monomer [Flory, 1971]. The free energy F of such a chain is:

$$\frac{F}{kT} = (1 - 2\chi)\frac{N^2 a^3}{R_F^3} + \frac{R_F^2}{Na^2} \qquad (2.47),$$

where k is Bolzmann's constant, T is temperature and χ is the Flory-Huggins interaction parameter. The first term on the right hand side of the equation is related to enthalpic effects between solvent molecules and monomers. When the chain size increases the free energy decreases, which is favourable: this is the *excluded volume effect*. Monomers cannot be too close to each other. On the other hand, the other ratio (second term on the right hand side of the equation) increases due to an unfavourable effect on entropy: an expanding chain has fewer conformations to choose from. The minimisation of the free energy imposes the equilibrium size of the chains.

The closer χ to zero the more favourable the solvent-monomer interactions, that is the better the solvent. Practically, solvents whose Flory-Huggins interaction parameter χ with a given polymer ranges from 0 to 0.5 are considered good. Experimental values of χ are tabulated [Brandrup *et al.*, 1999]. It can also be predicted using an equation proposed by Flory [1971]:

$$\chi \approx 0.34 + \frac{V}{RT}(\delta_S - \delta_P)^2 \qquad (2.48),$$

where V is the solvent molar volume, δ_S is the solubility parameter of the solvent and δ_P is the solubility parameter of the polymer.

Supposing that the number of chains increases, at some stage they will start to come into contact often and even overlap. In this situation the monomer volume fraction ϕ_0^* (or concentration) in a coil is roughly equal to that of the chains in solution:

$$\phi_0^* = \frac{Na^3}{R_F^3}, \qquad \text{hence} \qquad \phi_0^* \cong N^{-4/5} \qquad (2.49)$$

The volume fraction depends on the size or polymerisation index of chains. Above ϕ_0^* the system is in semi-dilute regime with frequent chain entanglements. We can predict the value of ϕ_0^* for PDMS samples of various polymerisation indices (see Table 2.7).

	PDMS molecular mass (10^3 g.mol^{-1})						
	162	110	80.5	49	15.2	8.1	5.5
$\phi^*(\%)$	0.29	0.21	0.37	0.55	1.41	2.34	3.18

Table 2.7 Critical volume fraction for a series of PDMS samples.

2.2.2. Preparation of polymer monolayers and sub-monolayers

A monolayer is a film of thickness the size of one macromolecule and covering the whole substrate surface without free space in between neighbouring sites. A sub-monolayer is a layer whose chains are separated by some free space (not all surface sites are occupied). Polymer monolayers are formed by anchoring or grafting polymer chains onto appropriate substrates. The grafting mechanism (see Fig. 2.4) can be chemical or of acid-base type (e.g. covalent bond, hydrogen bond) or purely physical (van der Waals interactions, physisorption) and can occur either at the end or on the backbone of the polymer chain.

End-anchoring also referred to as end-tethering can be done by using polymers with ends made up of a specific chemical group. Some common examples are thiol-terminated polymers on gold substrates, where the thiol group forms a covalent bond with gold or diblock-copolymers where one of the blocks has a physical affinity to the substrate while the other block prefers the solvent/air.
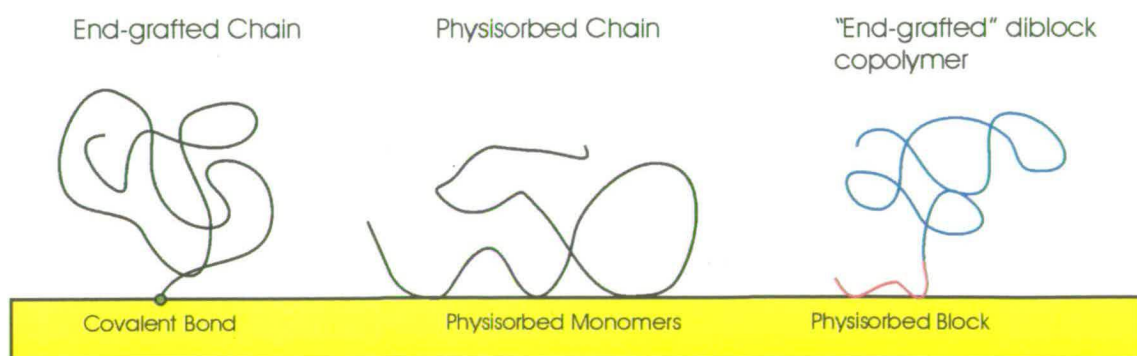

Fig. 2.4. Polymer chains anchored to a substrate through three processes.

Anchoring to the surface is performed by bringing the clean or freshly cleaved substrate into contact with a polymer medium that, depending on the type of polymer, can be a dilute or semi-dilute polymer solution or a pure polymer melt. Dipping the substrate into the polymer medium (solution or melt) is one possibility but spin coating, or simple deposition of a drop of the polymer medium onto the substrate are also being employed. In any case, to form a monolayer it is necessary to subsequently rinse and/or immerse the treated substrate in a good solvent to remove any polymer excess (chains that are not surface-anchored but entangled to the anchored ones). Anchoring is sometimes a reversible phenomenon, that is physisorbed chains can be readily desorbed from the substrate if immersed in a good solvent for adequate time) and sometimes irreversible (e.g. chemisorbed chains or strong acid-base interactions like H-bonds).

The surface density of the polymer on the substrate can be controlled by a variety of methods:

- incubation time in the polymer medium,
- the anchoring mechanism and its kinetics,
- polymer concentration,
- the presence of small molecules which self assemble on the substrate trapping and reducing the number of anchoring sites available for polymer adsorption.

2.2.3. Polymers at surfaces

<u>Theoretical aspects:</u>

Much theoretical and simulation work has been done on the structure and physical properties of anchored polymer layers over the past 30 and even 40 years. For example see the pioneering work done by Alexander [1977], De Gennes [1980] [1987], Milner *et al.* [1988] as well as important reviews [Milner, 1991] [Halperin, 1991].

Studies based on random phase approximation (RPA) [Ross, 1992], RPA combined with numerical mean field analysis [Yeung, 1993], scaling analysis [Tang, 1994], Monte Carlo (MC) [Lai, 1992] [Soga, 1995] and Molecular Dynamics Simulations (MD) [Grest, 1993] showed that below the θ-temperature (i.e. for poor or bad solvent conditions) and for rather moderate grafting densities, polymer monolayers organise in the form of polymer-rich clusters or dimples (tubes). At high grafting densities homogeneous monolayers are predicted. A scaling analysis has been developed based on the comparison between the free

energy of a homogeneous brush with that of a micelle-like structure [Williams, 1993] [Zhulina *et al.*, 1995]. This model is more appropriate in the strong segregation limit (bad solvent or dry state) and predicts that many chains fuse to form a compact core that is connected to the surface through the grafted tethers.

We now summarise the main results regarding the structure of polymer chains at surfaces obtained from scaling theory that provides simple power laws [De Gennes, 1979] [Rubinstein & Colby, 2003] [Léger *et al.*, 1999]. Those are correct to an approximation of a constant at the order of unity. The importance of the results of the simple scaling theory is that it gives approximate but simple analytical formulas to describe the structure and physical properties of monolayers.

At low grafting densities, polymer chains are isolated and their structure resembles individual "mushrooms": (the so-called mushroom regime). Their size to first approximation (if the effect of tethering and the interactions with the surface are negligible) is equal to the size R_0 of an unperturbed polymer chain in the bulk (see Fig. 2.5). This size depends on the solvent conditions:

- $R_0 \cong aN^{3/5}$,   good-solvent conditions (athermal solvent: $\chi = 0$)

- $R_0 \cong aN^{1/2}$, θ-solvent or melt

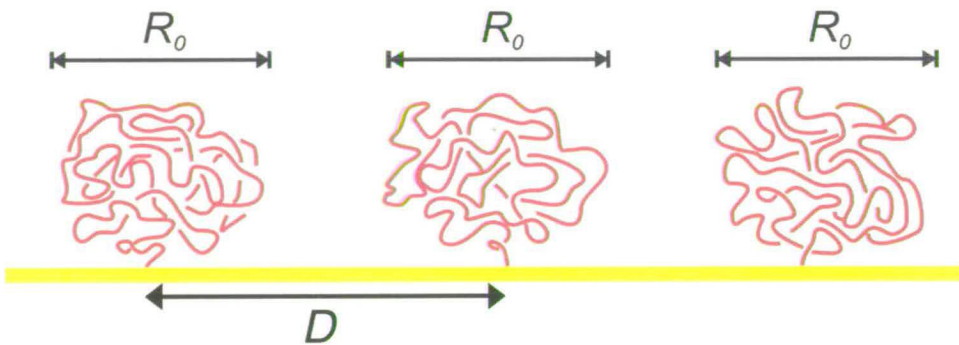- $R_0 \cong aN^{1/3}$,   bad-solvent conditions

Fig. 2.5. Mushroom regime. Isolated end-grafted polymer chains of size R_0.

The dimensionless grafting density is defined as $\Sigma = \dfrac{a^2}{D^2}$, where D is the average distance between two grafting sites.

At higher grafting densities the chains start to overlap according to a scenario similar to that described in § 2.2.1 for free chains in a solution. In good-solvent conditions the critical overlap density $\Sigma_{overlap} \cong N^{-6/5}$. They then form a polymer *"brush"* (see Fig. 2.6) of thickness H_0:

- $H_0 \cong aN\Sigma^{1/3}$,   good-solvent conditions
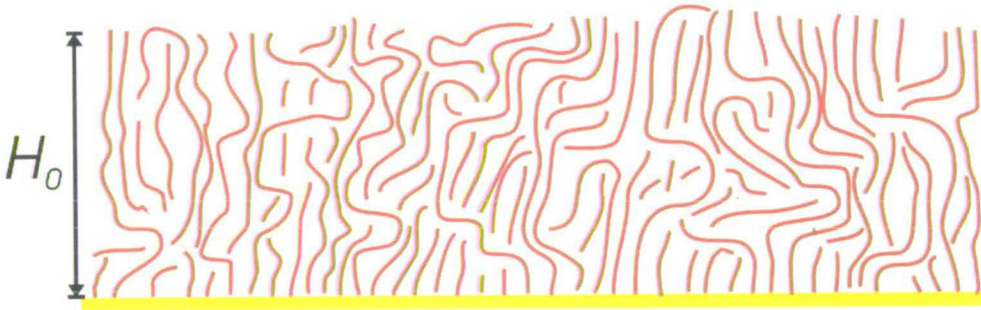
- $H_0 \cong aN\Sigma$,   bad-solvent conditions

Fig. 2.6. Polymer brush. Beyond the critical overlap density, the end-grafted chains form a polymer brush of thickness H_0.

In the particular case of irreversible end-grafting and/or adsorption from semi-dilute solutions of volume fraction ϕ_0 or melt ($\phi_0 = 1$), the dry thickness was first given by [Déruelle *et al*, 1994] and later by [Léger *et al.*, 1999]:

$$H_0 \approx aN^{1/2}\phi_0^{7/8} \qquad (2.50)$$

The thickness of such a polymer brush has to be interpreted as an average distance since at moderate grafting densities ($N^{-4/3} < \Sigma < N^{-1/2}$) and in poor or bad solvent conditions, the polymer chains could microphase separate laterally and organise in pinned "micelles" (see Fig. 2.7) [Williams, 1993] [Zhulina, 1995] [Koutsos, 1997]. The scaling theory predicts $n \cong N^{4/5}\Sigma^{3/5}$ chains per micelle.
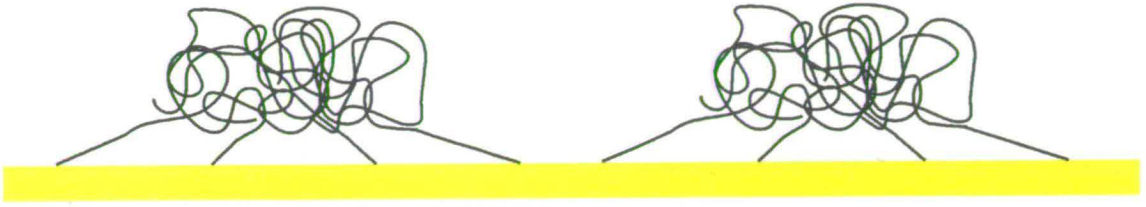
Fig. 2.7. End-grafted polymer chains forming pinned micelles at moderate grafting densities.

In the case of an adsorbed polymer monolayer, that is adsorption from several monomers along the backbone of the polymer chains, the layer is made of a continuous succession of loops (see Fig. 2.8) resembling a highly polydisperse polymer brush of loops. This monolayer is called a "pseudo-brush" and in the particular case of irreversible adsorption from semi-dilute solutions of volume fraction ϕ_0 and/or melt ($\phi_0 = 1$), the thickness in good solvent conditions is given by [Guiselin, 1992] [Léger *et al.*, 1999]:
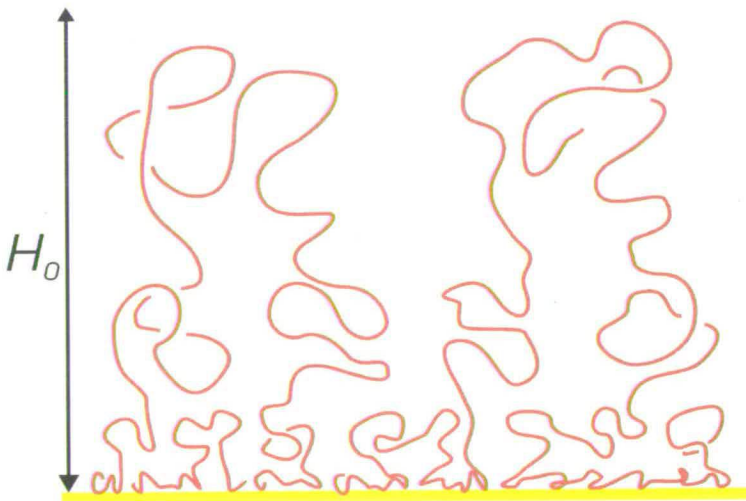
$$H_0 \cong aN^{5/6}\phi_0^{7/24} \tag{2.51}$$

Fig. 2.8. Polymer pseudo-brush. Adsorbed *not-grafted* chains.

Experimental aspects:

Several studies have been performed on *diblock copolymers* grafted/adsorbed on surfaces. O'Shea *et al.* [1993] studied adsorbed PEO/PS block copolymers on mica and observed agglomeration at monolayer coverage in solvents of different quality. Meiners *et al.* [1995] observed that the adsorption of PS-PVP block copolymers from a selective solvent onto mica leads to a highly regular array of spherical micelles. Spatz *et al.* [1996] spin casted ultra-dilute chloroform solutions of a symmetrical PSb-P2VP block copolymer onto mica and observed microscale phase separation. Siqueira *et al.* [1995] used end-functionalised diblock copolymers and observed the three theoretically predicted regimes: homogeneous layer, dimples/tubes and isolated islands when the surface coverage was decreased. Stamouli *et al.* [1996] imaged isolated islands of P2VP/PS diblock copolymer adsorbed onto mica from toluene that were interpreted as surface-octopus micelles (pinned micelles). Not all the adsorbed diblock-copolymer on surfaces studies involve a monomolecular layer (monolayer). We can cite, for example, a more recent study by Zhao *et al.* [2005] showing that symmetric PS-b-P4VP diblock copolymers adsorbed onto mica undergo an island-to-ribbon transition with increasing solution concentration but the polymer layer can be comprised of several alternative layers of self-assembled diblock copolymers.

End-grafted homopolymer chains by chemical bond is another system that has been extensively studied. End-grafted polystyrene chains spun onto silicon substrates were found to tangle together and form islands [Zhao *et al.*, 1994]. Koutsos *et al.*[1997] [1998] [1999] studied systematically the chemisorption of thiol-terminated polystyrene (PS-SH) on gold surfaces from different solvent conditions. This process resulted in the formation of a monolayer of polymer chains. The monolayers were imaged by CFI-SFM (see § 3.1.4) in bad-solvent conditions (water or air). For very dilute polymer solutions in toluene (good solvent) and relatively short incubation times, single polymer chains have been identified. The polymer chains were collapsed individually into globular particles and no clustering was observed. When the grafting density was increased, arrays of aggregated polymer islands were observed. The dimensions of the microclusters were found to be consistent with the scaling laws that were predicted for pinned micelles. The chemisorption of PS-SH molecules to gold from poor-solvent conditions produced a qualitatively different result where the polymer monolayer (arrays) organises itself in the form of semi-continuous dimples (tubes).

Furthermore, several studies focus on the microstructure and physical properties of adsorbed (not necessarily end-grafted) homopolymer chains. In particular, there is considerable interest on various polyectrolytes [Senden *et al.*, 2000] [Feiler *et al.*, 2003] [Haschke *et al.*, 2004] and PDMS [Migler *et al.*, 1993] [Déruelle *et al.*, 1995] [Al-Maawali *et al.*, 2001]. It is usually assumed that the adsorption is strong and a homogeneous layer is formed. In these studies emphasis is put on frictional and adhesive interactions of the monolayer with another other solid (SFM tip) or elastomeric surfaces. Interestingly, infrared dichroism measurements of PDMS adsorption showed a bimodal distribution of conformations [Soga & Granick, 1998]: chains adsorbed from several segments leading to flat conformations and chains adsorbed from few segments leading to perpendicular conformations.

2.3. References

Al-Maawali, S; Bemis, J.E; Akhremitchev, B.B; Leecharoen, R; Janesko, B.G; Walker, G.C. (2001) *Study of the polydispersity of grafted poly(dimethylsiloxane) surfaces using single-molecule atomic force microscopy*, Journal of Physical Chemistry B. **105**(18), 3965-3971.

Adamson, A.W. (1990) *Physical chemistry of surfaces*, Wiley-Interscience, New York, 383-384.

Alexander, S. (1977) *Adsorption of chain molecules with a polar head. A scaling description*, Journal de Physique. **38**(8), 983-987.

Andrieu, C; Sykes, C; Brochard, F. (1994) *Average spreading parameter on heterogeneous surfaces*, Langmuir. **10**(7), 2077-2080.

Bellon-Fontaine, M.N; Cerf, O. (1990) *Experimental determination of spreading pressure in solid/liquid/vapour systems*, Journal of Adhesion Science and Technology. **4**(6), 475-480.

Böhme, G; Hohn, P; Krupp, H; Rabenhorst, H; Schnabel, W; Walter, G. (1973) *Adhesion of gold particles to silicon and gold substrates in ultrahigh vacuum*, Journal of Applied Physics. **44**(9), 3914-3918.

Bolger, J.C; Michaels, A.S. *Molecular structure and electrostatic interaction at polymer-solid interface*. In: *Interface conversion for polymer coatings,* Weiss, P; Dale Cheever, G editors (1968), Elsevier, New York, USA.

Brandrup, J; Immergut, E.H; Grulke, E.A. (1999) *Polymer handbook 4th edition*, John Wiley & Sons, New York, USA.

Busscher, H.J; van Pelt, A.W.J; de Jong, H.P; Arends, J. (1983) *Effect of spreading pressure on surface free energy determinations by means of contact angle measurements*, Journal of Colloid and Interface Science. **95**(1), 23-27.

Busscher, H.J; Kip, G.A.M; van Silfhout, A; Arends, J. (1986) *Spreading pressures of water and n-propanol on polymer surfaces*, Journal of Colloid and Interface Science. **114**(2), 307-313.

Chaudhury, M.K. (1987) *The Hamaker constant and the dispersion force component of the surface tension of liquid mercury*, Journal of Colloid and Interface Science. **119**(1), 174-180.

Chaudhury, M.K. (1996) *Interfacial interaction between low-energy surfaces*, Materials Science and Engineering R-Reports. **16**(3), 97-159.

Christenson, H.K. (1988) *Non-DLVO forces between surfaces - solvation, hydration and capillary effects*, Journal of Dispersion Science and Technology. **9**(2), 171-206.

De Gennes, P.G. (1979) *Scaling concepts in polymer physics*, Cornell University Press, Ithaca, USA.

De Gennes, P.G. (1980) *Conformations of polymers attached to an interface*, Macromolecules. **13**(5), 1069-1075.

De Gennes, P.G. (1987) *Polymers at an interface: a simplified view*, Advances in Colloid and Interface Science. **27**(3-4), 189-209.

Della Volpe, C; Siboni, S. (1997) *Some reflections on acid-base solid surface free energy theories*, Journal of Colloid and Interface Science. **195**(1), 121-136. The program for the calculation of acid-base solid surface free energy components referred to in the text is called SurfTen 4.3. It can be found and tested at http://macsibo.ing.unitn.it:8080/.

Della Volpe, C; Maniglio, D; Morra, M; Siboni, S. (2002) *The determination of a 'stable-equilibrium' contact angle on heterogeneous and rough surfaces*, Colloids and Surfaces A: Physicochemical and Engineering Aspects. **206**(1-3), 47-67.

1 - Della Volpe, C; Maniglio, D; Siboni, S; Morra, M. (2003) *Recent theoretical and experimental advancements in the application of van Oss-Chaudhury-Good acid-base*

theory to the analysis of polymer surfaces I. General aspects, Journal of Adhesion and Science Technology. **17**(11), 1477-1505.

2 - Della Volpe, C; Siboni, S Maniglio, D; Morra, M; Cassinelli, C; Anderle, M; Speranza, G; Canteri, R; Pederzolli, C; Gottardi, G; Janikowska, S; Lui, A. (2003) *Recent theoretical and experimental advancements in the application of van Oss-Chaudhury-Good acid-base theory to the analysis of polymer surfaces II. Some peculiar cases*, Journal of Adhesion and Science Technology. **17**(11), 1425-1456.

Déruelle, M; Tirrell, M; Marciano, Y; Hervet, H; Léger, L. (1994) *Adhesion energy between polymer networks and solid surfaces modified by polymer attachment*, Faraday Discussions. **98**, 55-66.

Déruelle, M; Léger, L; Tirrell, M. (1995) *Adhesion at the solid-elastomer interface - Influence of the interfacial chains*, Macromolecules. **28**(22), 7419-7428.

Douillard, J.M; Zoungrana, T; Partyka, S. (1995) *Surface Gibbs free energy of minerals: some values*, Journal of Petroleum Science and Engineering. **14**(1-2), 51-57.

Douillard, J.M. (1997) *Concerning the thermodynamic consistency of the "surface tension components" equations*, Journal of Colloid and Interface Science. **188**(2), 511-515.

Douillard, J.M; Zajac, J; Malandrini, H; Clauss, F. (2002) *Contact angle and film pressure: study of a talc surface*, Journal of Colloid and Interface Science. **255**(2), 341-351.

Drago, R.S; Vogel, G.C; Needham, T.E. (1971) *A four-parameter equation for predicting enthalpies of adduct formation*, Journal of the American Chemical Society. **93**(23), 6014-6026.

Drago, R.S; Burton Parr, L; Chamberlain, C.S. (1977) *Solvent effects and their relationship to the E and C equation*, Journal of the American Chemical Society. **99**(10), 3203-3209.

Dupré, A. (1869) *Théorie mécanique de la chaleur*, Gauthier-Villars, Paris, France, 369.

Feiler, A; Plunkett, M.A; Rutland, M.W. (2003) *Atomic force microscopy measurements of adsorbed polyelectrolyte layers. 1. Dynamics of forces and friction*, Langmuir. **19**(10), 4173-4179.

Flory, P.J. (1971) *Principles of polymer chemistry*, Cornell University Press, Ithaca, USA.

Fowkes, F.M. (1963) *Additivity of intermolecular forces at interfaces. 1. Determination of contribution to surface and interfacial tensions of dispersion forces in various liquids*, Journal of Physical Chemistry. **67**(12), 2538-2541.

Fowkes, F.M; Mostafa, M.A. (1978) *Acid-base interactions in polymer adsorption*, Industrial & Engineering Chemistry Product Research and Development. **17**(1), 3-7.

Fowkes, F.M. (1980) *Surface effects of anisotropic London dispersion forces in n-alkanes*, Journal of Physical Chemistry. **84**(5), 510-512.

Fowkes, F.M; Tischler, D.O; Wolfe, J.A; Lannigan, L.A; Ademu-John, C.M; Halliwell, M.J. (1984) *Acid-base complexes of polymers*, Journal of Polymer Science Part A - Polymer Chemistry. **22**(3), 547-566.

Fowkes, F.M; Joslin, S.T. (1985) *Surface acidity of ferric oxides studied by flow microcalorimetry*, Industrial & Engineering Chemistry Product Research and Development. **24**(3), 369-375.

Gaboriaud, R. (1996) *Physico-chimie des solutions*, Masson, Paris, France.

Gindl, M; Sinn, G; Gindl, W; Reiterer, A; Tschegg, S. (2001) *A comparison of different methods to calculate the surface free energy of wood using contact angle measurements*, Colloids and Surfaces A: Physicochemical and Engineering Aspects. **181**(1-3), 279-287.

Girifalco, L.A; Good, R.J. (1957) *A theory for the estimation of surface and interfacial energies. I. Derivation and application to interfacial tension*, Journal of Physical Chemistry. **61**(7), 904-909.

Good, R.J; Chaudhury, M.K; van Oss, C.J. *Theory of adhesive forces across interfaces. 2. Interfacial hydrogen bonds as acid-base phenomena and as factors enhancing adhesion.* In: *Fundamentals of adhesion,* Lee, L-H editor (1991), Plenum Press, New York, USA, 153-172.

Good, R.J. *Contact angle, wettability and adhesion: a critical review.* In: *Contact Angle, Wettability and Adhesion,* Mittal, K.L editor (1993), VSP, 3-36.

Grest, G.S; Murat, M. (1993) *Structure of grafted polymeric brushes in solvents of varying quality. A molecular-dynamics study,* Macromolecules. **26**(12), 3108-3117.

Guiselin, O. (1992) *Irreversible adsorption of a concentrated polymer-solution,* Europhysics Letters. **17**(3), 225-230.

Gutowski, W. *Thermodynamics of adhesion.* In: *Fundamentals of adhesion,* Lee, L-H editor (1991), Plenum Press, New York, USA, 87-135.

Halliday, D; Resnick, R; Walker, J. (2001) *Fundamental of Physics 6th edition,* John Wiley & Sons, New York USA.

Halperin, A; Tirrell, M; Lodge, T.P. (1992) *Tethered chains in polymer microstructures,* Advances in Polymer Science. **100**, 31-71.

Hamaker, H.C. (1937) *The London-van der Waals attraction between spherical particles,* Physica. **4**, 1058-1072.

Haschke, H; Miles, M.J; Koutsos, V. (2004) *Conformation of a single polyacrylamide molecule adsorbed onto a mica surface studied with atomic force microscopy,* Macromolecules. **37**(10), 3799-3803.

Helmy, A.K; Ferreiro, E.A; de Bussetti, S.G. (2003) *The surface energy of montmorillonite,* Journal of Colloid and Interface Science. **268**(1), 263-265.

Hu, P; Adamson, A.W. (1977) *Adsorption and contact angle studies II. Water and organic substances on polished polytetrafluoroethylene*, Journal of Colloid and Interface Science. **59**(3), 605-614.

Hutter, J.L; Bechhoefer, J. (1993) *Manipulation of van der Waals forces to improve image resolution in atomic-force microscopy*, Journal of Applied Physics. **73**(9), 4123-4129.

Israelachvili, J.N. (1992) *Intermolecular & surface forces*, Academic Press, San Diego, USA.

Isaacs, E.D; Shukla, A; Platzman, P.M; Hamann, D.R; Barbiellini, B; Tulk, C.A. (1999) *Covalency of the hydrogen bond in ice: a direct x-ray measurement*, Physical Review Letters. **82**(3), 600-603.

Jasper, J.J. (1972) *The surface tension of pure liquid compounds*, Journal of Physical and Chemical Reference Data. **1**(4), 841-1009.

Jensen, W.B. (1980) *The Lewis acid-base concept*, Wiley-Interscience, New York, USA.

Koutsos, V; van der Vegte, E.W; Pelletier, E; Stamouli, A; Hadziioannou, G. (1997) *Structure of chemically end-grafted polymer chains studied by scanning force microscopy in bad-solvent conditions*, Macromolecules. **30**(16), 4719-4726.

Koutsos, V; van der Vegte, E.W; Grim, P.C.M;Hadziioannou, G. (1998) *Isolated polymer chains via mixed self-assembled monolayers: morphology and friction studied by scanning force microscopy*, Macromolecules. **31**(1), 116-123.

Koutsos, V; van der Vegte, E.W; Hadziioannou, G. (1999) *Direct view of structural regimes of end-grafted polymer monolayers: a scanning force microscopy study*, Macromolecules. **32**(4), 1233-1236.

Krupp, H. (1967) *Particle adhesion. Theory and experiment*, Advances in Colloid and Interface Science. **1**(2), 111-239.

Kwok, D.Y; Lam. C.N.C; Li, A; Leung, R; Wu, R; Mok, E; Neumann, A.W. (1998) *Measuring and interpreting contact angles: a complex issue*, Colloids and Surfaces A: Physicochemical and Engineering Aspects. **142**(2-3), 219-235.

Lai, P.Y; Binder, K. (1992) *Structure and dynamics of polymer brushes near the theta point. A Monte-Carlo simulation*, Journal of Chemical Physics. **97**(1), 586-595.

Layman, K.A; Hemminger, J.C. (2004) *Determination of surface OH acidity from the formation of acid/base complexes on ultrathin films of γ-Al$_2$O$_3$ on NiAl(100)*, Journal of Catalysis. **222**(1), 207-213.

Lee, L-H. *The chemistry and physics of solid adhesion*. In: *Fundamentals of adhesion,* Lee, L-H editor (1991), Plenum Press, New York, USA, 1-86.

Lee, L-H. (1996) *Correlations between Lewis acid-base surface interaction components and linear solvation energy relationship solvatochromic α and β parameters*, Langmuir. **12**(6), 1681-1687.

Lee, L-H. (2001) *The unified Lewis acid-base approach to adhesion and solvation at the liquid-polymer interface*, Journal of Adhesion. **76**(2), 163-183.

Léger, L; Raphaël, E; Hervet, H. (1999) *Polymers in confined environments*, Advances in Polymer Science. **138**, 185-225.

Li, D; Neumann, A.W. (1990) *A reformulation of the equation of state for interfacial tensions*, Journal of Colloid and Interface Science. **137**(1), 304-307.

Li, D; Neumann, A.W. (1991) *Thermodynamics of contact angle phenomena in the presence of a thin liquid film*, Advances in Colloid and Interface Science. **36**, 125-151.

Li, D; Neumann, A.W. (1992) *Equation of state for interfacial tensions of solid-liquid systems*, Advances in Colloid and Interface Science. **39**, 299-345.

Lide, D.R. (2001) *CRC handbook of chemistry and physics 82nd edition*, CRC Press, New York, USA.

Malandrini, H; Sarraf, R, Faucompré, B; Partyka, S; Douillard, J.M. (1997) *Characterization of quartz particle surfaces by immersion calorimetry*, Langmuir. **13**(5), 1337-1341.

Marcus, Y. (1993) *The properties of organic liquids that are relevant to their use as solvating solvents*, Chemical Society Reviews. **22**(6), 409-416.

McCafferty, E. (2003) *Lewis acid/Lewis base effects in corrosion and polymer adhesion at aluminium surfaces*, Journal of the Electrochemical Society. **150**(7), 342-247.

Médout-Marère, V; Malandrini, H; Zoungrana, T; Douillard, J.M; Partyka, S. (1998) *Thermodynamic investigation of surface of minerals*, Journal of Petroleum Science and Engineering. **20**(3-4), 223-231.

Médout-Marère, V. (2000) *A simple experimental way of measuring the Hamaker constant A_{11} of divided solids by immersion calorimetry in apolar liquids*, Journal of Colloid and Interface Science. **228**(2), 434-437.

Médout-Marère, V; Partyka, S; Dutartre, R; Chauveteau, G; Douillard, J.M. (2003) *Surface heterogeneity of passively oxidized silicon carbide particles: vapor adsorption isotherms*, Journal of Colloid and Interface Science. **262**(2), 309-320.

Meiners, J.C; Ritzi, A; Rafailovich, M.H; Sokolov, J; Mlynek, J; Krausch, G. (1995) *2-Dimensional micelle formation of polystyrene-poly(vinylpyridine) diblock copolymers on mica surfaces*, Applied Physics A-Materials Science & Processing. **61**(5), 519-524.

Meyer, E; Hug, H.J; Bennewitz, R. (2004) *Scanning probe microscopy. The lab on a tip*, Springer-Verlag, Berlin, Germany.

Migler, K.B; Hervet, H, Léger, L. (1993) *Slip transition of a polymer melt under shear-stress*, Physical Review Letters. **70**(3), 287-290.

Milner, S. T; Witten, T.A; Cates, M.E. (1988) *Theory of the grafted polymer brush*, Macromolecules. **21**(8), 2610-2619.

Milner, S. T.(1991) *Polymer brushes,* Science. **251**(4996), 905-914.

Neumann, A.W; Good, R.J; Hope, C.J; Sejpal, M. (1974) *An equation-of-state approach to determine surface tensions of low-energy solids from contact angles*, Journal of Colloid and Interface Science. **49**(2), 291-304.

Ninham, B.W; Parsegian,V.A. (1970) *Van der Waals forces: special characteristics in lipid-water systems and a general method of calculation based on Lifshitz theory*, Biophysics Journal. **10**(7), 646-663.

O'Shea, S.J; Welland, M.E; Rayment, T. (1993) *An atomic force microscope study of grafted polymers on mica*, Langmuir. **9**(7), 1826-1835.

Palik, E.D. (1985) *Handbook of optical constants of solids*, Academic Press Inc.

Parsegian, V.A; Weiss, G.H. (1981) *Spectroscopic parameters for computation of van der Waals forces*, Journal of Colloid and Interface Science. **81**(1), 285-289.

Rabinovich, Y.I; Derjaguin, B.V. (1988) *Interaction of hydrophobized filaments in aqueous-electrolyte solutions*, Colloids and Surfaces. **30**(3-4), 243-251.

Ross, R.S; Pincus, P. (1992) *Bundles-end-grafted polymer layers in poor solvent*, Europhysics Letters. **19**(2), 79-84.

Rubinstein, N; Colby, R.H. (2003) *Polymer physics*, Oxford University Press, New York, USA.

Senden, T.J; Di Meglio, J.M; Silberzan, I. (2000) *The conformation of adsorbed polyacrylamide and derived polymers*, Comptes Rendus de l'Académie des Sciences Série IV: Physique Astrophysique. **1**(9), 1143-1152.

Shafrin, E.G; Zisman, W.A. (1960) *Constitutive relations in the wetting of low energy surfaces and the theory of the retraction method of preparing monolayers*, Journal of Physical Chemistry. **64**(5), 519-524.

Shalel-Levanon, S; Marmur, A. (2003) *Validity and accuracy in evaluating surface tension of solids by additive approaches*, Journal of Colloid and Interface Science. **262**(2), 489-499.

Siqueira, D.F; Kohler, K; Stamm, M. (1995) *Structures at the surface of dry thin-films of grafted copolymers*, Langmuir. **11**(8), 3092-3096.

Soga, I; Granick, S. (1998) *Infrared dichroism and surface conformational dynamics of adsorbed poly(dimethylsiloxane)*, Macromolecules. **31**(16), 5450-5455.

Soga, K.G; Guo, H; Zuckermann, M.J. (1995) *Polymer brushes in a poor solvent*, Europhysics Letters. **29**(7), 531-536.

Spatz, J.P; Sheiko, S; Moller, M. (1996) *Substrate-induced lateral micro-phase separation of a diblock copolymer*, Advanced Materials. **8**(6), 513-517.

Stamouli, A; Pelletier, E; Koutsos, V; van der Vegte, E.W; Hadziioannou, G. (1996) *An atomic force microscopy study on the transition from mushrooms to octopus surface "micelles" by changing the solvent quality*, Langmuir. **12**(13), 3221-3224.

Tadros, M.E; Hu, P; Adamson, A.W. (1974) *Adsorption and contact angle studies I. Water on smooth carbon, linear polyethylene, and stearic acid-coated copper*, Journal of Colloid and Interface Science, **49**(2), 184-195.

Tang, H; Szleifer, I. (1994) *Phase-behavior of grafted polymers in poor solvents*, Europhysics Letters. **28**(1), 19-24.

Van den Tempel, M. (1972) *Interaction forces between condensed bodies in contact*, Advances in Colloid and Interface Science. **3**(2), 137-159.
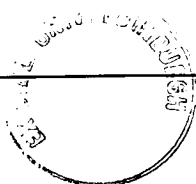
Van Oss, C.J; Chaudhury, M.K; Good, R.J. (1988) *Interfacial Lifshitz-van der Waals and polar interactions in macroscopic systems*, Chemical Reviews. **88**(6), 927-941.

Van Oss, C.J; Ju, L; Chaudhury, M.K; Good, R.J. (1989), *Estimation of the polar parameters of the surface tension of liquids by contact angle measurements on gels*, Journal of Colloid and Interface Science. **128**(2), 313-319.

Villette, S; Valignat, M.P; Cazabat, A.M; Jullien, L; Tiberg, F. (1996) *Wetting on the molecular scale and the role of water. A case study of wetting of hydrophilic silica surfaces*, Langmuir. **12**(3), 825-830.

Williams, D.R.M. (1993) *Grafted polymers in bad solvents – octopus surface micelles*, Journal de Physique II. **3**(9), 1313-1318.

Xu, Z; Liu, Q; Ling, J. (1995) *An evaluation of the van Oss-Chaudhury-Good equation and Neumann's equation of state approach with mercury substrate*, Langmuir. **11**(3), 1044-1046.

Yaws, C.L. (1999) *Chemical properties handbook*, McGraw-Hill, New York, USA.

Yeung, C; Balazs, A.C; Jasnow, D. (1993) *Lateral instabilities in a grafted layer in a poor solvent*, Macromolecules. **26**(8), 1914-1921.

Young, T. (1805) *An essay on the cohesion of fluids*, Philosophical Transactions of the Royal Society of London. **95**, 65-87.

Zhao, W; Krausch, G; Rafailovich, M.H; Sokolov, J. (1994) *Lateral structure of a grafted polymer layer in a poor solvent*, Macromolecules. **27**(11), 2933-2935.

Zhao, J.C; Tian, S.Z; Wang, Q; Liu, X.B; Jiang, S.C; Ji, X.L; An, L.J; Jiang, B.Z. (2005) *Nanoscopic surface patterns of diblock copolymer thin films*, European Physical Journal E. **16**(1), 49-56.

Zhulina, E.B; Birshtein, T.M; Priamitsyn, V.A; Klushin, L.I. (1995) *Inhomogeneous structure of collapsed polymer brushes under deformation*, Macromolecules. **28**(25), 8612-8620.

Zisman, W.A. (1964) *Relation of equilibrium contact angle to liquid and solid constitution*, Advances in Chemistry Series. **43**, 1-51.

3. Experimental techniques and sample preparation

In this chapter we describe the various experimental techniques that were used to characterise the organic films and the methods of sample preparation. The former include non-destructive imaging techniques: scanning white light interferometry (SWLI), scanning force microscopy (IC-SFM); x-ray photoelectron spectroscopy (XPS), a surface chemical analysis technique and finally contact angle goniometry (CAG), a surface tension probing technique.

3.1. Experimental techniques

3.1.1. Scanning White Light Interferometry (SWLI)

As was shown in Young's famous double-slit interference experiment in 1801, waves coming from slit S_1 and slit S_2 (coherent light) that recombine at an arbitrary point P give rise to interference fringes (see Fig. 3.1) because ray r_1 and ray r_2 have travelled different distances on arriving at point P. The phase difference between the two rays is directly related to the path length difference or optical path difference ΔL [Halliday *et al.*, 2001].
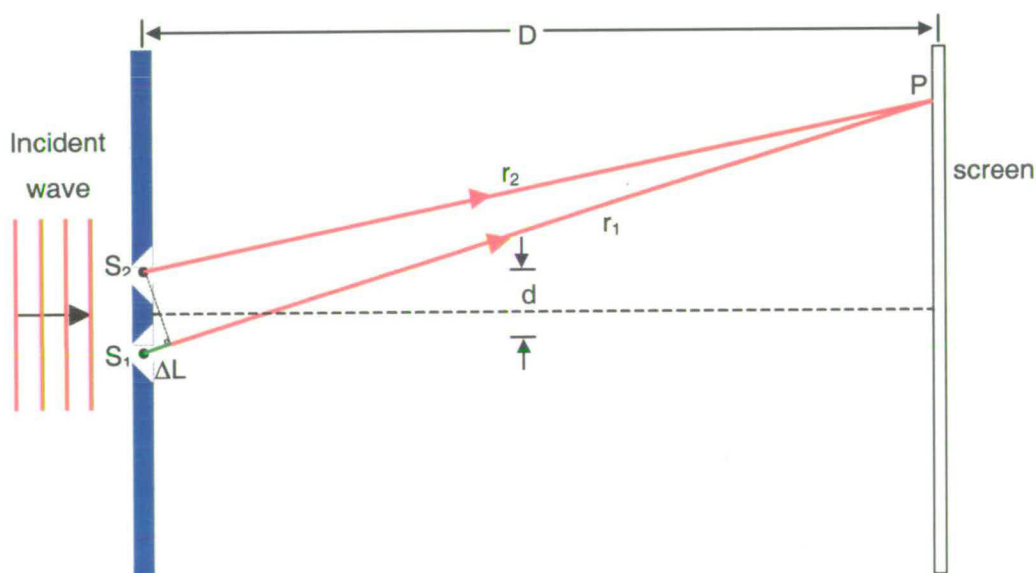

Fig. 3.1. Young's double slit experiment [Halliday *et al.*, 2001]. Ray r_1 arrives at point P later than ray r_2 because it travels longer distance. The path length difference is approximately ΔL if $D \gg d$.

It can be shown that:

$$\phi = k\Delta L + \phi_0, k = \frac{2\pi}{\lambda}$$
(3.1),

where ϕ is the phase difference, ϕ_0 is a constant phase offset, k is the wave vector and λ is the wavelength. This relationship is at the base of the development of interferometric techniques to measure surface topography through precise determination of phase difference.

Phase shifting interferometry (PSI):

Traditional laser interferometers often use the well-known Michelson configuration [Onuma *et al.*, 1994]. The main elements of such a two-beam interferometer (see Fig. 3.2) are a laser source, a beam splitter, a photodetector, a reference mirror, an object mirror and a beam splitter that divides the incoming beam into two portions. One travels a longer distance than the other. The round-trip optical path difference (OPD) between the two mirrors is ΔL.
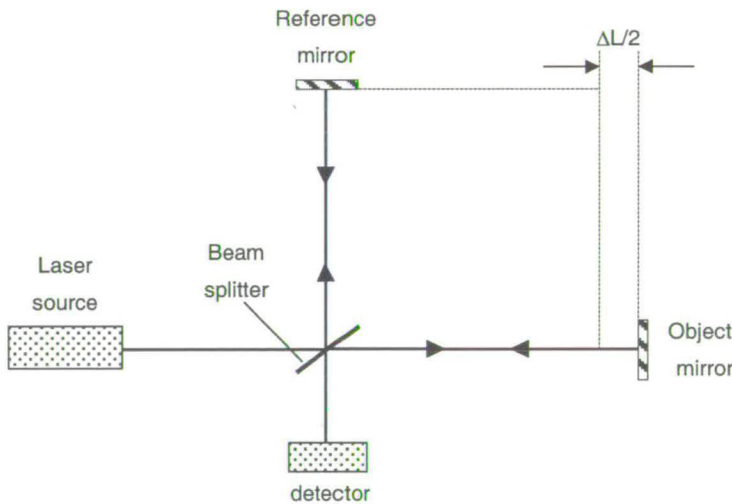

Fig. 3.2. Michelson interferometer [De Groot, 1993]. The laser beam that hits the object mirror (i.e. the sample) travels the longer distance: the path length difference is ΔL.

When the object mirror is scanned backwards so as to increase the OPD, the intensity measured by the detector varies sinusoidally. If the interferometer is well-balanced:

$$I = \frac{1}{2}\left(1 + \cos\phi\right)$$
(3.2)

In phase shifting interferometry, the wavelength λ is known. The phase offset ϕ_0, a parameter that is characteristic of the interferometer and of the material properties of the mirrors, can be determined or fixed arbitrarily. The phase difference ϕ is determined by taking data at a few sample points on the intensity versus OPD sinusoidal curve and transforming the data into the frequency domain by means of an integrating bucket algorithm [McWaid et al., 1992]. The topographic height (one-way trip OPD) at a given location of the sample surface is then:

$$h = \frac{\lambda}{4\pi}(\phi - \phi_0) = \frac{\phi - \phi_0}{2k} \qquad (3.3)$$

While single-wavelength phase shifting interferometry can have precision as high as $\lambda/1000$ [Harasaki et al., 2000], it has limited dynamic range. Phase calculations are only free of ambiguity within the range $\pm\pi$, which corresponds to surface height range of $\pm\lambda/4$. Outside this range the measurement is modulo 2π. To be able to deal with surfaces such that the height difference between two neighbouring datapoints is bigger than $\lambda/4$, one solution is to use two wavelengths [Cheng & Wyant, 1984]. It can be shown that the maximum height difference between two neighbouring pixels is $\lambda_{eq}/4$, where λ_{eq} is given by:

$$\lambda_{eq} = \frac{\lambda_1\lambda_2}{|\lambda_1 - \lambda_2|} \qquad (3.4)$$

By carefully selecting the two wavelengths λ_1 and λ_2, the dynamic range can increase up to several micrometres [Harasaki et al., 2000]. That approach is particularly well suited to step height measurements but not to rough surfaces. A broad range of wavelengths ("white light") and the vertical scanning approach allows for the measurement of almost unlimited range of step heights as well as rough surfaces but at the expense of precision. The challenge in combining phase data and vertical scanning data for higher precision (that offered by classical PSI) over the whole range has been addressed for approximately ten years with partial success. One possible route consists in processing white light interferograms (see Fig. 3.3) by Fourier analysis [De Groot et al., 2002]. That method will be described in detail in the following section.
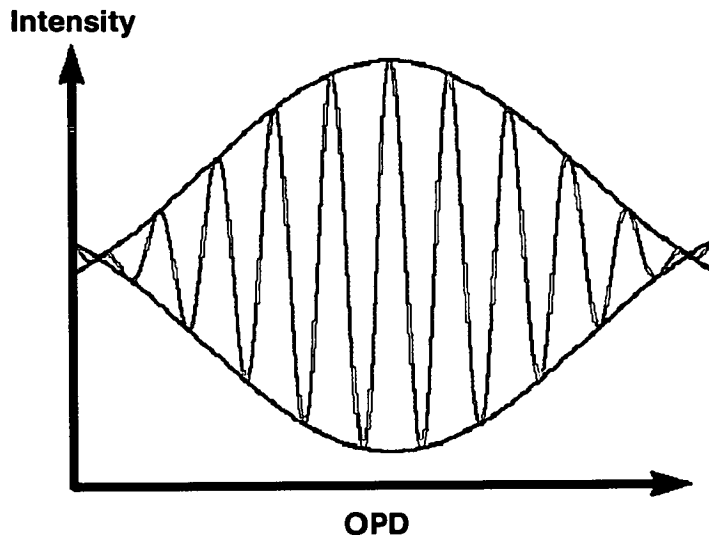
Intensity

OPD

Fig. 3.3. Typical white light interferogram [Wyant, 2002]. The interferometric intensity depends on OPD. High contrast fringes appear when the two path lengths are closely matched at approximately the best focus position.

Scanning white light interferometry (SWLI):

The instrument we have used in this work is a *New View 100, Zygo Corp* (see Fig. 3.4 and Fig. 3.5), the design of which was carried out by De Groot & Deck [1995]. This paper gives a detailed account of this instrument: hardware, data acquisition and data processing. We summarise here the most relevant sections.

A white light source (incandescent lamp) illuminates an interferometric microscope objective via a filter that selects a 200nm bandwidth about a mean value of around 530nm and a beam-splitter prism. The objective's beam splitter directs 50% of the incoming beam towards the reference mirror and the remaining 50% towards the object mirror. After *normal* reflection from the two mirrors, the beams are recombined and projected onto a charge-coupled device video camera, which generates a signal proportional to the resultant beam intensity produced by the *interference* effect. The objective lens focuses the image of the object (sample) surface onto the sensing element of camera, so that each pixel in the digital *image* corresponds to a small region of surface (size is magnification dependent). The objective is driven by a piezoelectric scanner capable of precise vertical scans so as to vary the OPD of the interferometer. A sequence of intensity data frames are acquired by the camera and stored in the computer's memory during a continuous scan of the objective lens. The stored data consists of an array of interferograms, one for each pixel, representing the variation in intensity as a function of scan position.
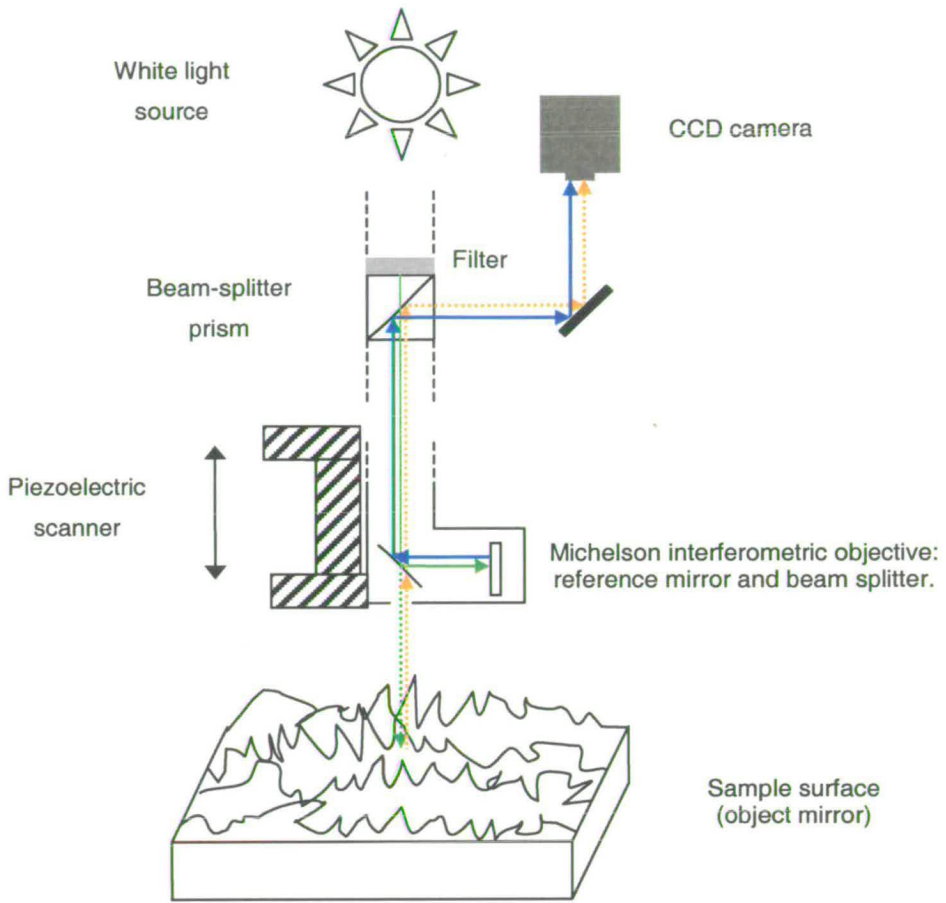
White light source

CCD camera

Filter

Beam-splitter prism

Piezoelectric scanner

Michelson interferometric objective: reference mirror and beam splitter.

Sample surface (object mirror)

Fig. 3.4. Schematic of the New View 100 operating a x2.5 Michelson interferometer.

Interferometric microscopy live image of a glass surface (interference pattern)

Mirau-type interferometric objective

3D map

Motorised X, Y stage
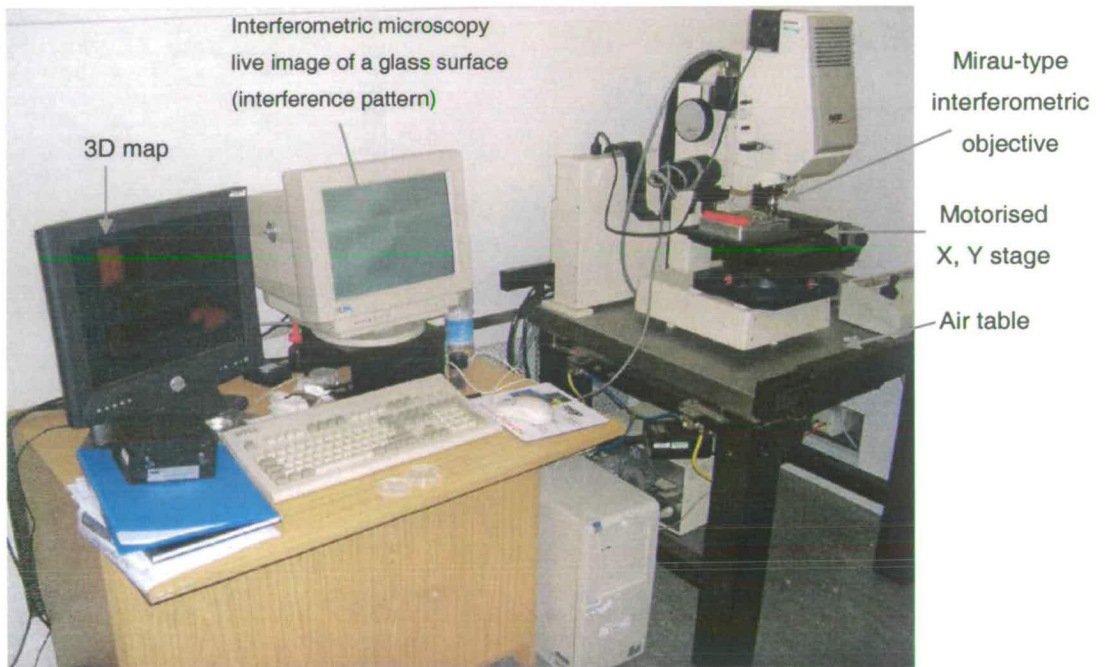
Air table

Fig. 3.5. New View 100 on an air table. Note interference pattern (white monitor).

Once the data has been acquired, the computer analyses each of the stored interferograms to discover its composition in terms of wavenumbers and corresponding phases. Starting with a single-column array of N intensity values I_i taken at equally spaced OPD positions Z_i, the contribution to the interferogram for a particular wave vector k_j is found by the discrete *Fourier* transform:

$$P_j = \sum_i I_i \exp(-ik_j Z_i) \tag{3.5}$$

The complex quantity Pj can be expressed as:

$$P_j = |P_j| \exp(i\phi_j) \text{ with } \phi_j = \tan^{-1}\left[\frac{\operatorname{Im}(P_j)}{\operatorname{Re}(P_j)}\right] \tag{3.6}$$

The transformed interferograms now represent, for each pixel, the relative strength $|P_j|$ and the desired interferometric phase ϕ_j as a function of wavenumber k_j. Most of the useful information in the Fourier transformed data is contained in the region where the relative strengths are large. When the region of interest in the Fourier transformed data is identified, either by prediction or by automatic search, a series of pairs (ϕ_j, k_j) are collected from this region for use in surface height calculation. The modulo 2π ambiguities already referred to in the phase shifting interferometry section is eliminated by applying a simple recursive algorithm:

$$\phi_j = \phi_j - 2\pi Int\left\{\frac{(\phi_j - \phi_{j\pm 1})}{2\pi}\right\} \tag{3.7}$$

The $j\pm 1$ index stands for the direction of recursion: positive for increasing values of j, negative for decreasing values of j.

For a "white light" source, the various wave vectors k_j present result in a separate interferogram that adds *incoherently* to the others to produce the final white light fringes. The relative phase of each of these interferograms can be expressed in terms of a Taylor series expansion about a mean wave vector k_0:

$$\phi = \phi_0 + (k - k_0)\frac{d\phi}{dk}\bigg|_{k_0} + \frac{(k - k_0)^2}{2}\frac{d^2\phi}{dk^2}\bigg|_{k_0} + \dots \tag{3.8}$$

The first term ϕ_0 is constant. It is the phase for $k = k_0$ and can be written:

$$\phi_0 = k_0 Z_0 \tag{3.9}$$

The second term is the first order variation of phase with wave vector, in other words the term that is the most directly related to surface topography determination according to Young's experiment and the principle of phase shifting interferometry (see (3.1) and (3.3)):

$$\left.\frac{d\phi}{dk}\right|_{k_0} = Z_0 + \left.k\frac{dZ}{dk}\right|_{k_0} = G_0 \qquad (3.10)$$

The distance G_0 is the group velocity OPD for $k = k_0$. Unless the interferometer has been perfectly compensated for *dispersion*, G_0 will be somewhat different from Z_0 the phase velocity OPD. The phase as a function of wave vector can then be written:

$$\phi = k_0 Z_0 + (k - k_0)G_0 + \left.\frac{(k - k_0)^2}{2}\frac{dG}{dk}\right|_{k_0} + ... \qquad (3.11)$$

Since the determination of the phase values (free of 2π ambiguity) as a function of wave vector near the mean wave vector k_0 by *Frequency Domain Analysis* (FDA) can be done as explained above (see (3.5) through (3.7)), it is then possible, after fitting a polynomial to the (ϕ_j, k_j) data pairs, to estimate the components of (3.11). Supposing there is not a major amount of second order dispersion, a first order polynomial is enough to fit the experimental data. Its slope gives direct access to the group velocity OPD. This quantity is related to the surface topography through the group velocity index n_G:

$$h = \frac{G_0}{2n_G} \qquad (3.12)$$

For maximum accuracy, the first, constant term in (3.11) $k_0 Z_0$ must be taken into account. This gives rise to another formulation for the surface topography h':

$$h' = \frac{1}{2n}\left[\frac{(\phi_0 - \alpha)}{k_0} - \frac{2\pi}{k_0}Int\left\{\frac{(\phi_0 - \alpha) - (2k_0 hn)}{2\pi}\right\}\right] \qquad (3.13)$$

n is the index of refraction (phase velocity index of refraction), which is by nature different from n_G. α is the constant phase offset, consequence of various phenomena such as phase change on reflection. When not equal to zero it acts as a systematic error applied to all pixels in the same way, which means it does not alter the surface shape but only the absolute height values. The height resolution of SWLI is close to 0.1nm. The lateral resolution depends only on the lens being used. A x2.5 Michelson objective lens in combination with a CCD camera (x20) provides a total magnification of x50, which translates in terms of lateral

resolution to about 4.5μm. In the same configuration a x40 Mirau objective lens provides a lateral resolution of about 0.7μm. Reference mirrors being imperfect (flatness $\cong \lambda/20$), data acquired with a large field of view objective such as the x2.5 needs correcting using a reference surface (SiC optical flat: flatness $\cong \lambda/110$, roughness $= 1.16$ Å rms) whose topography is subtracted from that of sample surfaces.

3.1.2. Imaging ellipsometry

Ellipsometry:

Like SWLI ellipsometry is an optical technique that is sensitive to the intensity of a light beam reflected off of an interface, but unlike SWLI it also measures the change in state of polarisation of this beam. From analysis of this rich composite information, it is possible to gain insights about the structure of the interface [Keddie, 2001], namely its optical properties and its thickness if, for instance, it consists of a thin film coated on a substrate surface.

Single interface:

The reflection coefficients for a polarised light beam of wavelength λ incident upon an interface separating two media that can exhibit some degree of opacity to light (see Fig. 3.6) are as follows:

$$r_{12}^{P} = \frac{\underline{n}_1 \cos\theta_2 - \underline{n}_2 \cos\theta_1}{\underline{n}_1 \cos\theta_2 + \underline{n}_2 \cos\theta_1}, \quad r_{12}^{S} = \frac{\underline{n}_1 \cos\theta_1 - \underline{n}_2 \cos\theta_2}{\underline{n}_1 \cos\theta_1 + \underline{n}_2 \cos\theta_2} \tag{3.14}$$
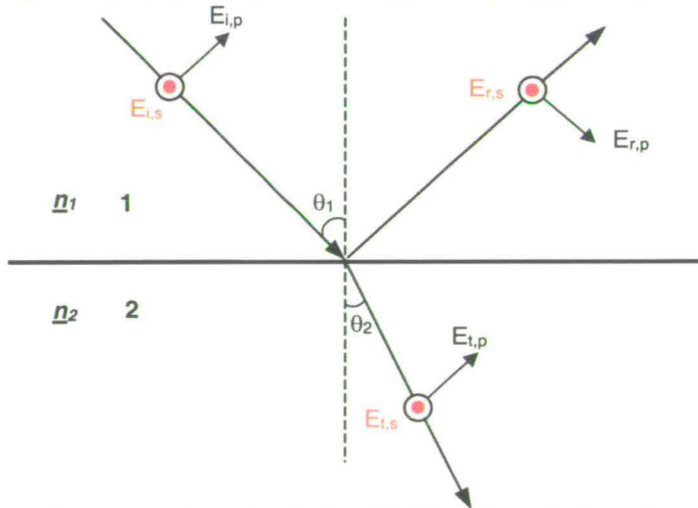
where $\underline{n} = n - jk$.

Fig. 3.6. Reflection and transmission of polarised light at the interface between two media. $E_p(E_s)$ is the component of the electric field that is parallel(normal) to the plane of incidence.

Two or more interfaces:

If a thin film that is at least partially transparent is placed in between the two media, there are an infinity of reflections (see Fig. 3.7) and the reflection coefficients take on a more complex mathematical form [Kim & Kim, 1999]:

$$R^P = \frac{E^P_{r,1} + E^P_{r,2} + E^P_{r,3} + E^P_{r,4} + \ldots}{E^P_i} = \frac{r^P_{01} + r^P_{12}e^{(-2j\beta)}}{1 + r^P_{01}r^P_{12}e^{(-2j\beta)}} \qquad (3.15)$$

$$R^S = \frac{E^S_{r,1} + E^S_{r,2} + E^S_{r,3} + E^S_{r,4} + \ldots}{E^S_i} = \frac{r^S_{01} + r^S_{12}e^{(-2j\beta)}}{1 + r^S_{01}r^S_{12}e^{(-2j\beta)}} \qquad (3.16)$$

where β is the phase change that the wave is subjected to as it crosses the film. Its mathematical form is as follows:

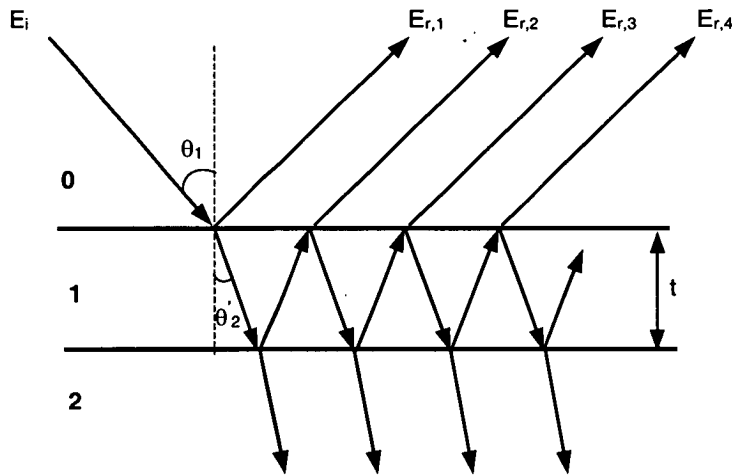$$\beta = \frac{2\pi}{\lambda} t \underline{n}_1 \cos\theta_2 \qquad (3.17)$$

Fig. 3.7. Multiple reflection of polarised light due to a transparent thin film on a substrate.

What an ellipsometer measures is the complex ratio of R^P to R^S. It is common practice to express this ratio in terms of the amplitude and phase terms [Jin *et al.*, 1996]:

$$\frac{R^P}{R^S} = \tan\Psi e^{j\Delta}, \quad \Delta = \left(\beta^P_r - \beta^P_i\right) - \left(\beta^S_r - \beta^S_i\right) \qquad (3.18)$$

By using appropriate models it is possible to calculate the refractive and extinction indices as well as the thickness of the layers involved from the measured Ψ and Δ. The resolution in thickness attainable by ellipsometry is of order of 0.1nm.

Imaging ellipsometry:

A widely used ellipsometric setup consisting of a combination of polariser-compensator-sample-analyser (PCSA) is described by Wang *et al.* [2003]. By placing an objective lens in between the sample and the analyser and substituting a CCD camera for the classical photodetector [Jin *et al.*, 1996], it is possible to turn ellipsometry into an imaging technique in much the same way as what is being done in SWLI (see Fig. 3.8).
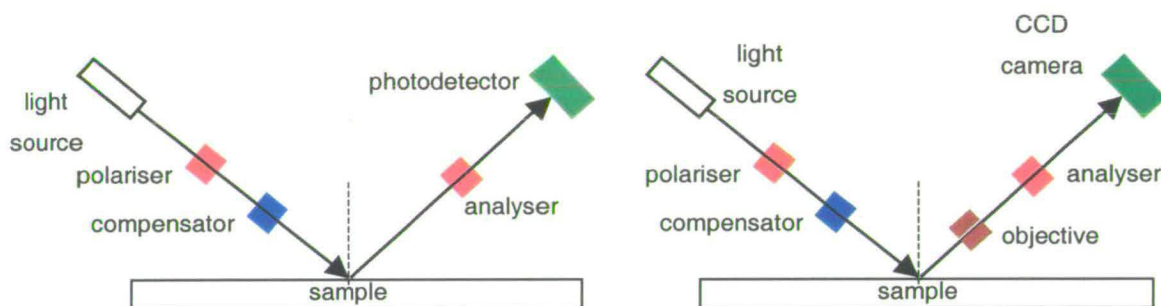

Fig. 3.8. Left: typical setup of a PCSA ellipsometer. Right: imaging ellipsometer based on the same setup.

The imaging ellipsometry data to be found in this document (see § 4.2.1 and § 4.2.4) were obtained by the Nanofilm application team on their EP[3] (www.nanofilm.de). A photograph of this instrument is presented in Fig. 3.9. It corresponds to the setup presented on Fig. 3.8.
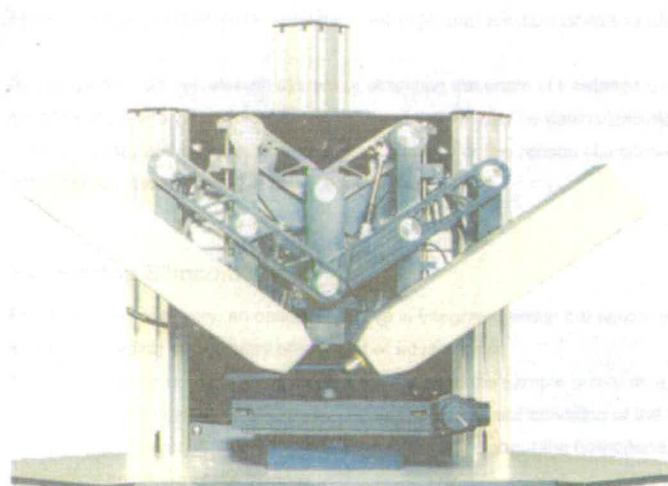

Fig. 3.9. Imaging ellipsometer EP[3]. www.nanofilm.de.

3.1.3. X-ray photoelectron spectroscopy (XPS)

<u>General aspects:</u>

X-ray photoelectron spectroscopy is a vacuum analysis technique based on the photoelectric effect: X-rays ionise external or even core-level electrons (see Fig. 3.10) some of which have enough kinetic energy to exit the surface and be detected by an appropriate sensor providing the vacuum is high enough to avoid any interaction that would deviate the electron from its initial trajectory and/or cause too big an energy loss [Briggs & Seah, 1983]. A sufficient vacuum corresponds to pressures of order 10^{-8} to 10^{-10} mbar [Watts & Wolstenholme, 2003]. Besides photoelectrons, Auger electrons can be emitted and recorded on an XPS spectrum. They are usually easy to spot as they do not give rise to single peaks.
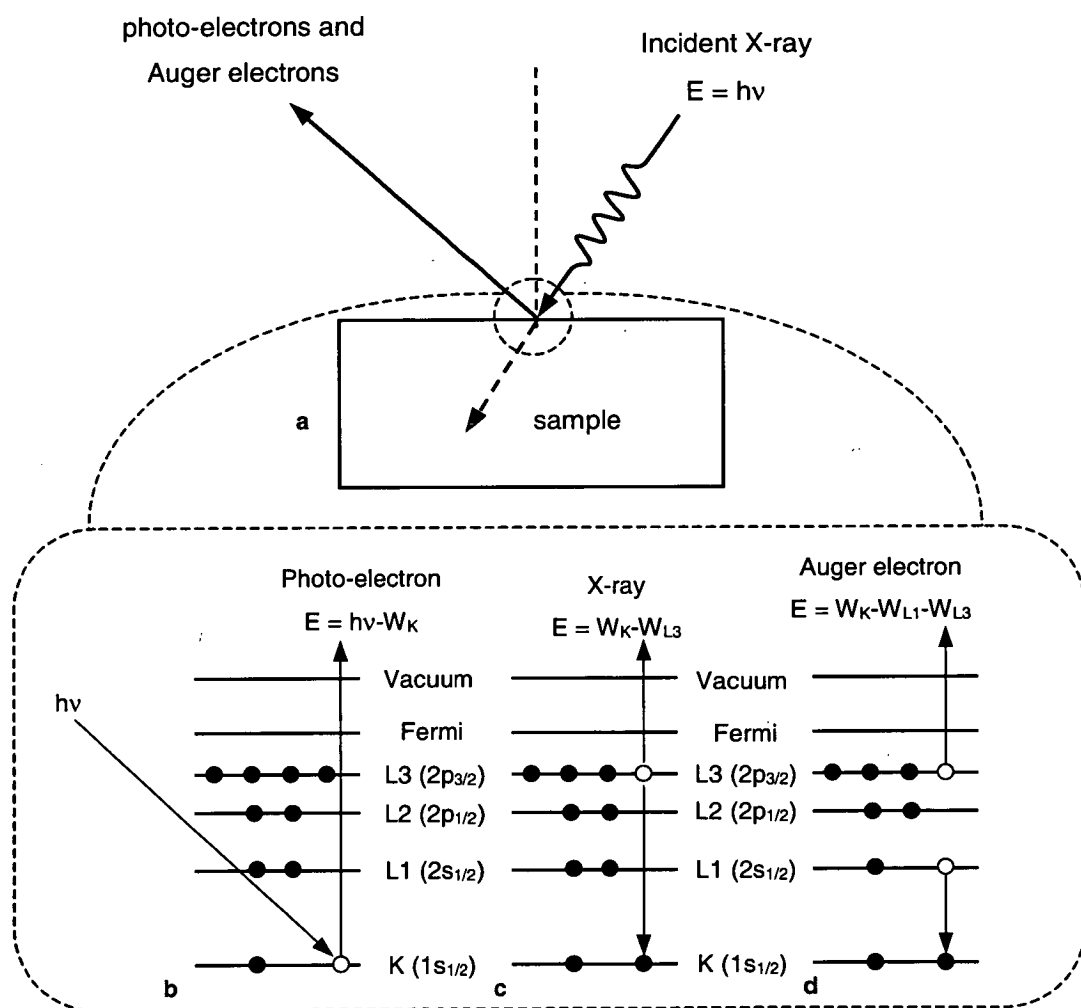

Fig. 3.10. Photo-electric effect. a: sketch at the macroscopic scale. b, c, d: atomistic scale. b: excitation of a K shell by an X-ray (spectroscopists use the quantum notation $1s_{1/2}$). c: deexcitation through X-ray emission. d: deexcitation through Auger electron emission.

Generally the energy of incident X-rays is of order of 1 keV ($E_{AlK\alpha}$ = 1486.6 eV), which gives an upper limit to the ejected electrons' kinetic energy. Since electrons carry an electrical charge, they tend to interact a lot more with surrounding atoms than X-rays do. Their *interaction cross-section* is roughly 10^8 times higher than that of X-rays [Eberhart, 1997], therefore their *inelastic mean free path*, that is the distance between two consecutive interactions involving energy loss, is of order of some nanometres for electrons such as those ejected by X-rays produced by an aluminium source. It follows that XPS is a surface characterisation technique. As a rule, the probability of ionising a subshell is maximum when the X-ray energy to subshell binding energy ratio is just above one [Eberhart, 1997]. The kinetic energy carried by the detected electrons is related to the binding energy of the subshell they originate from. "Small" shifts - some eV to a fraction of one eV - from the tabulated values of binding energy for pure species can be related to a particular bond in which the ionised atom was engaged. Thus it is theoretically possible to distinguish between elemental photoelectron peaks, oxides and so forth. Obviously to achieve that sort of analysis it is essential that the *absolute resolution* in energy of the spectra be as good as possible. This quantity is often taken as the full width at half maximum height [Briggs & Seah, 1983]. It is also covenient to have a constant resolution throughout the energy range. This is generally done by irradiating samples with monochromated X-rays and by using a hemispherical sector analyser (HSA), also known as concentric hemispherical analyser (CHA). Monochromated AlKα X-rays have a reduced line width compared to that of the "natural" rays: 0.25 eV as opposed to 0.9 eV [Watts & Wolstenholme, 2003].

Some elements of instrumentation:

Prior to entering the analyser electrons need being slowed down otherwise the resolution in energy that is aimed for could not be obtained. This task is performed by transfer lenses placed before the analyser (see Fig. 3.11). For a standard HSA the absolute resolution is estimated by:

$$\Delta E = \frac{0.63 wE}{R_0} \qquad (3.19),$$

where w is the slit width, R_0 is the radius of the median equipotential surface and E is the pass energy. The pass energy is defined by the electrostatic field applied to the HSA. Only those electrons with an energy equal or very close to the pass energy can progress to the detector, R_0 corresponding to the "ideal" trajectory. The faster electrons move towards the

outer hemisphere while the slower ones are deviated towards the inner hemisphere. Equation (3.10) shows that the absolute resolution varies linearly with the pass energy, hence to get a spectrum with constant resolution throughout the energy range it is necessary that the pass energy be the same whatever the photoelectron's kinetic energy. This mode is called constant analyser energy (CAE). In this mode the difference of potential (ΔV) across the two hemispheres is constant, hence to record a spectrum, the potentials must be varied on each hemisphere with the kinetic energy of photoelectrons to be detected. A schematic of such a spectrometer is presented in Fig. 3.11 along with a photograph in Fig. 3.12.
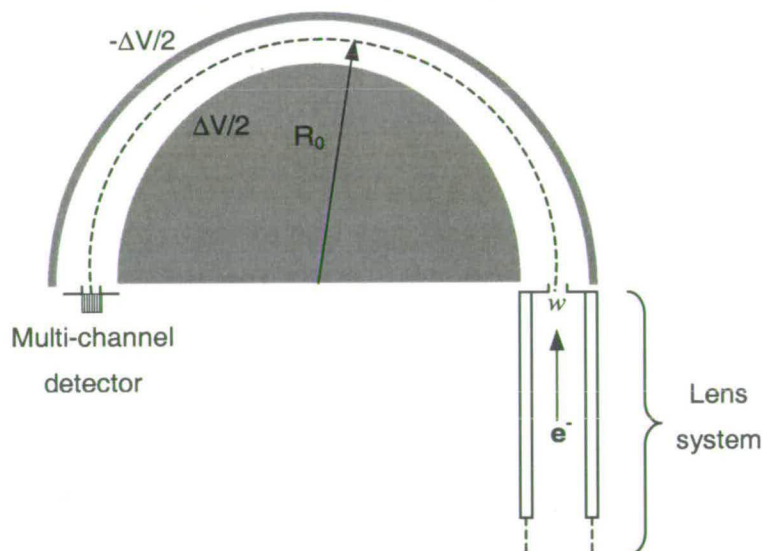

Fig. 3.11. Schematic of the detection system of a photoelectron spectrometer: lens system, hemispherical sector analyser (HSA) and multi-channel detector.
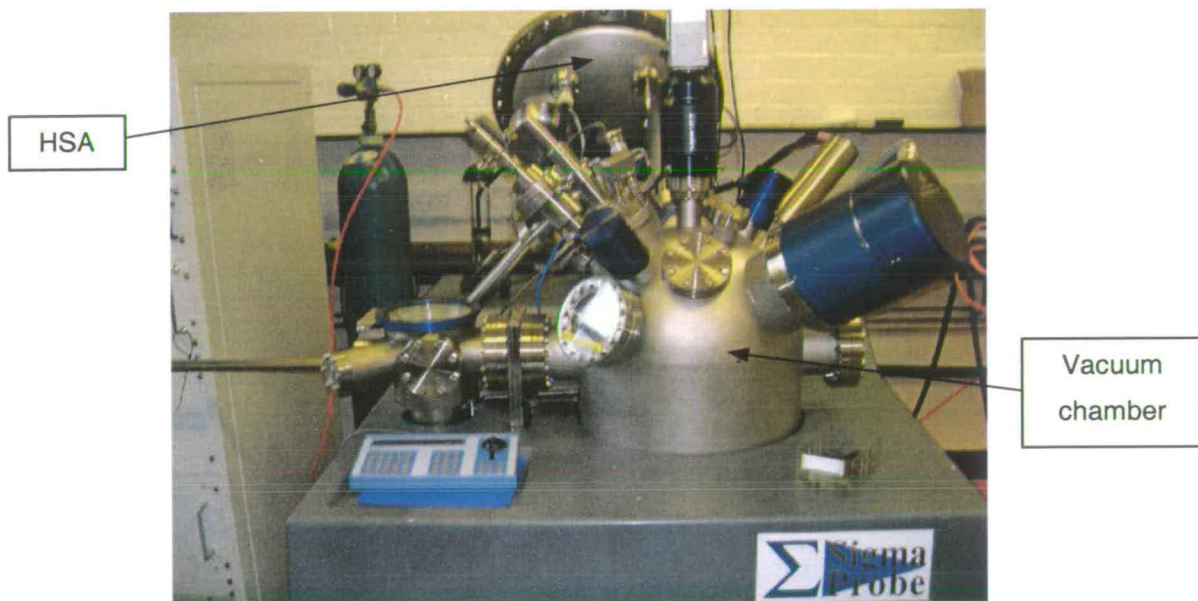

Fig. 3.12. X-Ray photoelectron spectrometer (Sigma Probe, Thermo Electron).

Qualitative analysis:

The acquisition of data in constant analyser energy mode leads to a spectrum such as that of Fig. 3.13. This figures represents the characteristic spectrum of a superficially oxidized silicon wafer Si(111) for photoelectrons of kinetic energy ranging from about 600 eV to 1500 eV. It is usually preferred to scale the energy in *binding energy* rather than *kinetic energy* as it is independent of the energy of the X-ray source of excitation. There is a simple relationship between these two energy scales:

$$E_B = h\nu - E_K - W \qquad (3.20),$$

E_B is the binding energy of an electron that belongs to a particular subshell, $h\nu$ is the energy of the incident X-ray, E_K is the kinetic energy of a detected photoelectron and W is the spectrometer work function [Watts & Wolstenholme, 2003]. The latter is partly related to the work that an electron has to provide to overcome the energy barrier of a material' surface. Practically this quantity is measured internally so that users only choose the scale they like better.
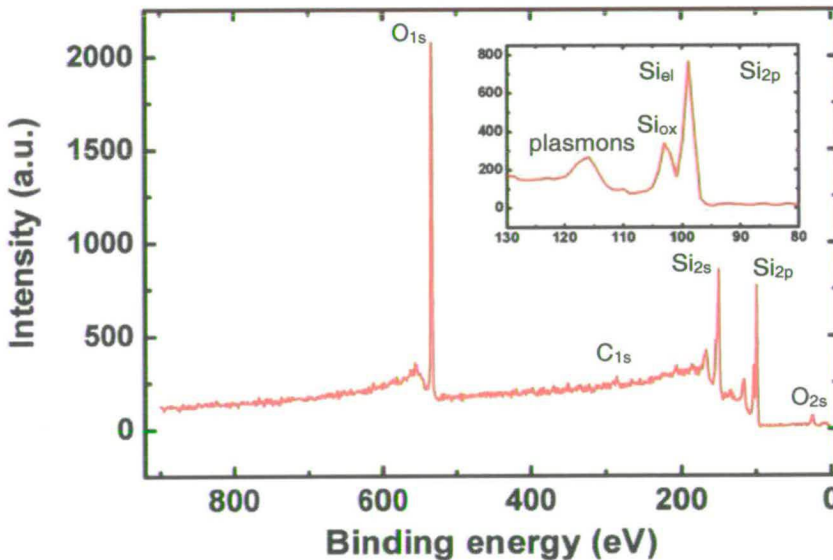

Fig. 3.13. Survey spectrum of a clean silicon wafer surface in CAE mode. Pass energy = 80 eV, X-ray spot diameter = 800μm. Insert: detailed spectrum of the Si2p photoelectron line.

The spectrum provides a wealth of information about the material's surface being analysed. The main present elements are oxygen, silicon and a small fraction of carbon corresponding to unwanted adventitious contamination. The peaks are narrow (some eV

wide) and are followed by a much less intense background at higher 'apparent binding energy' that is lower kinetic energy: peaks correspond to photoelectrons that undergo no energy loss as they travel towards the transfer lens while the background corresponds to electrons that have been inelastically scattered. Both oxygen and silicon are present in the form of two different subshells. The insert shows a detailed portion of the spectrum around the Si2p photoelectron line. The peak is made up of two components: a more intense peak at about 100 eV and a less intense one at about 103 eV. The former comes from elemental silicon, the latter comes from oxidised silicon. Thus XPS proves its capability to perform both qualitative elemental and chemical analysis. The reason why the silicon oxide contribution to the Si2p line is located at higher binding energy (*positive chemical shift*) than that of elemental silicon is as follows: a silicon atom covalently bonded to one to two oxygen atoms which are significantly more electronegative (the electronegativity of O in Pauling's scale is 3.5 as opposed to 1.9 for Si) results in the Si2p electrons being more strongly bonded and hence requiring extra energy to be ejected [Watts & Wolstenholme, 2003].

At even higher binding energy (117-118 eV) a badly resolved peak can be seen. This feature is a consequence of photoelectron energy loss by plasmons: outgoing electrons excite collective oscillations of electrons in the conduction band. This phenomenon is characteristic of clean metal or semi-metal (silicon, germanium) surfaces. Such features make XPS spectra more complex and have to be accounted for by users in order to avoid wrong interpretations.

Quantitative analysis and thin film thickness determination:

We have seen that XPS could distinguish between most elements (from Boron onwards) and various chemical forms involving those elements. We will see now that peak intensity of an XPS spectrum can be related to the atom concentration of particular species. It is common practice to use the peak surface areas rather than peak heights to limit noise effects. In a solid that can be considered homogeneous within the analysis volume, the relationship that gives the intensity of a photoelectron peak is [Watts & Wolstenholme, 2003][1]:

$$I = JK\rho\sigma AL \qquad (3.21),$$

J is the X-ray flux, K is a term that takes into account all of the instrumental factors such as the spectrometer transmission function and the detector efficiency, ρ is the atom

---

[1] It is proportional to the pass energy too. There is a trade off between sensitivity and resolution.

concentration of the atom, σ is the photoionization cross-section for the considered electron transition and AL is the electron attenuation length. The latter is particularly important and deserves a more detailed explanation. Unlike the inelastic mean free path (IMFP), an intrinsic property of a material that only takes into account inelastic collisions, the electron attenuation length combines the effects of both elastic and inelastic collisions. This parameter is necessary as the electron flux measured in a particular direction (see Fig. 3.14) is affected by both elastic and inelastic collisions, in particular those electrons that contribute to a peak formation have not been scattered or have been scattered elastically.

A more complex expression of photoelectron intensity that models elastic-scattering effects, that is the dependence of intensity on photoelectron emission angle θ (see Fig. 3.14) has been proposed by Seah and Gilmore [2001]:

$$I = JK\rho\sigma\lambda QL(\gamma)\cos\theta \qquad (3.22)$$

Here λ stands for inelastic mean free path (IMFP). Q is an elastic scattering parameter so that the λQ product is roughly equivalent to the electron attenuation length (AL). $L(\gamma)$ is the angular asymmetry factor, a function of the angle between the X-ray beam and the photoelectron flux intercepting the centre of the lens (see Fig. 3.14). For standard spectrometers γ is simply the sum of the emission angle and of the angle between the X-ray beam and the surface normal. The Thermo Electron Σ probe or even Θ probe (see Fig. 3.14 b) has a different geometry, so that γ is a function of θ and has a more complicated form:

$$\gamma(\theta) = \cos^{-1}\left(\sin(30°)\sin(\theta)\cos(70° - 180°) + \cos(30°)\cos(\theta)\right) \qquad (3.23)$$

$L(\gamma)$ affects the angular dependence of the photoemission from a given orbital. Being an atomic effect, it depends only on the subshell being considered and not on whether the atom is in an elemental state or engaged in covalent bonds with heteroatoms. Its mathematical expression is:

$$L(\gamma) = 1 + \frac{1}{2}\beta_{eff}\left(\frac{3}{2}\sin^2\gamma - 1\right) \qquad (3.24)$$

β_{eff} is the effective asymmetry parameter in condensed matter where emission is affected by elastic scattering as opposed to gases for which β values are tabulated [Band *et al.*, 1979] [Reilman *et al.*, 1976] [Yeh & Lindau, 1985]. It is thought to be an atomic effect the magnitude of which is independent of the chemical environment [Thermo Electron, 2004].

Rather than determining experimentally or calculating every quantity present in the intensity equation, it is preferred to use atomic sensitivity factors (F) for the various accessible sub-shells. They comprise all of the terms on the right hand side of equation (3.21) or (3.22) apart from the atom concentration one. Wagner *et al.* [1981] proposed factors valid for a spectrometer operating in CAE mode and with a contamination layer of standard thickness ($\cong 0.75$ nm) [Briggs & Seah, 1983]. The atom percentage of element X is then:

$$[X]\% = \frac{\left(I_X / F_X \right)}{\sum_{i=1}^{n} \left(I_i / F_i \right)} \times 100 \qquad (3.25)$$

The precision of such a method is of the order of 10% [Briggs & Seah, 1983] and the limit of detection is of order of 1000 ppm in weight [Eberhart, 1997]. Only the major and minor elements can be detected.
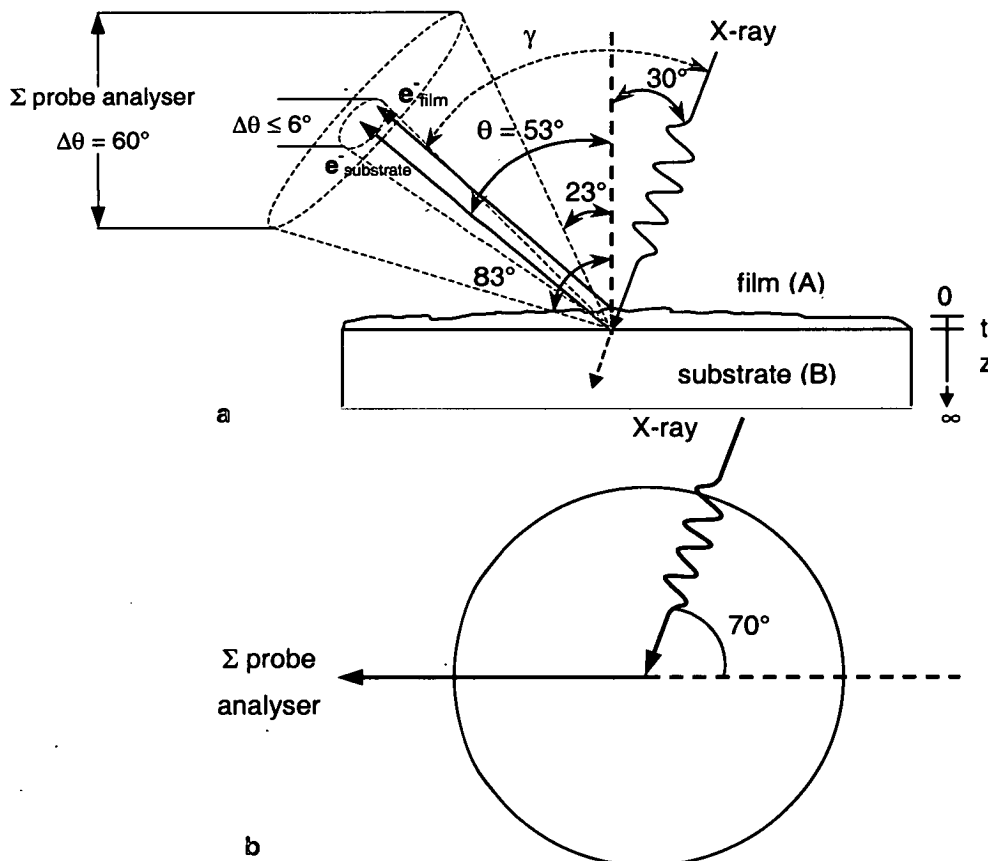

Fig. 3.14. a: Schematic drawing of photoelectron collection. In *blue* large acceptance angle (Σ probe, Thermo Electron) and in *red* small acceptance angle (Θ probe or standard spectrometer). b: plan view of the Σ (Θ) probe setup.

Should this precision be judged insufficient it is possible to retrieve *AL*, *IMFP*, *Q* and β_{eff} values in the literature [Powell & Jablonski - 1, 2001], [Seah & Spencer, 2002] or better to work out the most useful parameters for quantitative analysis, namely *AL*, *Q* and β_{eff}.

For standard spectrometers (case *1*) where the plane formed by the X-ray beam and the sample surface normal on the one hand and the plane formed by the surface normal and the photoelectron flux intercepting the lens centre on the other hand are the same, and where the emission angle θ is roughly lower than 60° (elastic scattering effects are negligible), the fits proposed by Seah and Gilmore [2001] are appropriate. In case where those planes are different (case 2) and the emission angle is bigger than ~ 60°, as is the case for the Σ probe (see Fig. 3.14 b), the numerical treatment implemented by Powell and Jablonski [2 - 2001] in a computer program is better suited. It is the result of a thorough theoretical study on the concept of electron attenuation length by the same authors [Jablonski & Powell, 2002].

Case *1*: for $0° < \theta < 58°$ and $\gamma > 45°$

$$\left(\frac{AL}{\lambda} \right)_i = 0.979[1 - \omega_i(0.955 - 0.0777\ln Z_i)] \tag{3.26}$$

AL is the attenuation length being searched for, λ is the IMFP, ω_i is the ratio $\lambda/(\lambda + \lambda_{tr})$ where λ_{tr} is the transport mean free path (TMFP) and *Z* is the atomic number. ω_i values as well as λ and λ_{tr} values can be calculated using the computer program already referred to [Powell & Jablonski - 2, 2001]. For a compound material equation (3.26) becomes:

$$\left(\frac{AL}{\lambda} \right)_{compound} = \sum_{i=1}^{n} X_i \left(\frac{AL}{\lambda} \right)_i \tag{3.27}$$

where X_i is the atomic fraction of the ith element.

For $0° < \theta < 70°$

$$\left(\frac{\beta_{eff}(\theta)}{\beta} \right)_i = 0.876[1 - \omega_i(0.955 - 0.0777\ln Z_i)](0.0868\cos^2\theta - 0.208\cos\theta + 1.121) \tag{3.28}$$

Obviously the formula that gives the asymmetry parameter for a compound is similar to (3.27), which suggests that the reduction of the asymmetry parameter is matrix-dependent:

$$\left(\frac{\beta_{eff}(\theta)}{\beta} \right)_{compound} = \sum_{i=1}^{n} X_i \left(\frac{\beta_{eff}(\theta)}{\beta} \right)_i \tag{3.29}$$

Likewise for Q, the other elastic scattering parameter:

$$Q_i(\theta) = Q_i(0)\left(0.863 + 0.308\cos\theta - 0.171\cos^2\theta\right) \qquad (3.30)$$

$$\text{for } \omega > 0.245, \quad Q_i(0) = (1-\omega)^{0.5}\left[0.091 + 0.923\left(\frac{1+1.908}{1+1.908(1-\omega)^{0.5}}\right)\right] \qquad (3.31)$$

$$\text{for } \omega < 0.245, \quad Q_i(0) = (1-\omega)^{0.5}(1+0.412\omega) \qquad (3.32)$$

The relationship that gives Q for a compound is:

$$Q_{compound}(\theta) = \sum_{i=1}^{n} X_i Q_i(\theta) \qquad (3.33)$$

Case 2: for $0° \leq \theta \leq 90°$ and $0° \leq \gamma \leq 180°$

The so-called *practical effective attenuation length* (*EAL*) that we will identify to the attenuation length (*AL*) for simplicity's sake is defined as:

$$AL = \frac{1}{\cos\theta}\frac{t}{\left[\ln\int_0^\infty \phi(z,\theta)dz - \ln\int_t^\infty \phi(z,\theta)dz\right]} \qquad (3.34)$$

where $\phi(z, \theta)$ is the emission depth distribution function: this quantity is related to the probability for an electron coming from depth z to reach the surface at angle θ without energy loss. Its mathematical expression is complex and beyond the scope of this thesis. For further details the reader is referred to the paper by Jablonski and Powell [2002]; t is the material's thickness: the program was designed to help characterise films deposited on substrates but it can just as well model the behaviour of 'thick' materials. The program also provides users with the other correction parameters: β_{eff} and Q.

XPS can also perform another type of quantitative analysis: estimate the thickness of a thin film deposited on a substrate. We will see that the previous procedure that leads to the calculation of the atom concentration helps in estimating the thickness.

Assuming the presence of a uniform overlayer thinner than 10 nanometres, that is almost free of holes of order or bigger than the wavelength of the electromagnetic waves being used (~1 nm for AlKα x-rays), if this film has a thickness t, is made of material A and covers a substrate made of material B, the attenuation of the signal emanating from A or B

obeys in first approximation a simple Beer-Lambert law with exponential decay of the intensity [Ton-That *et al.*, 2000] [Watts & Wolstenholme, 2003]:

$$I_A = \frac{I_A^\infty}{AL_{A,A}\cos\theta} \int_0^t \exp(-\frac{z}{AL_{A,A}\cos\theta})dz \qquad (3.35)$$

where θ is the photoelectron emission angle, I_A^∞ is the signal for pure material A and $AL_{A,A}$ is the attenuation length for a particular photoelectron line originating from A and being scattered within A.

$$I_B = \frac{I_B^\infty}{AL_{B,A}\cos\theta} \int_t^\infty \exp(-\frac{z}{AL_{B,A}\cos\theta})dz \qquad (3.36)$$

where I_B^∞ is the signal for pure material B and $AL_{B,A}$ is the attenuation length for another or the same photoelectron line originating from B and interacting with A. After integrating these expressions, we calculate their ratio:

$$R = \frac{I_A}{I_B} = R_0 \frac{[1 - \exp(-t/AL_{A,A}\cos\theta)]}{\exp(-t/AL_{B,A}\cos\theta)} \qquad (3.37)$$

where R_0 is the ratio I_A^∞/I_B^∞.

R_0 can be either measured experimentally or calculated. When possible the pure materials can be analysed separately in the same experimental conditions and with the same surface cleanness state. It is however generally difficult to keep the instrumental factors constant on changing sample, especially a stable intensity or ensure a constant contamination level. For problems such as a natural oxide on its metal (or a metalloid like silicon), it is then preferred to analyse several samples with various oxide thicknesses and similar surface cleanness. If the chosen photoelectron lines are the same for the film and the substrate, the difference in kinetic energy of the corresponding electrons is often negligible relative to other error sources $(E_K(Si_{2p}^{Si}) = 1387$ eV, $E_K(Si_{2p}^{SiO_2}) = 1383$ eV). It is therefore fair to assume that the corresponding attenuation lengths in SiO_2 are equal [Seah & Spencer - 1, 2003], which simplifies equation (3.37) and leads to the equation of a simple straight line:

$$I_{SiO_2} = R_0 \left(I_{Si}^\infty - I_{Si} \right) \qquad (3.38)$$

By plotting some intensity values for SiO_2 against intensity values for Si, R_0 is easily obtained from the slope of the resulting straight line.

For more general thin film problems or if the measurements are questionable so that the previous method cannot be used, a predictive formula based on equations (3.21) or preferably (3.22) offers an alternative:

$$R_0 = \frac{JK\sigma_A N_A \lambda_{A,A} Q_{A,A} L_{A,A}(\gamma)\cos\theta}{JK\sigma_B N_B \lambda_{B,B} Q_{B,B} L_{B,B}(\gamma)\cos\theta} \qquad (3.39)$$

where N_A is the atom density (atoms per unit volume), a parameter that is related to the material's density and molecular mass, so that after some simple algebra equation (3.39) becomes:

$$R_0 = c \times \frac{\sigma_A d_A \lambda_{A,A} Q_{A,A} L_{A,A}(\gamma) M_B}{\sigma_B d_B \lambda_{B,B} Q_{B,B} L_{B,B}(\gamma) M_A} \qquad (3.40)$$

where d_A is the density of material A, M_A is the molecular mass of material A and c is a coefficient related to the stoichiometry of the element(s) chosen in both compound A and B. If the same photoelectron line is used in material A and material B, equation (3.40) becomes:

$$R_0 = c \times \frac{d_A \lambda_{A,A} Q_{A,A} M_B}{d_B \lambda_{B,B} Q_{B,B} M_A} \qquad (3.41)$$

Substituting (3.41) into (3.37) and rewriting the resulting equation, we get for the general case:

$$\frac{I_A F_B}{I_B F_A} = R_0 \left\{ \exp\left(\frac{t}{AL_{B,A}\cos\theta} \right) - \exp\left[\frac{t}{\cos\theta}\left(\frac{1}{AL_{B,A}} - \frac{1}{AL_{A,A}} \right) \right] \right\} \qquad (3.42)$$

We recall that F are atomic sensitivity factors that correct peak intensities for different elements and/or subshells so that their ratio can be related to thickness. Data recorded at only one emission angle θ suffices to calculate the thickness of the film but it is essential that the spectrometer acceptance angle be smaller than roughly $\pm 6°$ [Watts & Wolstenholme, 2003] [Seah & Spencer - 1, 2003]. This is often the case for standard spectrometers but not for the spectrometers we used, namely the Σ probe and the Θ probe the analyser acceptance angle of which is $60°$ ($23° \leq \theta \leq 83°$). However the latter has an angle-resolving lens and a two-dimensional detector that disperses energy in one direction and angular distribution in the other, which makes it possible to channel the outgoing electrons emitted in a small angular range ($\Delta\theta \cong 3°$ range) throughout the range of

acceptance angle. This method is called angle resolved X-ray photoelectron spectrometry (ARXPS). Unlike the minimal method in which data at only emission angle is taken to infer film thickness, ARXPS is able to provide a more reliable thickness value and check the homogeneity of the film. The benefit of this is more obvious when the chosen photoelectron lines for A and B are the same. Equation (3.37) takes a much simpler form:

$$\ln\underbrace{\left(1+\frac{I_A}{I_B R_0}\right)}_{y} = \frac{t}{AL_A}\underbrace{\frac{1}{\cos\theta}}_{x} \tag{3.43}$$

It is a straight line of slope t/AL_A, parameter from which the thickness can be easily inferred. In fact it is only a straight line for emission angles lower than 60° in most cases and particularly for SiO_2 on Si [Watts & Wolstenholme, 2003]. Beyond that limit, that is electrons collected at almost grazing angle, elastic scattering effects are important, which results in the substrate peak intensity being larger than expected and therefore to the straight line turning into a curve with a logarithmic shape. Qualitatively, at grazing angle the probability to collect a lot of film electrons travelling a long distance through it without getting inelastically scattered is lower than that of collecting substrate electrons travelling a shorter distance thanks to elastic collisions. A possible trip for the substrate electrons is as follows: first a trajectory normal to the surface and then a change in trajectory towards the lens.

The limit of detection of XPS in terms of film thickness is close to 0.2 nm [Watts & Wolstenholme, 2003]. The accuracy[2] and precision[2] depend on the uncertainty in the estimation of AL and R_0. According to a study carried out by Cumpson and Seah [1997] before the redefinition of electron attenuation length was made [Jablonski & Powell, 2002], the accuracy of film thickness determination by XPS is ± 20%. We believe this interval to be an upper limit. The accuracy has been estimated to be ± 0.1 nm for *ultra-thin films* (films thinner than 3 nm) with an excellent precision too (not true of thicker films) through intercomparison between a variety of techniques [Shallenberger *et al.*, 2000]. Another more recent multiple-technique study on silicon dioxide/silicon established that XPS, unlike most other surface techniques, gives a thickness value of zero when no oxide is present however

---

[2] Accuracy is usually defined in metrology as the distance to the true or expected value of the quantity being estimated. The precision corresponds to the scatter in a set of measurements.

large the adventitious contamination level is. This is a hint that systematic errors do not affect XPS as much as other techniques, making it possibly more reliable.

For heterogeneous films that have an island-type structure, it is best to turn to Tougaard's treatment [1996] that was implemented in a commercial package called QUASES.

3.1.4. Scanning Force Microscopy (SFM) and Force Spectroscopy (FS)

General aspects:

Routine imaging techniques such as optical microscopy and scanning electron microscopy (SEM) are far-field techniques that offer only 'limited' spatial resolution. In optical microscopy the limit is roughly half the wavelength: the so-called Abbé limit, in other words ~ 200nm [Meyer et al., 2004]. In SEMs the situation is a bit different as the *matter wave* associated with the electron beam usually has a De Broglie [Halliday et al., 2003] wavelength shorter than a fraction of one angstrom, which would provide atomic resolution if it was the only factor affecting the spatial resolution. Practically the limits in focussing the beam as well as the collection of secondary electrons from an enlarged area and the dependence on atomic number worsens the resolution to 5-10 nm [Eberhart, 1997]. Furthermore the impression of 3D in an SEM image that is mainly due to the big 'depth of field' of the technique [Eberhart, 1997] does not correspond to a true three-dimensional image. The possiblility of measuring distances precisely is therefore questionable. Besides SEM is a vacuum technique that requires conducting samples to perform imaging, which involves coating a surface with carbon or a metal layer. For all these reasons it is preferable, in order to image a material's surface at the nanoscale, to turn to a true *near-field* technique. The wanted effect is that of a sensor interacting with a sample in such a way that the magnitude of these interactions depends strongly on the distance between the outermost atoms of the sample surface and the sensor (ideally of order of one covalent bond). The family of techniques referred to as Scanning Probe Microscopy (SPM) are based on that principle. Scanning Tunneling Microscopy (STM) is limited to conducting surfaces. The 'sub-family' of techniques derived from (STM) and capable of imaging the surface of any sample at the nanoscale, be it conductive or not, is called Scanning Force Microscopy (SFM). It is based on the force sensed by a microfabricated probe interacting with a surface (see Fig. 3.15).
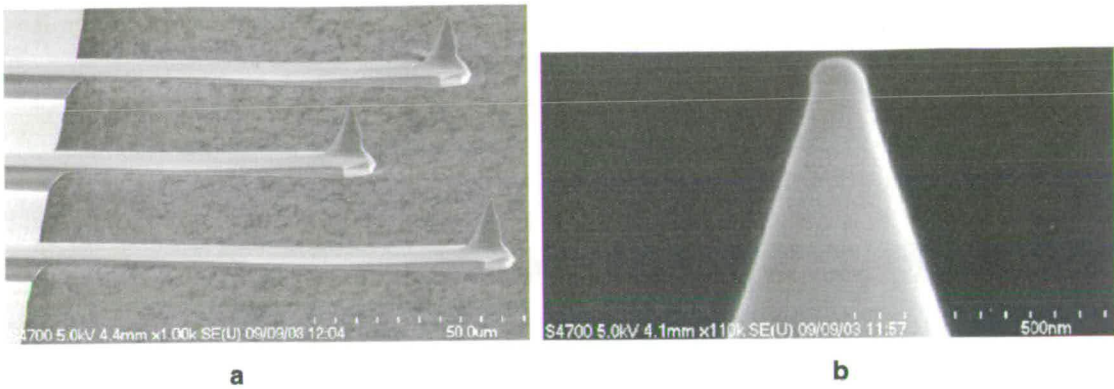
a   b

Fig. 3.15. Scanning electron micrographs of silicon SFM probes (Mikromasch). a: macroscopic silicon chip and its microscopic beam-shaped cantilevers with their 'conical' tips. b: zoom in on the tip apex of the middle cantilever (shortest).

Contact Force Microscopy or Constant Force Imaging (CFI):

This mode of operation consists in the static measurement of the deflection of a cantilever that is scanned (usually rastered) across a surface as depicted in Fig. 3.16. As the distance between tip and sample decreases, the cantilever bends normally because of various forces acting on it. When in contact with the surface, the relationship between the force felt by the tip and its deflection (taken equivalent to z-piezo extension) is Hooke's law:

$$F = kz \tag{3.44},$$

where k (N/m) is the spring constant of the cantilever. This situation corresponds, at the molecular scale, to repulsive Coulomb forces between ion cores. These forces vary rapidly with the position of the outermost tip atom, which is a true near-field interaction.
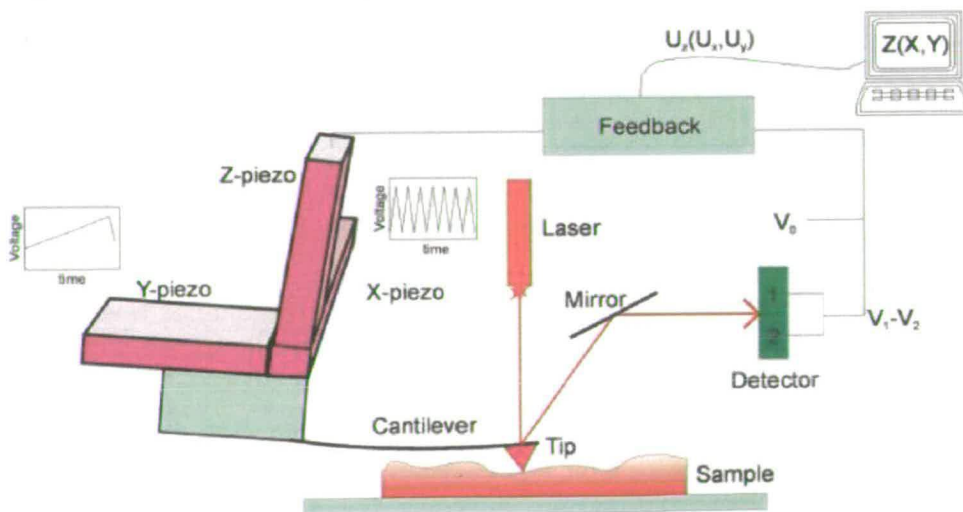

Fig. 3.16. Imaging of a surface topography in constant force microscopy.

Any change in deflection will bring about a change in trajectory of the laser beam that is being reflected at the backside of the cantilever up towards a position-sensitive photodiode. The resulting voltage V_1-V_2 is being compared with the user-defined setpoint V_0 by means of a feedback circuit that is connected to the z piezoelectric drive. The output signal Uz, which adjusts the vertical position of the sample to achieve a constant cantilever deflection, can be recorded as a function of the (x, y) coordinates which are determined by corresponding voltages Ux and Uy applied to the other piezoelectric drives. The resulting signal $Uz(Ux, Uy)$ is finally translated into the topography $z(x, y)$ thanks to the knowledge we have of the sensitivities of the three orthogonal piezoelectric drives [Wiesendanger, 1994]. To determine the value of the piezoelectric drives sensitivities calibration grids with periodic features are being imaged using the piezoelectric drives to be calibrated.

Atomic resolution cannot easily be achieved in contact force microscopy not only because of the finite size of the tip apex (radius of curvature ranging from some nm to some 10s of nm) but also because of the attractive van der Waals (vdW) forces (in air) that make the SFM tip jump into contact with the surface, which deforms both. The resulting tip-sample contact has a size larger than an average atomic radius [Hutter & Bechhoefer - 1, 1993]. This defines the lateral resolution of the technique: typical values of lateral resolution range from 2 to 10 nm in ambient atmosphere [Meyer *et al.*, 2004] and can be smaller than 1 nm in an approriate liquid where vdW forces are eliminated, that is no deforming jump into contact occurs [Hutter & Bechhoefer - 1, 1993].

Aside from normal bending, cantilevers can also bend sideways through torsion. A four-segment photodiode can record this lateral force that is related to frictional effects (see Fig. 3.17). This effect is at the origin of another imaging technique called *friction force microscopy*. An interesting aspect of the lateral force is that its contrast is partly material-specific, so that one can distinguish between different phases [Meyer *et al.*, 2004].
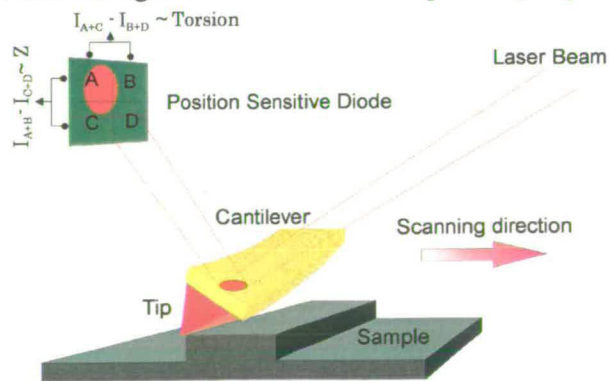

Fig. 3.17. Torsional bending of a cantilever being recorded by a four-segment detector.

Amongst the forces acting on a tip, long range attractive van der Waals forces can be a nuisance due to their magnitude. For a sphere (tip apex) interacting with a semi-infinite medium (sample surface) the van der Waals force is proportional to the radius of curvature of the tip apex [Meyer *et al.*, 2004]. An average commercial cantilever tip is hence likely to give rise to situations where the total force acting on the tip is attractive ('loose' contact) while the outermost tip atoms are in the strong repulsive regime (close contact). This can lead to surface deformation especially when imaging soft materials [Wiesendanger, 1994]. Friction forces can also drag material around, so that another technique is needed to image compliant materials such as self-assembled monolayers (SAMs), polymers or biological systems.

Intermittent Contact Scanning Force Microscopy (IC-SFM):

Amplitude signal:

While in contact force microscopy the control parameter is the cantilever deflection (equivalent to a force) at the tip region, in IC-SFM it is the amplitude of an oscillating cantilever. A cantilever that vibrates at a frequency close to its resonant frequency is driven towards a sample surface, which has the effect of decreasing the vibration amplitude due to tip sample interaction. The feedback loop makes sure that the vibration is always equal or very close to a user-defined amplitude (A_0 see Fig. 3.18) corresponding to good imaging conditions by commanding the z piezoelectric drive to adjust the position of the cantilever. The amplitude signal is therefore used to map the topography of the surface. Although the cantilever spends most of its time 'in the air', it does contact the surface periodically hence this mode of operation cannot be considered non-contact. However it is thought to cause significantly less damage to a soft sample. More importantly risks of dragging are reduced as lateral forces are of a much smaller magnitude [Meyer *et al.*, 2004].

Phase signal:

On top of amplitude, the phase delay of the measured signal relative to the excitation signal contains a good deal of information. It seems that the phase contrast and the surface physical properties it reveals, depends on the experimental conditions (amplitude of free oscillations and amplitude setpoint). Contrast in phase images has been interpreted as variations in stiffness or adhesive properties. Most workers in the field seem to agree on the fact that phase images exhibit larger contrast than topographic images and provide extra

information that, unlike friction force microscopy, are essentially material-dependent and, to a large extent, independent on the topography [Meyer *et al.*, 2004]. Just like in contact force microscopy, the lateral resolution is limited by the size of tip-sample contact, so the resolution ranges from 1-10 nm too.
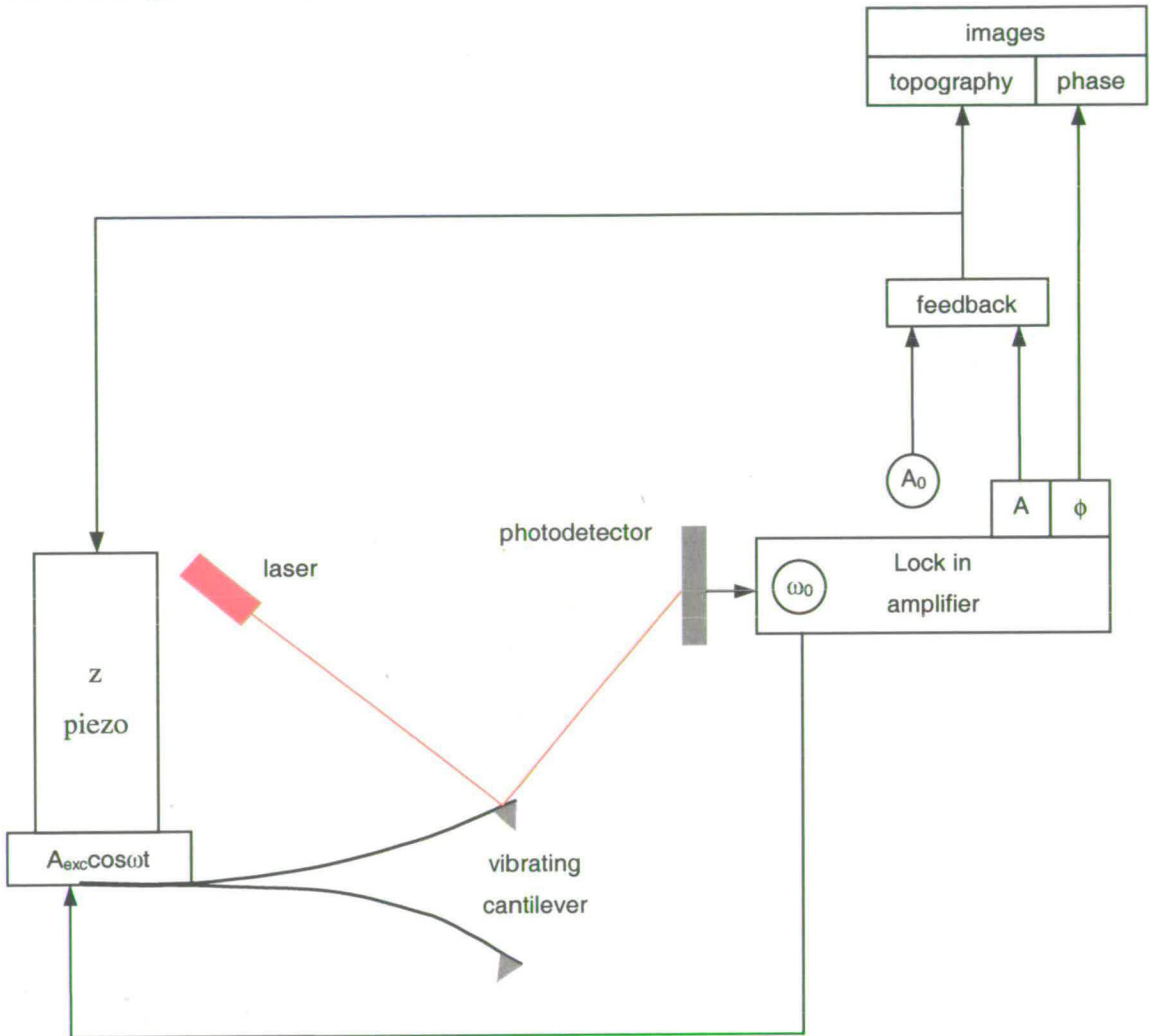
Fig. 3.18. Block diagram of the functions of a scanning force microscope imaging in intermittent contact mode. After Meyer *et al.* [2004].

Most of our experiments were performed with a PicoSPM (Molecular Imaging) that enables users to perform constant force imaging and intermittent contact imaging. A picture of this instrument is presented in Fig. 3.19. The tip actuator is, in this case, a unique piezoelectric drive that performs lateral scanning by bending sideways. This brings about artefacts (bow) that are corrected by image analysis. For some particularly challenging

samples we used the Bioscope (Veeco), an instrument that combines an inverted optical microscope and a scanning force microscope so that a region of interest can be located precisely. We used rectangular-shaped silicon cantilevers by Mikromasch with a nominal spring constant of 1.75 N/m (shortest cantilever in Fig. 3.15).
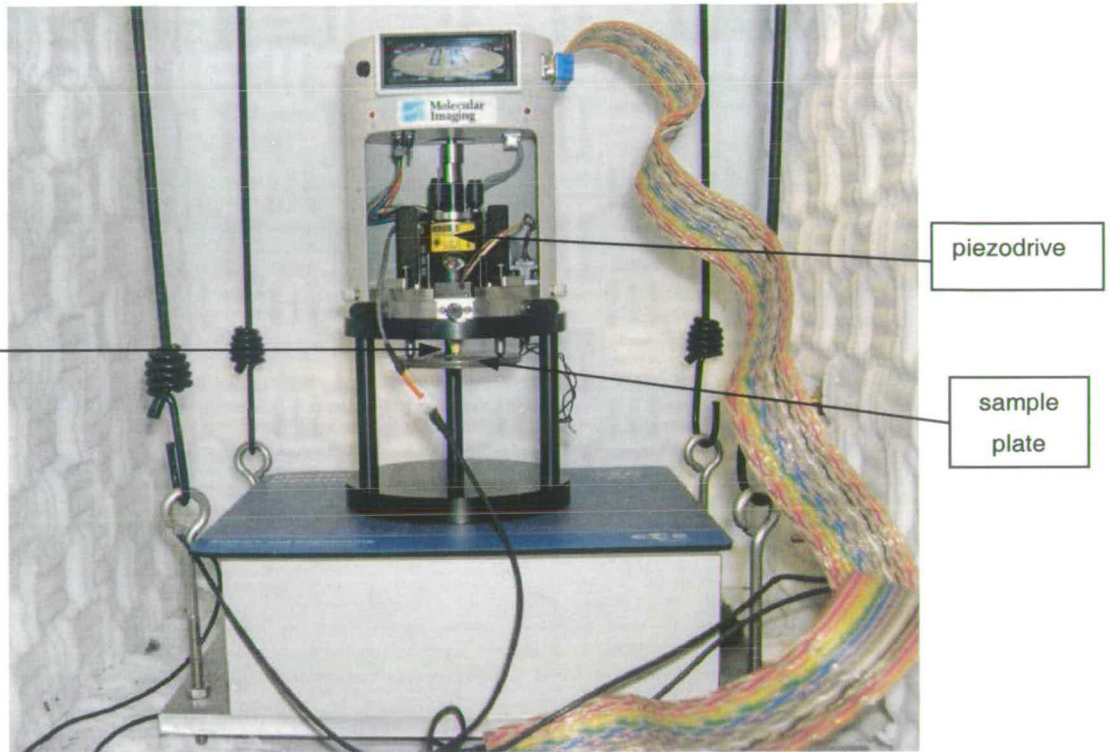

Fig. 3.19. PicoSPM (Molecular Imaging) set for IC-SFM in its anti-vibration chamber.

Force spectroscopy:

Scanning force microscopes operated in contact force microscopy can be used to record the force sensed by the probe as a function of the z coordinate of the probe. It is customary to first record the force as the tip-sample distance decreases until the cantilever deflection saturates the photodetector (approach curve) and then record the force corresponding to the withdrawal of the probe (retraction curve). This method gives insights into the adhesive properties of the sample, tip or tip-sample pair. Up until 2003 commercial microscopes used piezoelectric scanners that suffered from hysteresis, non-linearity which made the quantitative analysis of the so-called force-distance curves difficult. Moreover nominal values of cantilever spring constant provided by manufacturers can be up to 100% and

sometimes even further off the true value [Hutter & Bechhoefer - 2, 1993]. This is why we turned to the MFP-1D by Asylum Research, a dedicated force-measuring device capable of detecting forces as small as some pN. A photograph of the instrument is presented in Fig. 3.20.
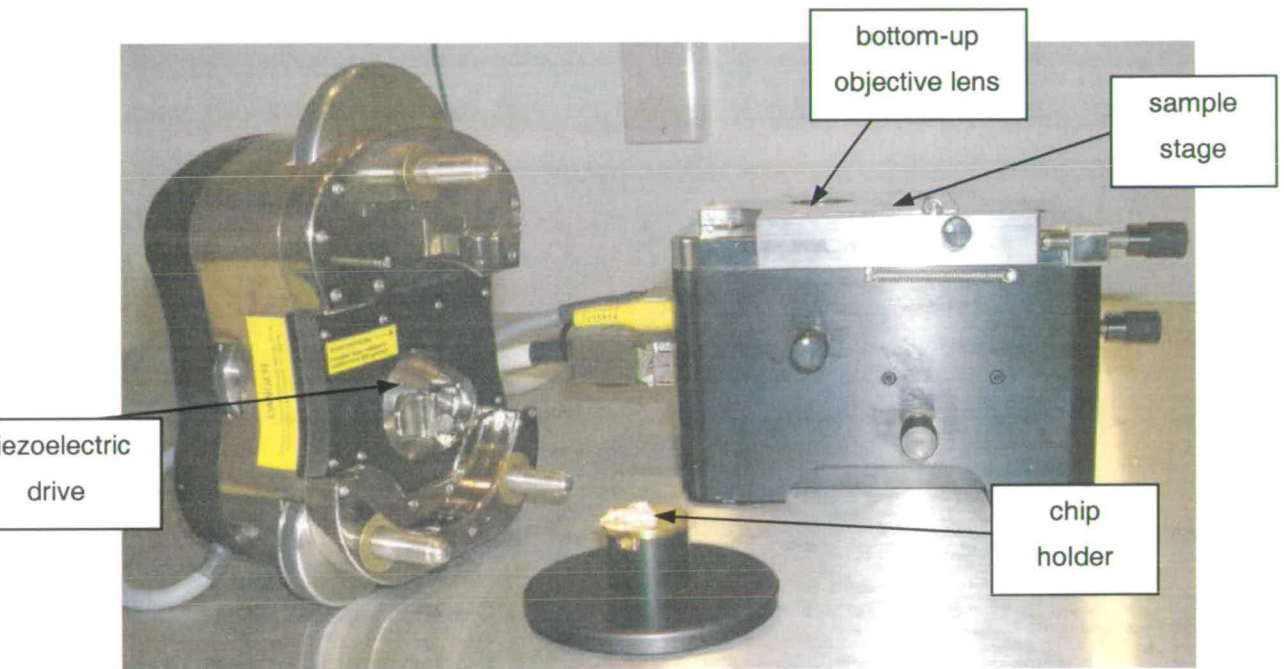
Fig. 3.20. Molecular force probe sitting on an air table (MFP-1D, Asylum Research).

This instrument allows for the recording of force-distance curves, with a sensitivity in terms of force of some pN. A feedback loop corrects the z piezoelectric response by means of a device that measures distances precisely, a linear variable differential transformer (LVDT) displacement transducer. Also the instruments implements a passive method for measuring the spring constant of SFM cantilevers [Hutter & Bechhoefer - 2, 1993].

3.1.5. Contact Angle Goniometry (CAG)

In the field of adhesion, a fundamental parameter is surface tension. It is defined elsewhere (see § 2.1.3). Unlike liquids that deform easily and therefore the surface tension of which can be measured easily, solids do not. One way of estimating their surface tension

is to measure the contact angle that liquids make on their surface. The magnitude of the contact angle depends on the type and magnitude of molecular interactions between drop and sample surface. There are three widely used methods for carrying out this task, namely the sessile drop method, the Wilhelmy method and the capillary-rise method [Gutowski, 1991]. The last two involve either using a capillary-shaped material or immersing most of a sample into a liquid, which did not suit us, that is why we used the sessile drop method also referred to as axisymmetric drop shape analysis-profile (ADSA-P) [Kwok *et al.*, 1998]. A picture of a sessile drop along with the parameters used for ADSA-P analysis are shown in Fig. 3.21. The contact angle θ is calculated from the tangent (green) to the drop profile at the intersection between the drop profile (yellow) and the baseline (blue).
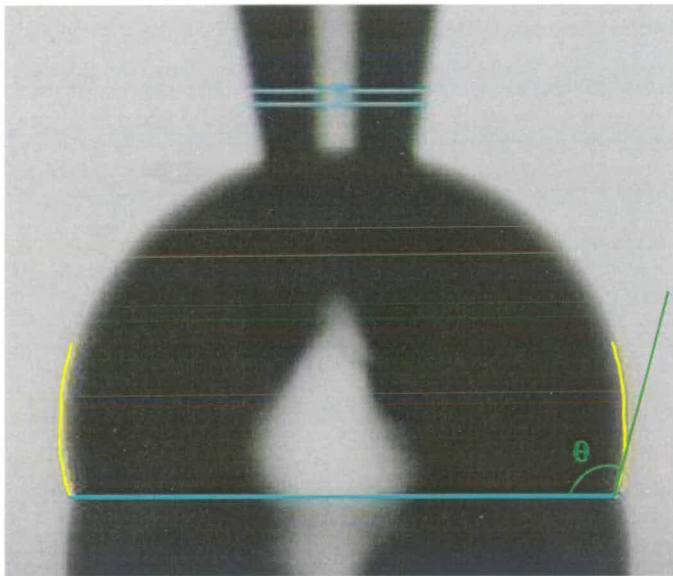

Fig. 3.21. Sessile drop of water deposited on polymer coated silicon wafer. Note the presence of the tip of the syringe needle inside the drop. The optical reflection of the drop provides the location of the three-phase contact line (baseline in blue).

There are three main types of contact angle measurements that can be made through axisymmetric sessile drop shape analysis-profile: 'passive' static angles, 'passive' dynamic contact angles and 'active' static contact angle. By passive we mean that no external force is applied to the liquid drop so that it is not forced to adopt a particular equilibrium or metastable state. Active methods consist in transferring energy to liquid drops by means of acoustic vibrations. A quite convincing experimental study has been proposed by Meiron *et*

al. [2004] and to a lesser degree by Della Volpe *et al.* [2001]. The purpose is to obtain an 'equilibrium contact angle' equivalent to the real Young's contact angle (see § 2.1.3 and equation (2.16)). Static contact angles are said to undergo dynamic changes so that it takes a drop some time to reach equilibrium [Cherry & El Muddaris, 1970]. The law that gives the dependence of contact angles on time is as follows:

$$\cos\theta_\infty = \cos\theta_{eq}\left[1 - a\exp(-ct)\right]$$ (3.45),

where *a* and *c* are experimental constants and *t* is time.

It seems that advancing contact angles provide more useful data for surface tension estimations than receding ones, in particular when the plane surface is an organic monolayer and for advancing rates up to, at least, 1 mm/min [Lam *et al.*, 2002]. However there is no guarantee as to whether or not advancing contact are always equivalent to Young's contact angles. Meiron *et al.* [2004] have observed that a 'global energy minimum' (GEM) exists for water and ethylene glycol drops on dispersive media such as wax (see § 2.1.1). It corresponds to an angle situation somewhere between the advancing contact angle (max) and the receding contact angle (min). GEM angles cannot be predicted by using existing formulas by Johnson and Dettre [1970] or by Andrieu *et al.* [1994]. It is however noteworthy that Meiron *et al.* [2004] have worked with drops of size one or even two orders of magnitude bigger than the capillary length. This quantity is a characteristic distance beyond which gravity can deform drops so that contact angles do not reflect only interface tension effects (interactions between solid and liquid) but also gravity effects. The mathematical definition of the capillary length is given by [Stelmashenko *et al.*, 2001]:

$$\kappa = \sqrt{\frac{\gamma_{LV}}{\rho_L g}}$$ (3.46),

where γ_{LV} is the liquid surface tension, g is the free-fall acceleration, ρ_L is the density of the liquid.

We used the FTA 200 by First Ten Angstroms (see Fig. 3.22), a contact angle goniometer that is capable of taking photographs or films of both sessile and pendant drop thanks to a 60 Hz CCD camera. The microscope can be tilted in order to measure drops located away from the sample edge and still be able to determine the location of the three-phase (liquid, solid, vapour) contact line or baseline. The syringe is connected to a pump enabling the user to measure dynamic contact angles: either advancing or receding ones.

Vibrations affect greatly the accuracy of the measurements that is why it is essential that the system be placed on an air-table.
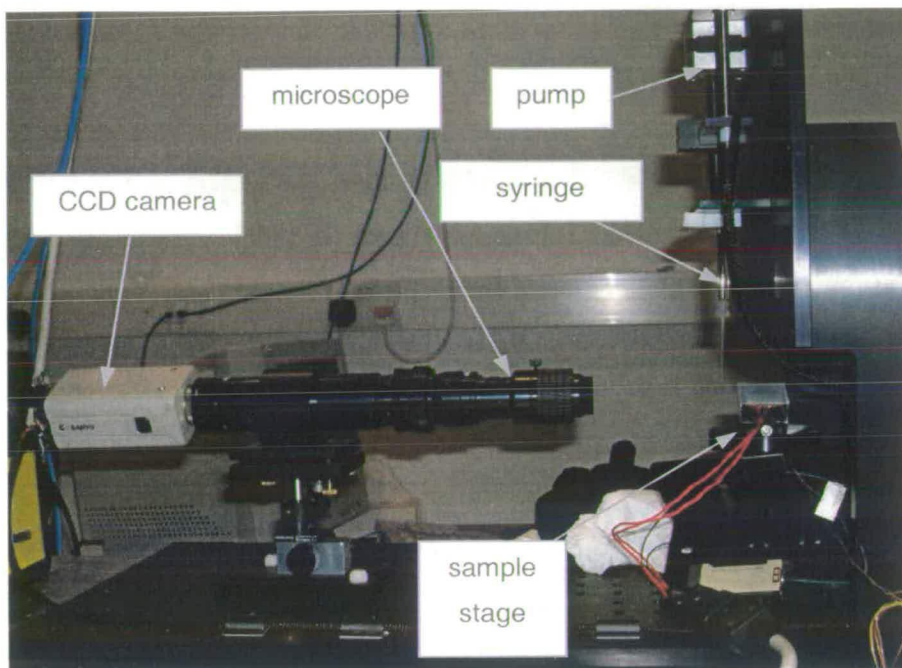

Fig. 3.22. Contact angle goniometer FTA 200 (First Ten Angstroms) on an air table.

3.2. Sample preparation

3.2.1. Substrates

<u>Transparent substrates:</u>

Engravings were made with a diamond-tipped pen on the backside of fused silica and brosilicate glass slides in order to make it easier to locate the organic layer for XPS, SFM and SWLI work as shown in Fig. 3.23. By backside we mean the side that is not going to be coated with an organic film.
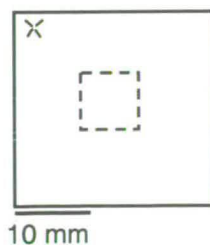

10 mm

Fig. 3.23. Engravings made on the basckisde of a 1mm thick glass slide.

Prior to coating the substrates most if not all of the organic contamination was removed by dipping the slides into a Caro or sulfuric piranha mixture [Ermolieff *et al.*, 2002]. A viscous mixture of concentrated sulfuric acid (> 95 wt%) and hydrogen peroxide (> 31 wt%) in a 8:2 ratio brings about the production of water and of Caro's acid according to the following process [Wei & Verhaverbeke, 1998]:

$$H_2O_2 + H_2SO_4 \leftrightarrow H_2O + H_2SO_5 \tag{3.46}$$

The production of water and the use of diluted hydrogen peroxide are factors that make the heat of dilution of sulfuric acid heat up the piranha mixture. Caro's acid's strong oxidising character brings in an instability that shifts the equilibrium towards the reactants' side. It is then necessary to add in hydrogen peroxide to produce the constituent (Caro's acid) that effectively removes organic contamination from the sample surface [Wei & Verhaverbeke, 1998].

Instead of adding hydrogen peroxide to shift back the equilibrium towards the right, we made a mixture with an excess of hydrogen peroxide [Tardivat, 1998]. The characteristics of the mixture was then: sulfuric acid (>98 wt%) and hydrogen peroxide (>59 wt%) in a 8:3 ratio. After 15 to 30 min the solution stopped bubbling up which was a sign of equilibrium shift towards the left. The substrate was then taken out and thoroughly washed with deionised water (resistivity = 17 MΩ.cm) to get rid of all of the viscous fluid. The wet and hydrophilic substrates were then dried under a dry flow of oxygen free nitrogen.

Other substrates:

Silicon wafers are opaque, there was therefore no point in making engravings on their back surface to help locate the coated region. Substrates prepared for SWLI work were small pieces of silicon wafer of surface area ≤ 20 mm^2, and cleaned in the same way as described above. Millimetre sized wafers can be easily and rapidly imaged by SWLI so that the presence of a coated cannot possibly be missed. SFM imaging is only being performed on local (some squared micrometres) areas, while the sample has to be of order of one squared centimetre or larger to manipulate it easily and ensure that the SFM tip lands on it. 'SFM silicon samples' were therefore entirely covered in organic molecules. Contact angle goniometry work was performed on Caro cleaned entire wafers (diameter = 50 mm) with a polymeric coating covering the whole surface apart from a narrow region by the edge.

Mica foils were used as cleaved, which is a process that is meant to provide contaminant free and atomically smooth surfaces. No engravings were made prior to coating mica surfaces, the coated areas were however surrounded by a fine indentation to help locate the film boundaries by SWLI.

3.2.2. Polymeric films and Self Assembled Monolayers (SAMs)

Polydimethylsiloxane (PDMS):

The preparation of PDMS monolayers was carried out according to the method developed by Déruelle [1995]. It lies on the adsorption of PDMS chains (see Fig. 3.24 a) diluted in a good solvent onto a silica surface. A study of the adsorption kinetics shows that the anchoring of polymer chains stops after 24 hours at a temperature of 110°C [Déruelle, 1995]. It is also possible to control the amount of polymer adsorbed by varying the volume fraction Φ of the solution and sealing the substrate covered in PDMS solution in an appropriate crucible. As we wanted to produce dense monolayers, we did not take advantage of this property and restricted our work to PDMS *melts*, that is solvent-free polymer samples. In fact we used two procedures to produce monolayers from PDMS melts:

- Primary melts: PDMS is a fluid polymer at ambient temperature (T_{glass} = -125°C and $T_{melting}$ = -40°C) whose viscosity is controlled by its molecular weight. High molecular weight PDMS (see Table 3.1) has a cold honey-like viscosity therefore a scalpel blade was used to pick up some polymer and deposit it onto a clean silica surface. Low molecular weight PDMS is much runnier and could be deposited with the help of a simple pipette. The obtained sample was then transferred into a vacuum oven (Heraeus VT 6025) for 24 hours at a temperature T = 110°C and under a pressure $P \sim 9$ mbar. This rough vacuum is thought to help keep the surface clean. The next step consisted in washing away the 'macroscopic' excess of polymer by rinsing abundantly with toluene, a rather good (and cheap) solvent of PDMS [Favre, 1996]. To remove the excess of polymer (non-adsorbed chains) the sample was immersed into a toluene bath (100 ml in volume) for at least 2 hours. Finally the sample was dried under an oxygen free nitrogen flow.

- Secondary melts: these are defined as polymer melts resulting from the evaporation of the solvent used to make a solution of that polymer. Practically we made PDMS solutions in octane with a volume fraction ranging from 0.1 to 0.2. Octane was

chosen because it is a better solvent of PDMS than toluene (see Table 3.2), has a lower vapour pressure: P_{vap}(octane) ~ 9 mmHg at 20°C while P_{vap}(toluene) ~ 22 mmHg at 20°C and is purely dispersive unlike toluene (see § 2.1.2). For comparison's sake let us recall that P_{vap}(water) ~ 17 mmHg at 20°C [Yaws, 1999]. Some samples were subjected to a fast evaporation process where, once the liquid droplets had been deposited, they were transferred immediately into the vacuum oven for the same amount of time and with the same settings as above. Other samples were subjected to a so-called slow evaporation process. This involved a step where the polymer solution was allowed to evaporate in ambient conditions (T ~ 18°C and P ~ 1 bar) for 18 hours, which is believed to leave a macroscopic film of melt on the substrate. After that the sample was transferred into the oven (see primary melt section). The rinsing steps were carried out exactly in the same way as those for primary melts.

Polystyrene (PS):

PS is an amorphous solid material at ambient temperature ($T_{glass} = 100°C$) that contains aromatic rings (see Fig. 3.24 b), therefore to obtain a melt of it, a solution of PS had to be prepared first (secondary melt route). Toluene is a good solvent of PS (see Table 3.2) it was therefore used to make a solution with a PS volume fraction of 0.1. A droplet was then deposited onto a borosilicate glass substrate and allowed to evaporate as in the PDMS case. The only difference regards the rinsing steps where methyl ethyl ketone (MEK) was used instead of toluene as it is a slightly worse solvent of PS than toluene (see Table 3.2) and PS was suspected to have poorer adhesion to glass than PDMS.

γ-aminopropyltriethoxysilane (APS):

The preparation of APS coated glass slides was performed by our colleague Nhan Thanh Pham in post-doctoral studies at the School of Physics and Astronomy, The University of Edinburgh.

After cleaning the glass substrates in a piranha mixture (see §3.2.1) for 1 hour, they were thoroughly rinsed with deionised water and stored under deionised water until use. An APS solution in a 95:5 ethanol:water mixture at a volume fraction of 0.001 was made and applied onto an oxygen plasma treated PDMS network stamp with a cotton swab. The hydrophilised stamp surface had a saw tooth pattern with 'standing out' lines of width ~ 30 μm and spacings of width ~ 20 μm. The solvent was allowed to evaporate and then the stamp was

placed in contact (microcontact printing) with the glass substrate for 30 seconds. This brings about hydrolysis of the ethoxy groups (see Fig. 3.24 c) and the formation of a siloxane bridge, that is chemisorption. No rinsing was applied to the APS coated glass surface [Geissler *et al.*, 2003].

The samples were kept in Fluoroware petri dishes. These low surface energy containers (fluorocarbon) have been shown to limit the carbonaceous contamination of isopropyl alcohol (IPA) cleaned silicon wafers to less than 0.26 nm for a storage period of 100 days [Seah & Spencer - 2, 2003].
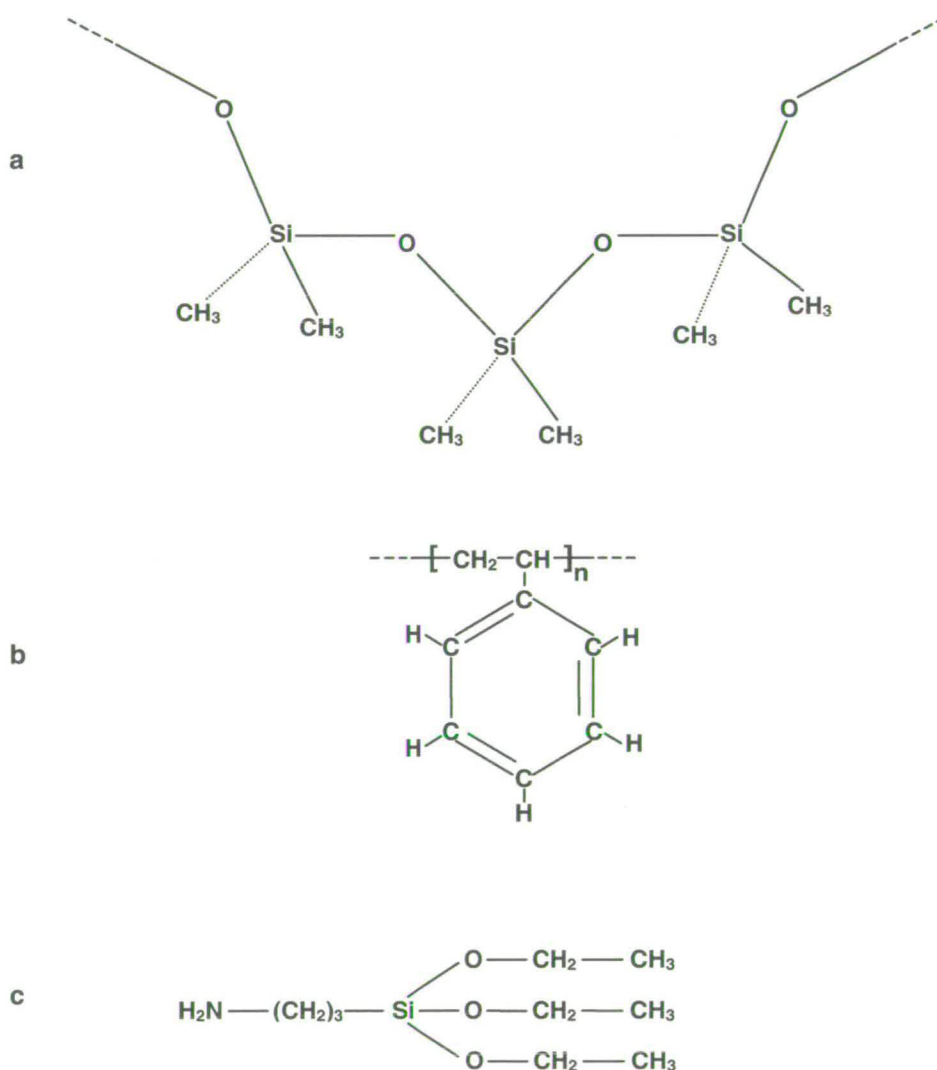

Fig. 3.24. Chemical structures of the studied organic molecules. a: Polydimethylsiloxane (PDMS). b: Polystyrene (PS). c:γ-aminopropyltriethoxysilane (γ-APS).

3.2.3. Metal coatings

Chemical vapour deposition (CVD) is a technique that consists in heating a metal in a vacuum until it turns into vapour so that some evaporated atoms move up towards a sample and deposit on its surface [Barnes *et al.*, 2000]. The apparatus that we have used is an Edwards E306. Evaporation takes place in a vacuum chamber, $P_{evap} = 10^{-5}$ mbar. The manufacturer claims that a quartz sensor allows for the monitoring of metal film thicknesses ranging from some angstroms to micrometres with an accuracy of $\pm 10\%$.

We used CVD to deposit aluminium and gold on various monolayer or multilayer coated substrates in order to modify the optical properties of the samples (reflectivity) for SWLI work.

Gold is a noble metal that does not get oxidised, so that the effective optical properties are likely to be close to the theoretical ones and to be long lasting. On the other hand gold is known for not providing very uniform coatings due to its diffusion properties. Furthermore the reflection coefficient of the air/gold interface varies from 39% to 95% across the spectrum relevant to our optical profilometer: ~430 nm to ~630 nm. Aluminium is bound to form more uniform films by CVD because of the relatively high vapour pressure of aluminium at the filament temperature. Moreover the reflective coefficient of the air/aluminium interface is high and almost constant at a value of 92% across the spectrum mentioned above. Unfortunately aluminium does corrode.

The data relevant to our work and regarding the substrates, coatings and other chemicals used to make films are compiled in Table 3.1. These data will be often referred to in Chapter 4 and Chapter 5.

Materials (chemicals)	n_{bulk}	k_{bulk}	n_ε	k_ε	M_W kg/mol	PI	Kinematic viscosity 10^4 cSt	Purity or contents
Fused silica, multi lab	~ 1.46	~ 0	1.459[1]	0.044[1]	-	-	-	99.995% SiO₂
Borosilicate glass, Menzel-Glaser	~ 1.53	~ 0	1.523	0.014	-	-	-	> 70% SiO₂
Mica, Agar	~ 1.57[2]	~ 0	-	-	-	-	-	-
Silicon, Siltronix	~ 4.12	~ 0.048	-		-	-	-	10^2 to 10^4 S.m⁻¹
PS, Aldrich	~ 1.59	~ 0	-	-	280	> 2	Solid	?
(α, ω) CH₃-PDMS, Polymer Source	~ 1.40	~ 0	-	-	162	1.35	~ 15	~ 100%
	~ 1.40	~ 0	-	-	80.5	1.15	~ 2.5	~ 100%
	~ 1.40	~ 0	-	-	8.1	1.09	~ 0.02	~ 100%
(α, ω) HO-PDMS Gelest α HO-PDMS, Polymer Source	~ 1.40	~ 0	1.544	0.000	110	> 2	~ 5	~ 100%
	~ 1.40	~ 0	-	-	49	> 2	~ 0.5	~ 100%
	~ 1.40	~ 0	-	-	5.5	1.10	~ 0.02	~ 100%
	~ 1.40	~ 0	-	-	15.2	1.17	~ 0.04	~ 100%
γ-APS, Aldrich	~ 1.42	~ 0	-	-	0.22	-	-	~ 100%
Sulfuric acid, Fisher	-	-	-	-	-	-	-	> 98%
Hydrogen peroxide, Fisher	-	-	-	-	-	-	-	> 59% w/v
DI water, Purite select	-	-	-	-	-	-	~ 0.0001	~ 17 MΩ.cm
Gold, ?	0.40	2.54	-	-	-	-	-	?
Aluminium, Balzers	0.91	6.55	-	-	-	-	-	99%

Table 3.1. Some important physical properties of the constituents used in the preparation of polymeric films or self assembled monolayers (SAMs). PI is the polydispersity index of the various PDMS samples. Refractive and extinction index are taken at ~ 530 nm, the centre of the light spectrum used in SWLI as well as the laser wavelength used in the ellipsometric measurements (ε) performed by the Nanofilm application team. The typical bulk indices values were found in [Palik, 1985]. [1] These values are for the 10.9 nm thick outermost layer, the measured values for the material underneath that superficial layer are $n = 1.447$ and $k = 0.000$. [2] Transmittance measurements [Gauthier-Manuel, 1998].

3.2.4. Probe liquids

The assessment of PDMS surface tension and of its components (see § 2.1.3) by contact angle goniometry involves measuring the contact angle that at least three different liquids make on a PDMS surface. These liquids must develop interactions of different nature with the PDMS chains and must not modify their conformation through swelling for instance [Sedev *et al.*, 1996]. It is customary to call these liquids, probe liquids as they really probe the surface properties of a material.

The probe liquids that were chosen are: deionised water (not milliQ), hexadecane, dimethyl sulfoxide and mercury. All of these were obtained from commercial source and used without further purification, except for mercury.

This metal liquid tends to get oxidised, and as a result develops a sort of rusty crust that is significantly lighter than metal mercury and that does not adhere well to the metal. A separating funnel was used to purify mercury by leaving the oxide on top while the 'pure' metal was retrieved in a vial placed underneath the separating funnel [Carré & Visovsky, 1998].

Some important data about the compatibility of certain liquids and the used polymers are compiled in Table 3.2. For detailed information about the Flory-Huggins interaction parameter see § 2.2.1.

	Purity	Solubility parameter δ $((J.cm^{-3})^{1/2})$ @ 25°C	Molar volume V $(cm^3.mol^{-1})$ @ 25°C	$\chi_{liq-PDMS}$ @ 25°C	χ_{liq-PS} @ 25°C
DI water, Purite select	~ 17 MΩ.cm	47.81	18.07	~ 8.08	-
DMSO, Fisher	99.96%	26.34	71.33	~ 3.90	-
Hexadecane, Acros Organics	99%	15.94	294.1	~ 0.40	-
Mercury, Fisher	99.999%	64.69	14.87	~ 15.03	-
Octane, Fisher	> 99%	15.32	163.51	~ 0.34 *≤ 0.42*	-
Toluene, Fisher	99.9%	18.35	106.56	~ 0.76 *≥ 0.50*	~ 0.37 *≥ 0.42*
Hexamethyldisiloxane, Gelest	~ 100%	12.58	213.59	~ 0.94 *≤ 0.34*	-
MEK, Fisher	99.82%	18.80	90.20	-	~ 0.40 *< 0.63*

Table 3.2. Interactions between various liquids (solvents and non-solvents) and polydimethylsiloxane and polystyrene. Precise experimental evaluations of the Flory Huggins parameter for particular volume fractions, polymer molecular weight and temperature are shown in italics [Brandrup *et al.*, 1999]. Rougher estimates of the same parameter from Flory's simple relationship (see § 2.2.1), the tabulated values of liquid solubility parameter and molar volume are shown in normal characters [Yaws, 1999]. PS's solubility parameter was taken equal to 17.50 $(J.cm^{-3})^{1/2}$ while that of PDMS was taken equal to 15.22 $(J.cm^{-3})^{1/2}$ [Brandrup *et al.*, 1999].

The interaction parameter of the PDMS/toluene pair seems to be underestimated by the calculation while the measured value for $\phi = 0.2$ keeps toluene in the good to theta solvent region. However imprecise the calculation of the interaction parameter may be, hexadecane is bound to be a rather good solvent of PDMS so caution will be needed to interpret the contact angle values of this liquid on a PDMS monolayer.

3.3. References

Band, I.M; Kharitonov, YU.I; Trzhaskovskaya, M.B. (1979) *Photoionization cross sections and photoelectron angular distributions for x-ray line energies in the range 0.132-4.509 keV*, Atomic Data and Nuclear Data Tables. **23**(5), 443-505.

Barnes, M.C; Kim, D-Y; Ahn, Y.S; Lee, C.O; Hwang, N.M. (2000) *Deposition mechanism of gold by thermal evaporation: approach by charged cluster model*, Journal of Crystal Growth. **213**(1-2), 83-92.

Brandrup, J; Immergut, E.H; Grulke, E.A. (1999) *Polymer handbook 4th edition*, John Wiley & Sons, New York, USA.

Briggs, D; Seah, M.P. (1983) *Practical surface analysis by Auger and x-ray photoelectron spectroscopy*, John Wiley & Sons, Chichester UK, **Chapter 1**, 6-7.

Carré, A; Visovsky, N. (1998) *Adhesion and wetting hysteresis of a metal (mercury) on an oxide glass in air and nitrogen*, Journal of Adhesion. **68**(3-4), 301-313.

Cheng, Y-Y; Wyant, J.C. (1984) *Two-wavelength phase shifting interferometry*, Applied Optics. **23**(24), 4539-4543.

Cherry, B.W; El Muddaris, S. (1970) *Wetting, kinetics and strength of adhesive joints*, Journal of Adhesion. **2**, 42-48.

Cumpson, P.J; Seah, M.P. (1997) *Elastic scattering corrections in AES and XPS. II. Estimating attenuation lengths and conditions required for their valid use in overlayer/substrate experiments*, Surface and Interface Analysis. **25**(6), 430-446.

De Groot, P. (1993) *What is frequency domain analysis ?*, Zygo R&D Technical Bulletin-www.zygo.com, 1-7.

De Groot, P; Deck, L. (1995) *Surface profiling by analysis of white-light interferograms in the spatial frequency domain*, Journal of Modern Optics. **42**(2), 389-401.

De Groot, P; Colonna de Lega, X; Kramer, J; Turzhitsky, M. (2002) *Determination of fringe order in white-light interference microscopy*, Applied Optics. **41**(22), 4571-4578.

Della Volpe, C; Maniglio, D; Siboni, S; Morra, M. (2001) *An experimental procedure to obtain the equilibrium contact angle from the Wilhelmy method*, Oil & Gas Science and Technology – Revue de l'IFP. **56**(1), 9-22.

Déruelle, M. (1995) *Les polymères aux interfaces, application à l'adhésion solide élastomère*, Thèse de doctorat, Université Paris VI, France.

Eberhart, J.P. (1997) *Analyse structurale et chimique des matériaux*, Dunod, Paris, France.

Ermolieff, A; Marthon, S; Rochet, X; Rouchon, D; Renault, O; Michallet, A; Tardif, F. (2002) *Silicon wafer cleaning processes and ozone oxide growth as studied by angle-resolved x-ray photoelectron spectroscopy (ARXPS) and ellipsometry*, Surface and Interface Analysis. **33**(5), 433-436.

Favre, E. (1996) *Swelling of crosslinked polydimethylsiloxane networks by pure solvents: influence of temperature*, European Polymer Journal. **32**(10), 1183-1188.

Gauthier-Manuel, B. (1998) *Simultaneous determination of the thickness and optical constants of weakly absorbing thin films*, Measurement Science and Technology. **9**(3), 485-487.

Geissler, M; Kind, H; Schmidt-Winkel, P; Michel, B; Delamarche, E. (2003) *Direct patterning of NiB on glass substrates using microcontact printing and electroless deposition*, Langmuir. **19**(15), 6283-6296.

Halliday, D; Resnick, R; Walker, J. (2001) *Fundamental of physics 6th edition*, John Wiley & Sons, New York USA.

Harasaki, A; Schmit, J; Wyant, J.C. (2000) *Improved vertical-scanning interferometry*, Applied Optics. **39**(13), 2107-2115.

1 - Hutter, J.L; Bechhoefer, J. (1993) *Manipulation of van der Waals forces to improve image resolution in atomic-force microscopy*, Journal of Applied Physics. **73**(9), 4123-4129.

2 - Hutter, J.L; Bechhoefer, J. (1993) *Calibration of atomic-force microscope tips*, Review of Scientific Instruments. **64**(7), 1868-1873.

Jablonski, A; Powell, C.J. (2002) *The electron attenuation length revisited,* Surface Science Reports. **47**(2-3), 33-91.

Jin, G; Jansson, R; Arwin, H. (1996) *Imaging ellipsometry revisited: Developments for visualization of thin transparent layers on silicon substrates.* Review of Scientific Instrumentation. **67**(8), 2930-2936.

Johnson R.E; Dettre, R.H. (1970) *Contact angles and monolayer depletion*, Journal of Adhesion. **2**, 3-15.

Keddie, J.L. (2001) *Structural analysis of organic interfacial layers by ellipsometry*, Current Opinion in Colloid & Interface Science. **6**(2), 102-110.

Kim, S-W; Kim, G-H. (1999) *Thickness-profile measurement of transparent thin-film layers by white-light scanning interferometry*, Applied Optics. **38**(28), 5968-5973.

Kwok, D.Y; Lam. C.N.C; Li, A; Leung, R; Wu, R; Mok, E; Neumann, A.W. (1998) *Measuring and interpreting contact angles: a complex issue*, Colloids and Surfaces A: Physicochemical and Engineering Aspects. **142**(2-3), 219-235.

Lam, C.N.C; Wu, R; Li, D; Hair, M.L; Neumann, A.W. (2002) *Study of the advancing and receding contact angles: liquid sorption as a cause of contact angle hysteresis*, Advances in Colloid and Interface Science. **96**(1-3), 169-191.

Lee, L-H. (1991) *Fundamentals of adhesion*, Plenum Press, New York, USA.

McWaid, T; Vorburger, T; Song, J.F; Chandler-Horowitz, D. (1992) *The effects of thin films on interferometric step height measurements*, Proceedings of the Society of Photo-Optical Instrumentation Engineers (SPIE). **1776**, 2-13.

Meiron, T.S; Marmur, A; Saguy, I.S. (2004) *Contact angle measurement on rough surfaces*, Journal of Colloid and Interface Science. **274**(2), 637-644.

Meyer, E; Hug, H.J; Bennewitz, R. (2004) *Scanning probe microscopy. The lab on a tip*, Springer-Verlag, Berlin, Germany.

Onuma, K; Kameyama, T; Tsukamoto, K. (1994) *In situ study of surface phenomena by real time phase shift interferometry*, Journal of Crystal Growth. **137**(3-4), 610-622.

Palik, E.D. (1985) *Handbook of optical constants of solids*, Academic Press Inc.

1 - Powell, C.J; Jablonski, A. (2001) *Effects of elastic-electron scattering on measurements of silicon dioxide film thicknesses by x-ray photoelectron spectroscopy*, Journal of Electron Spectroscopy and Related Phenomena. **114**, 1139-1143.

2 - Powell, C.J; Jablonski, A. (2001) *NIST electron effective-attenuation-length-database – version 1.0*, National Institute of Standards and Technology, Gaithersburg, MD, USA.

Reilman, R.F; Msezane, A; Manson, S.T. (1976) *Relative intensities in photoelectron spectroscopy of atoms and molecules*, Journal of Electron Spectroscopy and Related Phenomena. **8**(5), 389-394.

Seah, M.P. (2003) *Intercomparison of silicon dioxide thickness measurements made by multiple techniques: The route to accuracy*, Journal of Vacuum Science and Technology A. **22**(4), 1564-1571.

Seah, M.P; Gilmore, I.S. (2001) *Simplified equations for correction parameters for elastic scattering effects in AES and XPS for Q, β and attenuation lengths*, Surface and Interface Analysis. **31**(9), 835-846.

Seah, M.P; Spencer, S.J. (2002) *Ultrathin SiO2 on Si II. Issues in quantification of the oxide thickness*, Surface and Interface Analysis. **33**(8), 640-652.

1 - Seah, M.P; Spencer, S.J. (2003) *Ultrathin SiO2 on Si IV. Intensity measurements in XPS and deduced thickness linearity*, Surface and Interface Analysis. **35**(6), 515-524.

2 - Seah, M.P; Spencer, S.J. (2003) *Ultrathin SiO2 on Si I. Quantifying and removing carbonaceous contamination*, Journal of Vacuum Science and Technology A. **21**(2), 345-352.

Sedev, R.V; Petrov, J.G; Neumann, A.W. (1996) *Effect of swelling of a polymer surface on advancing and receding contact angles*, Journal of Colloid and Interface Science. **180**(1), 36-42.

Shallenberger, J.R; Cole, D.A; Novak, S.W; Moore, R.L; Edgell, M.J; Smith, S.P; Hitzman, C.J; Kirchhoff, J.F; Principe, E; Biswas, S; Bleiler, R.J; Nieveen, W; Jones, K. (2000) SiO_2 *thickness determination by XPS, AES, SIMS, RBS, TEM and ellipsometry*, Journal of Vacuum Science & Technology B. **18**(1), 440-444.

Stelmashenko, N.A; Craven, J.P; Donald, A.M; Terentjev, E.M; Thiel, B.L. (2001) *Topographical contrast of partially wetting water droplets in environmental scanning electron microscopy*, Journal of Microscopy. **204**(2), 172-183.

Tardivat, C. (1998) *Étude des mécanismes d'adhésion entre un élastomère et du verre. Renforcement de l'interface par une couche d'adhésif, ou par des chaînes connectrices*, Thèse de doctorat, Université Paris XI Orsay, France.

Thermo Electron, internal documentation VG014T, www.thermo.com.

Ton-That, C; Shard, A.G; Bradley, R.H. (2000) *Thickness of spin-cast polymer thin films determined by angle-resolved XPS and AFM tip-scratch methods*, Langmuir. **16**(5), 2281-2284.

Tougaard, S. (1996) *Quantitative XPS: non-destructive analysis of surface nano-structures*, Applied Surface Science. **101**, 1-10. Further information on the package referred to in this paper can be found at: www.quases.com

Wagner, C.D; Davis, L.E; Zeller, M.V; Taylor, J.A; Raymond, R.H; Gale, L.H. (1981) *Empirical atomic sensitivity factors for quantitative analysis by electron spectroscopy for chemical analysis*, Surface and Interface Analysis. **3**(5), 211-225. The data reported in this paper is also to be found at: www.uksaf.org/data/sfactors.html.

Wang, G; Arwin, H; Jansson, R. (2003) *Optimization of azimuth settings in polarizer-compensator-sample-analyzer off-null ellipsometry*, Applied Optics. **42**(1), 38-44.

Watts, J.F; Wolstenholme, J. (2003) *An introduction to surface analysis by XPS and AES*, John Wiley & Sons, Chichester UK.

Wei, J; Verhaverbeke, S. (1998) *Cleaning technology in semiconductor device manufacturing V*, PV 97-35, The Electrochemical Society, Pennington NJ USA, 496-.

Wiesendanger, R. (1994) *Scanning probe microscopy and spectroscopy*, Cambridge University Press, Cambridge UK, **2**, 226-230.

Wyant, J.C. (2002) *White light interferometry*, Proceedings of the Society of Photo-Optical Instrumentation Engineers (SPIE). **4737**, 98-107. This paper can be downloaded from: www.optics.arizona.edu/jcwyant/pdf/Meeting-papers/WhiteLightInterferometry.pdf.

Yaws, C.L. (1999) *Chemical properties handbook*, McGraw-Hill, New York, USA.

Yeh, J.J; Lindau, I. (1985) *Atomic subshell photoionization cross sections and asymmetry parameters: $1 \leq Z \leq 103$*, Atomic Data and Nuclear Data Tables. **32**(1), 1-155.

4. 3-D imaging of thin films by SWLI, comparison with other techniques and metrology issues

In this chapter we prove that SWLI can be used as an alternative to *imaging ellipsometry* to map entire thin films of lateral size up to the centimetre range or even larger. We show how the boundaries of a thin film can be located precisely so as to perform SFM measurements (nanostructure) on regions of interest thanks to a special sample plate of our design as well as XPS analysis with a spectrometer that has got a motorised x, y, z sample stage. We then propose a way of measuring the film thickness by XPS in spite of the large acceptance of the Σ Probe (see Fig. 3.14). The study of the mapping capabilities of SWLI follows this introductory work. We focus on PDMS chains adsorbed on silica surfaces and try to characterise roughly the nature of this adsorption as well as compare the various polymer deposition methods. The last subsection of this chapter deals with the metrology issues in SWLI measurements. The comparison with XPS and SFM, two techniques that do not depend on the optical properties of the system being studied helps in determining the limits of SWLI as regards absolute film thickness determination (precision and accuracy).

4.1. Preliminary measurements

4.1.1. Locating boundaries of PDMS monolayers for SFM and XPS work

As was explained in § 3.1.1, SWLI combines interferometry to measure heights (z axis) and optical microscopy to image surfaces in the horizontal plane (x, y). Depending on the magnification of the interferometric objective being used the field of view will vary in size. A x 2.5 Michelson objective (Zygo New View 100) has a field of view of approximately 2.82 mm by 2.13 mm. It is also possible to join several fields of view provided that the sample stage is motorised (see Fig. 3.5), the resulting stitched image is then larger. An example of such a stitched map is given in Fig. 4.1 a. The instrument performs both interferometric and 'ordinary' microscopy so that with an objective whose focus depth is 185 μm one can image simultaneously features within the interference depth (4 μm) and features located at least as far as ten times the focus depth: for instance engravings (see § 3.2.1) made with a diamond-tipped pencil at the back of a 1 mm thick glass slide. Those engravings appear as wide black scratches in Fig. 4.1 b. The vertical grey and white stripes correspond to the stage surface (steel) and the lines crossing each other at right angle

correspond to the various stitched fields of view. Since the two images share the same system of coordinates, overlaying one on top of the other is easy (see Fig. 4.1 c).
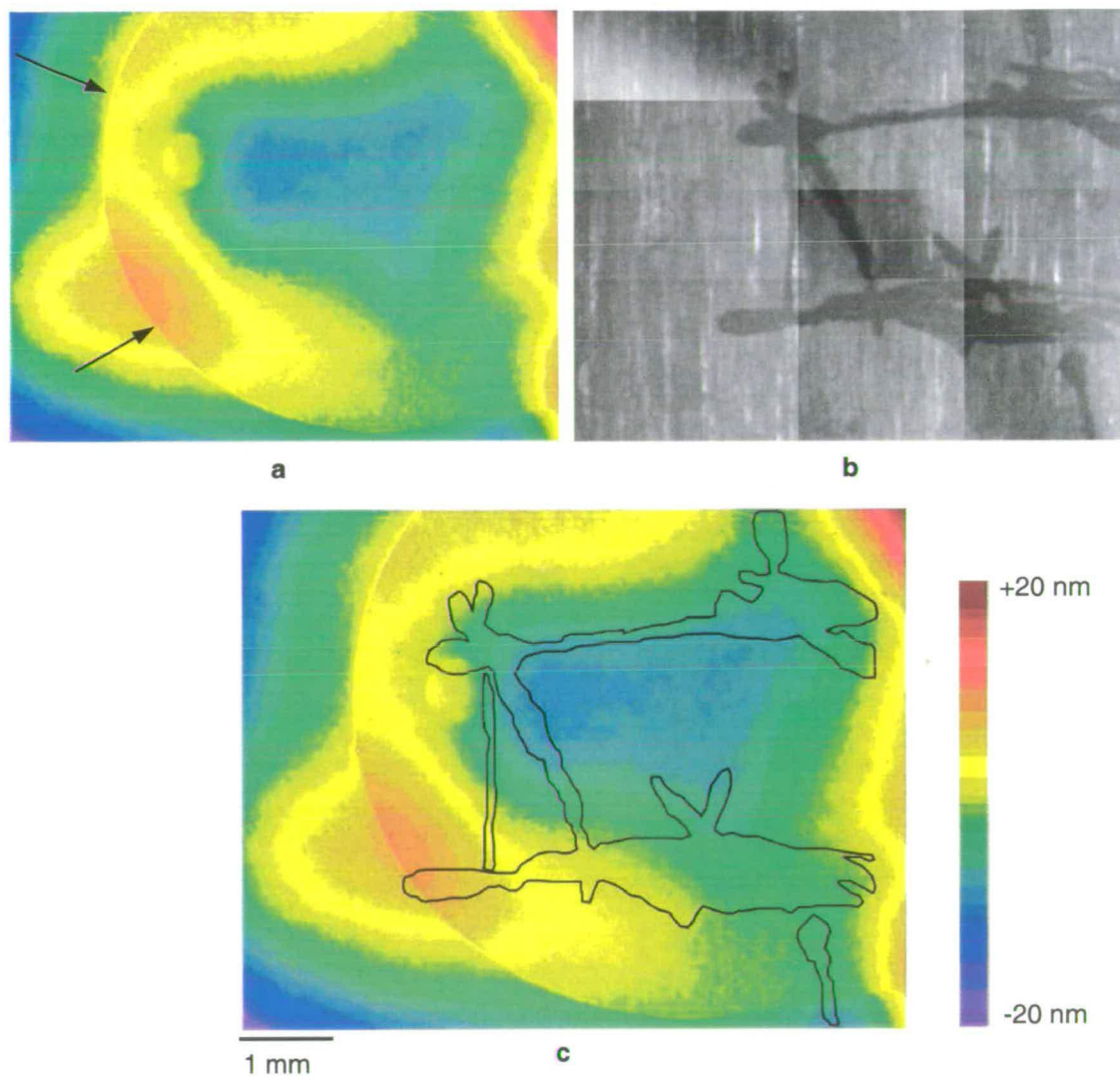

Fig. 4.1. Location of the boundaries of a PDMS film relative to engravings made on the back of a glass slide. a: SWLI surface map of the PDMS film with boundaries (black arrows). b: Optical micrograph (engravings). c: Superimposition of a and b.

The precise knowledge of the film location (boundaries) in the shape of an image such as Fig. 4.1 c and the use of a fully motorised x, y, z sample stage enabled us to easily position the X-ray spot of the Sigma Probe X-ray photoelectron spectrometer. On the other hand the Pico SPM (Molecular Imaging) scanning force microscope does not have such a motorised stage therefore an appropriate manual sample plate had to be designed (see Fig. 4.2).
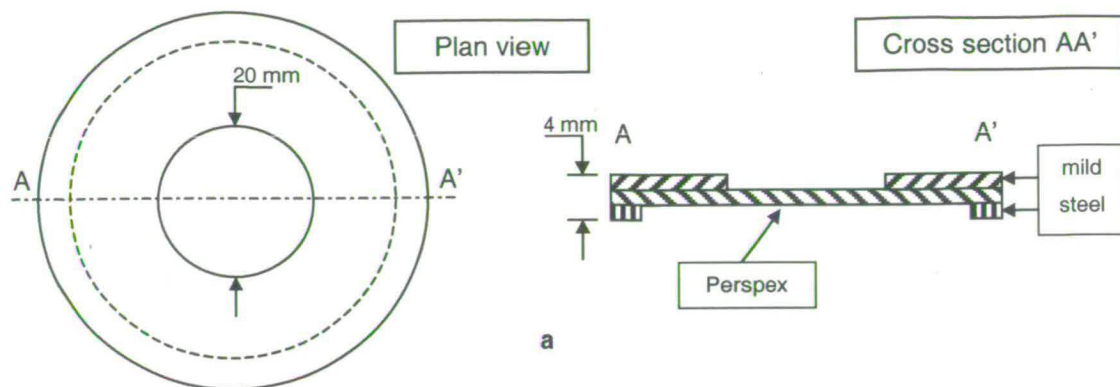
Fig. 4.2. See-through SFM sample plate. a: schematic. b: sample plate mounted on magnetic legs and 45° mirror. c: Zoom in (x9 lens) on squared engravings (black arrow) made on a fused silica substrate and silicon chip (grey arrow).

It was then possible to position the SFM tip within about 0.3 mm of the desired location, it will be seen further on in this chapter that this ability is useful.

4.1.2. Film thickness determination by wide acceptance angle XPS

It has been mentioned in § 3.1.4 that the determination of a film thickness through a simple Beer-Lambert law (equation 3.43) requires, aside from the ratio of intensities of the sample to be analysed, the knowledge of R_0, AL and θ. The first two parameters are relatively easy to obtain and therefore their case will be dealt with last. The third one poses a bigger problem as equation 3.43 is valid only when the analyser acceptance angle is smaller than say, 6°. This condition is not met in the case of the Sigma Probe spectrometer that is why a piece of p-doped (boron) silicon was sent to the manufacturer for analysis with a Theta Probe. We recall here that this instrument has a particular feature namely, an angle resolved transfer lens, which makes the use of equation (3.43) possible for a number of angles. Furthermore elemental silicon is always covered in an ultra-thin natural oxide layer, which provides users with two peaks easy to resolve (see Fig. 4.3 a). The same sample was then analysed using our Sigma Probe (Σ), and the Theta Probe (Θ) with the angle resolving option deactivated. The comparison of the obtained intensity ratios (surface area of the peaks) is presented in Fig. 4.3 b. Only those ratios corresponding to emission angles smaller than 65° were used since beyond that limit elastic scattering effects alter the ratios too much to be of any use in film thickness determination. It is clear that both instruments give similar results so that an effective emission angle θ_{eff} can be inferred and applied to equation (3.43), at least in the case of ultra-thin films. Its value is estimated to be $\theta_{eff} = (54.5 \pm 2)°$. This is very near the emission angle at the middle of the transfer lens 53°, which obviously corresponds to the likeliest path for photoelectrons to enter into the transfer lens.

R_0 was determined experimentally on several fused silica substrates coated with PDMS chains of various molecular weight (from 40 kg mol^{-1} to 260 kg mol^{-1}), using equation (3.38) where I_{PDMS} plays the role of I_{SiO2} and I_{SiO2} plays the role of I_{Si}. The resulting plot is presented in Fig. 4.4 a. The slope of the straight line is R_0. $R_0 \cong 0.66$ a bigger value than 0.52 as calculated using equation (3.41). The uncertainty on the density of PDMS as a thin film can explain that discrepancy. The attenuation length of Si2p photoelectrons in PDMS was calculated using Powell's and Jablonski's database program [2001]. Key user-provided data were the band gap energy E_g taken equal to that of SiO_2 [Eder *et al.*, 1997] as well as

Cumpson's suggested values of inelastic mean free path [2001]. The variables were the emission angle θ and the film thickness. The former was varied from 23° to 83° and the latter from 1 nm to 10 nm, which is roughly the entire analysis depth of the technique (see Fig. 4.4 b). For a given film thickness, the average attenuation length was obtained by integration below the curve so as to take into account the elastic scattering effects at large angles (see Fig. 4.4 b and c).
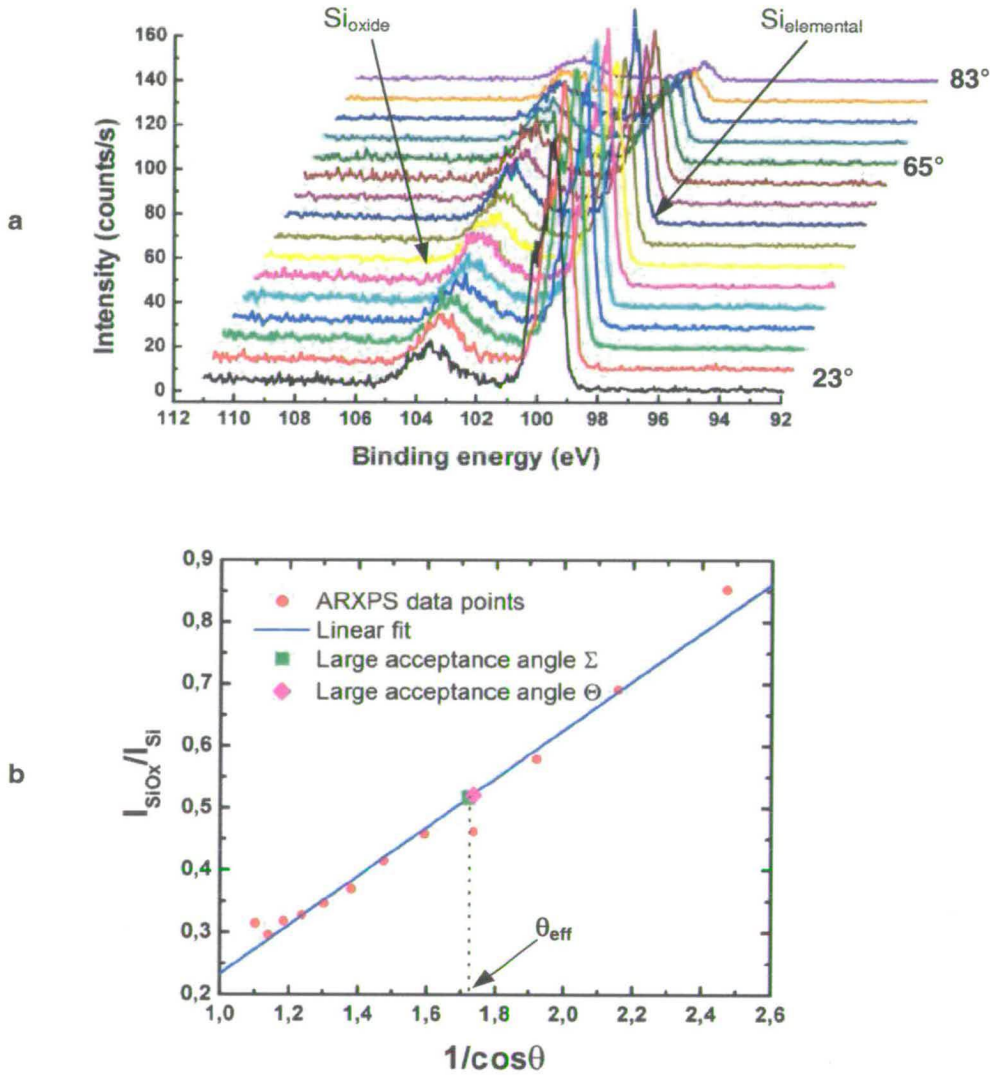

Fig. 4.3. Intensity analysis of the Si2p photoelectron line of elemental and oxide silicon. a: multiple spectra obtained by ARXPS (Theta Probe) from 23° to 83°. b: Comparison between the intensity ratios obtained by ARXPS and large acceptance angle XPS. Determination of the effective emission angle θ_{eff}.
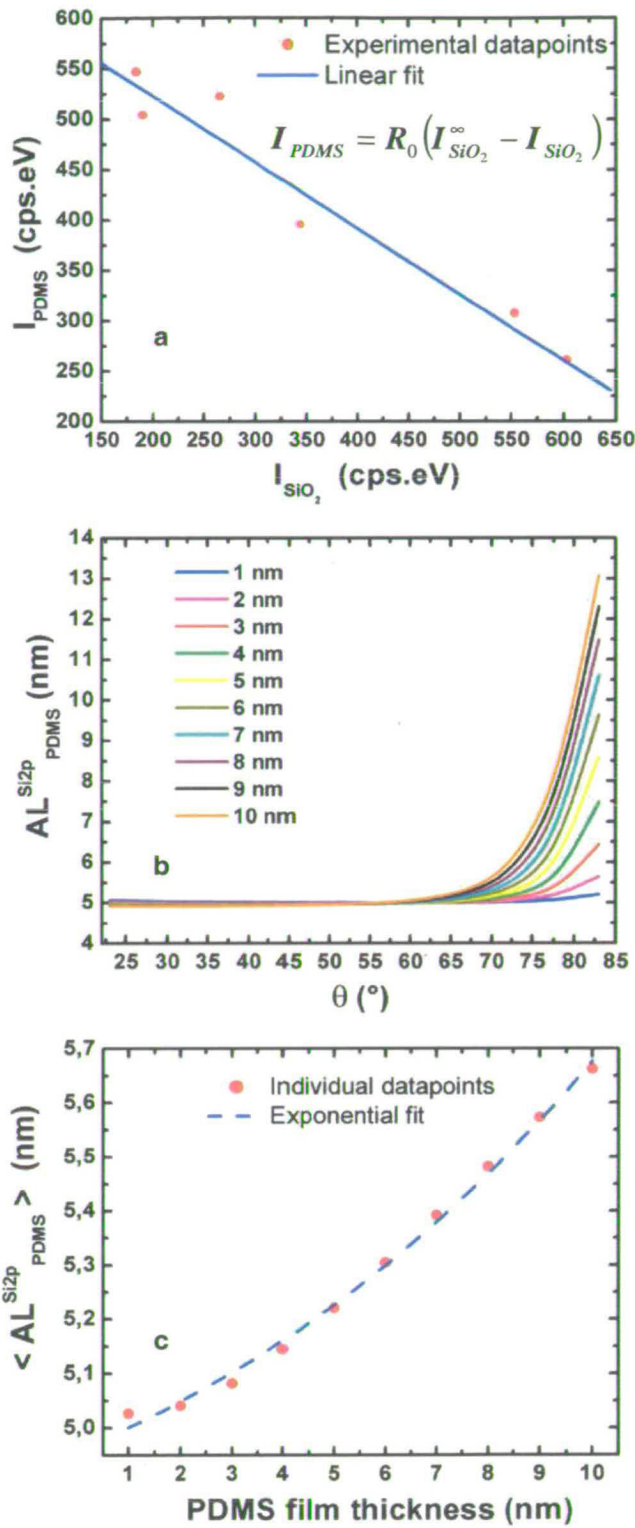
Fig. 4.4. Estimation of R_0 and AL from Si2p photoelectrons for a PDMS film deposited on fused silica. a: experimental determination of R_0. b: variation of AL as a function of film thickness and emission angle. c: practical averaged values of AL for various thicknesses.

4.2. Results

4.2.1. 3-D imaging capabilities of SWLI in the nanometre range

PDMS films:

Fused silica substrates were coated with PDMS chains according to the 'pure melt route' described in detail in § 3.2.1 and § 3.2.2. In Fig. 4.5 the 3D map corresponds to a substrate that was covered in (α, ω) OH-terminated chains of average molecular mass $M_w = 110$ kg mol^{-1} and polydispersity PI > 2, while that in Fig. 4.6 was coated with less polydisperse (PI = 1.35), (α, ω) CH$_3$-terminated chains of average molar mass $M_w = 162$ kg mol^{-1}.

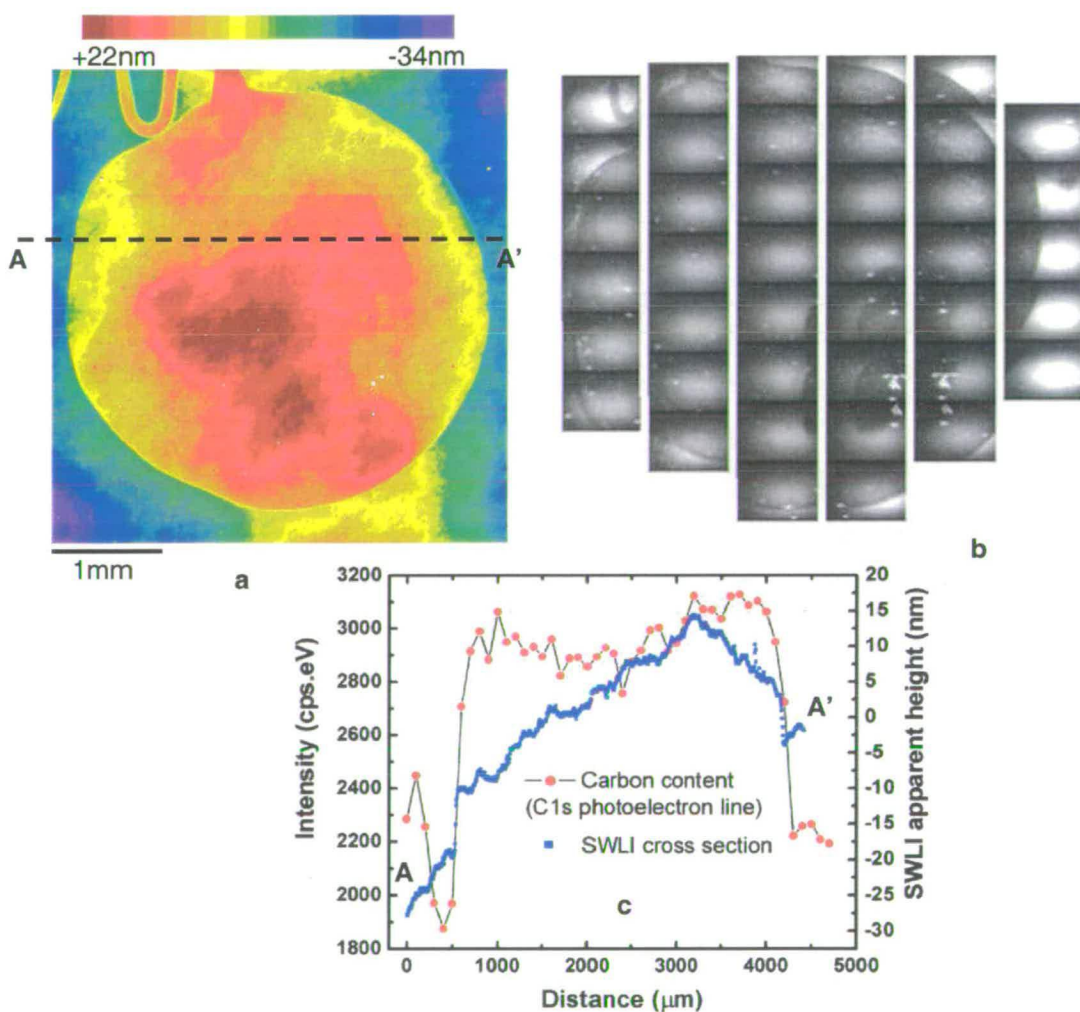Fig. 4.5. (α, ω) OH-PDMS layer deposited as a primary melt onto a fused silica substrate. a: 3-D SWLI map. b: Surface map obtained by Imaging ellipsometry. The third dimension is expressed in terms of ellipsometric contrast and not height. c: SWLI cross-section AA' superimposed to a measure of the surface carbon concentration performed by XPS.
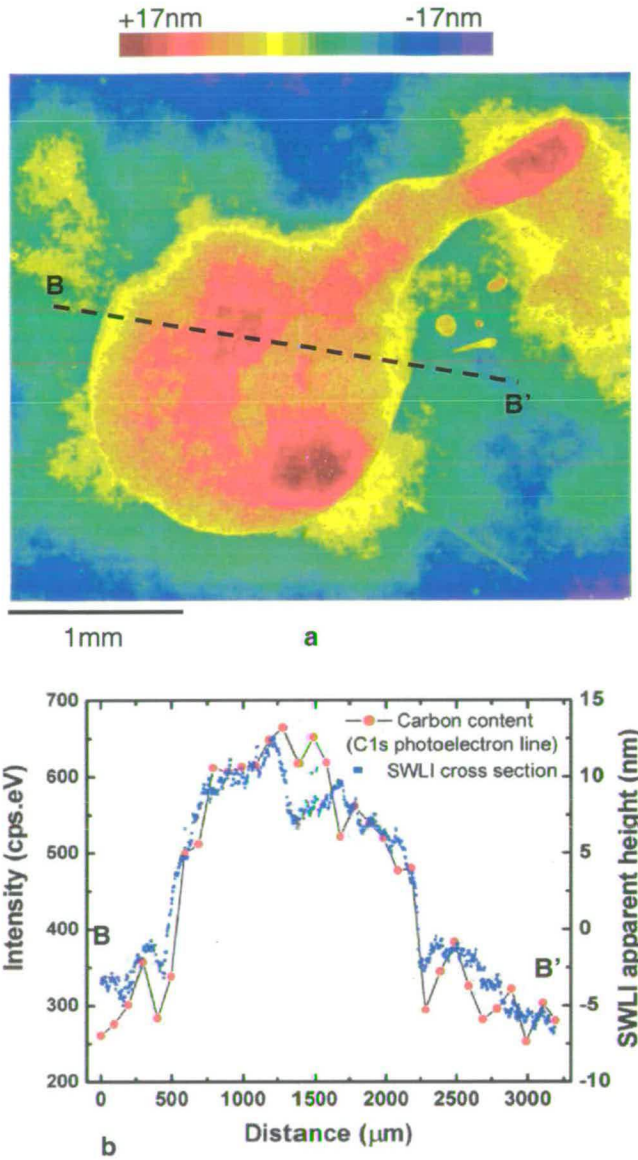
Fig. 4.6. (α, ω) CH$_3$-PDMS layer deposited as a primary melt onto a fused silica substrate. a: 3-D SWLI surface mapping. b: SWLI cross-section BB' superimposed to a measure of the surface carbon concentration performed by XPS.

The poor quality of the ellipsometric contrast map presented in Fig. 4.5 b[1] does not keep the reader from noticing a certain similarity with the SWLI map (Fig. 4.5 a). In particular the general round shape and the loop feature located on the top left corner are elements that indicate that both techniques give comparable images of the same polymer layer. A region located on the bottom right corner of the ellipsometric contrast image can be interpreted as a

---

[1] Nanofilm provided us with this jigsaw kind of image that we had to include as is.

probably denser and therefore thicker polymer layer. This interpretation can be made because ellipsometry is, unlike SWLI, insensitive to substrate topography. This characteristic is one of the reasons why imaging ellipsometry has established itself as the reference technique for this type of investigation. This possibly thicker region doe not appear at first glance in the SWLI map presented in Fig. 4.5 a, however the measurement of the surface carbon concentration by XPS, a PDMS tracer, along section AA' confirms the location of the layer boundaries. This is important as, unlike imaging ellipsometry, XPS is not dependent on the optical properties of the surface and provides purely chemical information so that the hypothetical presence of any optical artefacts cannot alter the measurement. Although the amount of contamination carbon cannot be easily subtracted from the PDMS carbon signal, the increase in carbon concentration across the step is large enough not to raise any ambiguities. The SWLI cross-section reveals also abrupt steps: the distance between blue rectangles in the step regions is significantly longer than it is either inside or outside the layer. It is interesting to note that the carbon concentration varies little along section AA', which is probably also the case throughout the layer. It is difficult at this stage to propose more than an approximate value for the layer thickness as the substrate variations prevail. At the edge of the film: apparent thickness = (8 ± 2) nm. Interestingly the apparent thickness in the winding loop region (top left corner) is higher: (13 ± 2) nm.

The case presented in Fig. 4.6 also shows that films highlighted in SWLI mapping are not artefacts but true structures. However the steps are more difficult to make out. In particular the location of the right-hand side step can only be guessed by analogy with the XPS C1s linescan. Besides the reader should not be misled by the similarity between the bell-like central part of the SWLI cross-section and the XPS linescan. This has probably more to do with the local substrate shape (waviness and/or roughness) than with the presence of the PDMS film though the latter does contribute to the bump. Unlike what has been noticed in Fig. 4.5 regarding the carbon concentration across the layer, it varies strongly with the position along section BB'. The maximum is located somewhere near the centre of the layer and the concentration decreases towards the layer boundaries. Here the layer thickness is expected to be higher at the 'centre' than at the edge. Apparent thickness at the edge: (5 ± 2) nm. At the centre the apparent thickness is estimated to be (9 ± 3) nm.

Again in the spirit of investigating the capabilities of SWLI, other materials (more) commonly found in labs and used as substrates, in particular for SFM work, were tried out, namely: white mica, borosilicate glass and p-doped silicon (111). Because of the viscosity

of PDMS samples of average molar weight higher than 100 kg mol^{-1} (similar to cold honey), it was thought beneficial to minimise the time for PDMS chains to come into contact with the substrate and adsorb by employing the secondary melt route (slow solvent evaporation). PDMS layers consisting of (α, ω) OH-terminated chains of average molar mass $M_w = 110$ kg mol^{-1} were imaged by SWLI only. The resulting maps are presented in Fig. 4.7 for mica, in Fig. 4.8 for borosilicate glass and in Fig. 4.9 for air-oxidised silicon.
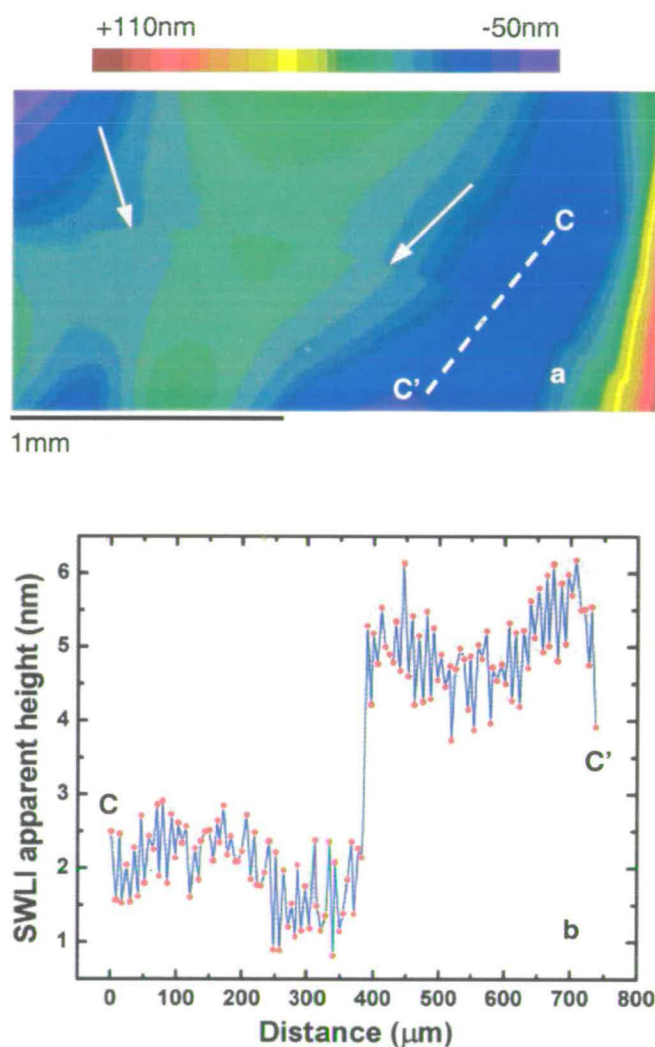

Fig. 4.7. PDMS film (secondary melt, (α, ω) OH-terminated chains) on white mica. a: detail of the SWLI surface map on the boundary region. The white arrows indicate the location of the layer step. b: Cross-section CC' (dashed line) across the step. Unlike fused silica, the surface of cleaved mica has a lot of form therefore a best fit sphere had to be removed from the data and not a simple best-fit plane to highlight the layer boundary.

The choice of mica as a substrate leads to a layer of apparent thickness close to 3 nm (see Fig. 4.7 b), which is significantly smaller than what was obtained with a primary melt of the same macromolecules on fused silica (see Fig. 4.5 c). Besides the step is so discrete and the mica surface has so much form that a best-fit sphere had to be removed otherwise it would have remained undetected. It is usual practice to remove a best-fit plane to compensate for the tilt of the sample stage, which does not affect the data (z values).
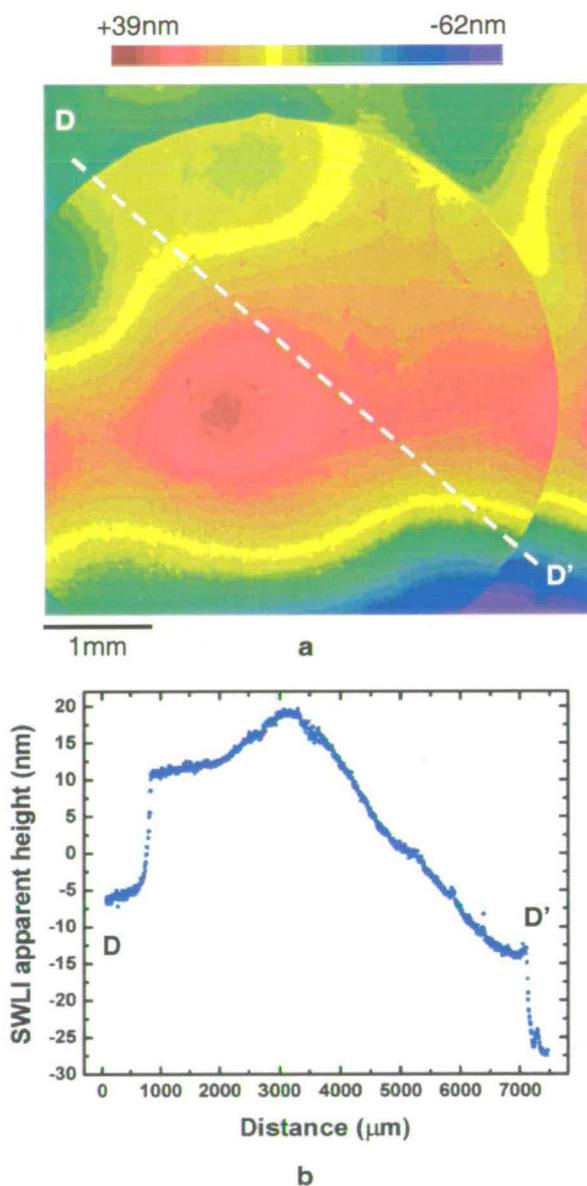

Fig. 4.8. PDMS film (secondary melt (α, ω) OH-terminated chains) on borosilicate glass. a: Global plane view of the SWLI surface map. It is almost perfectly circular. b: Cross-section DD' (dashed line) across the step. The steps stand out clearly and the apparent as determined at the edges is about 14 nm.
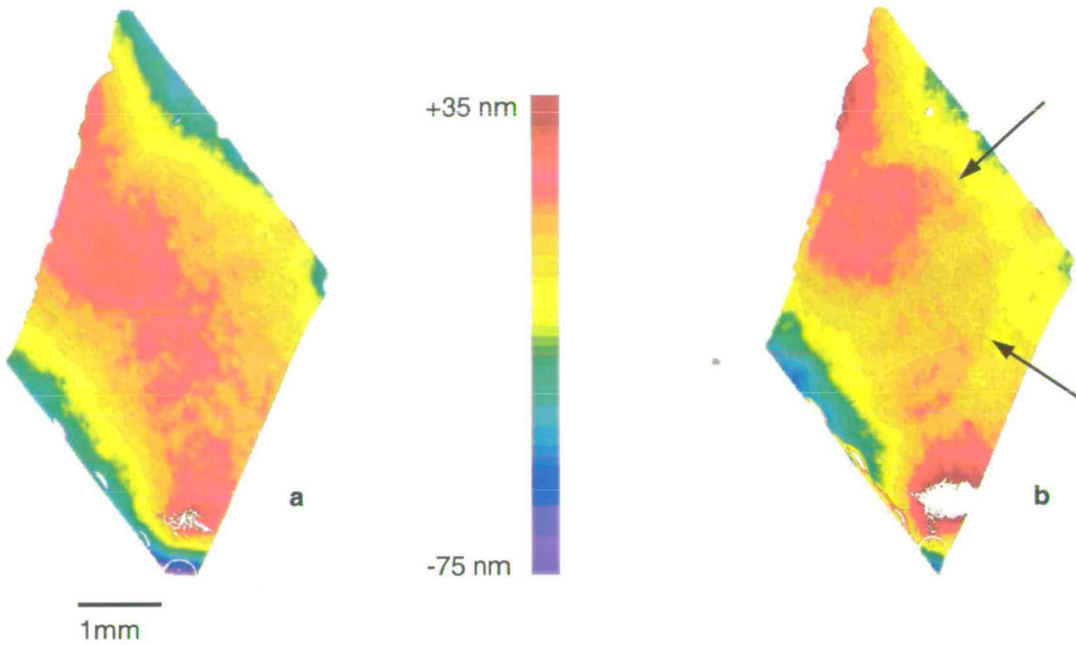
+35 nm

-75 nm

1mm

Fig. 4.9. SWLI images of PDMS (secondary melt (α, ω) OH-terminated chains) coated silicon wafers. a: Surface map of the as-coated wafer: no layer is to be seen. b: Surface map of the as-coated wafer with a $\approx$ 5 nm thick aluminium overlayer deposited by CVD. The PDMS layer is visible (two black arrows point towards an oval feature). The apparent layer thickness at the boundary is (6 ± 1.5) nm.

On borosilicate glass (see Fig. 4.8) the apparent thickness at the edge is as large as (13 ± 2) nm, the steps are nearly vertical and the layer is of 'superb' roundness. This shows that the drop of PDMS solution in octane set in instantly, forming a nearly spherical drop characteristic of hydrophobic liquids interacting with hydrophilic surfaces like glass and most silica surfaces in trying to minimise the interfacial energy [van Oss *et al.*, 1988]. The PDMS coated silicon wafers posed an unusual problem as no layer could be seen when the surface was imaged as-is (see Fig. 4.9 a). Following a suggestion made by Flaherty and O'Connor [2003], a thin metal overlayer was deposited over the whole surface by CVD. We chose to use aluminium because of its high and constant reflectivity (see § 3.2.3). The thickness of the deposited aluminium layer was tuned to a value of (5 ± 1) nm. The apparent thickness of the PDMS film in the boundary region was (6 ± 1.5) nm. Such a low value compared to that determined on borosilicate glass is surprising.

Other organic molecules:

After investigating the surface imaging capabilities of SWLI in the case of a liquid-like polymer (PDMS) deposited on a variety of silica and silicate substrates, we report some results obtained for other types of film on borosilicate glass (ordinary microscope slide). Films of polystyrene (PS, polydisperse sample) were prepared from a solution in toluene with chains of average molecular mass $M_w = 280$ kg mol^{-1}. This polymer is an amorphous solid at room temperature. Films of γ-aminopropyltriethoxysilane (γ-APS), a short silane molecule often used as coupling agent, were prepared according to a more involved procedure described in detail in § 3.2.2. The outcome of these experiments is presented in Fig. 4.10 for PS and in Fig. 4.11 for γ-APS.
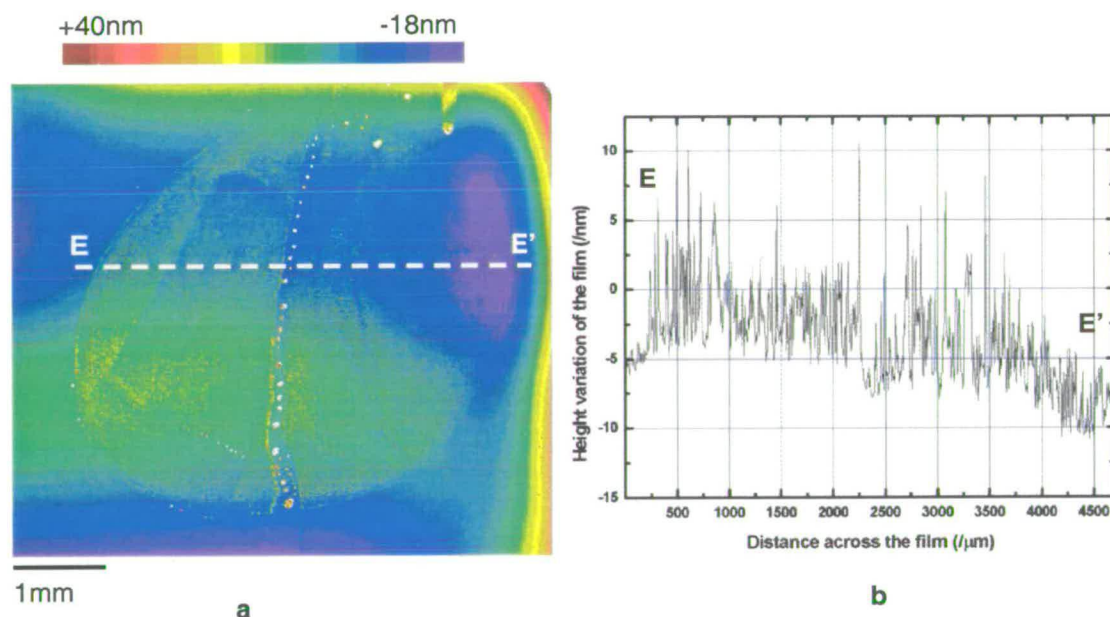

Fig. 4.10. Secondary melt of polystyrene deposited on borosilicate glass. a: SWLI surface map of a PS film. b: Cross-section EE'. The resulting film is not homogeneous: patches of polymer and patches of seemingly non-coated glass of lateral size ranging from 20 to 50 μm share the area within the oval boundary.
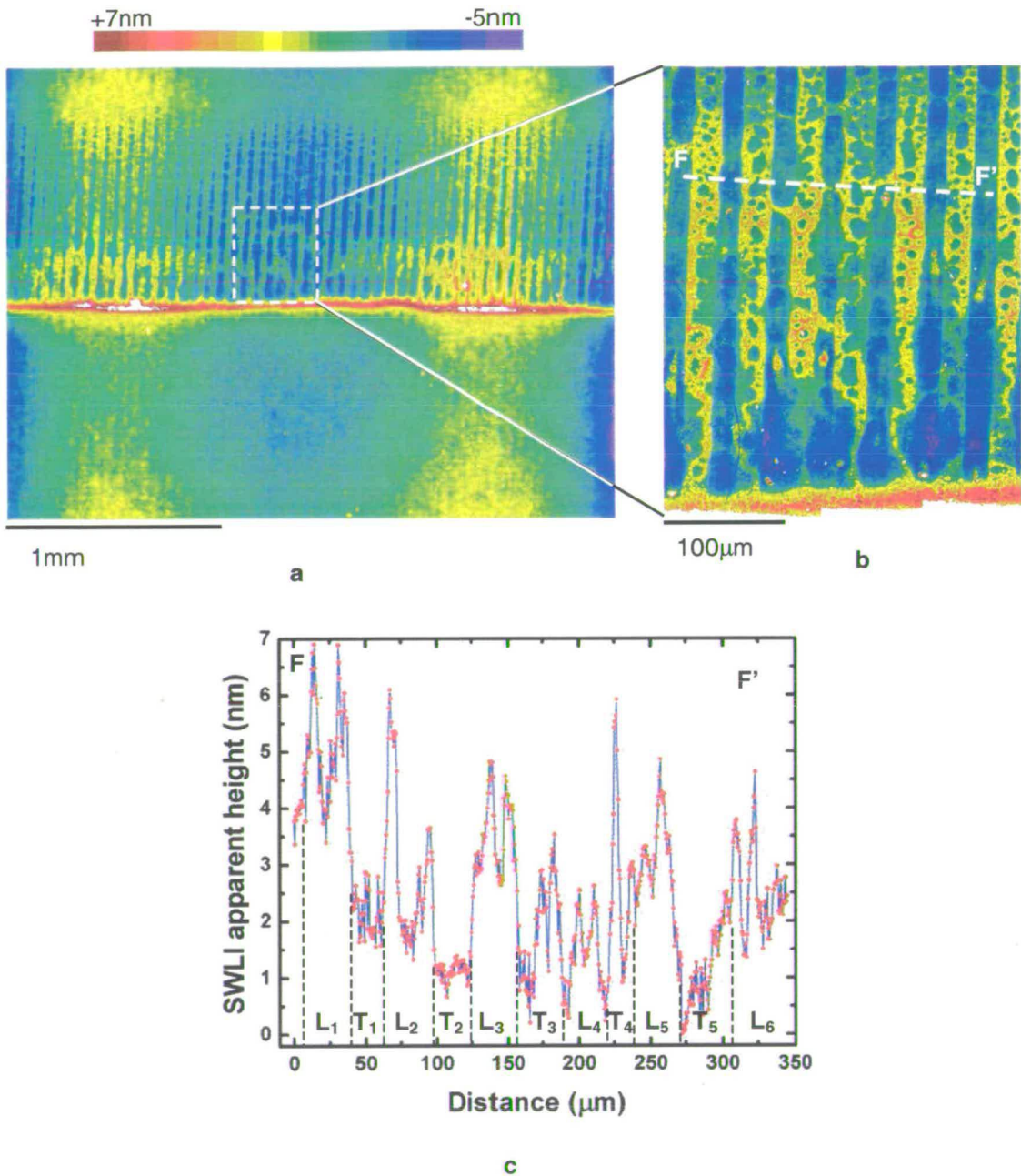
Fig. 4.11. Micropatterning of a silane molecule: γ-APS on borosilicate glass. a: SWLI surface map acquired with a x2.5 Michelson objective. The top half of the surface was CVD-gold coated (thickness ≅ 10 nm). b: Zoom in on the gold coated region acquired with a x40 Mirau objective. The z scale is common to a and b. c: Cross section FF'. The pattern is irregular showing that the γ-APS deposition process is not optimised. Vertical dashed lines are displayed to help locate the γ-APS lines (L_n) and the troughs (T_n) that should correspond to bare glass.
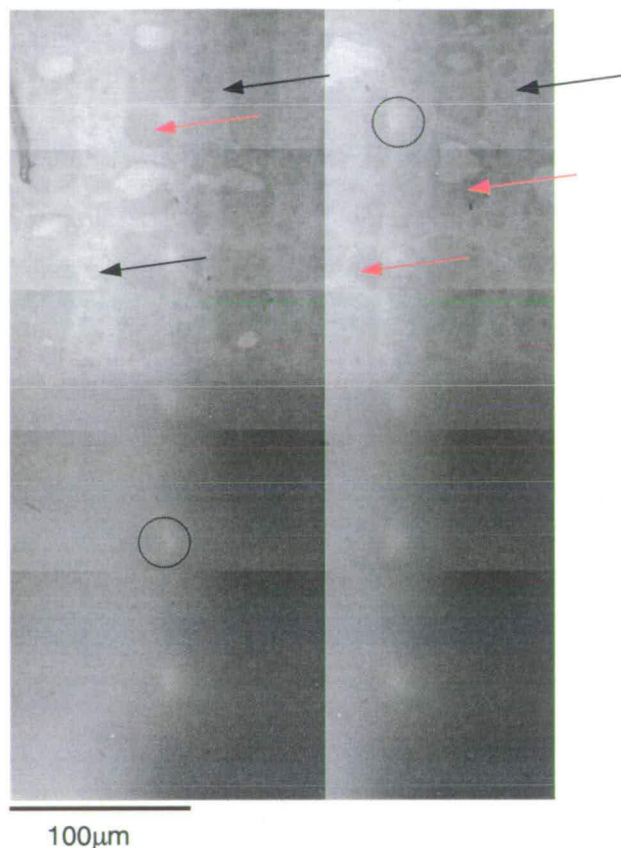
100μm

Fig. 4.12. Stitched scanning interferometric micrograph of another silane patterned glass sample. Silane lines are marked by black arrows, bare glass by red ones. Only the top half is gold coated. Bright pixels correspond to highly reflective portions of the surface (gold coated) while darker ones correspond to bare glass. Note the hot spots present on each field of view.

What remains of polystyrene after the desorption step (see Fig. 4.10) forms a heterogeneous layer. This is very clear on the cross-section with its spiky structure never obtained with PDMS. In spite of the limited lateral resolution (≈ 4.5 μm) that prevents one from judging whether some polymeric chains are present outside the spikes, it seems fair to say that the layer is made of PS solid lumps about 35 μm in lateral size separated by non-coated areas. The PS-rich regions may consist partly of monolayers and partly of aggregates since the SWLI apparent heights range from 3 nm to 15 nm and the polydispersity of the polymer makes it possible to adsorb giant macromolecules. Besides it is worth mentioning that there was no film to be 'seen' when the solvent used to wash away the excess of polymer was toluene instead of MEK.

The mapping of γ-APS patterned surfaces turned out to be quite challenging. While all other films deposited on borosilicate glass did not pose any problems as regards surface imaging, it was almost impossible to detect the presence of the silane lines with the x2.5 Michelson objective (see Fig. 4.11 a, bottom half). They were totally invisible with the x40 Mirau objective. Moreover bright spots can be seen that render the reflected light intensity level uneven (see Fig. 4.12). To make the silane lines detectable by SWLI it was necessary to apply the same method as that applied to the silicon wafer case, that is coat the sample surface with a metal layer. However the metal used to cover the sample was gold instead of aluminium (thickness ≈ 10 nm). The presence of the gold overlayer does reveal the presence of the silane lines in a striking manner (see Fig. 4.11 a top half, b and Fig. 4.12). As the sensitivity of the technique drops when the reflectivity of the surface being measured is close to the limit of detection (4 %), we believe that an objective with a lower magnification - hence a larger field of view - gathers more light back from the surface, resulting in an intensity level above the detection threshold. This would explain why shadows of the silane lines can be observed in the image obtained with the x2.5 objective (see bottom half of Fig. 4.11 a) and not in the one obtained with x40 Mirau objective (see Fig. 4.12). Depositing gold onto the surface has the effect of increasing the reflection coefficient of the air-sample interface to 65% or more depending on the wavelength considered if the surface reflectivity is assumed to be that of pure gold [Palik, 1985]. The amount of light entering into the CCD camera is no longer of order of the limit of detection of the system and images acquired with the two objectives provide detailed information of the γ-APS lines. However this does not eliminate the hot spots that are clearly still present in the coated portion of the surface (see Fig. 4.12).

Cross-section FF' (see Fig. 4.11 c) shows that the width of the silane lines and that of the free spaces in between corresponds roughly to the dimensions of the PDMS stamp (respectively 30 μm and 20 μm). The vertical dashed lines as well as the line and trough labels (L_n, T_n) are guides for the eye. Besides, careful observation of the close up map and of cross-section FF' (see Fig. 4.11 b and c) provides an extra piece of information regarding the structure of the silane lines. Assuming a uniform gold coverage, the structure is irregular indicating that the density of the γ-APS layer is quite inhomogeneous which might explain why the lines do not stand out when the sample is imaged as is. The heterogeneity of these layers was pointed out by Chiang et al. [1982] in studying the adsorption of γ-APS onto silica powder by solid-state nuclear magnetic resonance of ^{13}C. They concluded that grafting

a dense monolayer of that silane was very difficult as the amino-group of the molecule can form a loop onto the substrate or even hydrogen bond with itself. Going back to the analysis of cross-section FF', it is noticeable that troughs T_3 and T_4 are either partially covered in silane or affected by the hot spots, while most of the lines have thick edges and a thinner centre. Since after the stamping of the lines the sample was not rinsed, they are expected to be made of a multilayer of γ-APS. In this situation, the thickness as determined by ellipsometry and SFM is about 2 nm [Geissler *et al.*, 2003]. This value is close to the apparent height of the lines estimated at the centre. The edges are 1 nm to 2 nm higher. Still supposing that the gold overlayer is uniform and smooth, this means that either more silane was deposited at the edges during the stamping process or the material has moved during gold deposition is vacuum at or near the melting temperature of gold. Now if the gold layer is not uniform, some may have accumulated at the silane line edges. However the most probable explanation for the centre of the lines to be lower is given by the hot spots. It is likely that they arise because of a lens-induced optical aberration and/or because in a Mirau-type interferometer, the object and reference mirrors are in the same optical axis. A way around this problem is to acquire a system error file on an optical flat with the x40 Mirau objective and subtract it from any measurement made on a sample. Line L_4 stands out as the shortest line, the apparent height of which is about to 0.7 nm. This value is similar to that of a true γ-APS monolayer standing normally to the surface: 0.64 nm according to Wang and Jones [1993]. The presence of a monolayer may be a one off event by direct patterning without any rinsing step.

4.2.2. Is the adsorption of PDMS onto silica reversible?

The relevance of a system such as PDMS on silica for the understanding of the nano-mechanical properties of PDMS and more generally polymers as well as the use of PDMS as a coating on oxides depends upon the nature of its adsorption. Here by nature we mean how long a time the film can keep its physical properties for. The determination through experimental work of the type of interaction PDMS chains develop with oxides and especially silicon oxide will be dealt with in more details in Chapter 5. In § 4.2.1 we have noticed that PDMS layers consisting of primary melts of (α, ω) CH_3-terminated chains are not homogeneous. Assuming that these layers are likely to be easier to remove than the (α, ω) HO-terminated ones, the sample whose surface was presented in Fig. 4.6 was subjected

to immersions in several good solvents of PDMS: toluene, octane and hexamethyldisiloxane (HMDS). The latter is the best solvent because it is chemically identical to a monomer of PDMS and toluene being the worst but still solvating solvent (see Table 3.2). Each desorption test with a given solvent gave rise to several cycles of drying, SWLI measurement and immersion. The change in thickness as a function of desorption time is summarised in Fig. 4.13.
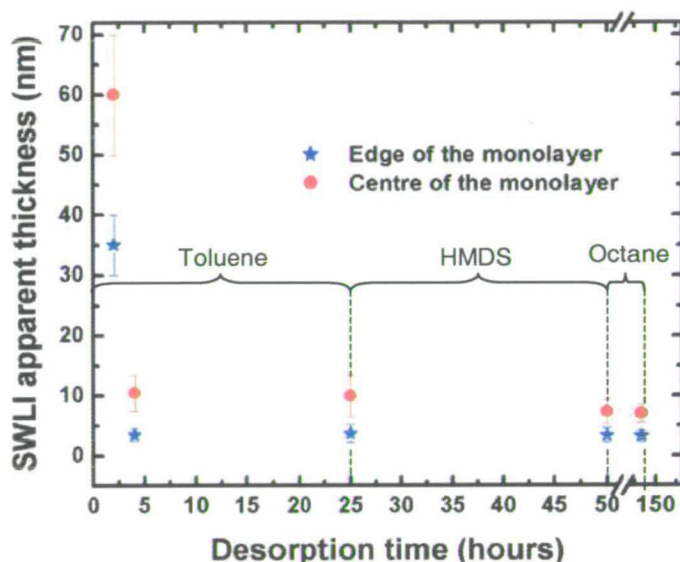

Fig. 4.13. Desorption of (α, ω) CH$_3$-terminated chains in three solvents: toluene, HMDS and octane (first stage in toluene, second stage in HMDS and last stage in n-octane). Estimates of the apparent film thickness were taken at the layer boundary region and near the centre of the layer. The latter are more questionable because of the waviness and/or roughness of the fused silica surface.

It can be observed that 2 hours in toluene is too short a time to get to the monolayer stage. The optimum duration seems to be 4 hours in toluene. Better solvents like n-octane or HMDS do not really bring about further desorption in the limit of 7 days that our study lasted. Only at the centre can we notice a significant drop in thickness, but only up to 50 hours of immersion and with the uncertainty on the thickness determination away from the boundary. It is fair to consider that the adsorption of PDMS on fused silica or more generally silica surfaces is *irreversible*.

4.2.3. Influence of deposition process on PDMS film quality

So far we have studied PDMS layers prepared from primary melts and secondary melts with slow evaporation of the solvent. There is however a third process defined in §3.2.2 as secondary melt with fast evaporation of the solvent. The idea behind this method is to eliminate the solvent (n-octane) as quickly as possible to create melt conditions right away. We present in Fig. 4.14 some three-dimensional SWLI maps of PDMS layers obtained by each of the processes described above.
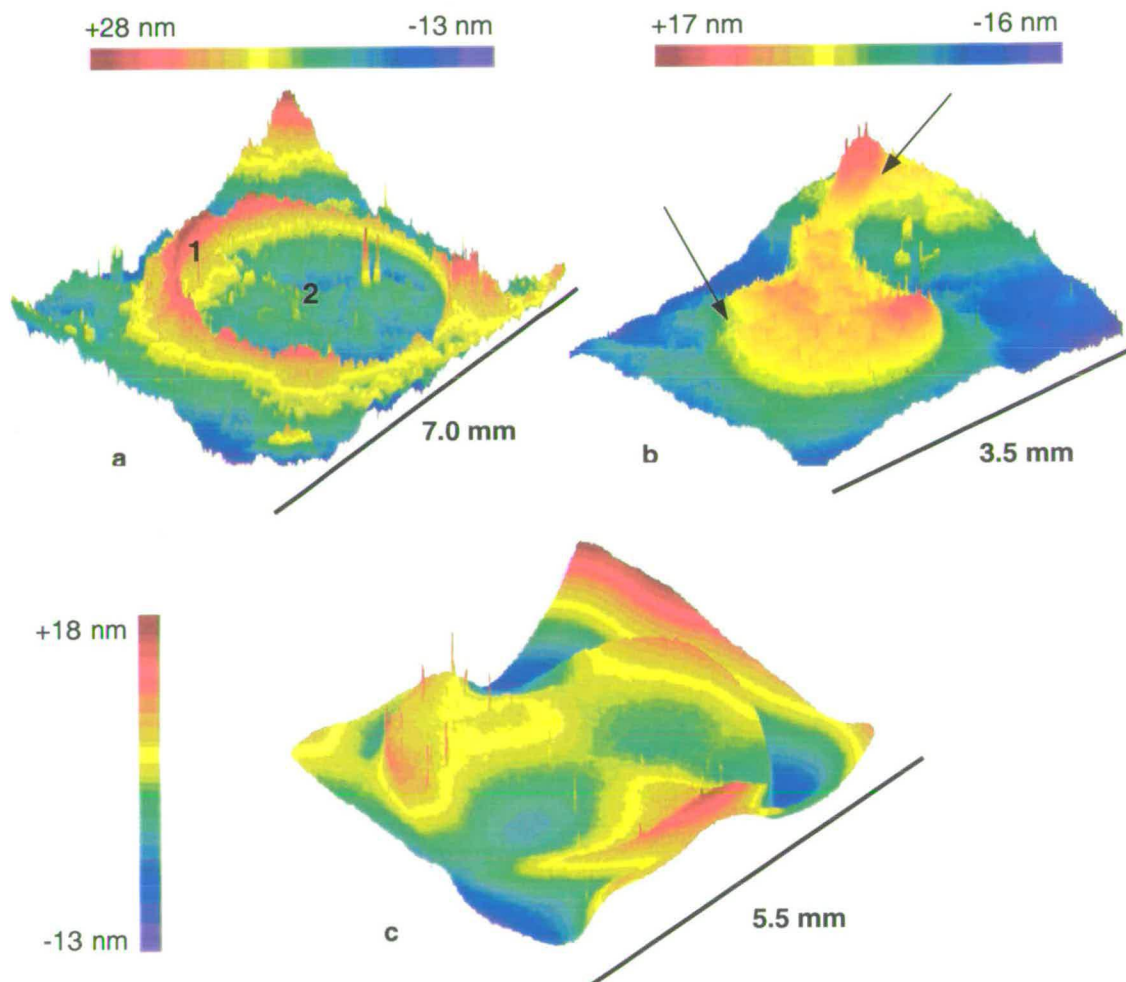
Fig. 4.14. SWLI images of PDMS films adsorbed onto fused silica substrates. a: fast evaporation of octane bringing about accumulation of material at the rim of the layer: 'coffee stain effect'. b: Primary melt: non-uniform coverage (arrows: layer thins out at the edges). c: slow evaporation of octane. Sharp edges, homogeneous coverage on a wavy substrate.

The surface mapped in Fig. 4.14 a presents a ring-like structure. It differs strongly from any surface we have dealt with so far. Concerned with the possibility of a technique-induced artefact and out of scientific curiosity, it was judged worthwhile checking whether such a heterogeneous structure highlighted by SWLI at the lateral microscale could be confirmed by SFM at the nanoscale. The custom-made SFM probe positioning system described in § 4.1.1 enabled us to make the SFM tip land on region 1 and region 2 (see Fig. 4.14 a). Topographic maps and cross-sections taken in IC-SFM mode are presented in Fig. 4.15.
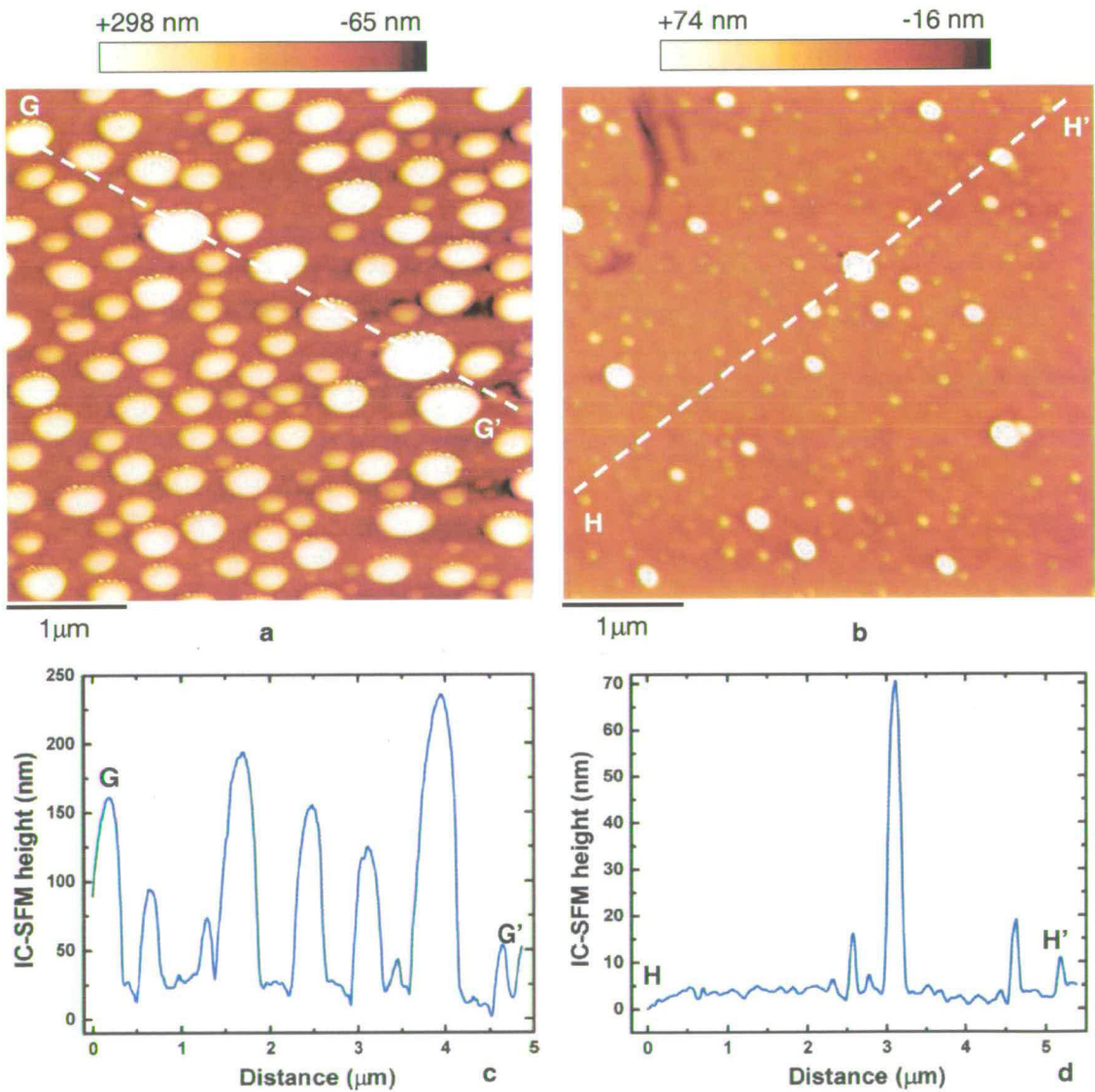

Fig. 4.15. IC-SFM study of a secondary melt of PDMS in the fast evaporation mode. a: Plane view of an area within region 1. b: Plane view of an area within region 2. c: Cross-section GG'. d: Cross-section HH'.

The accumulation of material as shown by SWLI on region 1 (see Fig. 4.14 a) is confirmed by intermittent-contact SFM in Fig. 4.15 a and c. Likewise the depleted character of region 2 is highligted by both techniques. This does not mean that region 2 is absolutely free of a PDMS monolayer, if anything in a loose form. The fact that IC-SFM backs SWLI as regards the reality of a ring-like deposit at the periphery of the initially deposited PDMS solution drop is evidence that we witness (the consequences of) a phenomenon sometimes referred to as 'coffee-stain' effect [Heim *et al.*, 2005]. It was observed and reported for polymeric materials, in particular ordered arragements of polystyrene latex particles by Denkov *et al.* [1992]. A convincing explanation along with a quantitative formulation was proposed quite recently by Deegan *et al.* [1997]. They claim that so long as the drop makes with the solid surface a contact angle higher than zero, the contact line is pinned to its initial position, the solvent evaporates, then evaporating liquid at the edge is replaced by liquid coming from within the drop. This outward capillary flow can transport almost all of the dispersed material contained in the drop, leaving a ring of dried solid.

In our case, the solute or dispersed material is not a solid but PDMS chains that behave like a liquid. However their size ($M_w = 110$ kg mol^{-1}) is so much larger than that of octane molecules that they play the same role with respect to octane as coffee particles do with respect to water. Moreover at 110°C and under 9 mbar of pressure, octane evaporates quickly. Lastly the surface tension of either octane or PDMS being much smaller than that of clean silica, the contact angle should be equal to zero. That is what we have observed for PDMS samples of molecular mass smaller than 10 kg mol^{-1} or alkanes corresponding to even rather long molecules like hexadecane. However the viscosity of a PDMS solution of volume fraction $\Phi = 0.2$ prevented the drop from reaching its equilibrium contact angle (zero) before most, if not all of the solvent had evaporated. Since the conditions mentioned above were fulfilled, we believe that what was mapped by SWLI and SFM are the result of a 'coffee stain' effect.

4.2.4. Metrology issues in SWLI and comparison with other techniques

Even though the capabilities of SWLI to map objects of height or thickness in the nanometre range are now proven, there are still some uncertainties as regards the precision and accuracy of the technique. To name a few: the range of values obtained for PDMS films on various substrates (pure silica, glass, mica, silicon), the necessity of sometimes

depositing a metal film onto samples to detect the organic layer and the presence of optical artefacts when using a high magnification Mirau-type objective. Following the pioneering work by McWaid *et al.* [1992], a systematic quantitative study of the influence of metal overlayer thickness on the measured organic film thickness was undertaken. To do so, two samples were given special attention: a primary melt of (α, ω) HO-terminated chains of mass $M_w = 110$ kg mol^{-1} and a secondary melt (slow evaporation) of the same type of chains already briefly touched on (see Fig. 4.5). They were also characterised by XPS, CFI-SFM, IC-SFM, 'surface manipulation' and ellipsometry. Extra SWLI tests were performed on two other PDMS monolayers adsorbed onto fused silica and mica (see Fig. 4.6 and Fig. 4.7).

- Primary melt of (α, ω) HO-terminated chains:
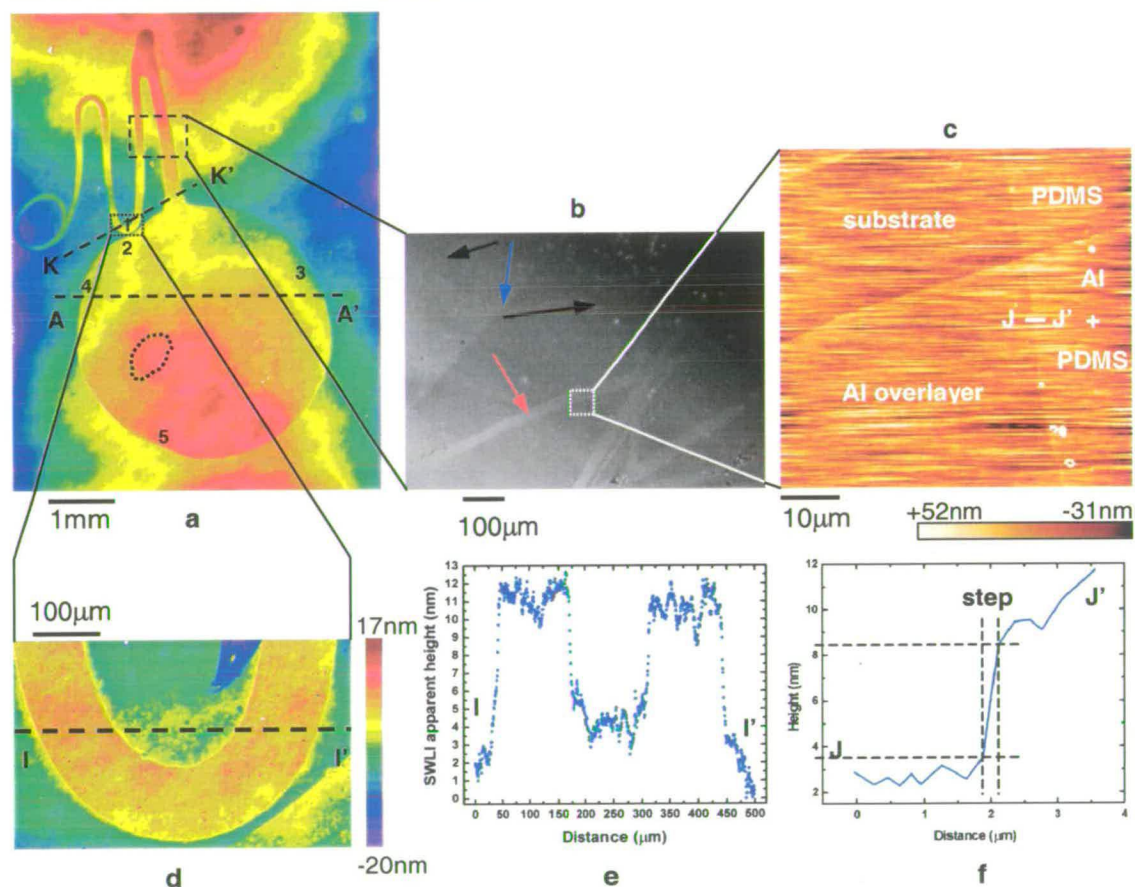
Fig. 4.16. Extensive study of a PDMS monolayer obtained from a primary melt of (α, ω) HO-terminated chains adsorbed onto fused silica (part 1). a: Global SWLI map (x2.5 Michelson objective). Note the winding loop. b: Optical micrograph taken with an inverted microscope (Zeiss, Aviovert). PDMS lines are not contrasty but visible (black arrows); scratch (red arrow); Al overlayer (blue arrow). c: CFI-SFM image of an area within the winding loop, across a PDMS monolayer boundary. d: SWLI zoom in with x40 Mirau objective. e: Cross-section II'. f: Cross-section JJ'.
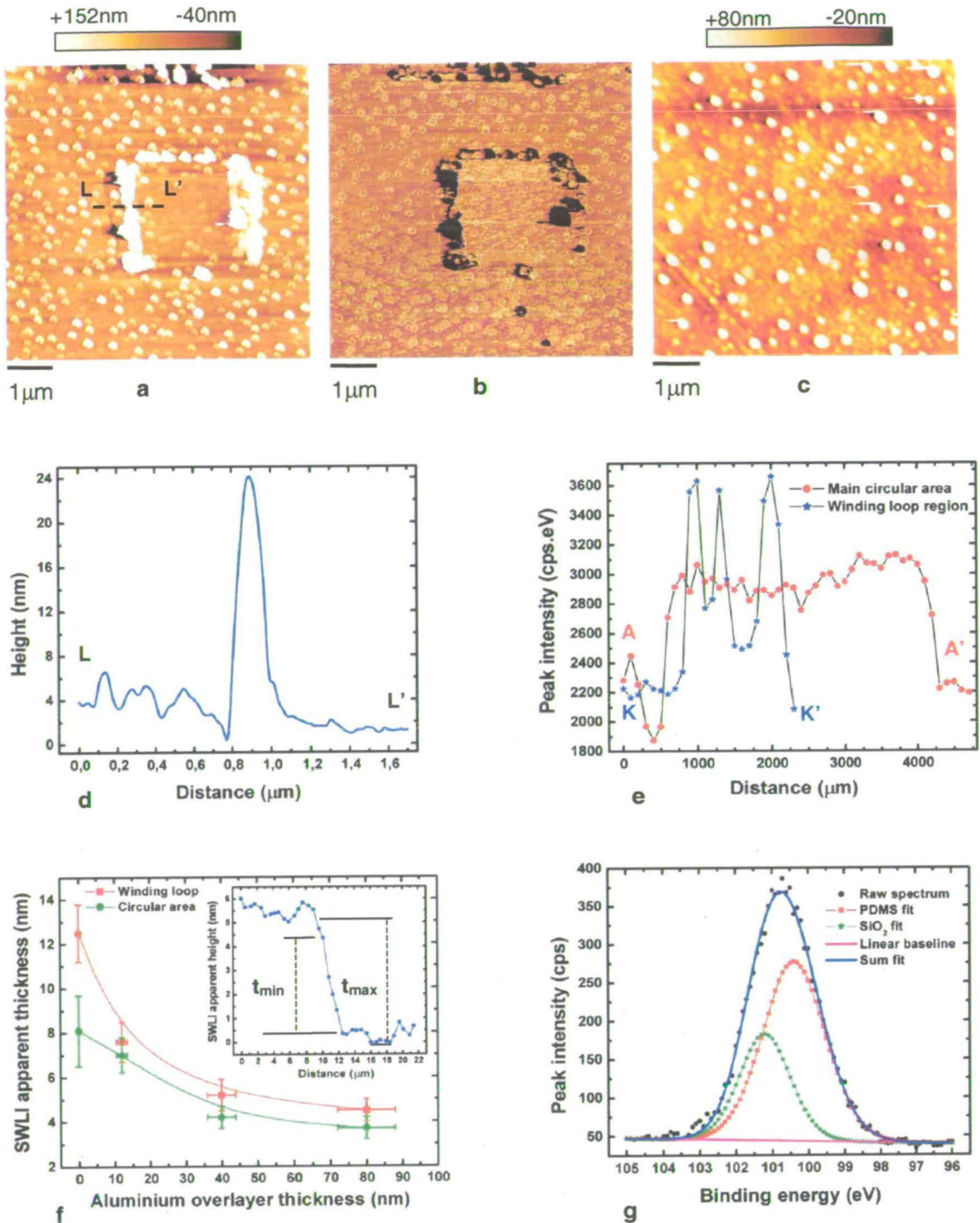
Fig. 4.17. Second part to Fig. 4.16. a: IC-SFM image of an area located within the circular layer. Tip tried to dig in the Al coated PDMS film. b: Corresponding phase image. c: IC-SFM image acquired elsewhere in the circular layer. d: Cross-section LL'. e: Comparison of carbon content across circular and winding loops (XPS, C1s). f: Influence of Al thickness on SWLI measured thickness. Insert: Method of measuring film thickness by SWLI at a film edge. g: XPS Si2p peak in main layer (see elliptic x-ray spot shape in Fig. 4.16 a). After deconvolution the film thickness can be calculated.

This sample surface has a strange feature which was referred to as the 'winding loop' (see Fig. 4.16 a). The reason for it is the way the viscous sample of polymer was deposited on the substrate. With a scalpel blade some polymer was extracted from its jar and, probably because of the applied shear force, a fine and narrow wire or string of polymer detached from the bulk and landed on the substrate surface first. By narrow we mean that this 'wire' was hardly visible with the naked eye. This explains the narrowness of the feature. As has already been mentioned, monolayer thickness as determined by SWLI on the winding loop without a metal overlayer is higher than anywhere else at the periphery of the layer. This fact is confirmed by semi-quantitative XPS (see Fig. 4.17 e) and this trend endures regardless of the thickness of the aluminium overlayer (see Fig. 4.17 f). Nevertheless, the apparent SWLI thickness does diminish significantly with the increase of aluminium thickness, especially in the winding loop case.

These non-destructive methods of characterisation give some information about the layer but not about the internal structure of it, yet it is precisely what we would need to better understand the seemingly complex morphology of this layer (originating from a primary melt). Here 'limited' instrumentation prevented us from imaging the layer, in the winding loop with the Pico SPM (Molecular Imaging). Indeed our simple see-through sample plate, mirror and magnifying glass ensemble could not let us locate the winding loop (see Fig. 4.2). Instead we studied an area somewhere within the circular layer (see Fig. 4.16 a). A typical topographic IC-SFM image is presented in Fig. 4.17 c. Roughly circular spots which can be interpreted as polymer aggregates sit on a smooth surface that could be the substrate or even polymer. The real nature of these spots is not our concern for now as this aspect will be dealt with in Chapter 5. The next step which we took was to use instead of regular imaging probes, that is silicon cantilever with silicon tips, 'surface manipulation' tips [Meyer et al., 2004]. These tips have to be harder because they not only interact gently with the surface for imaging purposes but they may also be subject to more severe stress as they scratch the surface in wear experiments for example. In our case we tried to use a silicon nitride coated silicon tip to make an excavation to see beneath a potentially deceiving surface. This tip was mounted on a short rectangular-shaped cantilever (length $\cong$ 90 μm) that qualifies both as CFI-SFM and as IC-SFM cantilever. The tip was operated in CFI mode for 15 minutes by keeping the feedback control on in order to reduce the risks of destroying it as it ploughed across the surface, within a centered square of surface area 4 μm^2. The scanning speed was kept low enough, that is about 2.6 μm/s to ensure good contact and the load set high. Since the signal saturated the detector (maximum = 10 V) it is difficult to give

a precise figure for the load. It can be supposed that the load ranged from 25 nN up to at least 100 nN. After that the tip was withdrawn from the surface, the IC-SFM switched on, the tip moved back down towards the sample and the surface mapped in IC-SFM mode. The result of this process is depicted in Fig. 4.17 a. There is no obvious change of height across the ploughed square apart from massive accumulation of material at its perimeter. Cross-section LL' in Fig. 4.17 d confirms this impression since no clear height difference is to be noticed. Furthermore the corresponding phase map in Fig. 4.17 b, more likely than the topographic map to distinguish between substrate and PDMS coating in case the latter is of sub-nanometre thickness, shows no clear contrast between the zone outside the square and that inside. Again, only the accumulation of material at the perimeter is to be noticed. It comes out in black, which indicates that it is soft matter. The layer would thus seem to be discontinuous but the sample was aluminium coated (thickness $\cong$ 12 nm) therefore that extra layer may have been too big an obstacle for the tip to go through. This argument has some strength however Mc Waid *et al.* [1992] have noticed that such metal films were more likely to have a heterogeneous morphology than form a planar homogneneous layer. We verified experimentally that, at least for layers thinner than 15 nm, CVD deposited aluminium layers are morphologically different from bulk crystalline aluminium. Two days of oxidation in air lead to a large amount of aluminium oxide (Al_2O_3) as shown in Fig. 4.18.
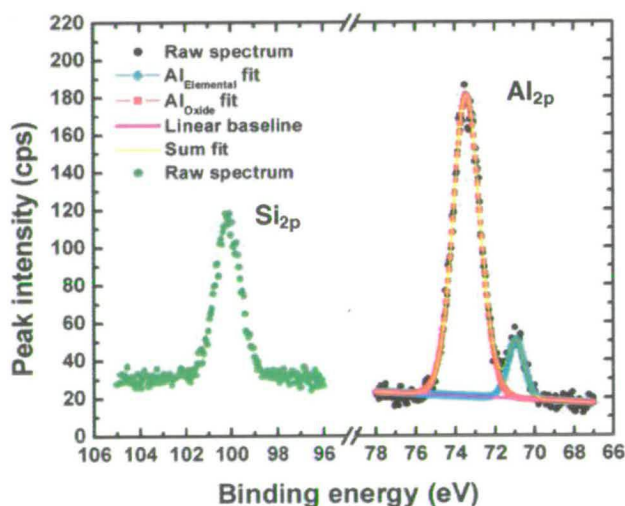

Fig. 4.18. XPS spectrum of an Al overlayer deposited onto a PDMS monolayer (primary melt (α, ω) HO-terminated chains) adsorbed onto fused silica. PDMS is still detected despite the presence of a metal overlayer (89% oxidised) of thickness 12 nm. Intensities are normalised to the Al2p peak. BE(Si2p)=100.2 eV, BE(Al2p metal)=70.9 eV, BE(Al2p oxide)=73.4 eV.

Signal from the silicon atom of PDMS or maybe even from fused silica managed to traverse the aluminium layer. This metal layer consists of aluminium oxide Al_2O_3 (89%) and only of little aluminium metal (11%). Observation of the binding energies of both peaks reveals that electron flooding during x-ray irradiation shifted BEs towards negative values. A 2 eV shift affected $Si2p^{PDMS}$ since it is expected to come out at 102.2 eV, likewise for $Si2p^{SiO2}$ expected to be centered around 103.2 eV and $Al2p^{metal}$ expected at 72.7 eV [Wagner et al., 1982]. Note that other sources give $Si2p^{PDMS}$ a smaller binding energy: 101.8 eV [Beamson & Briggs, 1992]. Sample charging up was therefore more than compensated for. Besides the measured Si2p peak must correspond to PDMS and not silica for a negative shift of 3 eV for an insulating material so deeply buried would not make much sense. As for aluminium oxide, its Al2p peak is still located at 73.4 eV, which is quite close to its theoretical value 73.9 eV [Wagner et al., 1982]. This confirms that insulating aluminium oxide is abundant (or thick) and badly coupled (electrically) to the layers situated below it as there is a double electron flux going in opposite direction through the multi-layered material [Vereecke & Rouxhet, 1998].

The conclusion we can draw from this study of the characteristics of aluminium overcoating is that seeing it as a two-phase compound rather than an oxide layer on top of a metal one is probably more realistic.

Recalling the procedure used for film thickness determination (see §3.1.3, equation (3.35) onwards) in XPS, appropriate manipulation of the Beer-Lambert relationship leads to an interesting result. 95% of the signal's intensity originates from a slice of material of thickness [Watts & Wolstenholme, 2003]:

$$t^{95\%} = 3AL\cos\theta \qquad (4.1)$$

This simple equation can then be used to estimate the maximum thickness of Al/Al_2O_3 compound that a Si2p photoelectron originating from PDMS is able go through to produce an XPS signal. Substituting θ_{eff} for θ (see § 4.1.2), the only unknown is the attenuation length of Si2p photoelectrons originating from PDMS in Al/Al_2O_3. We propose to work out the attenuation length in pure aluminium and then in pure alumina using the code developed by Powell and Jablonski [2001]. The attenuation length in the compound or more precisely the 'compound of compounds' will be the average of attenuation lengths in pure aluminium and pure alumina:

$$AL^{Si2p,PDMS}_{Al/Al_2O_3} = [Al]\% \times AL^{Si2p,PDMS}_{Al} + [Al_2O_3]\% \times AL^{Si2p,PDMS}_{Al_2O_3} \qquad (4.2),$$

where [Al]% is the molar fraction of aluminium metal in the compound and $[Al_2O_3]$% is the molar fraction of alumina in the compound. These are determined from the surface area of the peaks (see Fig. 4.18). This equation is similar to those proposed by Seah and Gilmore [2001] in their paper on elastic scattering effects and their consequences in quantitative XPS. Calculation of the inelastic mean free path (IMFP) is a compulsory step to get attenuation lengths and for inorganic compounds, values of density and band gap energy are needed. We used a value of 3.97 g.cm^{-3} for the density of Al_2O_3 [Lide, 2001] and a value of 8 eV for its band gap energy [Eder *et al.*, 1997]. The maximum distance that Si2p photoelectrons can travel is such a medium is thus *6.7* nm or even *8.9* nm if we allow for a coefficient 4 instead of 3 in equation (4.1). This is significantly lower than the thickness as measured by a crystal inside the CVD chamber. Either this estimate is off the mark and the aluminium layer is thinner than expected or it is correct but the layer is actually discontinuous in the sense expressed above [Mc Waid *et al.*, 1992] or horizontally continuous but with air and/or moisture-filled voids of size larger than 0.8 nm (wavelength of AlKα x-rays) in th z direction. Such a layer would be bound to offer poor resistance to a sharp silicon nitride tip and therefore the presence of a uniform PDMS monolayer is doubtful. The existence of such a layer can only be envisaged if it is of sub-nanometre thickness as suggested above and made up of trains collapsed on the substrate so that it forms a 2D structure without vertical extension.

The winding loop was also imaged by SFM but not with the Pico SPM as this area is narrow (see Fig. 4.16 a). Instead we used the Bioscope by Veeco that combines a Nanoscope IV SFM and an inverted optical microscope. The latter enabled us to locate the desired region and to record a micrograph presented in Fig. 4.16 b. In spite of a certain lack of contrast, two vertical linear features can be seen, marked with black arrows. We chose to image an area covering the bare substrate (Al overlayer easily removed by scratching the surface with an ordinary sharp steel needle), the PDMS coated substrate and the aluminium overlayer on top of PDMS. The resulting image was obtained in CFI mode because no decent image could be obtained in IC mode due to a very high noise level. The best we could obtain is presented in Fig. 4.16 c. The PDMS monolayer step is obvious and a typical 2D slice taken across it is presented in Fig. 4.16 f. Averaging over ten measurements, the step height is equal to (4.8 ± 0.7) nm. However the noise level was large as can be noticed on the map and this region was but a small area compared to the extension of the winding

loop. This abnormally high noise level arose probably from the sample not being tightly enough secured to the stage through a vacuum system.

Quantitative XPS analysis was applied to several areas located within the main circular area so as to calculate the PDMS film thickness (see x-ray spot elliptic shape in Fig. 4.16 a). Owing to the time it takes to acquire a spectrum of high resolution in energy for individual core levels analysis (pass energy = 10 eV), only large and intense x-ray spots were used. This prevented us from studying quantitatively the winding loop region that required x-ray spots of diameter $\cong$ 100 μm. The reader is referred to Fig. 4.17 e to find out what semi-quantitative information XPS delivers with spots of this size but with poorer energy resolution (pass energy = 80 eV). To calculate the thickness according to the simplified Beer-Lambert relationship given by equation (3.43) in § 3.1.3, the emission angle θ, the attenuation length AL and the intensity ratio of pure substances R_0 have to be known. Moreover the photoelectrons used to calculate the experimental intensity ratio R, one being characteristic of the substrate and the other of the film must have the same kinetic energy. The first three parameters have been determined in § 4.1.1 although AL is thickness-dependent as shown in Fig. 4.4 c, so we will have to assume a thickness value based on the PDMS step height determined by CFI-SFM, that is (4.8 ± 0.7) nm. The exponential function used to fit the calculated AL values for different thicknesses provides an easy means to calculate the most likely AL value for our monolayer. The value is: $AL \cong 5.2$ nm. R will be calculated from the components of the deconvoluted Si2p photoelectron line presented in Fig. 4.17 g. The method used to locate the substrate and film components lies on the knowledge of the stoichiometry of both materials as well as expected binding energy of the chosen photoelectron lines. As has been mentioned above, the binding energy of Si2p electrons in silica is about 1 eV than in PDMS. Even if possible physical or chemical interactions might alter this gap, it is not likely to be more than a few tenths of 1 eV [Leadley & Watts, 1997] [Mundry *et al.*, 2000]. In other words, the contribution to the convoluted peak from silica should be located at a higher binding energy than the contribution from PDMS. The elemental composition of silica and PDMS differs only in the presence of methyl groups in the DMS monomer. It is therefore the measure of the concentration of carbon (through the C1s photoelectron line) on the surface that is going to enable us to estimate the proportion of the convoluted Si2p peak that corresponds to silica and that for PDMS. Assuming that the slice of material that provides Si2p electrons is pure PDMS, the atom percentage of carbon should be 50 and that of silicon 25 as a (P)DMS

monomer consists of 2 atoms of carbon, 1 atom of silicon, 1 atom of oxygen and 6 atoms of hydrogen but the latter are not detected by today's XPS detectors due to the very low photoionisation cross-section of H1s [Scofield, 1976]. Besides some of the detected carbon results from adventitious contamination, often in the shape of hydrocarbons partly because of the vacuum pump oil. It is chemically similar to PDMS's carbon and therefore it is particularly difficult to distinguish on a spectrum except when the C1s peak has a shoulder characteristic of the presence of contamination. C and O are always present as contaminants on the surface being analysed, especially on reactive surfaces like metal, which imposes to work in ultra high vacuum. Their concentration increases linearly with irradiation time [Briggs & Seah, 1983]. The benefit of working in a vacuum of 10^{-10} to 10^{-9} mbar is that it takes about 40 minutes to form a monolayer of oxygen as opposed to a couple of seconds at 10^{-6} mbar [Eberhart, 1997]. Work by Vereecke and Rouxhet [1998] [1999] on PDMS-coated sodium chloride surfaces shows that the amount of carbon originating from adventitious contamination can be as high as 30% of the total surface carbon. Our own measurements on pure silica and pure PDMS in an average vacuum of 4.10^{-9} mbar showed that this figure was closer to 20%. Thus the surface area below the C1s peak was measured and compared to that of non-deconvoluted Si2p peak (see Fig. 4.17 g), the resulting ratio R_1 is expressed as follows:

$$R_1 = \frac{A_{C1s}F_{Si2p}}{A_{Si2p}F_{C1s}} = 1.68 \qquad (4.3).$$

After correction for adventitious contamination this ratio becomes R_2:

$$R_2 = (1 - 20\%)R_1 = 1.35 \qquad (4.4).$$

The difference between 2 (pure PDMS) and R_2 gives the proportion of PDMS contributing to the Si2p photoelectron line:

$$PDMS(\%) = \frac{R_2 \times 100}{2} = 67.3 \qquad (4.5).$$

The remainder 22.7% being necessarily the silica contribution, the ratio of PDMS to silica is:

$$R = \frac{A_{Si2p}^{PDMS}}{A_{Si2p}^{SiO_2}} = \frac{67.3}{22.7} \cong 2.1 \qquad (4.6).$$

This parameter R is no other than the one we need to calculate the PDMS film thickness. We could use it straight away to calculate the thickness via equation (3.43) but it is scientifically more rigorous to check that this ratio gives rise to a sensible deconvolution of the experimental spectrum. R will .be used as a first constraint to the deconvolution program (Avantage, Thermo Electron), that is the ratio of surface areas of the two fitting peaks. The second constraint is a constraint of shape. The width of a peak is, as a rule, partly random (Gaussian) and partly due to core hole lifetime effects [Watts & Wolstenholme, 2003] [Himpsel et al., 1988]. That physical phenomenon is usually represented by a Lorentzian curve. It can be prominent for certain metals [Watts & Wolstenholme, 2003]. We chose to fit the experimental spectrum with fitting peaks with a mixed 70% Gaussian and 30% Lorentzian curve, which is comparable to what authors working on a the same system have used [Mundry et al., 2000]. We let the program some flexibility as regards full width at half maximum (FWHM), peak height and even binding energy. The chosen constraints turned out to suffice to prevent the fitting program from providing us with a mathematically perfect but physically meaningless fit. The PDMS and silica peaks with appropriate surface area ratio come out at the right location (see Fig. 4.17 g). Furthermore the fact that only two constrained parameters were enough to get a good fit with individual peaks situated as expected is a hint that our surface area ratio described the reality of the system.

We can now apply equation (3.43) with some confidence. Isolating the thickness from the rest of the parameters:

$$t_{PDMS} = \left\langle AL_{PDMS}^{Si2p} \right\rangle \cos\theta_{eff} \ln\left(1 + \frac{I_{PDMS}^{Si2p}}{I_{SiO_2}^{Si2p} R_0}\right) \tag{4.7},$$

where $< AL_{PDMS}^{Si2p} > = (5.2 \pm 0.1)$nm, $\theta_{eff} = (54.5 \pm 2)°$, $I_{PDMS}^{Si2p} = (487 \pm 10)$ cps eV, $I_{SiO2}^{Si2p} = (246 \pm 5)$ cps eV .and $R_0 = 0.66 \pm 0,02$.

Hence, $t_{PDMS} = 4.2$ nm. The error bars can be estimated by calculating the logarithmic differential of function $t(< AL_{PDMS}^{Si2p} >, \theta_{eff}, I_{PDMS}^{Si2p}, I_{SiO2}^{Si2p}, R_0)$:

$$d\ln t_{PDMS} = \frac{dt_{PDMS}}{t_{PDMS}} = \frac{d\left(\left\langle AL_{PDMS}^{Si2p}\right\rangle \cos\theta_{eff} \ln\left(1 + \frac{I_{PDMS}^{Si2p}}{I_{SiO_2}^{Si2p} R_0}\right)\right)}{\left\langle AL_{PDMS}^{Si2p}\right\rangle \cos\theta_{eff} \ln\left(1 + \frac{I_{PDMS}^{Si2p}}{I_{SiO_2}^{Si2p} R_0}\right)} \tag{4.8}.$$

After some simple algebra we get the following expressions:

$$\frac{dt_{PDMS}}{t_{PDMS}} = XdI_{PDMS}^{Si2p} + YdI_{SiO_2}^{Si2p} + ZdR_0 + Td\theta_{eff} + Ud\langle AL_{PDMS}^{Si2p}\rangle$$

$$X = \frac{1}{\left(I_{SiO_2}^{Si2p}R_0 + I_{PDMS}^{Si2p}\right)\ln\left(1 + \frac{I_{PDMS}^{Si2p}}{I_{SiO_2}^{Si2p}R_0}\right)}, \quad Y = -\frac{I_{PDMS}^{Si2p}}{I_{SiO_2}^{Si2p}\left(I_{SiO_2}^{Si2p}R_0 + I_{PDMS}^{Si2p}\right)\ln\left(1 + \frac{I_{PDMS}^{Si2p}}{I_{SiO_2}^{Si2p}R_0}\right)}$$

$$Z = -\frac{I_{PDMS}^{Si2p}}{R_0\left(I_{SiO_2}^{Si2p}R_0 + I_{PDMS}^{Si2p}\right)\ln\left(1 + \frac{I_{PDMS}^{Si2p}}{I_{SiO_2}^{Si2p}R_0}\right)}, \quad T = -\tan\theta_{eff}, \quad U = \frac{1}{\langle AL_{PDMS}^{Si2p}\rangle} \qquad (4.9)$$

The desired error bars Δt_{PDMS} is given by:

$$\Delta t_{PDMS} = t_{PDMS} \times \left(|X|\Delta I_{PDMS}^{Si2p} + |Y|\Delta I_{SiO_2}^{Si2p} + |Z|\Delta R_0 + |T|\Delta\theta_{eff} + |U|\Delta\langle AL_{PDMS}^{Si2p}\rangle\right) (4.10),$$

substituting numerical values for the symbols used in equation (4.10) we obtain $\Delta t = 0.7$ nm, therefore:

$$t_{PDMS} = (4.2 \pm 0.7)\ \text{nm.}$$

- Secondary melt of (α, ω) HO-terminated chains:

We applied exactly the same methodology with the same arsenal of imaging and analytical techniques to a PDMS film adsorbed onto a borosilicate glass surface through the secondary melt route in the slow evaporation process (see § 3.2.2). The results are presented in graphical form in Fig. 4.19.
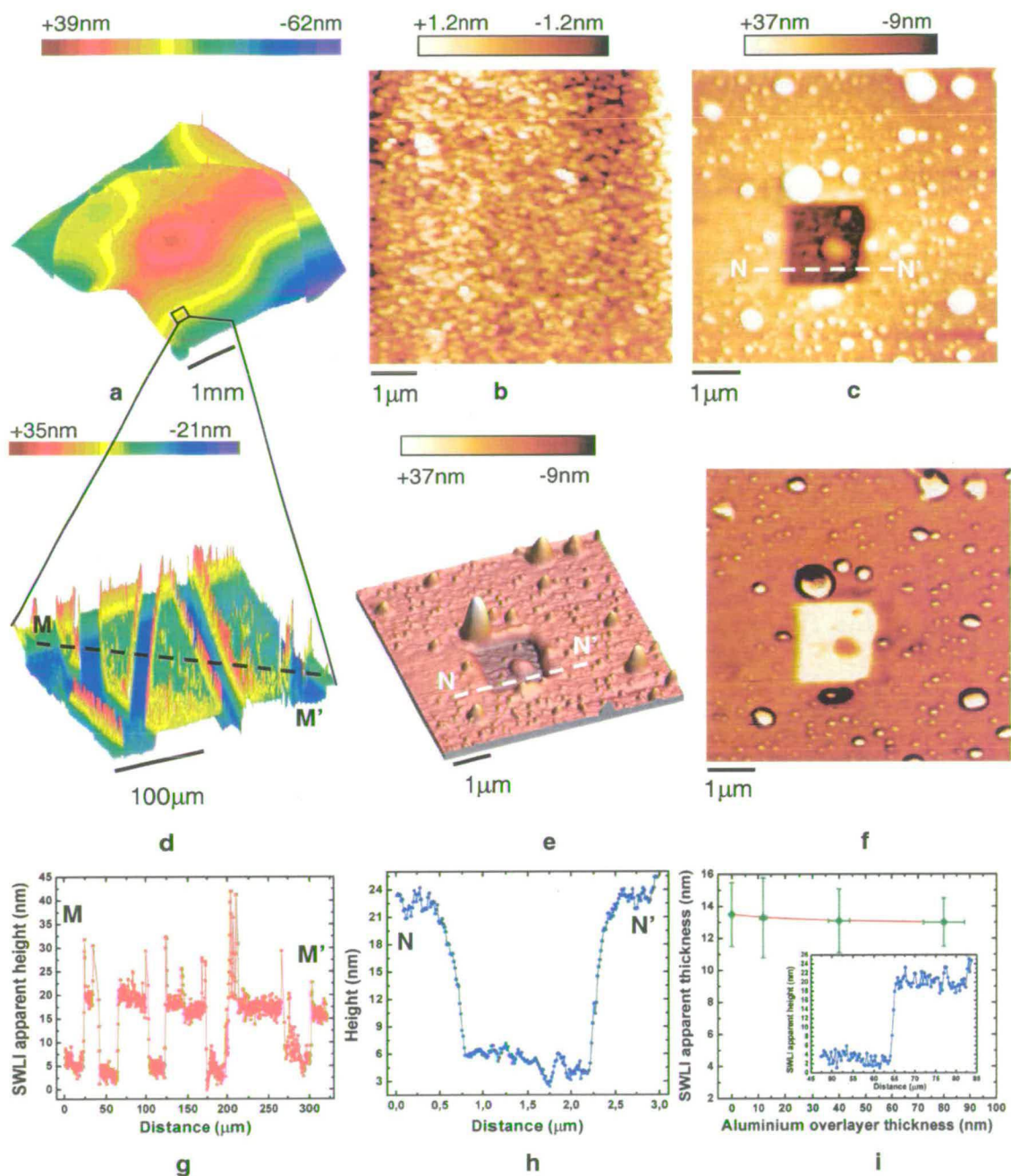
Fig. 4.19. Study of a PDMS monolayer obtained from a secondary melt of (α, ω) HO-terminated chains adsorbed onto borosilicate glass (slow evaporation). a: Global SWLI map (x2.5). Sharp edges. b: CFI-SFM topographic image of bare borosilicate glass. c: IC-SFM topographic image of the tip-ploughed monolayer (plane view). d: SWLI zoom in map (x40) after being scratched with a steel needle. e: Same as c (3D view). f: Phase image corresponding to c. Contrast between PDMS (brown) and substrate (white, yellow) is obvious. g: Cross-section MM'. h: Cross-section NN'. i: Influence of Al thickness on SWLI apparent thickness. Insert: Method of measuring film thickness by SWLI. No need to pick datapoints in the vicinity of or on a step when they are higher than 12 nm.

We notice that irrespective of the thickness of the metal overlayer, SWLI measurements always give for this monolayer thickness values around 14 nm (see Fig. 4.19 i). This estimate is confirmed by our procedure of SFM-tip digging shortly followed by mapping in intermittent contact mode (see Fig 4.19c, e and h). The thickness as determined by IC-SFM is around 16 nm, which indeed compares favourably with SWLI. The CFI-SFM topographic image of a bare borosilicate glass surface presented in Fig. 4.19 b reveals details of the surface that are not to be seen on any of the images where a PDMS coating is present. Furthermore the phase map in Fig. 4.19 f is very contrasty and we have seen in §3.1.4 that this quantity (phase) was related to certain materials properties such as stiffness (or hardness) and adhesion. It is clear that the material disclosed by the action of the SFM tip is stiffer than the surroundings and therefore is thought to be the substrate (borosilicate glass). This is a strong argument in favour of the monolayer being homogeneous. Unlike the previous case study, it was not possible to estimate the PDMS monolayer thickness by quantitative XPS because it is precisely too thick for the analysis depth of the method: 11nm according to the method used in the previous case study (see equation (4.1)), taking into account possible elastic scattering effects (large acceptance angle analyser) and supposing the PDMS layer to be 15 nm thick.

On the other hand it was possible to obtain the atom percentages for elemental carbon, elemental oxygen and elemental silicon. C, O and Si. Assuming that Wagner's empirical atomic sensitivity factors derived in constant analyser energy mode (CAE) apply to our setup in similar conditions, then $F_C = 0.25$, $F_O = 0.66$ and $F_{Si} = 0.27$. Equation (3.25) gives the following percentages:

- $[C]\% = 52.8$
- $[O]\% = 27.5$
- $[Si]\% = 19.7$

These figures are close enough to pure PDMS but not totally in accordance with what theory states since the simple stoichiometry of a (P)DMS monomer should lead to [C]% = 50, [O]% = 25, [Si]% = 25. It is clear that the unexpectedly small percentage of silicon is a consequence of the sample being to some degree contaminated by alien carbon and oxygen. This is doubtless related to the slightly insufficient vacuum in our instrument's irradiation chamber ($\sim 4.10^{-9}$ mbar). Nevertheless these percentages are comparable to those published by other groups [Beamson & Briggs, 1992] [Mundry et al, 2000] [Duel & Owen, 1983].

All of the important results previously commented on are summarised in Table 4.1.

	SWLI thickness (nm) *Bare samples*	**Ellipsometric** thickness (nm)	**XPS** thickness (nm)	**IC-SFM or CFI-SFM** thickness (nm)	SWLI thickness (nm) *Al-coated samples*[†]
PDMS-OH on **silicon** (*secondary melt, slow evap*)	0	-	-	-	6.0 ± 1.5[‡]
PDMS-OH on **mica** (*secondary melt, slow evap*)	3.3 ± 0.5	-	-	-	3.5 ± 0.7
PDMS-CH₃ on **fused silica** (*primary melt*)	9.0 ± 3.0[1'] 5.0 ± 2.0[2']	-	-	-	2.7 ± 0.6[1'] 1.5 ± 0.4[2']
PDMS-OH on **fused silica** (*primary melt*)	13.0 ± 2.0[1] 8.0 ± 2.0[2 to 5]	3.5 ± 0.4[1] 3.7 ± 0.4[2] 4.3 ± 0.4[3] 4.2 ± 0.4[4] 3.3 ± 0.4[5]	> 4.2 ± 0.7[1] 4.2 ± 0.7[2 to 5]	4.8 ± 0.7[CFI]	4.5 ± 0.6[1] 3.7 ± 0.5[2 to 5]
PDMS-OH on **borosilicate glass** (*secondary melt, slow evap*)	13.5 ± 2.0	-	> 11	17.3 ± 1.4[IC]	13.0 ± 1.5

Table 4.1. Quantitative characterisation of PDMS monolayers adsorbed onto silicates according to two different processes: primary (solvent-free) melt and octane-based secondary melt (slow evaporation of the solvent). Comparison of measurements made by SWLI, XPS, IC and CFI-SFM and imaging ellipsometry. The SWLI step height measurements are given with an uncertainty to 1σ. [1 to 5]: locations where measurements were made by ellipsometry and the other tehcniques (see Fig. 4.16 a). Note that the surface area covered by one pixel in imaging ellipsometry is 4 μm², while it is either 0.5 μm² (x40 objective) or 20 μm² (x2.5 objective). [1']: location corresponding to the thicker regions of the monolayer made of (α, ω) CH₃-terminated chains. [2']: thinner regions of the same monolayer. [CFI]: constant force imagng mode (contact). [IC]: intermittent contact mode (tapping). [†]: Aluminium overlayer of thickness (80 ± 8)nm unless otherwise stated. [‡]: Aluminium overlayer of thickness (5 ± 1) nm.

4.3. Discussion

4.3.1. Optical reflectivity effects

We have seen in § 3.1.1 that SWLI was an intensity-sensitive technique, which means that only those materials forming with air an interface with a high enough reflection coefficient can have their surface topography measured. Now in what ways does this principle affect the possibility of detecting or not detecting a coating and even provide precise thickness measurements?

Fresnel's relationships were already recalled in § 3.1.2 in a general case. For a light beam[2] travelling in air and incident on a plane sample normally to its surface, the reflection coefficient in energy is given by:

$$R_{air/sample} = \frac{\left(n_{air} - n_{sample}\right)^2 + k_{sample}^2}{\left(n_{air} + n_{sample}\right)^2 + k_{sample}^2} \qquad (4.11),$$

where n is the refractive index and k is the extinction index, that is the ability of a material to absorb or attenuate an electromagnetic wave, here visible light. Unlike the reflection coefficient in amplitude, the reflection coefficient in energy can be directly used to compare incident intensity with reflected intensity. Since we have the optical properties of the various materials (see Table 3.1) used in this study, we can compare their reflection coefficient in energy with air.

Reflection coefficient in energy of the air/material interface in (%)				
PDMS ε values	Borosilicate Glass ε values	Fused silica ε values	Mica bulk values	Silicon bulk values
4.57	4.29	3.51	4.91	37.16

Table 4.2. Reflection coefficients in energy for various interfaces. n and k values were either taken from tabulated bulk values or from ellipsometric (ε) measurements performed by Nanofilm (EP[3]) at 532 nm. For references about individual optical constants see Table 3.1.

---

[2] We consider the component of the oscillating electric field that is parallel to the plane of incidence.

It can be seen that PDMS in the form of an ultra-thin film adsorbed onto fused silica exhibits a higher reflection coefficient than any substrate with which we have experimented except for silicon. Therefore we expect the film to reflect enough light to be detected when deposited onto a transparent substrate. That is what we observe. On the contrary, silicon is so much more reflective than a transparent film that the latter is likely to be invisible and only the silicon topography, that is the surface located beneath the natural silica layer which is itself buried beneath the PDMS film, will be mapped. Again that is what we observe. Besides precise measurements are dependent upon the uniformity of the surface reflectivity as expressed by equation (3.13) and especially by the parameter α.[3] Considering a fused silica substrate, the pixel located just outside the film boundary corresponds to a region of the surface that reflects 3.51% of the incident intensity, while the pixel situated on the PDMS film would reflect 4.56% of the incident light. That discrepancy can be enough to bring about a phase offset hence a height offset after the data processing stage where intensity interferograms are converted into interferometric phases. Borosilicate glass's reflectivity being closer to that of PDMS the offset can be expected to alter the height values less strongly.

This very basic reasoning neglects some important phenomena occurring within transparent films referred to as film thin effects. They are a consequence of light traversing the film and thus giving rise to a second reflection. The optical path distance of light within a film is given by:

$$OPD = 2n_{film}t_{film}$$
(4.12),

where n_{film} is the refractive index of the film and t_{film} is the film thickness. When this distance is smaller than the interference depth of the instrument, that is the vertical distance over which interference can occur, then extra or attenuated intensity reaches the detector. The interference of New View 100 being roundabout 4 μm for all objectives, this condition is fulfilled for the type of films in which we are interested. In fact, thin film effects bring about more than one extra-reflected ray as multiple reflections are expected. A more accurate model is then given by equation (3.15) through (3.17). If we rewrite those in a form

---

[3] Zygo Corp. claims that offsets in step height measurements up to 40 nm (positive or negative) can occur when a reflective material (metal) is next to a less reflective material like polymers or ceramics.

that applies to our case study: normal incidence and normal reflection, reflection coefficient in energy rather than in amplitude, film considered totally transparent to light, we get:

$$R = \left(\frac{\left| r_{01} + r_{12} e^{-2j\beta} \right|}{\left| 1 + r_{01} r_{12} e^{-2j\beta} \right|} \right)^2 \left.\vphantom{\frac{1}{1}}\right\} \quad (4.13),$$

$$r_{01} = \frac{n_0 - n_1}{n_0 + n_1}, \quad r_{12} = \frac{n_1 - n_2}{n_1 + n_2}, \quad \beta = \frac{2\pi}{\lambda} n_1 t$$

where R is the total reflection coefficient in energy, r_{01} is the reflection coefficient in amplitude at the air-film interface while r_{02} is the reflection coefficient in amplitude at the film-substrate interface. β denotes the phase change of the reflected wave with t being the film thickness. Assuming that the optical constants of both PDMS films and substrates vary little within the 430 to 630 nm range, we can plot the reflection coefficient in energy for the main situations we have studied (see Fig. 4.20).
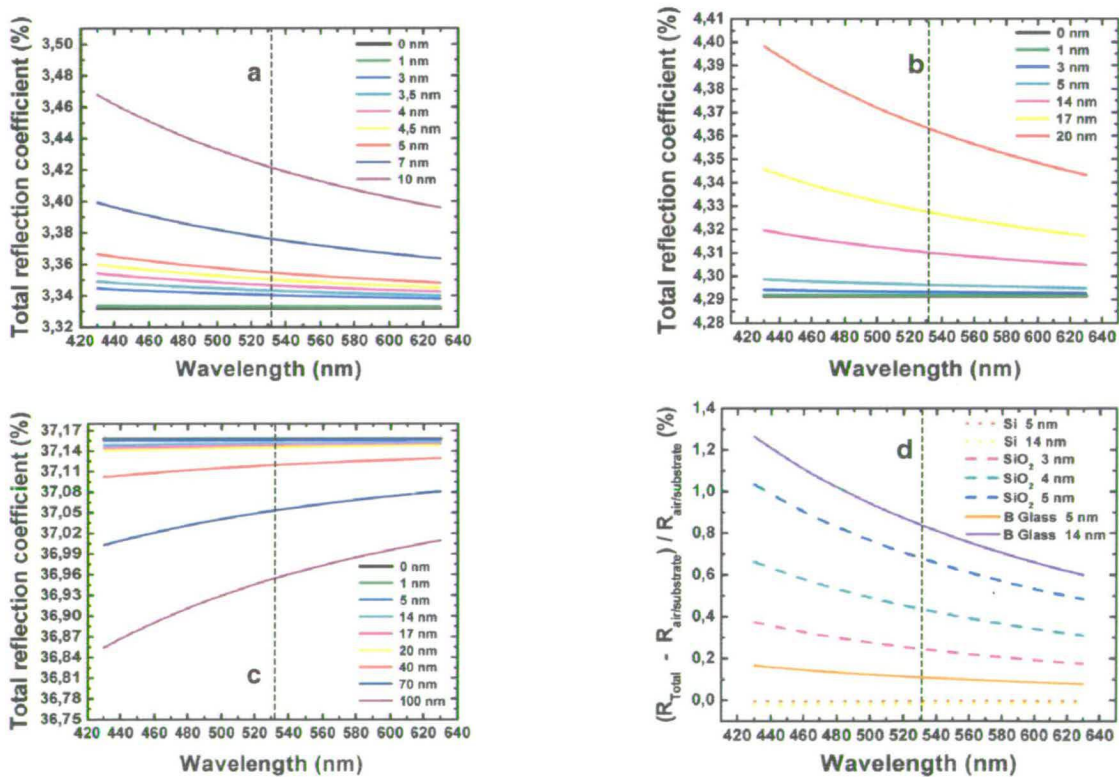

Fig. 4.20. Total reflection coefficient at the air-PDMS-substrate 'interface' versus wavelength and PDMS film thickness. a: Fused silica. b: Borosilicate glass. c: silicon. d: Influence of substrate and film thickness on the total reflection coefficient relative to the reflection coefficient of the air-substrate interface. Dashed lines: most reliable values 532 nm.

Multiple reflection analysis shows that films of thickness such as those we measured affect little the total reflection coefficient. It is primarily governed by the substrate's optical constants (see Fig. 4.20 a to c). This is particularly true of silicon. Interestingly, the influence on the reflection coefficient of a 5 nm thick PDMS film on fused silica is as big as that of a 14 nm thick PDMS film on borosilicate glass (see Fig. 4.20 d). This is a direct consequence of fused silica's optical constants being more different from those of PDMS than borosilicate glass's optical constants are. This can explain why the influence of an aluminium overlayer is much greater on a PDMS monolayer thickness measured by SWLI when it is deposited on fused silica than when it is on borosilicate glass. Furthermore the reflection coefficient of the air-fused silica interface is on the lower end if not smaller than the limit of detection of the instrument, while that for borosilicate glass is 1% higher. This may have some importance for the precision of the measurements. Lastly our fused silica substrates do not consist of a single layer as is the case for borosilicate glass, as a matter of fact ellipsometric investigations proved that there was an uppermost layer of thickness $\cong 1.1$ nm with slightly different optical constants than the bulk[4]. That means that the physical situation is more complex, so that our simple model may not predict the total reflection as sensed by the detector precisely. Therefore a larger discrepancy between the reflection coefficient of the air-PDMS-fused silica system on the one hand and the air-fused silica interface on the other hand cannot be excluded.

From what we have just discussed, it is clear that an homogeneous metal coating preventing light from experiencing multiple relflections and providing uniform reflectivity would eliminate the phase offsets. Mc Waid *et al.* [1992] have studied a system consisting of a fused silica substrate coated with a 5 nm thick layer of chromium topped by a 5 nm thick silicon dioxide layer. In a mathematical model neglecting multiple reflections they calculated the thickness of a metal overlayer (chromium or platinum) that is necessary to get rid of phase offsets and transform an apparent step height measurement into a true step height measurement. This system differs from those we have studied, only PDMS on silicon resembles it. They conclude that too thin a metal overlayer leads to the step height being underestimated. For instance a 5 nm chromium overlayer leads an apparent step height of about 4 nm. This is similar to our finding that a 5 nm aluminium overlayer on PDMS-coated silicon underestimates the layer thickness (see Table 4.1). According to them a 80 nm thick

---

[4] This is probably related to the way the slides were manufactured at the factory. Glass and pure silica sheets often have nano-outer layers with optical constants differing from those of the bulk.

chromium or platinum overlayer is needed to provide enough light absorption and eliminate offsets because thinner metal films are physically different from bulk materials. We noted the same thing regarding aluminium through XPS chemical analysis (see § 4.2.4 and Fig. 4.18). Table 4.1 shows that only thick aluminium coatings led to SWLI step height measurements that compared favourably to ellipsometric, XPS or SFM measurements. All four techniques give consistent results apart from two situations: the SFM tip-dug pit region and the winding loop region.

IC-SFM measurements give a thickness 3 to 4 nm higher than SWLI. Here we tend to think that this discrepancy arises from a wrong calibration of the piezoelectric drive in the nanometre region. Based on height piezoelectric calibration done with a 1750 nm step height standard, step height measurements are absolutely accurate down to at least 200 nm. However a test made with a 20 nm step height standard showed that the interferometer provided an apparent thickness of about 15 nm. Regarding IC-SFM measurements a possible although unlikely overestimation of the layer thickness could be due to the silicon nitride-coated tip digging through the 'softer' glass substrate over a couple of nanometres. Provided that the miscalibration of the piezoelectric drive is compensated for, SWLI measurements compared favourably with XPS, ellipsometry and SFM.

The winding loop region (see Fig. 4.16 a) has been subjected to many measurements as it consistently appeared as thicker than the circular area by SWLI, while ellipsometric measurements showed the opposite. As has already been mentioned, this feature is a consequence of mishandling by the experimentalist of a sample of PDMS melt. A fine string of polymer separated itself from the bulk and fell off. We have reasons[5] to think that the chains constituting this string were offered better adsorbing conditions than the rest. The strongest argument in favour of the winding loop corresponding to a thicker layer is actually not a fully quantitative result. It is a series of XPS spectra (C1s photoelectron line) taken along lines (linescans) presented in Fig. 4.17 e. The amount of carbon, in other words the polymer density is clearly higher in the winding loop region than in the circular layer, even though it is not possible to estimate the difference in terms of thickness. Supposing the PDMS layer morphology to be rather different in these two regions, it is fair to assume that optical constants as determined by ellipsometry in the circular area could be different from the real constants of the winding loop region. If this hypothesis is correct, it is likely that the ellipsometric model applied with accuracy and precision to regions in the circular area could

---

[5] Those will be put forward in details in § 4.3.3.

be less accurate in the winding loop region. As a matter of fact, ellipsometry is known to underestimate film thicknesses when the uniform layer approximation fails to describe the reality or when the model's parameters are not well fixed [Serna *et al.*, 1998] [Beyerlein *et al.*, 2002]. If the optical constants of thin films and especially PDMS monolayers depend on how continuous an interface they make, then important parameters could be: the number of chains per unit area and, more generally, their morphology if they differ in structure at a scale similar to the resolution limits of optics: ~ 200 nm. Our simple multiple reflection model assumed identical PDMS optical constants for the 14 nm thick and SFM determined as continuous PDMS monolayer on borosilicate glass and the more challenging layer adsorbed onto fused silica. We may conjecturate that the thick monolayer has optical constants closer to those of glass, which would make the air-PDMS-borosilicate glass reflection coefficient even more similar to that of the air-borosilicate glass interface (see Fig. 4.20 d) explaining why SWLI apparent thickness is essentially constant whatever the thickness of the aluminium overlayer.

4.3.2. Noise, roughness and waviness effects

Changes in light intensity level affect the interferometric phases and thus bring about some noise in the data, and so does temperature change. An easy way around this is to acquire several images at the same location and average out. A rule of thumb has it that if 9 measurements are taken, the noise level is divided by $9^{1/2} = 3$. A second type of noise that is not electronics-related is the substrate topography-induced noise. A scanning white light interferometer is an instrument designed to map the topography of a surface, therefore roughness and waviness are the desired information. In our case they complicate the interpretation of an image. The way they are dealt with depends upon the thickness of the film to be characterised. If the latter is thicker than, say 10 nm, and the substrate is as flat as an ordinary borosilicate glass slide, it suffices to pick a layer boundary and select one pixel a few pixels away from the top of the step and another pixel a few pixels away from the bottom of the step and measure the height difference. This is what has been done for the 14 nm thick PDMS monolayer on borosilicate glass (see Fig. 4.19 i, insert). If the film is thinner than this 10 nm limit and particularly if it is an ultra-thin film (thickness ≤ 4 nm) as was the case for the PDMS film on fused silica and the silane lines on borosilicate glass (see Fig. 4.11), the step's datapoints must be considered with caution. Applying the method

explained above would undoubtedly result in the step height being overestimated since the roughness or waviness of a surface increases with the scale at which it is viewed (result from fractal theory). Although the roughness and waviness effects vary in direction and magnitude throughout a field of view, electronics noise does not, it is therefore safe to consider those pixels along the step that are characterised by an abnormally big change in height (bigger than noise and bigger than roughness/waviness). The difficulty is to choose those pixels whose height is the most roughness/waviness free. In Fig. 4.17 f, we show that the lower end of the height estimate corresponds to pixels clearly separated by abrupt jumps in height. To select the upper end of the step height, one can choose the next pixel up from the top one and the next pixel down from the bottom one. This method is recommended especially when imaging with a low magnification objective because of the lateral distance that exists between two nearest pixels. This is how we got the errors bars for the SWLI measurements.

4.3.3. Adsorption parameters and monolayer history

Aside from all these metrological aspects that matter when it comes to validating a method for characterising nanometre-sized objects, SWLI turns out to provide a wealth of information regarding adsorption processes and more generally physico-chemical interactions between two surfaces in air or in a medium.

One of the most important pieces of information obtained by this technique is that complete, uniform and homogeneous PDMS monolayers are produced by the secondary melt route with slow evaporation of the solvent. As fast evaporation of the solvent of a polymer solution leads to 'coffee stain' effects (see § 4.2.3), it is best to work with a low vapour pressure solvent like octane while other common (and cheap) solvents like toluene have a higher vapour pressure. This might explain partly why the adsorption of the polystyrene film looked weak (see Fig. 4.10). The fact that a solution of OH-terminated PDMS chains in octane with $\Phi = 0.2$ gave rise to a much thicker layer than its equivalent from a primary melt may lie in the increased mobility of chains in a solvent that made it possible for more chains to come into contact with the clean silica surface. On the contrary it takes time for chains from a viscous melt to set in by gravity, which gives contaminants or moisture time to occupy surface adsorbing sites. We can also notice that amongst monolayers adsorbed onto fused silica from primary melts, those made up of OH-terminated

chains are thicker and less heterogeneous than layers consisting of CH_3-terminated chains (see Table 4.1). By less heterogeneous we mean that the difference between the thicker and the thinner regions is smaller. This suggests that OH-groups act as more effective binders than CH_3-groups. It has been observed by real-time ellipsometric monitoring of PDMS oils[6] that those oils made of OH-terminated chains stopped spreading long before oils made of CH_3-terminated chains did [Villette *et al.*, 1996]. This would explain why PDMS monolayers made of CH_3-terminated chains are much thinner at the edges since these locations receive the least amount of fluid from the reservoir located somewhere in the middle of the macroscopic drop. On the contrary OH-terminated chains with their better binding ability adsorb early to the surface, which inhibits macroscopic spreading and in the end gives rise to comparatively more homogeneous layers.

Furthermore as has been discussed in § 2.1.3, acid/base interactions sometimes prevail over van der Waals forces in the case of polymers at surfaces. In particular PMMA, a basic polymer form a dense monolayer on acidic surfaces such as silica [Fowkes & Mostafa, 1978]. Silica's acidic nature is related to the silanol (Si-OH) sites. Assuming that PDMS is basic and interacts primarily through acid/base effects with silica, we would have an explanation for the complete coating it provides in the best conditions. On the contrary adsorption of a secondary melt of OH-terminated PDMS on mica gave rise to a very thin layer. This can be explained by the fact that mica is not acidic and its surface bears few silanols if at all [Vallant *et al.*, 1998]. Another parameter was stressed: the influence of a solvent's properties on the adsorption of polymer chains. If the solvent develops favourable interaction with the surface it can act as a competitor for the chains. Since octane is a purely dispersive liquid, with no acidic or basic character it was a particularly appropriate solvent. Toluene is a weak base [Layman & Hemminger, 2004] but still a base and can compete with other weak polymer bases like polystryrene. We believe that this contributed to the seemingly poor adsorption of polystyrene on glass, as determined at the lateral microscale.

---

[6] With a viscosity of 200 cP they are far more runny than the samples with which we have worked.

4.4. Conclusion

SWLI is a powerful non-destructive thin and ultra-thin film characterisation technique. It is especially well suited to soft condensed matter deposited on either transparent or opaque substrates. In this case and provided that the step height calibration is accurate or the absolute error known, the fact that it is a direct thickness measuring technique makes it as good if not superior to imaging ellipsometry that is reliant on sometimes oversimplified models.

Qualitative information about a film can be obtained on a sample without any further modifications, while quantitative information of a precision equivalent to that of established techniques such as scanning force microscopy, x-ray photoelectron spectroscopy, ellipsometry or x-ray reflectometry can only be obtained if the sample is covered in metal. It is recommended that the thickness of the metal overlayer be 80 nm although this figure could be brought as far down as zero for situations where film and substrate have similar or identical optical constants.

Since SWLI only performs thin-film characterisation when a step is present (either naturally or man-made), it is not so easily applicable to hard films such as oxides thermally or naturally grown on semi-conductors or metals. The creation of steps for these materials requires the use of aggressive chemicals like hydrofluoric acid (HF) or better ammonium fluoride (NH_4F)[7].

The convoluted nature of the height information (substrate plus film) imposes that the data processing be done with extreme care. Indeed the thinner the film the more influence substrate waviness and/or roughness has on the measure of the film thickness. Only those pixels located along the step and such that the height difference between two nearest pixels is significantly larger than both the electronics noise level and the substrate-induced noise (waviness, roughness) level will be chosen to estimate the thickness. Ideally it would be possible to eliminate both sources of noise by mapping the bare substrate in a first stage, the coated substrate in a second stage, and calculating the difference. Unfortunately this is only possible with more recent instruments (ours is 15 years old) with controlled temperature and vibrations and a fully closed-loop system that eliminate drift and non-linearity in the height measurements in the nanometre range (more reliable accuracy over three or four orders of

---

[7] The latter has been shown to give rise to smoother etched surfaces [Higashi *et al.*, 1991].

magnitudes). This route is nevertheless promising, as it would lead to true three-dimensional maps of the film alone. Therefore in an effort to avoid any topographic modifications of the substrate (in particular, silicon wafers or glass slides) we believe that instead of using oxidising solutions (see § 3.2.1) that may well render the surface somewhat rougher, it is best to use gentler chemicals like isopropyl alcohol (IPA) according to a procedure described in details by Seah and Spencer [2 - 2003]. If, for some reason, the 'difference route' cannot be employed, it is advised that two narrow scratches be made with a steel-needle (softer material than the substrate) throughout the film crossing each other at the centre of the film and at right angle. The lateral distribution of the thickness can then be obtained as well as the knowledge of the homogeneity or non-homogeneity of the layer at the expense of compromising slightly with the claimed non-destructive character of the technique.

The study performed on silane-patterned glass surfaces reveals that for ultra-thin films especially if their characteristic size (thickness) lies in the sub-nanometre region, only a periodical and unambiguous pattern will make them detectable by SWLI.

The most interesting aspect of SWLI is that a technique design to perform routine quality-control measurements can provide a wealth of information on adsorbed ultra-thin films:

- compare the outcome of different adsorption processes,
- choose the best substrate for a given film,
- or choose the best film for a given substrate.

It is in that that lies the true power of SWLI to the eyes of a physical chemist of surfaces.

4.5. References

Beamson, G; Briggs, D (1992) *High resolution XPS of organic polymers. The scientific ESCA 300 database*, John Wiley & Sons, New York, USA, pp 268-269.

Beyerlein, D; Kratzmüller, T; Eichhorn, K-J. (2002) *Study of a novel polymer architectures on solid surfaces by variable angle spectroscopic and imaging ellipsometry*, Vibrational Spectroscopy. **29**(1-2), 223-227.

Briggs, D; Seah, M.P. (1983) *Practical surface analysis by Auger and x-ray photoelectron spectroscopy*, John Wiley & Sons, Chichester UK, **Chapter 1**, 6-7.

Chiang, C-H; Liu, N-I; Koenig, J.L. (1982) *Magic-angle cross-polarization carbon 13 NMR study of aminosilane coupling agents on silica surfaces*, Journal of Colloid and Interface Science. **86**(1), 26-34.

Cumpson, P.J. (2001) *Estimation of inelastic mean free paths for polymers and other organic materials: use of quantitative structure-property rerlationships*, Surface and Interface Analysis. **31**(1), 23-34.

Deegan, R.D; Bakajin, O; Dupont, T.F; Huber, G; Nagel, S.R; Witten, T.A. (1997) *Capillary flow as the cause of ring stains from dried liquid drops*, Nature. **389**(6653), 827-829.

Denkov, N.D; .Velev, O.D; Kralchevsky, P.A; Ivanov, I.B; Yoshimura, H; Nagayama, K. (1992) *Mechanism of formation of two-dimensional crystals from latex particles on substrates*, Langmuir. **8**(12), 3183-3190.

Duel, L.A; Owen, M.J. (1983) *ESCA studies of silicone release coatings*, Journal of Adhesion. **16**(1), 49-59.

Eberhart, J.P. (1997) *Analyse structurale et chimique des matériaux*, Dunod, Paris, France.

Eder, K; Semrad, D; Bauer, P; Golser, R; Maier-Komor, P; Aumayr, F; Peñalba, M; Arnau, A, Ugalde, J.M; Echenique, P.M. (1997) *Absence of a "threshold effect" in the energy loss of slow protons traversing large-band-gap insulators*, Physical Review Letters. **79**(21), 4112-4115.

Flaherty, T; O'Connor, G. (2003) *Application of spectral reflectivity to the measurement of thin-film thickness*, Proceedings of the Society of Photo-Optical Instrumentation Engineers (SPIE). **4876**, 976-983.

Fowkes, F.M; Mostafa, M.A. (1978) *Acid-base interactions in polymer adsorption*, Industrial & Engineering Chemistry Product Research and Development. **17**(1), 3-7.

Geissler, M; Kind, H; Schmidt-Winkel, P; Michel, B; Delamarche, E. (2003) *Direct patterning of NiB on glass substrates using microcontact printing and electroless deposition*, Langmuir. **19**(15), 6283-6296.

Heim, T; Preuss, S; Gerstmayer, B; Bosio, A; Blossey, R. (2005) *Deposition from a drop: morphologies of unspecifically bound DNA*, Journal of Physics - Condensed Matter. **17**(9), 703-716.

Higashi, G.S; Becker, R.S; Chabal, Y.J; Becker, A.J. (1991) *Comparison of Si(111) surfaces prepared using aqueous solutions of NH₄F versus HF*, Applied Physics Letters. **58**(15), 1656-1658.

Himpsel, F.J; McFeely, F.R; Taleb-Ibrahimi, A; Yarmoff, J.A; Hollinger, G. (1988) *Microscopic structure of the SiO₂/Si interface*, Physical Review B. **38**(9), 6084-6096.

Layman, K.A; Hemminger, J.C. (2004) *Determination of surface OH acidity from the formation of acid/base complexes on ultrathin films of γ-Al₂O₃ on NiAl(100)*, Journal of Catalysis. **222**(1), 207-213.

Leadley, S.R; Watts, J.F. (1997) *The use of XPS to examine the interaction of poly(acrylic acid) with oxidised metal substrates*, Journal of Electron Spectroscopy and Related Phenomena. **85**(1-2), 107-121.

Lide, D.R. (2001) *CRC handbook of chemistry and physics 82nd edition*, CRC Press, New York, USA.

McWaid, T; Vorburger, T; Song, J.F; Chandler-Horowitz, D. (1992) *The effects of thin films on interferometric step height measurements*, Proceedings of the Society of Photo-Optical Instrumentation Engineers (SPIE). **1776**, 2-13.

Meyer, E; Hug, H.J; Bennewitz, R. (2004) *Scanning Probe Microscopy. The Lab on a Tip*, Springer-Verlag, Berlin, Germany.

Mundry, T; Surmann, P; Schurreit, T. (2000) *Surface characterization of polydimethylsiloxane treated pharmaceutical glass containers by X-ray-excited photo- and Auger electron spectroscopy*, Fresenius Journal of Analytical Chemistry. **368**(8), 820-831.

Palik, E.D. (1985) *Handbook of optical constants of solids*, Academic Press Inc, USA.

Powell, C.J; Jablonski, A. (2001) *NIST electron effective-attenuation-length-database – version 1.0*, National Institute of Standards and Technology, Gaithersburg, MD, USA.

Scofield, J.H. (1976) *Hartree-Slater subshell photoionization cross-sections at 1254 and 1487 eV*, Journal of Electron Spectroscopy and Related Phenomena. **8**(2), 129-137.

2 - Seah, M.P; Spencer, S.J. (2003) *Ultrathin SiO2 on Si I. Quantifying and removing carbonaceous contamination*, Journal of Vacuum Science and Technology A. **21**(2), 345-352.

Serna, R; de Sande, J.C.G; Ballesteros, M; Afonso, C.N. (1998) *Spectroscopic ellipsometry of composite thin films with embedded Bi nanocrystals*, Journal of Applied Physics. **84**(8), 4509-4516.

Vallant, T; Brunner, H; Mayer, U; Hoffmann, H; Leitner, T; Resch, R; Friedbacher, G. (1998) *Formation of self-assembled octadecylsiloxane monolayers on mica and silicon surfaces studied by atomic force microscopy and infrared spectrometry*, Journal of Physical Chemistry B. **102**(37), 7190-7197.

Van Oss, C.J; Good, R.J; Chaudhury, M.K. (1988) *Additive and nonadditive surface tension components and the interpretation of contact angles*, Langmuir. **4**(4), 884-891.

Vereecke, G; Rouxhet, P.G. (1998) *Surface charging of insulating samples in x-ray photoelectron spectroscopy*, Surface and Interface Analysis. **26**(7), 490-497.

Vereecke, G; Rouxhet, P.G. (1999) *New method to correct for the influence of organic contamination on intensity ratios in quantitative XPS*, Surface and Interface Analysis. **27**(8), 761-769.

Villette, S; Valignat, M.P; Cazabat, A.M; Jullien, L; Tiberg, F. (1996) *Wetting on the molecular scale and the role of water. A case study of wetting of hydrophilic silica surfaces*, Langmuir. **12**(3), 825-830.

Wagner, C.D; Davis, L.E; Zeller, M.V; Taylor, J.A; Raymond, R.H; Gale, L.H. (1981) *Empirical atomic sensitivity factors for quantitative analysis by electron spectroscopy for chemical analysis*, Surface and Interface Analysis. **3**(5), 211-225. The data reported in this paper is also to be found at www.uksaf.org/data/sfactors.html.

Wagner, C.D; Passoja, D.E; Hillery, H.F; Kinisky, T.G; Six, H.A; Jansen, W.T; Taylor, J.A. (1982) *Auger and photoelectron line energy relationships in aluminium-oxygen and silicon-oxygen compounds*, Journal of Vacuum Science and Technology. **21**(4), 933-944.

Wang, D; Jones, F.R. (1993) *Surface analytical study of the interaction between γ-amino propyl triethoxysilane and E-glass surface. 2. X-ray photoelectron spectroscopy*, Journal of Materials Science. **28**(9), 2481-2488.

Watts, J.F; Wolstenholme, J. (2003) *An introduction to surface analysis by XPS and AES*, John Wiley & Sons, Chichester UK.

5. PDMS monolayers on silica: microstructure, elements of adhesion and friction

This chapter constitutes a second step in the study of PDMS monolayers. We focus on complete monolayers as defined in chapter 4 with the purpose of characterising them at the molecular scale. To begin with, we present the results of a contact angle goniometry study of the surface energetics of PDMS as a monolayer as well as those of air-oxidized p-boron doped silicon(111) in order to quantitatively estimate how much energy is involved when they interact with each other.

We then exploit the possibilities of combined IC-SFM and nanomanipulation (see § 4.2.4. Fig. 4.19) with the imaging tip to investigate the structure and morphology of monolayers prepared from mainly monodisperse PDMS samples varying in chain termination and molecular mass. We show the benefit of mapping and viewing a monolayer both in bad-solvent and good-solvent conditions and the power of phase-imaging to distinguish between phases and detect discrete features.

We also present preliminary results of nanoadhesion experiments (pull-off force tests) between air-oxidised silicon SFM tips and PDMS monolayers with different grafting density adsorbed onto borosilicate glass. A comparison between the change in interface free energy of the air or water or octane-PDMS pairs as determined by STC theories (see § 2.1.3) and pull-off tests will give this study a quantitative flavour.

Finally we will report the main results of a short friction study performed on a PDMS monolayer.

5.1. Surface energetics of PDMS monolayers and 'SiO$_2$ + Si'

5.1.1. Contact angle goniometry study on PDMS coated Si wafers

Chemical analysis of substrates:

We have performed high-resolution XPS analysis on several raw substrates both in large-acceptance angle XPS and ARXPS (see § 3.1.3). This enabled us to estimate the average thickness of the silicon oxide layer naturally grown during its stay in the lab on elemental silicon. A typical XPS spectrum of the Si2p photoelectron line, along with the deconvoluted peaks are presented in Fig. 5.1. According to the method presented by Mitchell *et al.* [1994], deconvolution has been performed taking into account spin-coupling phenomena. Each peak

was then fitted with doublet pairs at fixed separation (see Fig. 5.1). The shape of the symmetrical fitting peaks was the same as that used for PDMS and silica experiments reported in § 4.2.4 (Fig. 4.17). An extra peak was added to the elemental silicon peak (broad rose peak) in order to introduce some asymmetry in accordance to the behaviour of metals and semi-metals [Salvia & Castle, 1998].
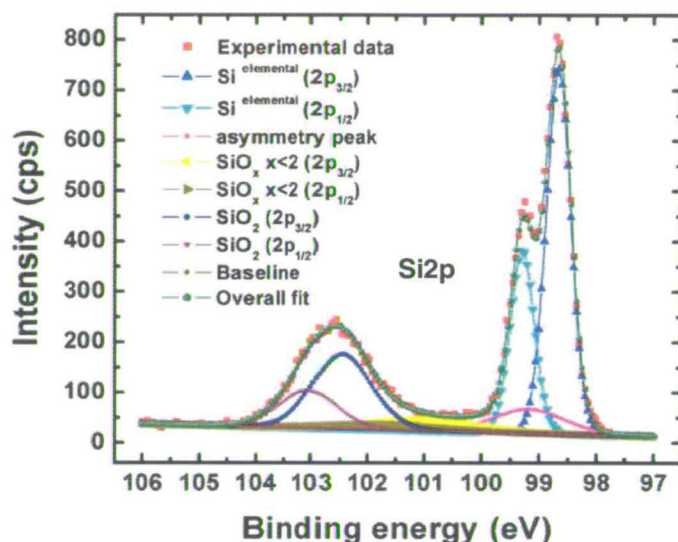

Fig. 5.1. XPS spectrum of the Si2p photoelectron line of an air-oxidised silicon wafer of the following type: p-boron doped Si(111). Electron spin-induced doublets are easily detected: note the clear shoulder on the elemental Si2p peak (~ 99 eV). SiO_2 is the dominant silicon oxide species.

Direct surface tension and contact angle measurements:

Applying the film thickness determination method described both in § 3.1.3 and § 4.2.4, the silicon oxide thickness was estimated to range between **0.9 nm and 1.5 nm** depending on the way R_0 was determined. Theoretical calculation of this parameter leads to thicknesses towards the upper end of the range, in rather good accordance with what Muto *et al.* [1993] have obtained for the same type of silicon only a bit higher. Experimental determination of R_0 leads to higher ratios, hence thinner layers [Seah & Spencer, 2002] [Seah & Spencer, 1 - 2003] of order of 1 nm or even smaller. This discrepancy is partly explained by the fact that many Si2p electrons, ejected from elemental atoms lose some energy to electrons located in the conduction band bringing about collective oscillations or plasmons (see Fig. 3.13). This

happens because our wafers are heavily doped (resistivity $< 1 \, \Omega$ cm). We feel the true average thickness must be slightly above 1 nm because this would fit better with the detailed experimental study of air-oxidising wafers (same type) by Morita *et al.* [1990].

Silicon wafers of the same type were coated with 'non-viscous' primary melts made up of polydisperse, strongly binding PDMS chains: $\overline{M}w = 49$ kg mol^{-1}, (α, ω) OH-terminated. The resulting PDMS monolayers were subjected to a series of surface tension and contact angle measurements by the sessile drop method with the following probe liquids:

- Hexadecane, a purely dispersive liquid,
- DMSO, a Lewis base or electron-pair donor or H-bond acceptor,
- Water, both a Lewis acid and a Lewis base but with a stronger acidic tendency,
- Mercury, a very high surface tension liquid.

Details on the surface tension components of each of these liquids, except mercury, can be found in § 2.1.3. The method used to measure contact angles has been presented in § 3.1.5 but we still have to give some information about the measurement of liquid surface tensions.

Bashford and Adams [1892] realised that the interfacial tension at the liquid-liquid or liquid-gas interface could be estimated from geometrical dimensions of a non-spherical but axially symmetric pendant or sessile drop. Their model was later refined by Adamson [1990]. For a pendant drop of liquid surrounded by a gas (air for instance):

$$\gamma_{LV} = g \Delta\rho \frac{d_e^2}{H} \tag{5.1},$$

where g is the acceleration of gravity, $\Delta\rho = \rho_L - \rho_{gas}$ the difference between the liquid density and that of the surrounding gas, d_e is a characteristic dimension of a pendant drop and $1/H = f\left(\dfrac{d_s}{d_e}\right)$ with d_s is another characteristic dimension. These ratios are tabulated [Adamson, 1990]. A similar treatment was applied by Staicopolus [1962] [1963] [1967] to sessile drops. Supposing a liquid drop in a gas medium:

$$\gamma_{LV} = g \Delta\rho \frac{h^2}{BG^2} = g \Delta\rho \frac{r^2}{BF^2} \tag{5.2},$$

where h and r are characteristic dimensions of a sessile drop, while B and G are functions of the ratio r/h [Staicopolus, 1962] [Staicopolus, 1963] [Staicopolus, 1967].

We present in Fig. 5.2 typical pictures of sessile and pendant drops. The numerical values are to be found in the figure caption.
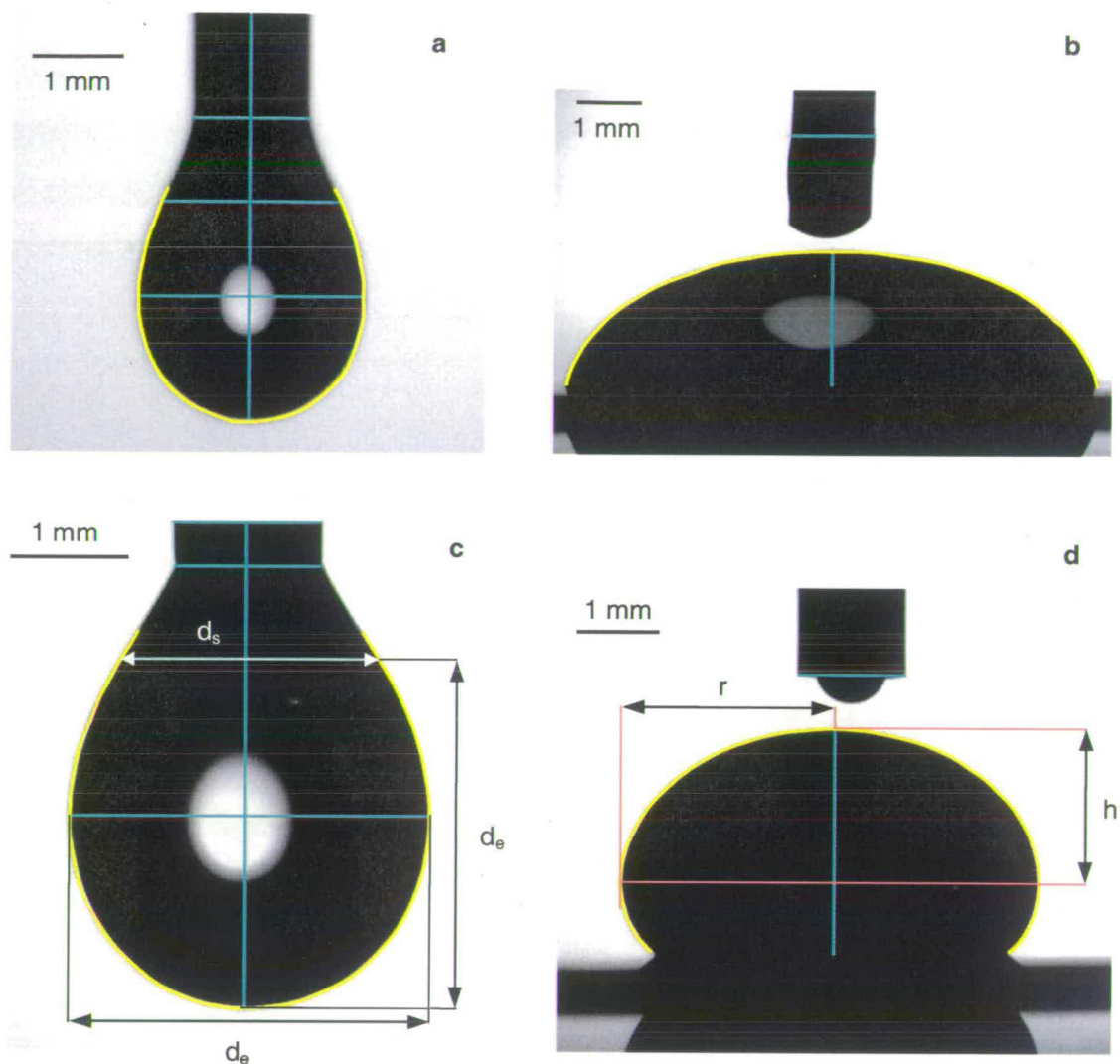

Fig. 5.2. Micrographs of pendant and sessile drops whose surface tension is being measured (T = 21.5 °C, RH = 46 ± 3 %). The blue lines correspond to the characteristic dimensions referred to in the text. The yellow lines highlight the profile of each drop. a: hexadecane: γ_{C16H34} = (27 ± 0.2) mJ m^{-2}. b: DMSO: γ_{DMSO} = (42.4 ± 1) mJ m^{-2}. c: water: γ_{H2O} = (70.5 ± 0.4) mJ m^{-2}. d: mercury: 460 mJ m^{-2} < γ_{Hg} < 481 mJ m^{-2}.

Of all four liquids, mercury is the only one whose surface tension varies significantly with time (sensitivity to lack of axisymmetry). At t=0 (small drop), the measured value is about 480 mJ m^{-2}, only 5 mJ m^{-2} less than the standard value of 484 or 485 mJ m^{-2} according

to most authors [Nicholas *et al.*, 1961] [Xu *et al.*, 1995] but it decreases with time and increasing drop size to reach 460 mJ m^{-2} after 150 s in air. The surface tension of water is about 2 mJ m^{-2} below the standard value (see § 2.1.3). The value for DMSO is also lower than that used by van Oss *et al.* [1989] or Lee [1996] but there is not the same consensus about DMSO's surface tension as there is about pure water's. Kwok *et al.* [1998] have measured with a refined setup a surface tension of (42.68 ± 0.09) mJ m^{-2} for a sessile drop, which is very close to our measurement (see Fig. 5.2). We usually utilised measured values of the density in equation (5.1) and equation (5.2). The estimation of each liquid's density was made by weighing 5 samples of a given volume using an automated Eppendorff pipettor. The volume was 800 µl for all liquids except for mercury (100 µl). This method gave sensible results for all liquids apart from mercury ($\approx$ 12 g cm^{-3}) for which tabulated values were used: 13.56 g cm^{-3} at 20°C [Lide, 2001].

In Fig. 5.3 we present plots of advancing contact angle as a function of time, along with the corresponding increase in drop width with time. The plotted contact angles are, for each frame, the average between the left-hand side contact angle and the right hand side one as determined in non-spherical mode. We tried to record data at slow rate $\approx$ 1mm/min in accordance with what Kwok *et al.* [1998] and Lam *et al.* [2002] have recommended and with drop size of order of the capillary length or smaller (see § 3.1.5).
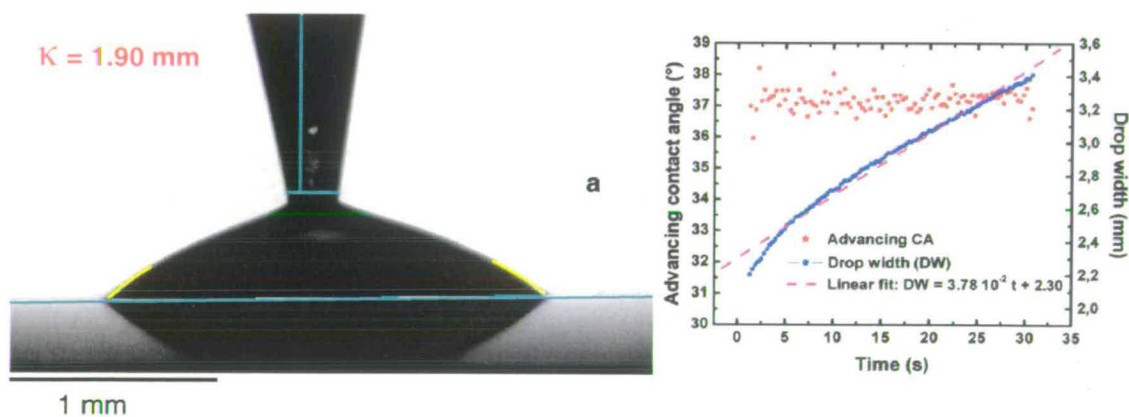

Fig. 5.3. Snapshots of sessile drops whose advancing contact angles (θ_{adv}) is being measured and plots of θ_{adv} and drop width versus time (2σ). a: hexadecane: $\theta_{adv} = (37.2 \pm 0.6)°$, rate $\cong$ 2.3 mm/min. b: DMSO: $\theta_{adv} = (75.6 \pm 0.8)°$, rate $\cong$ 1.8 mm/min. c: water: $\theta_{adv} = (104.8 \pm 1.0)°$, rate $\cong$ 1.3 mm/min. d: mercury: $\theta_{adv} = (139 \pm 5)°$ (2σ), rate $\cong$ 2.2 mm/min. Capillary lengths (κ) are given for each liquid (see § 3.1.5). T = 21°C, RH = (46 ± 3) %.
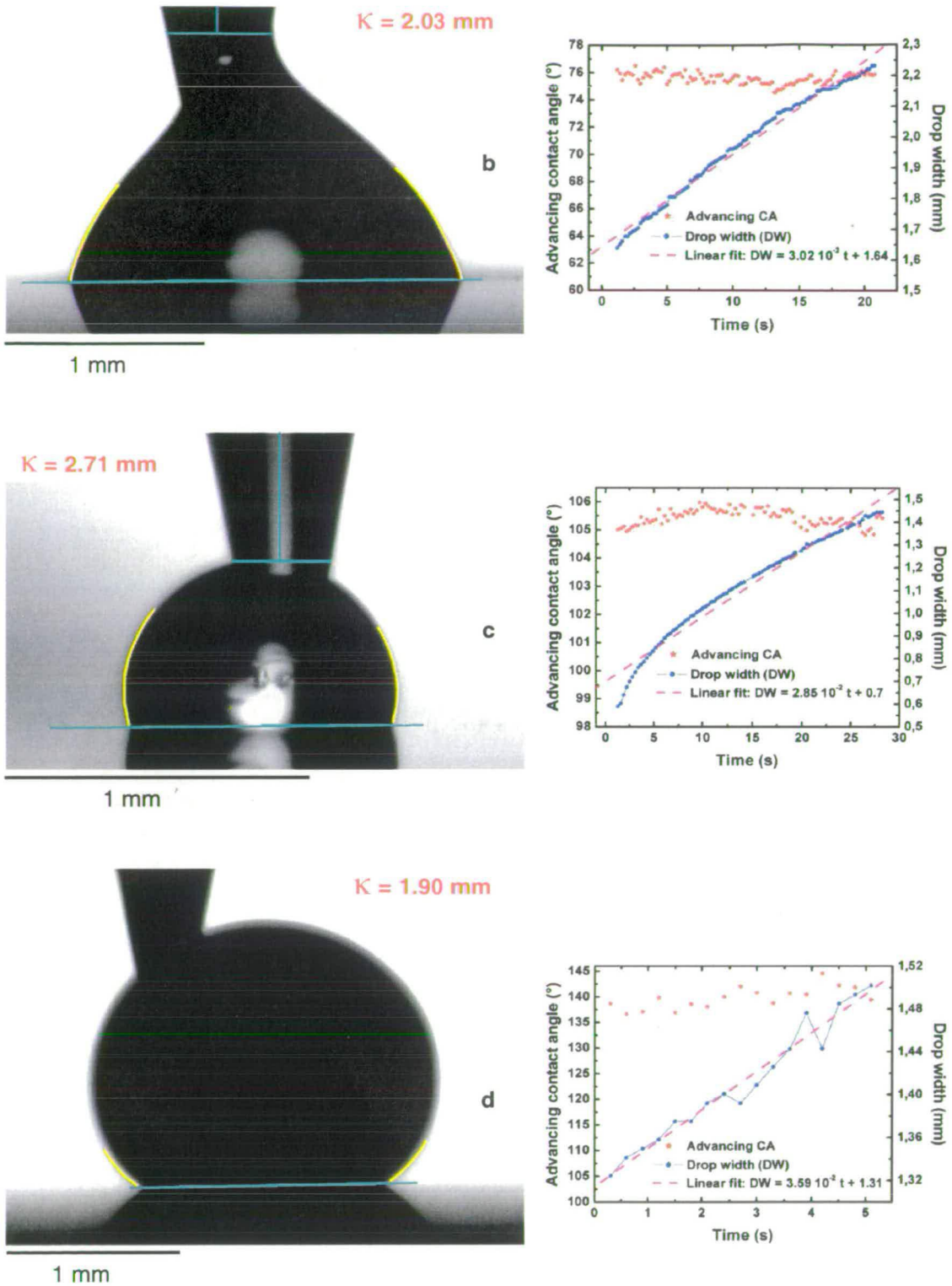
Fig. 5.3. (*continued*). Note the presence of a reflected image of the liquid drop, thanks to which the baseline (blue) can be precisely set. This is made easier by the lens looking down at an angle of about 3° so as to analyse drops placed on the surface away from an edge.

Hexadecane has the lowest surface tension of these probe liquids, it also has a high affinity for PDMS (see Table 3.2), which explains why it was not possible to keep the drop size below the capillary length limit as we did the other four liquids. Nevertheless the advancing contact angle of hexadecane on PDMS was quite constant, at any rate not less so than that made by the other three liquids on the same surface (see Fig. 5.3). The increase in drop width was regular and almost linear apart from the first 5 seconds after a drop touched the surface. No slip/stick behaviour was observed for DMSO as was reported by Kwok *et al.* [1998] on fluorocarbon coated silicon wafers. The hydrophobicity of this type of PDMS monolayers is probably not absolute because the advancing contact angle with water is about 105° (see Fig. 5.3 c), which is on the lower end of values reported elsewhere. Al-Maawali *et al.* [2001] for instance, indicate a 106° to 109° range for the advancing contact angle of water on an end-grafted PDMS monolayer (on silicon). Uilk *et al.* [2003] report advancing contact angles as high as 118° for cured PDMS networks used as coatings.

5.1.2. Contact angle goniometry study on Caro-cleaned Si wafers

Surface tension and wetting:

In this paragraph we report results of surface tension measurements in the sessile drop mode and make a selection of suitable probe liquids, considering that silicon oxide grown on silicon has a much higher surface tension than polymers in general and PDMS in particular. Chaudhury [1996] reports a critical surface tension (see § 2.1.3) of about 22 mJ m^{-2}. Reported values for amorphous silica vary widely: 220 mJ m^{-2} [Douillard *et al.*, 1995] for powder, 280 mJ m^{-2} for a polished glass sheet [Busscher *et al.*, 1986], 300 mJ m^{-2} for glass [Hetherington *et al.*, 1964] and finally 330 mJ m^{-2} for 'glass as determined by the pendant drop method at T = 2000 K [Mazurin *et al.*, 1983]. As for silicon, values of 1000 mJ m^{-2} are often proposed [Israelachvili, 1992] [Yaws, 1999], though Heck and van Horn [1953] have found 720 mJ m^{-2} for a pendant drop at T = 2000 K.

We present pictures of sessile drops of hexadecane, water and DMSO, three 'low-surface tension' liquids on Caro-cleaned silicon wafers in Fig. 5.4. Pictures of 'high surface-tension' liquids, namely mercury and a saturated solution of sodium chloride (26% wt of NaCl in deionised water) on the same substrates are presented in Fig. 5.5. This gives rise to a fluid of surface tension significantly higher than that of water: ~ 82.5 mJ m^{-2} [Lide, 1992].
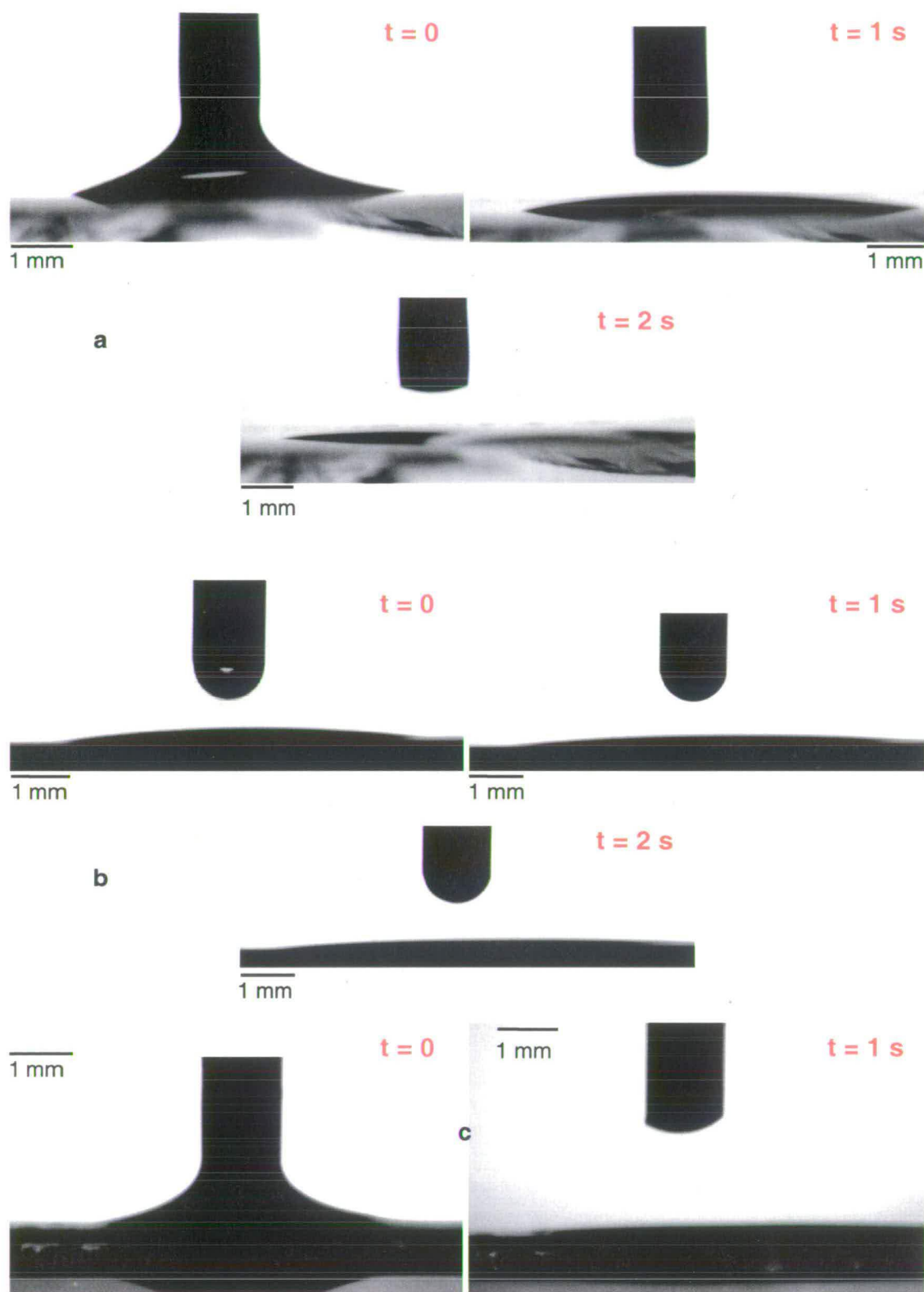
Fig. 5.4. Probe liquids wetting oxidised silicon wafers. a: hexadecane (borosilicate glass instead of silicon, identical result). b: water. c: DMSO.
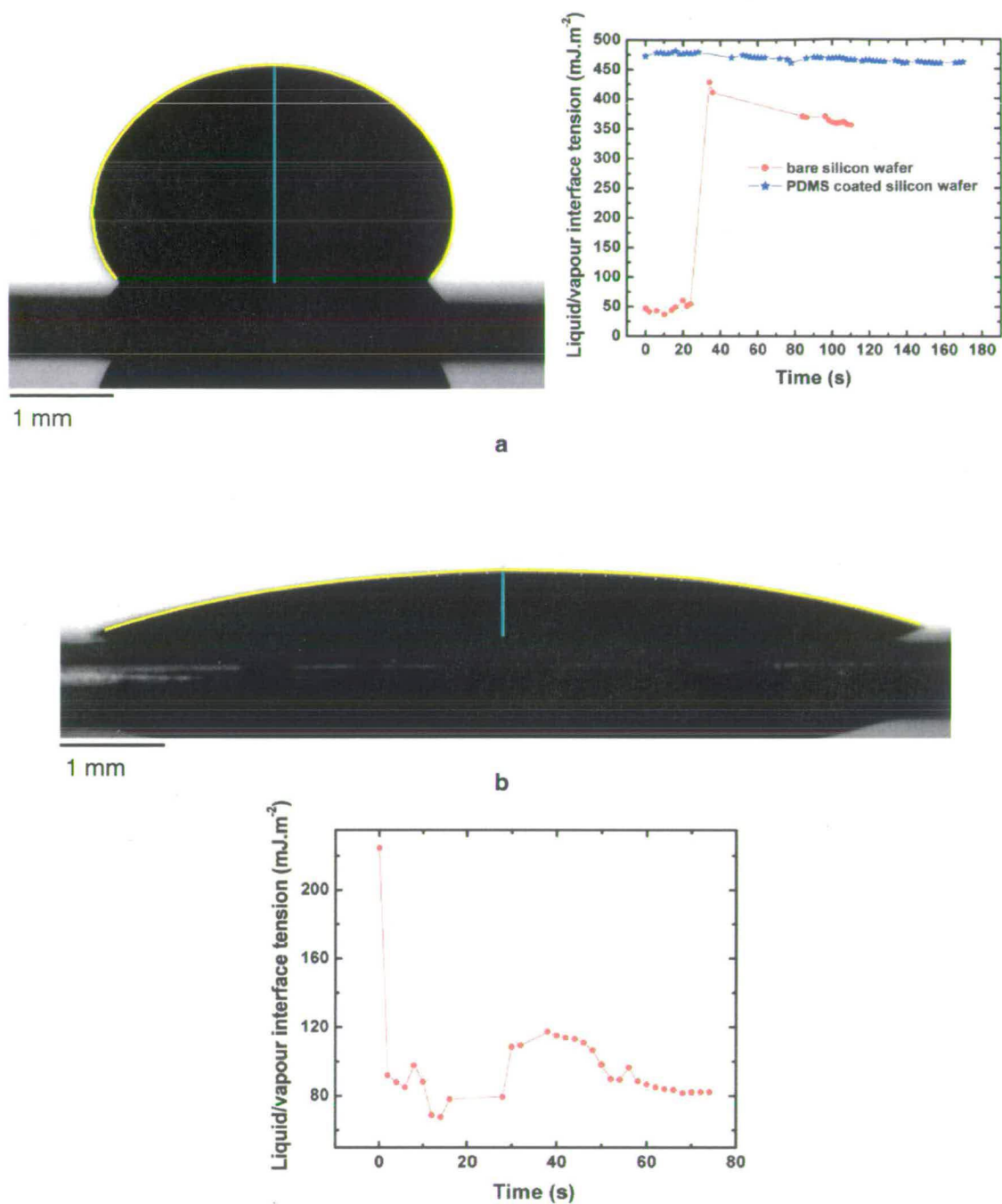
Fig. 5.5. Sessile drops of non-wetting probe liquids on silicon. Pictures and plots of liquid-vapour interface tension versus time ($\gamma_{LV}^{\cdot}$). a: mercury. b: saturated solution of NaCl. T = 21°C, RH = (52 ± 3) %.

Hexadecane, water and DMSO wet oxidised silicon and therefore cannot be used in surface energetics calculations (contact angle is essentially nil see Fig. 5.4). The question of

whether it is true, complete wetting or only partial wetting but with a contact angle so small (< 5°) that it cannot be measured reliably (hexadecane or borosilicate glass) is beyond the scope of this study. Likewise we will leave the complex issue of distinguishing between wetting in the form of a monomolecular film and what has been referred to as 'pancakes' [De Gennes, 1991] [Cazabat *et al.*, 1994].

Surface or interface-tension measurements by the sessile-drop method can only be given credit if the drop is big enough for the gravity effects to affect the drop shape more than surface tension effects do, as stated by the reformulated Young-Laplace law (see equations (5.1) and (5.2)). We observe that for both mercury and the solution of sodium chloride on a bare wafer, drops smaller than, say, 3 mm give rise to either much too low or much too large values (see Fig. 5.5 a and b). For mercury there seems to be two possible groups of values, one that corresponds to the minimum size for which the algorithm gives a sensible result ($\approx$ 425 mJ m^{-2}) and another one for the bigger drops where the curve seems to level off: 360 mJ m^{-2}. These values are significantly lower than the standard value of 485 mJ m^{-2} or than those obtained on a PDMS-coated wafer (see Fig. 5.5 a). However it has been reported that mercury could attract water vapour, which decreases its surface tension by as much as 50 mJ.m^{-2} at saturation pressure [Nicholas *et al.*, 1961]. Others propose a decrease of 25 mJ m^{-2} [Xu *et al.*, 1995]. Moreover our drops sit on a Caro-cleaned and therefore highly attractive substrate, which can bring about some extra adsorption. The measurements were performed in air and mercury was used without any chemical cleaning. It was only passed through a separating funnel to get rid of the visible oxide. Its intrinsic surface tension may then be smaller than the standard value, but certainly not as small as 360 mJ m^{-2}. Besides lack of axisymmetry in the drop can have a huge impact on the measured value [Kwok *et al.*, 1998] and it is very difficult to realise it while a measurement is being made as we only look at the drop from the side. The advantages of looking at a drop from the top to make sure that the roundness is satisfactory has been pointed out by Meiron *et al.* [2004]. Interestingly, the surface tension as measured on a PDMS-coated silicon wafer is in accordance with commonly accepted values. They tend to decrease though with the drop size increase and time in air. Values obtained for bigger drops (drop width $\approx$ 5 mm) are more reliable as the effect of gravity is more prominent and deforms them more (see Fig. 5.2 d). For surface energetics calculation, we will then consider that 460 mJ m^{-2} is the likeliest value for mercury in contact with a clean bare wafer. The surface tension of the solution of sodium chloride reaches a plateau (see Fig. 5.5 b) at drop sizes bigger than 6 mm. The changes in

surface tension values prior to reaching the plateau are probably related to the drop size being too small as mentioned above as well as a lack of axisymmetry (the drop deforms as more liquid is being pumped out) and possibly imperfect focus...and software. Unlike mercury, the saturated solution of sodium chloride exhibits the expected surface tension ($\approx$ 82 mJ m^{-2}) for drops of a size corresponding to good measurement conditions. This means that contamination by hydrocarbons or water vapour is negligible, which is essential. Regarding water it is not surprising that it does not affect the surface tension of a solution whose solvent is water (2.4 molecules of water per ion of sodium of chloride) and therefore is surrounded by its own water vapour. Since contamination by hydrocarbons can safely be ruled out, it is likely that the main reason the measured surface tension of mercury drops of a suitable size is smaller than the expected value is that water adsorption occurs [Nicholas *et al.*, 1961]. We can even suppose that on as hydrophilic a surface as Caro-cleaned oxidised silicon (water wets it, see Fig. 5.4 b), a mercury drop accumulates more vapour at the contact region. This region is where contact angles and to a lesser degree surface tensions are being measured.

Contact angles (dynamic and static):

Advancing and static contact angle measurements were also taken for the same two probe liquids on the same material (silicon). The results are presented in Fig. 5.6.
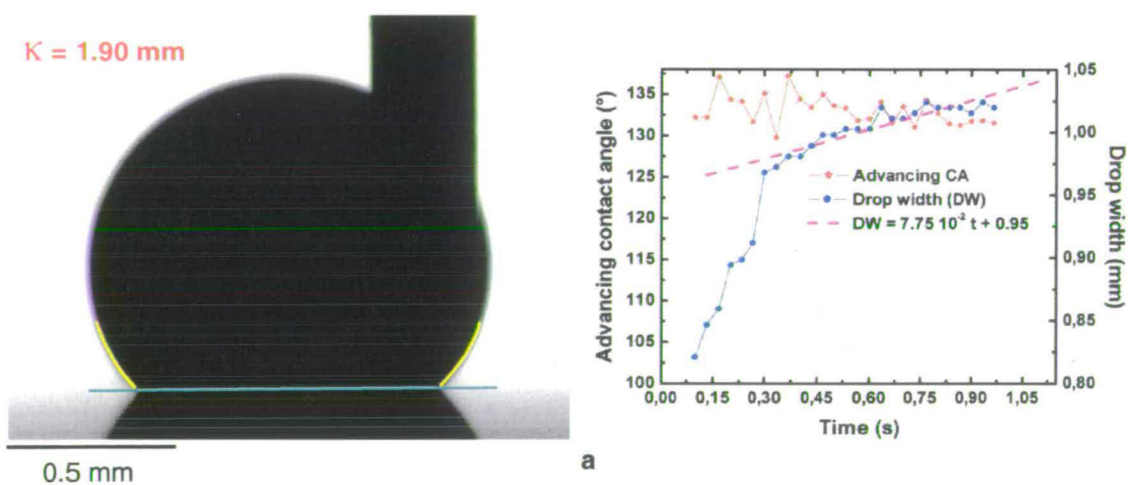

Fig. 5.6. Advancing (θ_{adv}) and static (θ_{stat}) CA of mercury and NaCl$_{aq}$ on oxidised silicon (2σ). Angles and drop size plotted against time. a: mercury: θ_{adv} = (132.2 ± 2.1)°, rate $\cong$ 4.7 mm/min. b: NaCl$_{aq}$: θ_{adv} not stabilised (rate $\cong$ 22.1 mm/min). c: NaCl$_{aq}$: non spherical fit, θ_{stat} = (18 ± 1)°. d: NaCl$_{aq}$: spherical fit, θ_{stat} = 17°. T = 21°C, RH = (52 ± 3) %.

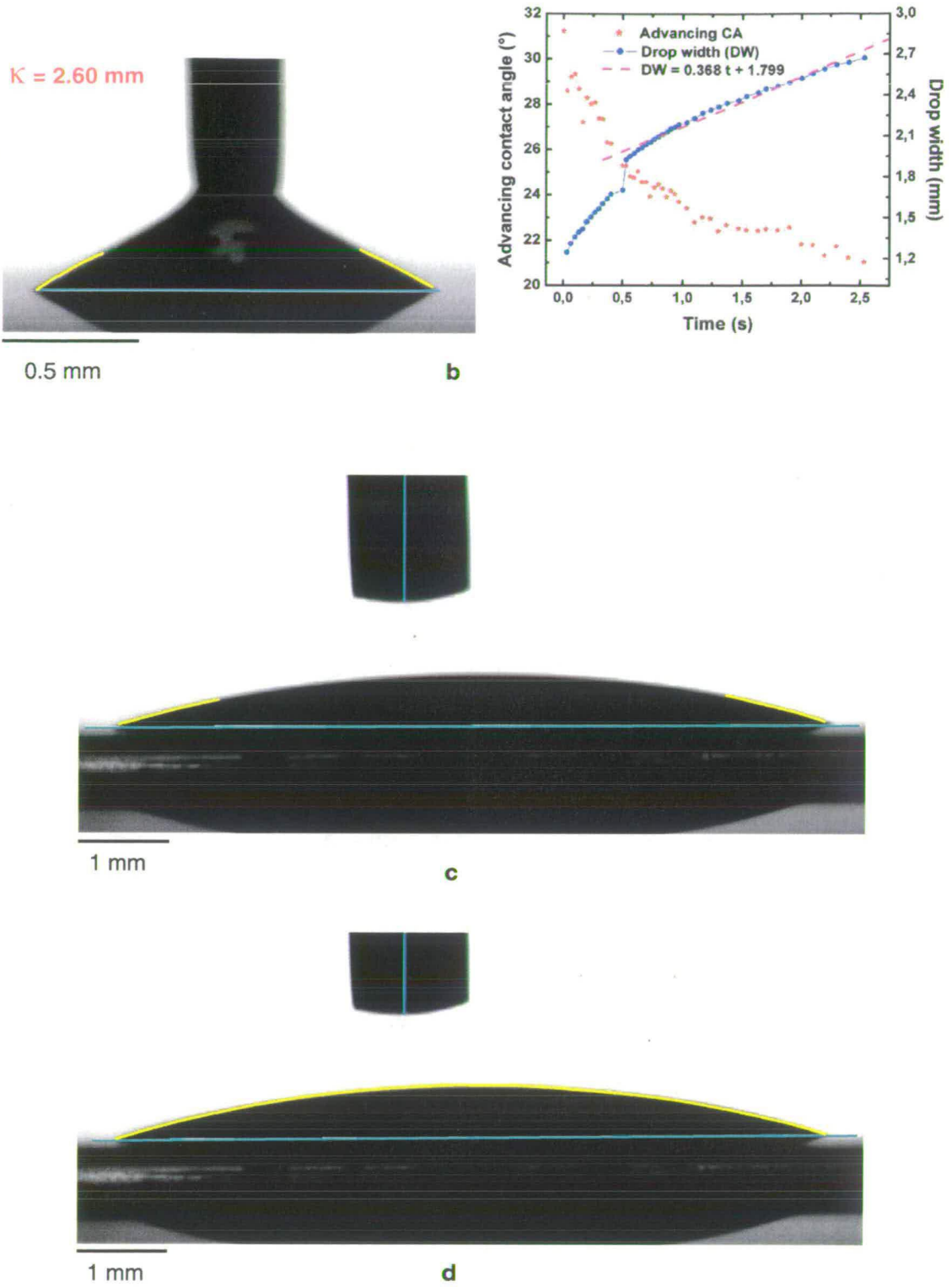K = 2.60 mm

0.5 mm

b

1 mm

c

1 mm

d

Fig. 5.6. (*continued*).

The advancing contact angle of mercury is roughly constant at a rate of about 5 mm/min (see Fig. 5.6 a) but the first tenths of second are characterised by an abnormally fast advancing rate: $\approx$ 80 mm/min. It is noteworthy that this region corresponds to oscillating contact angles. It is possible that this phenomenon is related to the physical properties of mercury (density, surface tension) that make the advancing flow rate of which difficult to control. Yet we thought that changing the needle shape from a conical capillary with unwanted pressure build up at the tip apex to a straight cylindrical-shaped needle would solve such problems (see Fig. 5.3 d and Fig. 5.6 a). Despite this artefact, reliable and constant advancing contact angle values are available at t > 0.6 s and there is a plateau at t > 0.9 s. The corresponding advancing contact angle is 132°.

The saturated solution of NaCl exhibits a strange behaviour as its advancing contact angle keeps decreasing (from 31° to 21°) and never reaches a constant value, at least for drops smaller than 3 mm (see Fig. 5.6 b). Although the advancing rate of 22 mm/min is significantly higher than the recommended slow rate limit of 1 mm/min [Lam et al., 2002], we think that this instability or rather 'out of equilibrium behaviour' has another origin. When in contact with air a solution of NaCl is probably subject to ion migration from the surface inward so as to minimise the interface energy. However our solution is saturated: 2.4 molecules of water per sodium or chloride ion, which means that the surface cannot probably be easily depleted of ions. The question is then as follows: is the first (maximum) contact angle recorded the relevant Young's contact angle for the solution-wafer interface or is it an hypothetical contact angle at equilibrium? The answer to that question is not obvious. We therefore processed frames initially taken with the purpose of measuring the interface tension and estimated the static contact angle (see Fig. 5.6 c and d). The chosen drop of sodium chloride solution gave rise to a surface tension that compared favourably with expected values (Fig. 5.5 b) and had more than 70 s to equilibrate, one can therefore consider that a static contact angle measured on such a drop is physically meaningful and can be used in surface energetics calculations [Cherry & El Muddaris, 1970]. Irrespective of the mathematical form of the curve fitting the drop profile (spherical or not), the contact angle is close to 18°. One can assume that this is the constant, equilibrium contact angle that one would have obtained if the run had lasted longer (see Fig. 5.6 b).

5.1.3. STC numerical analysis of PDMS monolayers and oxidised Si

PDMS monolayers:

We propose to use a surface tension component theory or semi-empirical model developed by van Oss *et al.* [1989] and later modified by Lee [1996] [2001] to work out the surface tension components of PDMS-coated oxidised silicon wafer and bare silicon wafer. For further details about these models and the associated (simple) mathematics the reader is referred to § 2.1.3. A too often overlooked and yet essential parameter to be included in any surface energetics equation is the film pressure of vapour on a solid and sometimes on a probe liquid. We showed in § 2.1.3 that it was a combination of two terms (see equations (2.24) and (2.33)): $\pi_{esv} + \pi_{elv}$. The experimentally easiest way of estimating it, has been proposed by Bellon-Fontaine and Cerf [1990]. It is based on the measurement of the contact angle that a mercury drop makes on a solid surface. In Fig. 5.7 we compare the work of adhesion between each of the four probe liquids and a PDMS coated silicon wafer, in equilibrium with a vapour (see equations (2.22) and (2.24)).
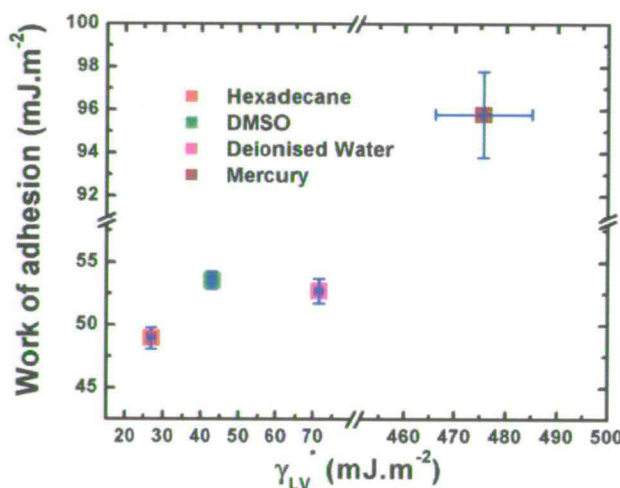

Fig. 5.7. Work of adhesion of hexadecane, DMSO, deionised water and mercury with a PDMS-coated, oxidised silicon wafer.

Bellon-Fontaine and Cerf [1990] use the work of adhesion between mercury and the solid as the maximum work of adhesion (no mercury vapour adsorbed) and then subtract the work of adhesion of another liquid with the same solid to determine the amount of vapour

adsorbed. Doing this we get over 40 mJ m^{-2} for each of the other three liquids, which seems far too high a number. The reliable measurement of contact angles higher than 130°-135° is doubtful with our data processing software, especially in conditions where the focus in not perfect. We have noticed a tendency of the software to underestimate such large angles in automatic mode. Mercury drops on low surface energy materials like PDMS fall in that category (see Fig. 5.3 d). The work of adhesion being a function of $\cos\theta$, any underestimation of large angles will lead to an overestimation of the work of adhesion. We will therefore ignore the mercury case for the present and focus on the other three liquids. DMSO gives rise to the second largest work of adhesion therefore we set the maximum work of adhesion to be that of DMSO with PDMS-coated oxidised silicon. We justify this choice by the fact that DMSO is a strong Lewis base (see § 2.1.3) with its oxygen atom linked to a sulfur atom through a double bond and no methyl groups around it to create unfavourable steric effect as is the case for PDMS. Thus a strong base interacting with a low critical surface tension [Chaudhury, 1996] and potentially basic material like PDMS is not likely to bring about any adsorption of DMSO vapour. Hexadecane seems to give rise a work of adhesion 3 to 4 mJ m^{-2} lower than the 'maximum' work of adhesion (no adsorbed vapour). We deduce that hexadecane does adsorb onto the surface as was also pointed out by Bellon-Fontaine and Cerf [1990] for most alkanes and other low surface tension liquids on PTFE and polypropylene (PP) sheets. On the other hand, Good [1993] reported calculations showing that the film pressure of hexadecane on PTFE is negligible, partly because of the low saturation pressure of this alkane ($P_{sat} \approx 9.10^{-4}$ mm Hg). The saturation pressure of mercury is $P_{sat} \approx 10^{-3}$ mm Hg.

In order to estimate the surface tension components of PDMS-coated oxidised silicon we will have to solve a system of three equations of the equation (2.33) type (one for each probe liquid) with three unknowns (γ^{LW} or γ^d, γ^- and γ^+)[1]. Although one can use matrix calculus to solve it [Gindl et al., 2001] [Della Volpe et al., 1998], we found it simpler to employ a two-stepped process. We first solve equation (2.33) for hexadecane. It is a purely dispersive liquid therefore $\gamma^-_{Hexa} = \gamma^+_{Hexa} = 0$, which simplifies greatly equation (2.33).

---

[1] We treat γ^{LW} and γ^d as if they were the same quantity since there is no way of distinguishing between van der Waals components.

After some algebra we obtain:

$$\gamma_{"PDMS"}^{LW(d)} = \left[\frac{\gamma_{Hexa/"PDMS"}^{*}(1+\cos\theta_{Hexa/"PDMS"}) + \pi_{Hexa/"PDMS"}^{Total}}{2\sqrt{\gamma_{Hexa}^{LW(d)}}} \right]^2 \qquad (5.3)$$

That leaves us, with a simple system of two equations with two unknowns. Eliminating either $\gamma_{"PDMS"}^{-}$ or $\gamma_{"PDMS"}^{+}$ in one of the two equations enables us to isolate one parameter, say $\gamma_{"PDMS"}^{-}$. Its mathematical expression is of the type:

$$\sqrt{\gamma_{"PDMS"}^{-}} = \frac{A - B}{C} \qquad (5.4)$$

$$A = \frac{\left[\gamma_{Water/"PDMS"}^{*}(1+\cos\theta_{DMSO/"PDMS"}) + \pi_{Water/"PDMS"}^{Total}\right]}{2} - \sqrt{\gamma_{"PDMS"}^{LW(d)}\gamma_{Water}^{LW(d)}}$$

$$B = \sqrt{\frac{\gamma_{Water}^{-}}{\gamma_{DMSO}^{-}}} \left\{ \frac{\left[\gamma_{DMSO/"PDMS"}^{*}(1+\cos\theta_{DMSO/"PDMS"}) + \pi_{DMSO/"PDMS"}^{Total}\right]}{2} - \sqrt{\gamma_{"PDMS"}^{LW(d)}\gamma_{DMSO}^{LW(d)}} \right\}$$

$$C = \sqrt{\gamma_{Water}^{+}} - \frac{\sqrt{\gamma_{Water}^{-}}\sqrt{\gamma_{DMSO}^{+}}}{\sqrt{\gamma_{DMSO}^{-}}}$$

The acidic component $\gamma_{"PDMS"}^{+}$ is then easily obtained by substituting the newly calculated parameters into equation (2.33) for water or DMSO. If DMSO values are chosen because of the confidence we have in the experimental results (see § 5.1.1) the equation becomes:

$$\sqrt{\gamma_{"PDMS"}^{+}} = \frac{1/2\left[\gamma_{DMSO/"PDMS"}^{*}(1+\cos\theta_{DMSO/"PDMS"}) + \pi_{DMSO/"PDMS"}^{Total}\right] - \sqrt{\gamma_{"PDMS"}^{LW(d)}\gamma_{DMSO}^{LW(d)}} - \sqrt{\gamma_{"PDMS"}^{-}\gamma_{DMSO}^{+}}}{\sqrt{\gamma_{DMSO}^{-}}}$$

$$(5.5)$$

We present in Table 5.1 the surface tension components of PDMS-coated oxidised silicon as calculated using Lee's initial surface tension components [2001] and assuming that:

- the film pressure of DMSO and water vapour on the surface is nil (maximum work of adhesion),

- the film pressure of hexadecane vapour ranges from 0 to 4 mJ.m^{-2}.

Likewise in Table 5.2 we present similar results for the classic vOCG parameters [van Oss *et al.*, 1989].

$\pi_{Hexa/"PDMS"}$ mJ m^{-2}	$\gamma_{"PDMS"}^{LW(d)}$ mJ m^{-2}	$\sqrt{\gamma_{"PDMS"}^{-}}$ (mJ m^{-2})$^{1/2}$	$\sqrt{\gamma_{"PDMS"}^{+}}$ (mJ m^{-2})$^{1/2}$	$\gamma_{"PDMS"}^{-}$ mJ m^{-2}	$\gamma_{"PDMS"}^{+}$ mJ m^{-2}	$\gamma_{"PDMS"}^{ab}$ mJ m^{-2}	$\gamma_{"PDMS"}^{Total}$ mJ m^{-2}
0	22.19	0.71	0.08	0.50	0.006	0.11	22.30
1	23.10	0.70	-0.02	0.49	0.0004	-0.03	23.07
2	24.02	0.70	-0.11	0.48	0.01	-0.16	23.86
3	24.97	0.69	-0.21	0.48	0.04	-0.29	24.68
4	25.93	0.69	-0.31	0.47	0.09	-0.42	25.51

Table 5.1 Surface tension components of an oxidised silicon surface coated with a PDMS monolayer (Lee's scale and parameters [Lee, 2001]). For each liquid, the surface tension and (advancing) contact angle used in equations (5.3) through (5.5) were: hexadecane: $\theta = 37.2°$, $\gamma_{LV} = 27.5$ mJ m^{-2}; DMSO: $\theta = 75.6°$, $\gamma_{LV} = 42.4$ mJ m^{-2}; deionised water: $\theta = 105.5°$, $\gamma_{LV} = 72.5$ mJ m^{-2}. Total surface tensions and surface tension components were corrected for temperature T = (21 ± 0.5)°C by linear interpolation.

$\pi_{Hexa/"PDMS"}$ mJ m^{-2}	$\gamma_{"PDMS"}^{LW(d)}$ mJ m^{-2}	$\sqrt{\gamma_{"PDMS"}^{-}}$ (mJ m^{-2})$^{1/2}$	$\sqrt{\gamma_{"PDMS"}^{+}}$ (mJ m^{-2})$^{1/2}$	$\gamma_{"PDMS"}^{-}$ mJ m^{-2}	$\gamma_{"PDMS"}^{+}$ mJ m^{-2}	$\gamma_{"PDMS"}^{ab}$ mJ m^{-2}	$\gamma_{"PDMS"}^{Total}$ mJ m^{-2}
0	22.19	1.31	-0.37	1.71	0.14	-0.97	21.22
1	23.10	1.32	-0.47	1.75	0.22	-1.26	21.84
2	24.02	1.34	-0.57	1.79	0.33	-1.54	22.48
3	24.97	1.35	-0.67	1.83	0.46	-1.84	23.13
4	25.93	1.37	-0.78	1.87	0.61	-2.13	23.80

Table 5.2 Surface tension components of an oxidised silicon surface coated with a PDMS monolayer (vOCG scale [van Oss *et al.*, 1989]). For each liquid, the surface tension and (advancing) contact angle used in equations (5.3) through (5.5) were: hexadecane: $\theta = 37.2°$, $\gamma_{LV} = 27.5$ mJ m^{-2}; DMSO: $\theta = 75.6°$, $\gamma_{LV} = 42.4$ mJ m^{-2}; deionised water: $\theta = 105.5°$, $\gamma_{LV} = 72.5$ mJ m^{-2}. Total surface tensions and surface tension components were corrected for temperature T = (21 ± 0.5)°C by linear interpolation.

It is not surprising that both scales give the same LW or dispersion component for PDMS-coated oxidised silicon as Lee's modifications apply essentially to acid-base components. The basic or H-bond accepting component is highly dependent of the chosen scale: using vOCG gives rise to basic components about 4 times as high as those obtained with Lee's parameters. This illustrates the well-known tendency of vOCG to skew values towards basicity. The problem of negative square roots for acidic components so often pointed out by workers in the field of surface energetics [Della Volpe *et al.*, 1997] [Good *et al.*, 1991] [Good, 1993] is not completely solved by using Lee's components but the magnitude of these 'artefacts' is lowered. The resulting acid-base component is therefore less negative and the total surface tension less altered. Good *et al.* [1991] envisaged a physical meaning behind these negative square roots which we will present later.

The consequence of the presence of a film pressure is to increase the LW or dispersion component, the acidic (negative) component and the total surface tension. This can be interpreted as the fact that liquid drops not only interact with PDMS but also with some of the substrate that is supposed to be acidic. The increase in surface tension is nevertheless low (15% at the most) so that PDMS is the main contributor. Interestingly, in the Lee scale when the film pressure equals zero the surface tension is comparable to the critical surface tension value of 22 mJ m^{-2} mentioned by Chaudhury [1996]. The surface is mainly dispersive with only a 2% basic character, negligible acidic character and all parameters are positive. It is noteworthy that Lee has defined his initial surface tension components as parameters corresponding to a surface in equilibrium with its own vapour (or vacuum). In other words using the initial components leads to the determination of the intrinsic surface tension of a substance. Furthermore it has been suggested that PDMS was almost purely dispersive because of the presence of methyl groups CH_3 screening the potentially hydrophilic (basic in this sense) oxygen atoms of its backbone [Chaudhury, 1996]. We conclude that Lee's scale is a more exact scale than the vOCG scale, at least for describing this type of materials.

The negative square root issue deserves a few comments as it applies to our interest for adhesion. As mentioned above, Good *et al.* [1991] suggest that a negative square root of γ_s^+ may not be a purely mathematical artefact. First of all, it does not necessarily bring about a negative γ_s (which would mean that the solid is not stable) as we can see for all cases in

Table 5.1 and Table 5.2. Secondly, they envisage that a negative square root of γ_s^+ resulting in a negative γ_{sl} (see equation (2.34 bis)) can actually favour adhesion because:

- it would help make ΔG_{sl}^a more negative, that is a stronger attraction between the two phases (see equation (2.22)),

- in the case of a liquid adhesive applied on a solid surface, a larger driving force would make particles of the adhesive go into pores and cavities than would be the case with a positive γ_{sl}. Therefore they will penetrate faster and in a more homogeneous way.

Oxidised silicon (SiO$_2$/Si):

Unlike PDMS-coated oxidised silicon, most common probe liquids wet bare oxidised silicon, therefore we had to turn to more unusual liquids to investigate this high surface tension material. In § 5.1.2 we showed that both mercury and saturated sodium chloride could be used as probe liquids since they form a drop on even a freshly Caro-cleaned surface. Mercury is usually considered as a liquid able to develop metallic and dispersive or more generally Lifshitz-van der Waals interactions with a solid surface [Carré & Visovsky, 1998] [Chaudhury, 1996]. A recent experimental study proved that the acid-base interactions of such a liquid are negligible [Xu et al., 1995]. Within the framework of vOCG or Lee, the surface tension of mercury can therefore be defined as:

$$\gamma_{Hg} = \gamma_{Hg}^{metal} + \gamma_{Hg}^{LW(d)} \qquad (5.6).$$

where $\gamma_{Hg}^{metal} \cong 284$ mJ m^{-2} [Chaudhury, 1996] and $\gamma_{Hg}^{LW(d)} = (200 \pm 7)$ mJ m^{-2} [Fowkes, 1964]. We will take $\gamma_{Hg}^{LW(d)} = 200$ mJ m^{-2} as suggested by Chaudhury [1996]. Given that mercury cannot possibly develop metallic interactions with p-doped elemental silicon because it is buried beneath a ~ 1 nm thick oxide layer and the range of metallic interactions does not go beyond 0.3 nm [Gutowski, 1991]. We then expect mercury to behave as a 'superalkane' in that it develops the same type of interactions as alkanes with insulating solid surfaces but with so high a surface tension that it always makes drops. Therefore we have our dispersive or LW liquid that will play the same role towards oxidised silicon as

hexadecane did towards PDMS-coated oxidised silicon with the benefit of being almost certain that there is no film pressure related to the presence of mercury [Carré & Visovsky, 1998] [Bellon-Fontaine & Cerf, 1990].

Adding sodium chloride to pure water has the effect of raising the surface tension of the liquid by as much as 10 mJ m^{-2} if the concentration of the solute reaches saturation [Lide, 1992]. This is what we have verified experimentally (see Fig. 5.5 b). Now the problem is to identify the surface tension components of such a solution. Assuming that the acid-base properties of the solution will be governed only by water since Cl^{-} and Na^{+} are not bound to contribute anything in that regard, the LW component must be the sum of water's contribution and that of the solute. On top of that, solvation forces between the solvent and the solute (ion-dipole interactions) and electrostatic forces between Cl^{-} and Na^{+} (ion-ion) play a role in the increased cohesion of the system (solution). These forces are long-range as presented in § 2.1.1. We propose a simple model supposing additivity of surface tension components that makes such a binary liquid usable as a probe liquid in the vOCG-Lee framework.

The total surface tension of a saturated sodium chloride solution, from now onwards referred to as NaCl$_{aq}$, can be expressed as:

$$\gamma_{NaClaq} = \gamma_{Water}^{LW(d)} + \gamma_{"NaCl"}^{LW(d)} + 2\sqrt{\gamma_{Water}^{+}\gamma_{Water}^{-}} + \gamma_{NaClaq}^{solvation} + \gamma_{NaClaq}^{electrostatic} \qquad (5.7),$$

where $\gamma_{"NaCl"}^{LW(d)}$ is the vDW contribution to the surface tension due to dissolved sodium chloride, the magnitude of which is probably far smaller than it is in a crystal form. The last two terms $\gamma_{NaClaq}^{solvation}$ and $\gamma_{NaClaq}^{electrostatic}$ contribute only to cohesion and are not involved in adhesion phenomena if the interacting solid surface is charge-free.

We propose that the excess of surface tension relative to pure water be shared equally between the LW component and the strictly cohesive solvation and electrostatic terms, so that the surface tension components of NaCl$_{aq}$ relevant to adhesion phenomena can be written:

$$\gamma_{NaClaq}^{LW(d)} = \gamma_{Water}^{LW(d)} + \frac{\gamma_{NaClaq}^{Total} - \gamma_{Water}^{Total}}{2} \qquad (5.8)$$

$$\gamma_{NaClaq}^{ab} = \gamma_{Water}^{ab} \qquad (5.9)$$

We will then consider this solution of saturated sodium chloride as our acidic probe liquid. It will play the same role with respect to oxidised silicon as water did with respect to PDMS-coated oxidised silicon. Unlike the case of mercury, one cannot assume that the film pressure of $NaCl_{aq}$ vapour (actually water) is negligible. As a matter of fact, the vapour pressure of a solution obeys Raoult's law as long as it is very dilute. This law stipulates that the vapour pressure of a solution, at a given temperature is equal to that of the pure solvent multiplied by its mole fraction. For a saturated solution, this simple law is not verified. The vapour pressure above a saturated solution of sodium chloride, expressed in terms of relative humidity (RH) is close to 76%. At 20°C, an exact figure is RH = (75.47 ± 0.14) % [Lide, 2001]. This important piece of information will be used later.

The procedure to calculate the LW or dispersive component of the surface tension of oxidised silicon (SiO_x) is exactly the same as the one used in the previous case, substituting mercury parameters for hexadecane ones. One gets:

$$\gamma_{SiOx}^{LW(d)} = \left[\frac{\gamma_{Hg/SiOx}^{*}\left(1+\cos\theta_{Hg/SiOx}\right)+\pi_{Hg/SiOx}^{Total}}{2\sqrt{\gamma_{Hg}^{LW(d)}}}\right]^2 \qquad (5.10)$$

The presence of a film pressure term should not surprise the reader as the experiment being carried out in air there is at least some water vapour always able to adsorb (RH ≈ 55%) even if mercury does not. We will suppose that it ranges from 0 to 20 mJ m^{-2} at this relative humidity, according to the work by Busscher et al. [1986] for glass.

Since we have only one more probe liquid, we cannot simply solve a system of two equations of type (2.33) with two unknowns. Instead, as a first step, we will try and determine the total surface tension of SiOx using the one-liquid method proposed by Helmy et al. [2003] (see § 2.1.3). Combining equation (2.43) and Young's equation (2.19) in its most generic form (including film pressure) and taking for probe liquid mercury we get:

$$k = \frac{\gamma_{SiOx} + \gamma_{Hg}}{\gamma_{SiOx} - \gamma_{Hg/SiOx}^{*}\cos\theta_{Hg/SiOx} - \pi_{Hg/SiOx}^{Total}} \qquad (5.11).$$

By varying γ_{SiOx} within a range of values where the actual surface tension is located, for instance 100 mJ m^{-2} to 1000 mJ m^{-2} for oxidised silicon we get a number of points for the

following function: $k = f\left(\gamma_{SiOx}\right)$. This set of calculated datapoints can then be fitted with a polynomial of the fourth order in γ_s of the type:

$$k = a_0 + a_1\gamma_{SiOx} + a_2\gamma_{SiOx}^2 + a_3\gamma_{SiOx}^3 + a_4\gamma_{SiOx}^4 \qquad (5.12)$$

Once the a_i coefficients are obtained, one can equate equation (5.11) and (5.12), eliminate k and solve for γ_{SiOx}. We use a simple graphical method to determine the value of γ_{SiOx}. From this we deduce the acid-base component of the surface tension of SiOx:

$$\gamma_{SiOx}^{ab} = \gamma_{SiOx} - \gamma_{SiOx}^{LW(d)} \qquad (5.13).$$

It is then possible to express the acidic component of the surface tension as a function of the basic component and of the acid-base component using equation (2.38):

$$\sqrt{\gamma_{SiOx}^+} = \frac{\gamma_{SiOx}^{ab}}{2\sqrt{\gamma_{SiOx}^-}} \qquad (5.14).$$

Substituting in an equation of the (2.33) type for $NaCl_{aq}$ we get:

$$\frac{\gamma_{NaClaq/SiOx}^*\left(1+\cos\theta_{NaClaq/SiOx}\right)+\pi_{NaClaq/SiOx}^{Total}}{2} - \sqrt{\gamma_{SiOx}^{LW(d)}\gamma_{NaClaq}^{LW(d)}} = \frac{\gamma_{SiOx}^{ab}\sqrt{\gamma_{NaClaq}^-}}{2\sqrt{\gamma_{SiOx}^-}} + \sqrt{\gamma_{SiOx}^-}\sqrt{\gamma_{NaClaq}^+} \qquad (5.15)$$

After rearranging equation (5.15) and raising $\sqrt{\gamma_{SiOx}^-}$ to the power 2, we obtain another equation of the second order in γ_{SiOx}^-:

$$\gamma_{SiOx}^{-2} + \left(\frac{2B'C' - A'^2}{C'^2}\right)\gamma_{SiOx}^- + \frac{B'^2}{C'^2} = 0 \qquad (5.16),$$

where $A' = \dfrac{\gamma_{NaClaq/SiOx}^*\left(1+\cos\theta_{NaClaq/SiOx}\right)+\pi_{NaClaq/SiOx}^{Total}}{2} - \sqrt{\gamma_{SiOx}^{LW(d)}\gamma_{NaClaq}^{LW(d)}}$, $B' = \gamma_{SiOx}^{ab}\sqrt{\gamma_{NaClaq}^-}$

and $C' = \sqrt{\gamma_{NaClaq}^+}$

The solutions of this second order equation are:

$$\gamma_{SiOx,1}^{-} = \frac{\dfrac{A'^2 - 2B'C'}{C'^2} - \sqrt{\Delta}}{2} \quad \text{and} \quad \gamma_{SiOx,2}^{-} = \frac{\dfrac{A'^2 - 2B'C'}{C'^2} + \sqrt{\Delta}}{2} \tag{5.17},$$

where $\Delta = \left(\dfrac{2B'C' - A'^2}{C'^2} \right)^2 - \dfrac{4B'^2}{C'^2}$.

The acidic components of the surface tension are easily obtained from equation (2.38) and (5.17):

$$\gamma_{SiOx,1}^{+} = \frac{\gamma_{SiOx}^{ab^{\,2}}}{4\gamma_{SiOx,1}^{-}} \quad \text{and} \quad \gamma_{SiOx,2}^{+} = \frac{\gamma_{SiO_x}^{ab^{\,2}}}{4\gamma_{SiOx,2}^{-}} \tag{5.18}$$

We present in Fig. 5.8 the graphical methods used to determine the total surface tension of oxidised silicon.
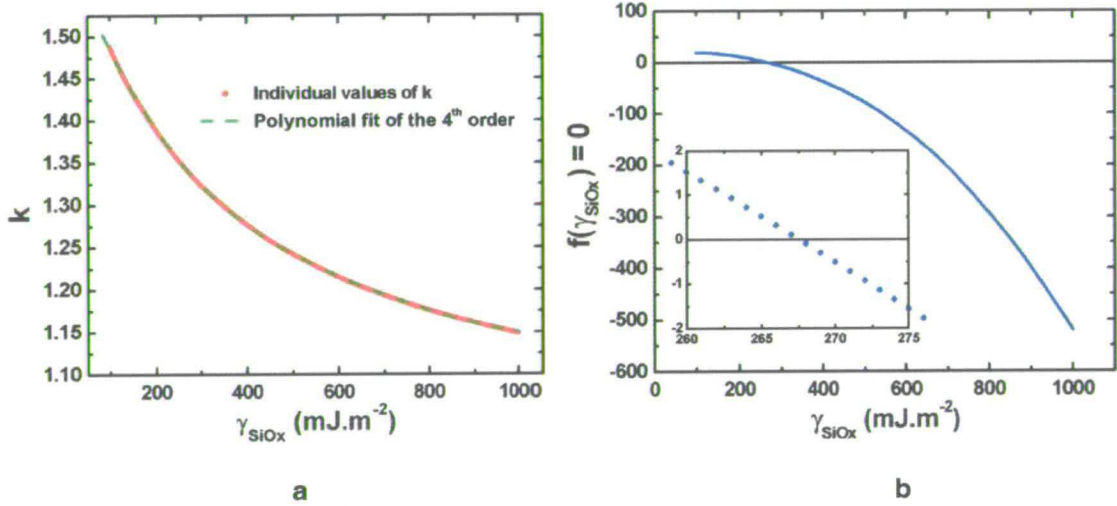

Fig. 5.8. Determination of the total surface tension of oxidised silicon (γ_{Hg} = 485 mJ m^{-2}, $\dot{\gamma}_{Hg/SiOx}$ = 460 mJ m^{-2}, $\theta_{Hg/SiOx}$ = 132°, $\pi^{Total}_{Hg/SiOx}$ = 15 mJ m^{-2}). a: plot of parameter k as a function of γ_{SiOx}. The polynomial fit gives the coefficients of equation (5.12): a_0 = 1.6194, a_1 = -1.6.10^{-3}, a_2 = 2.10^{-6}, a_3 = -2.10^{-9}, a_4 = 7.10^{-13}. B: graphical solution to the equation of 5th order in γ_{SiOx}: $f(\gamma_{SiOx})$ = 0. The solution is: γ_{SiOx} ≈ 268 mJ m^{-2}.

The surface tension components of oxidised silicon obtained from a variety of mercury surface tension and (essentially water) film pressure conditions are gathered in Table 5.3.

Lee's scale

$\gamma^{*}_{Hg/SiOx}$ mJ m⁻²	$\pi^{Total}_{Hg/SiOx}$ mJ m⁻²	γ_{SiOx} mJ m⁻²	$\gamma^{LW(d)}_{SiOx}$ mJ m⁻²	γ^{ab}_{SiOx} mJ m⁻²	$\pi^{Total}_{NaClaq/SiOx}$ mJ m⁻²	$\gamma^{-}_{SiOx,1}$ mJ m⁻²	$\gamma^{+}_{SiOx,1}$ mJ m⁻²	$\gamma^{-}_{SiOx,2}$ mJ m⁻²	$\gamma^{+}_{SiOx,2}$ mJ m⁻²
460	0	247	29	218	**107**	**68**	**175**	97	122
460	0	247	29	218	141	26	455	253	47
460	10	262	33	229	**116**	**71**	**185**	103	128
460	10	262	33	229	141	32	406	225	58
460	15	268	35	233	*119*	*79*	*172*	*96*	*142*
460	15	268	35	233	141	35	383	213	64
425	10	269	33	236	119	75	**186**	104	135
425	10	269	33	236	141	36	391	217	64
485	20	393	41	352	174	117	264	147	211

vOCG scale

$\gamma^{*}_{Hg/SiOx}$ mJ m⁻²	$\pi^{Total}_{Hg/SiOx}$ mJ m⁻²	γ_{SiOx} mJ m⁻²	$\gamma^{LW(d)}_{SiOx}$ mJ m⁻²	γ^{ab}_{SiOx} mJ m⁻²	$\pi^{Total}_{NaClaq/SiOx}$ mJ m⁻²	$\gamma^{-}_{SiOx,1}$ mJ m⁻²	$\gamma^{+}_{SiOx,1}$ mJ m⁻²	$\gamma^{-}_{SiOx,2}$ mJ m⁻²	$\gamma^{+}_{SiOx,2}$ mJ m⁻²
460	0	247	29	218	107	91	130	130	91
460	0	247	29	218	141	35	339	339	35
460	10	262	33	229	116	95	137	137	95
460	10	262	33	229	141	43	302	302	43
460	15	268	35	233	119	106	128	128	106
460	15	268	35	233	141	48	285	285	48
425	10	269	33	236	119	101	138	138	101
425	10	269	33	236	141	48	291	291	48
485	20	393	41	352	174	158	196	196	158

vOCG scale. 'Montpellier school' data

Surface	γ_{SiOx} mJ m⁻²	γ^{LW}_{SiOx} mJ m⁻²	γ^{ab}_{SiOx} mJ m⁻²	$\pi_{Water/SiOx}$ mJ m⁻²	γ^{-}_{SiOx} mJ m⁻²	γ^{+}_{SiOx} mJ m⁻²	Reference
Quartz	193	55	138	-	89	54	a
Silica	220	45	175	-	138	55	a
Quartz	267	43	224	120	140	90	b
Silica	249	30	219	-	148	81	c

Table 5.3 Surface tension and surface tension components of oxidised silicon wafer and other forms of silica (powder). We compare our data (two first sections of the table) for **plane surfaces** with those of the 'Montpellier school' for **powder**. Reference a: Douillard *et al.* [1995], reference b: Malandrini *et al.* [1997], reference c: Médout-Marère *et al.* [1998]. For $\gamma^{*}_{Hg/SiOx} = 460$ mJ m⁻² and $\gamma^{*}_{Hg/SiOx} = 425$ mJ m⁻², $\theta_{Hg/SiOx} = 132°$, while for $\gamma^{*}_{Hg/SiOx} = 485$ mJ m⁻², $\theta_{Hg/SiOx} = 130°$.

The reasoning behind the structure of Table 5.3 is as follows: for some representative combinations of $\gamma^{*}_{Hg/SiOx}$, $\theta_{Hg/SiOx}$ and $\pi^{Total}_{Hg/SiOx}$ that gave rise to a scientifically meaningful solution to the equation $f(\gamma_{SiOx}) = 0$, we have calculated the surface tension components of oxidised silicon. We have selected three values of mercury surface tension in accordance with our measurements (see § 5.12) and commonly accepted values[2], that is 425, 460 and 485 mJ m^{-2}. Four values of film pressure were selected according to data by Busscher et al. [1986], since we do not have any technical means of measuring film pressures ourselves. The surface tension of NaCl$_{aq}$ in equilibrium with ambient air and oxidised silicon was taken equal to 82 mJ m^{-2} and its contact angle on the same surface was taken equal to 18° in accordance to our measurements (see § 5.1.2).

Equation (5.16) has solutions only if Δ is strictly positive. This implies that the film pressure between NaCl$_{aq}$ and the surface be higher than a certain threshold that depends on the other parameters used in equations (5.10) through (5.18). In Table 5.3 we compare, for each combination of parameters mentioned above, the acid-base components of the surface tension of oxidised silicon for a water film pressure value just above the threshold and a *maximum* film pressure (141 mJ m^{-2}) that was obtained by Busscher et al. [1986] for water vapour on a clean glass surface. We believe this value to be higher than the actual (not measured) film pressure that was present when the experiments were being performed. However it is certain that there was potentially just as much vapour present in the vicinity of the surface since the 75.5% of relative humidity due to the solution was added to the average ambient relative humidity (RH $\approx$ 55%), which roughly amounts to 130% of P$_{sat}^{Water}$.

We notice that for calculations made in using Lee's scale, all the combinations that correspond to a 'moderate' film pressure (smaller than the set maximum) give rise to surfaces with a clear acidic character (H-bond donating) irrespective of the chosen solution, that is solution 1 or solution 2. Both pairs of values are even rather similar in magnitude, especially for the scientifically likeliest combination of parameters that happens to be also our preferred combination (see numbers in red, bold italics). On the other hand, if the film pressure is assumed to be equal to the maximum, then the pair of solutions is respectively acidic and basic. No conclusion regarding the surface properties can be drawn in this case. The contrast in magnitude between the basic and acidic component of each pair is so high that it is physically doubtful. Moreover Busscher et al. [1986] measured this high film

---

[2] The too low value of 360 mJ m^{-2} was dismissed as explained in § 5.1.2.

pressure on a sample that was degassed in vacuum (10^{-3} Torr) for 1 h. Our samples stayed in ambient conditions even though their cleanliness was ensured by Caro-cleaning and subsequent wetting tests with water. We consider that the film pressure, if it had been measured, would have been closer to the threshold than to the maximum.

The results corresponding to $\gamma^*_{Hg/SiOx} = 485$ mJ m^{-2} lead to a film pressure threshold higher than the maximum, the value is therefore rejected. The decrease in surface tension of mercury in ambient condition and in contact with oxidised silicon is likely.

Calculations made with the vOCG leads to 'mirrored' solutions. This is a consequence of the fact that water's basic and acidic components are equal in this scale and that it was the only liquid used in the calculation[3] ($NaCl_{aq}$). Again no conclusion can be drawn for this series of data other than vOCG is not able to distinguish between acidic and basic surfaces.

We also report results published by the 'Montpellier school' about silica in the form of powder (bottom part of Table 5.3). The total surface tension, LW component and acid-base component they measured for amorphous silica or quartz are similar to our estimated values, especially the data they published last (references b and c). On the other hand they find that silica surfaces are more basic than they are acidic. This may be due to their using the vOCG scale and maybe to an unfortunate choice of probe liquids. Their LW or dispersive probe liquid is n-heptane, their base is benzene and their acid is water [Médout-Marère et al., 1998]. Benzene is considered a weak base [Layman & Hemminger, 2004] and may not offer contrasty enough surface properties relative to the other two probe liquids for obtaining a good set of data. Furthermore all three liquids wet the studied surface, therefore they apply Young's equation at $\theta_{liquid/solid} = 0°$, which is not recommended [Adamson, 1990].

We believe Lee' scale to be more appropriate for characterising acidic surfaces like silica than the classic vOCG one. On the other hand we tend to disagree with Lee's stand that film pressures are only related to polarisation and induction effects (Debye and Keesom forces) [Lee, 2001]. Water wets acidic surfaces and its basic surface tension component, although lower than its acidic counterpart, is important enough to make it behave as a base with respect to silica. The inadequacy of van der Waals forces, that include polarisation and induction, to explain the adsorption of water on a surface like mica (a probable base due to

---

[3] It was actually $NaCl_{aq}$ but this probe liquid was attributed water's basic and acidic components.

its lack of silanol sites [Vallant *et al.*, 1998]) has also been stressed by Panella *et al.* [1996]. Therefore film pressures are certainly a combination of acid-base and van der Waals effects.

With our method, we have now a means of characterising both low surface tension materials like PDMS and high surface tension ones like silica with an appropriate choice of probe liquids. Not only can we work out the total surface tension but also the various components of which it is comprised. Acidic silica with its 4.6 silanol sites (Si-OH) per squared nanometer [Vallant *et al.*, 1998] can potentially develop H-bond with PDMS whose basicity, although weak (see Table 5.1), makes it a potential H-bond acceptor.

5.2. Morphology and structure of PDMS monolayers

5.2.1. Thickness and homogeneity study (SFM and nano-manipulation)

In § 4.2.4 we have reported the successful test of a form of coarse nanomanipulation technique referred to as SFM tip-digging or SFM tip-ploughing. In this section we report results of a systematic use of this technique on several monolayers made up of PDMS samples varying in average molecular weight, polydispersity and chain-termination. IC-SFM images of those excavations are presented in Fig. 5.9.
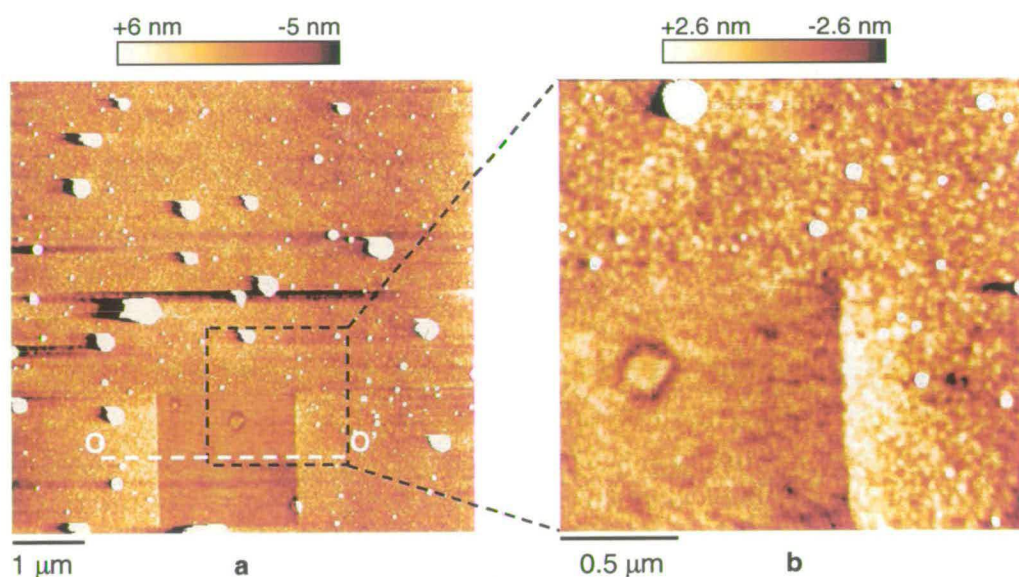
Fig. 5.9. IC-SFM images of PDMS monolayers adsorbed onto oxidised silicon. a: **monolayer 1**: α OH-terminated chains, PI = 1.10, M_W = 5.5 kg mol^{-1}, load $\geq$ 100 nN. b: zoom in on image a. c: **monolayer 2**: (α, ω) CH$_3$-terminated chains, PI = 1.09, M_W = 8.1 kg mol^{-1}, load $\geq$ 200 nN. d: **monolayer 3**: (α, ω) CH$_3$-terminated chains, PI = 1.15, M_W = 80.5 kg mol^{-1}, load $\geq$ 200 nN. e: **monolayer 4**: (α, ω) OH-terminated chains, PI >> 1, M_W = 49 kg mol^{-1}, load $\geq$ 100 nN. f: Cross-sections OO' through RR'. All the monolayers result from primary melts apart from monolayer 3 (image d).
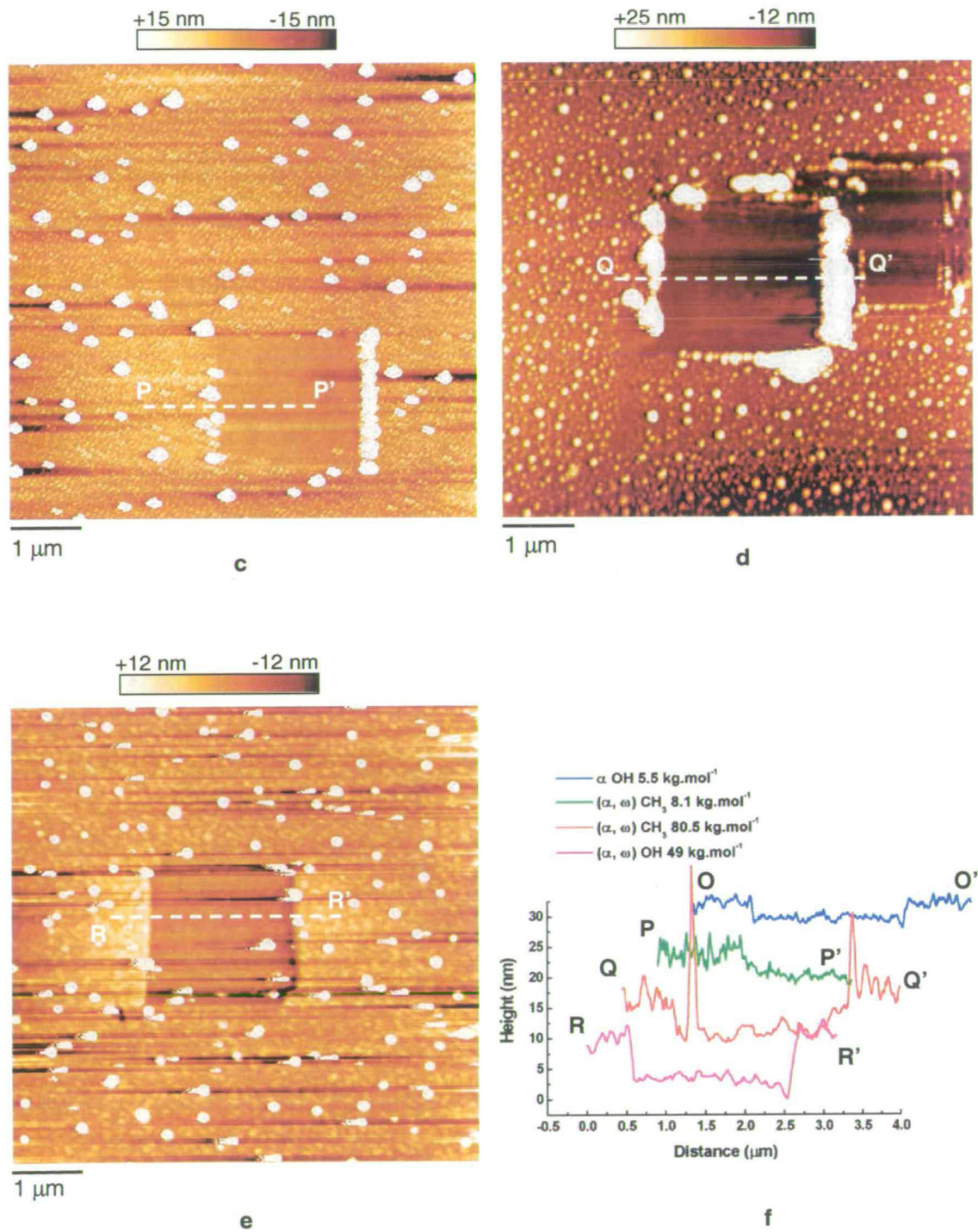
Fig. 5.9. (*continued*) IC-SFM image

PDMS monolayers made of chains that are OH-terminated are continuous, homogeneous and 'easy' to excavate: a load of 100 nN is enough to remove 'all' the chains clearly visible by IC-SFM imaging (see Fig. 5.9 a, b and e). The corresponding pits have sharp banks, which is particularly obvious on cross-sections OO' and RR' (see Fig. 5.9 f). Monolayers prepared from methyl-terminated chains seem to require at least twice as much load to be excavated. In fact, with this type of chains the coverage is not uniform. In order to see a clear step height, the substrate needs to be damaged, in other words excavated (see Fig. 5.9 d and f, section QQ'). This suggests that methyl-terminated PDMS chains do not form a uniform layer the thickness of which depends on the average chain size. The most daring hypothesis would be that of the existence of a uniform 2D layer of collapsed chains with no or very little (a few Angstroms at the most) vertical extension [Déruelle, 1995]. This point is further supported by the following thickness values corresponding to monolayers 1 through 4 as defined in Fig. 5.9 (see caption) and monolayer 5, a sample studied in details in § 4.2.4:

- Monolayer 1 : α OH-terminated 5.5 kg mol^{-1}: $H_0 = (2.5 \pm 0.5)$ nm,

- Monolayer 2: (α, ω) CH$_3$-terminated 8.1 kg mol^{-1}: $H_0 = (2.0 \pm 2.0)$ nm,

- Monolayer 3: (α, ω) CH$_3$-terminated 80.5 kg mol^{-1}: $H_0 = (4.5 \pm 3.0)$ nm,

- Monolayer 4: (α, ω) OH-terminated 49 kg mol^{-1}: $H_0 = (6.5 \pm 1.0)$ nm,

- Monolayer 5: (α, ω) OH-terminated 110 kg mol^{-1}: $H_0 = (17.3 \pm 1.4)$ nm.

We can note that the thickness of non-uniform monolayers is characterised by large error bars, a probable consequence of the damage done to the substrate during the digging process. The comparison of the thickness of these dry monolayers (bad-solvent conditions) with equation (2.50), a relationship proposed for PDMS $(1.05 < PI < 1.2)$ that derives from many ellipsometric and x-ray reflectivity measurements (linear fit), is presented in Fig. 5.10:
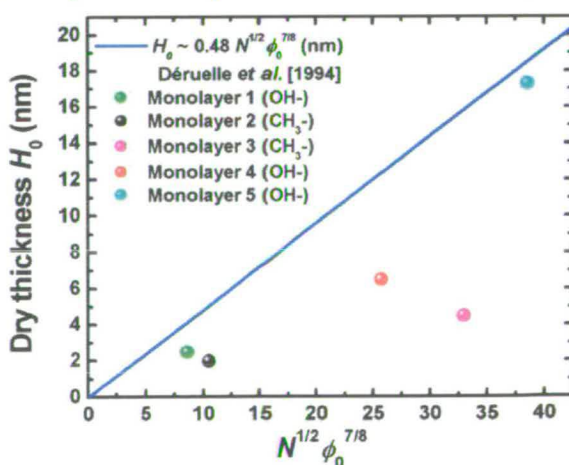

Fig. 5.10. Dry thickness of PDMS monolayers measured by IC-SFM after digging a pit with the imaging tip and fit of measurements made by integrating measurement techniques.

All the monolayers appear thinner than expected according to equation (2.50). That linear relationship being based on integrating measurement techniques (spot size in the millimetre range at best), the chances are that the clearly visible PDMS aggregates or blobs (see Fig. 5.9) only a fraction of a micrometer apart, contribute to the thickness measurements. Our IC-SFM thickness measurements avoid these blobs, which results in smaller but perhaps more accurate estimates of the thickness. Monolayers 2 and 3 are comparatively thin and consist of CH_3-terminated PDMS chains. They are also located farther away from the straight line than monolayers 1 and 5 are. On the contrary monolayers 1 and 5 consist of OH-terminated chains and behave almost as predicted by Déruelle's fit. Surprisingly monolayer 5 seems closer to the straight line than monolayer 1 though the former has been prepared from polydisperse PDMS and the latter from monodisperse PDMS. It has been suggested that equation (2.50) is more accurate for a polymerisation index $N > 100$ and does not hold as well for shorter chains [Déruelle et al., 1994]. Monolayer 4 is also OH-terminated and yet it does not nearly obey the scaling law as well as monolayer 5 does. The discrepancy may be related to the preparation procedure and/or to a differential polydispersity. Monolayer 4 was prepared from a pure melt whose viscosity was that of a rather runny liquid, which suggests the presence of many short chains while monolayer 5 was prepared from a solution in octane ($\phi_0 = 0.2$) of seemingly higher viscosity. This suggests that a great number of long chains control the solution's viscosity. Given that all the chains in the first layer of thickness equal to the radius of the chains in the fluid are able to attach rapidly to the surface [Déruelle et al., 1994], a large proportion of shorter chains can saturate the substrate surface before longer ones can come into contact with it (monolayer 4). On the other hand, a smaller proportion of shorter chains would not be able to statistically keep the long chains from adsorbing (monolayer 5).

We interpret the distance parallel to the x axis between the straight line and the datapoints corresponding to uniform monolayers, that is monolayers 1, 4 and 5, as a consequence of the chains being somewhat polydisperse. The average molecular weight of the chains constituting the homogeneous layer can be deduced from equation (2.50)[3]:

- Monolayer 4: $\overline{M_w^{eff}} = 14$ kg mol^{-1},

- Monolayer 5: $\overline{M_w^{eff}} = 96$ kg mol^{-1}.

---

[3] This does not mean that chains of molecular mass 49 kg mol^{-1} do not adsorb onto the substrate surface, only they are not in a majority.

These results suggest that OH-terminated chains bind much better to silica than CH₃-terminated ones as already conjectured in the conclusions of chapter 4. The quantitative analysis made from contact angle measurements showed that PDMS is probably a weak H-bond acceptor. We confirm this hypothesis here as well as a fact that chemists have known for two decades at least [Wilkinson, 1982]. H-bonds between silanol sites of silica and oxygen atoms of the PDMS backbone are not numerous enough to ensure complete coverage of the surface. PDMS chains with OH-ends are the key to complete wetting as put forward by Villette *et al.* [1996]. The latter even consider that water molecules can play an important role as molecular bridges to favour adsorption. Our process involves heating up sample at 110°C therefore we do not believe this effect to be predominant. PDMS chains could then be H-bond donors in much the same way as silanol sites (see Fig. 5.11). Others, using solid-state NMR have even suggested covalent end grafting [Litvinov *et al.*, 2002]. This could explain why the thorough XPS study that we carried out to detect possible H-bond-related chemical shifts of the Si2p photoelectron line did not give rise to any clear shift in the sense predicted by theory. Aplincourt *et al.* [2001] performed density functional calculations of core-electron binding energies (CEBEs) of water molecules, focussing on the O1s photoelectron line[4]. They show that H-bond between water dimers, a system that models reasonably well what we expect of the interactions between silanol sites and oxygen atoms of PDMS, are characterised by the following shifts:

- $\Delta(\text{BE}^{O1s}) = -1.26$ eV for the oxygen atom that is chemically bonded to the H-bond donating hydrogen atom,

- $\Delta(\text{BE}^{O1s}) = +0.63$ eV for the oxygen atom that is chemically bonded to the H-bond accepting hydrogen atom.
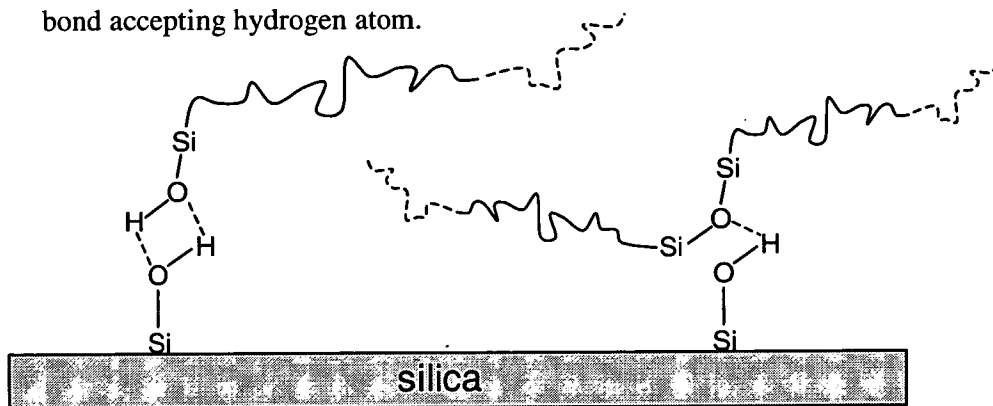

Fig. 5.11. Sketch of the most probable H-bonds between PDMS chains and silanol sites.

---

[4] Strange as it may seem, CEBEs of atoms such as O are more sensitive to the chemical environment than are more external levels [Cole *et al.*, 2002].

5.2.2. Semi-quantitative structural study of the monolayers by IC-SFM

In this section we propose to study more deeply the structure of a PDMS film by IC-SFM in bad and good-solvent conditions. In Fig. 5.12 and Fig. 5.13 we present typical topographic and phase maps of adsorbed PDMS monolayers on silicon wafers in dry state (air).
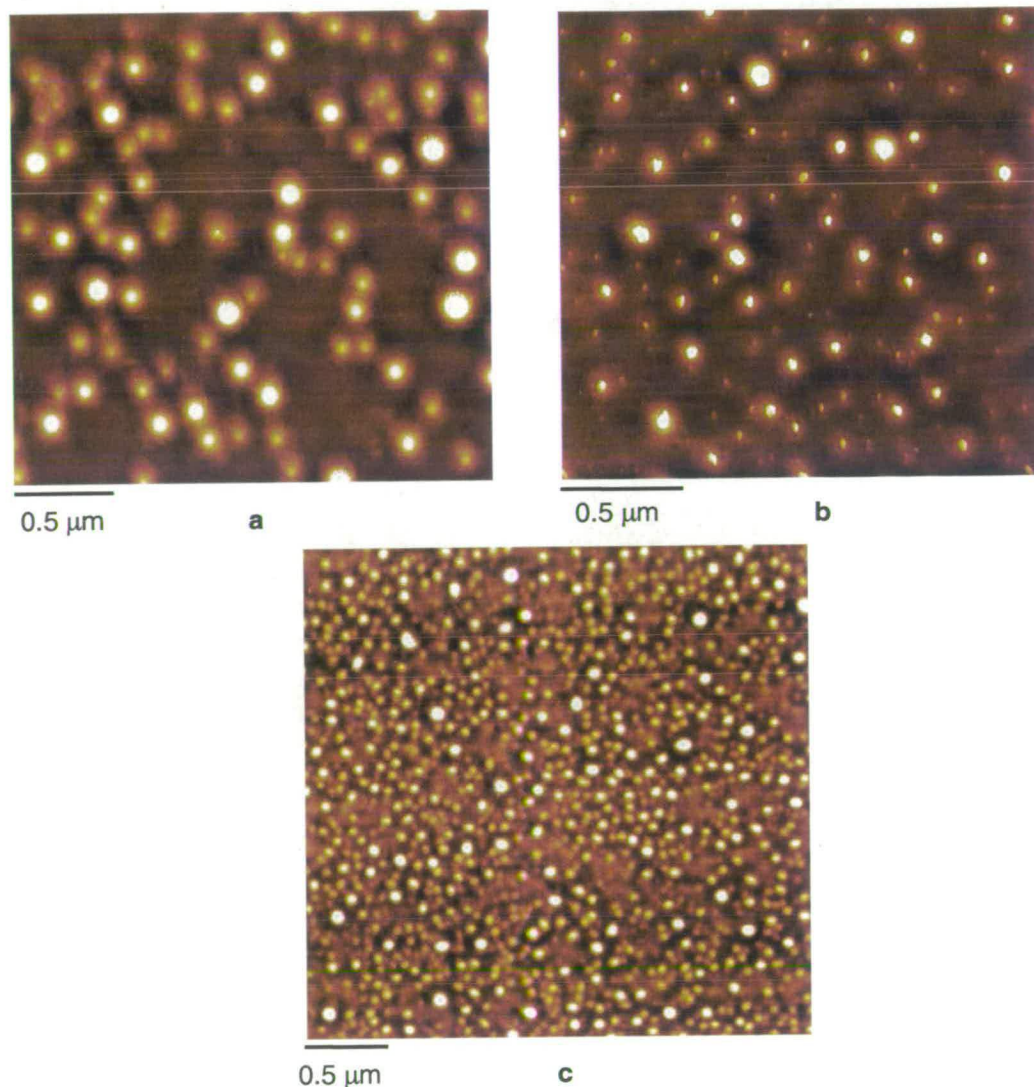

0.5 μm   **a**   0.5 μm   **b**

0.5 μm   **c**

Fig. 5.12. IC-SFM topographic images in air of PDMS films prepared from the secondary melt route. a: z range = 54 nm, (α, ω)-OH, 110 kg.mol^{-1}, PI >> 1, $\phi_0 = 0.2$ (1). b: z range = 32 nm, (α, ω)-OH, 110 kg.mol^{-1}, PI >> 1, $\phi_0 = 0.1$ (1). c: z range = 34 nm, (α, ω)-CH$_3$, 80.5 kg.mol^{-1}, PI ≈ 1.15, $\phi_0 = 0.1$ (1). Polymer islands are present on all three images (aggregations of weakly adsorbed chains upon drying of octane). Lower PDMS volume fraction results in smaller aggregates. Case c: no homogeneous layer hence more islands (instead) than on the other two images and smaller in size because chains are smaller in average and monodisperse (no huge chains on the surface).
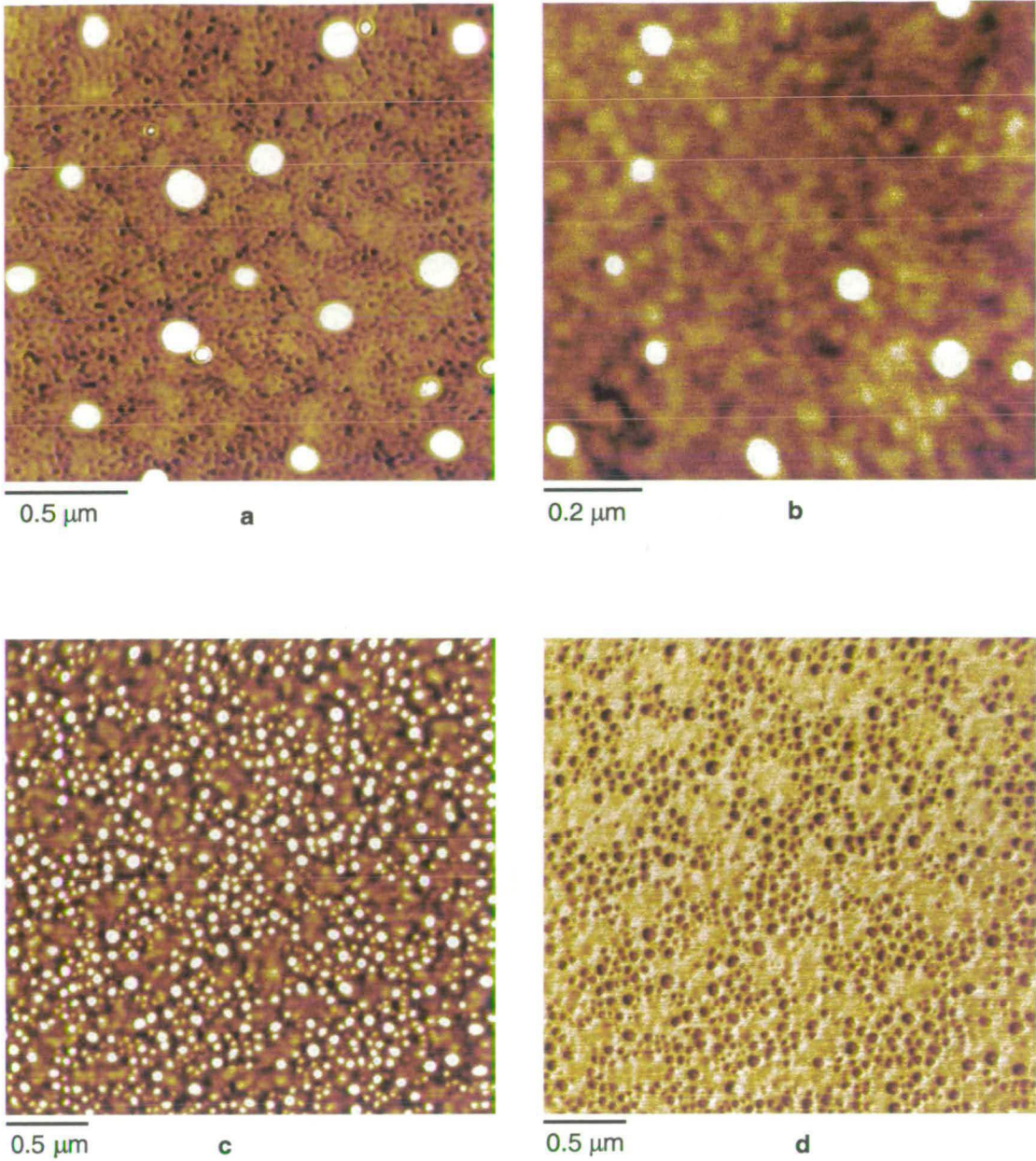
Fig. 5.13. IC-SFM topographic and phase images in air of PDMS films prepared from the primary and secondary melt route. a: z range = 36 nm, (α, ω)-OH, 49 kg.mol^{-1}, PI >> 1, $\phi_0 = 1$. b: z range = 13 nm, α-OH, 5.5 kg.mol^{-1}, PI $\approx$ 1.10, $\phi_0 = 1$. c: z range = 35 nm, (α, ω)-CH$_3$, 80.5 kg.mol^{-1}, PI $\approx$ 1.15, '$\phi_0 = 1$' (prepared from a solution of $\phi_0 = 0.1$). d: phase image of c, z range = 2.66 V. On maps a and to a lesser degree b, the ring-like fine structure of the monolayer stands out. Images c and d: phase contrast shows probably absence of homogeneous monolayer. Aggregates stand on a bare wafer or sub-nanometre layer.

A prominent feature of all images and for all molecular weights is the spherical polymer islands (nano-droplets) that are typically several tens of nanometers in diameter (laterally) and several nanometres in height. The height measurement is relatively accurate but the lateral size is overestimated due to the tip convolution effect. These structures are absent in topography images in good solvent conditions (see below for more details on the images in good solvent) but persisted in images in dry state even when the samples were immersed into good solvents repeatedly and for several days. We hypothesise that these structures were formed by aggregation of several chains (the smallest ones could also be single chains collapsed into globules) upon drying of the solvent (quenching from good solvent to bad solvent conditions). These chains were partially free to move and aggregate but surprisingly remained on the surface when the sample was in a good-solvent bath because they were either:

- adsorbed onto the surface by few monomer units,

- or trapped in the adsorbed monolayer by few surface-enhanced entanglements.

Granick [2002] has speculated the existence of such "surface enhanced" entanglements formed by a short loop (see entanglement of type A in Fig. 1 in [Granick, 2002]) between two strongly adsorbed trains and a non-adsorbed polymer chain. Furthermore, these speculations are consistent with infrared dichroism measurements of PDMS adsorption that showed a bimodal distribution of conformations: chains adsorbed from several segments leading to flat conformations and chains adsorbed from few segments leading to perpendicular conformations [Soga & Granick, 1998].

Moreover, experiments in different but similar systems: adsorption of polybutadiene on mica and polystyrene on graphite from dilute polymer solutions within our group [Glynos *et al.*, 2005] [Bright *et al.*, 2005] has shown the existence of similar features. These systems are characterised by a relatively weak physisorption (covalent and hydrogen bonds are not present) and we expect that the aggregates are formed by weakly adsorbed polymer chains on polymer surface that microphase separate upon the drying of the solvent (quenching to bad solvent conditions).

Phase imaging (see Fig. 5.13 d) in dry state has shown that these aggregations appear darker indicating different mechanical properties than the strongly adsorbed polymer ultra-thin polymer monolayer or substrate (more likely). Generally, darker features correspond to softer regions [Knoll *et al.*, 2001], which confirms our interpretation that the polymer islands are formed by weakly adsorbed/entangled flexible polymer chains. However, it has

to be noted that phase images are hard to interpret since the contrast is determined by competition between viscoelasticity and adhesion and in some systems/cases contrast reversal can happen [Bhushan & Qi, 2003] [Meyer *et al.*, 2004].

The presence of fine structure within the "homogeneous" monolayer of the strongly (and by many monomers) adsorbed chains (see Fig. 5.13 a) can be a micro/nanophase aggregation phenomenon similar to the formation of pinned micelles [Koutsos *et al.*, 1997] or tubes/dimples [Koutsos *et al.*, 1999]. However, one can also assume that it is a spinodal-like dewetting effect similar to the one seen in ultra-thin films of simple liquids that macroscopically wet the substrate [Macdonald *et al.*, 2004].

In Fig. 5.14 through Fig. 5.16 we present a collection of images of PDMS films obtained in octane. Acquiring images in good-solvent conditions proved challenging and suffered from instabilities. In Fig. 5.14 a through d, we can observe that both the topography and phase maps show a fine structure of long 'surface loops or rings'[5]. Also note the strange lichen-looking feature in Fig. 5.14 c. However, in the corresponding phase image there are features that do not resemble any of the visible topographic features. In Fig. 5.15 a and b the top parts are identical to Fig. 5.14 a and b but in the middle of the image the SFM tip lost contact of the surface for a few scan lines and, upon re-establishing contact, the topography appeared different from anything that we had observed so far. A somewhat blurred image was acquired with the striking characteristic of matching to a large extent the phase image (see Fig. 5.15 a and b bottom half).

Fig. 5.15 c and d is an example of an image with good correspondence between topography and phase but again the topography shows a diffuse (blurred) layer. In Fig. 5.16 a and b, the fine structure seems to consist of shorter surface loops ($M_w = 80.5$ kg mol^{-1}) and in Fig. 5.16 c and d even shorter features ($M_w = 15.2$ kg mol^{-1}). In both cases we observe the appearance of extra features in the phase images. This particularly true of Fig. 5.16 d. As we have mentioned the IC-SFM phase signal is a complex function of adhesion and viscoelastic properties of the sample and it is still a matter of debate for studies in the dry state. Our measurements have the complication of being performed in liquid on a partially adsorbed, partially swollen polymer monolayer. Therefore, we tentatively associate the fine structure of surface loops to PDMS conformations of strongly adsorbed parts of the chains (trains).

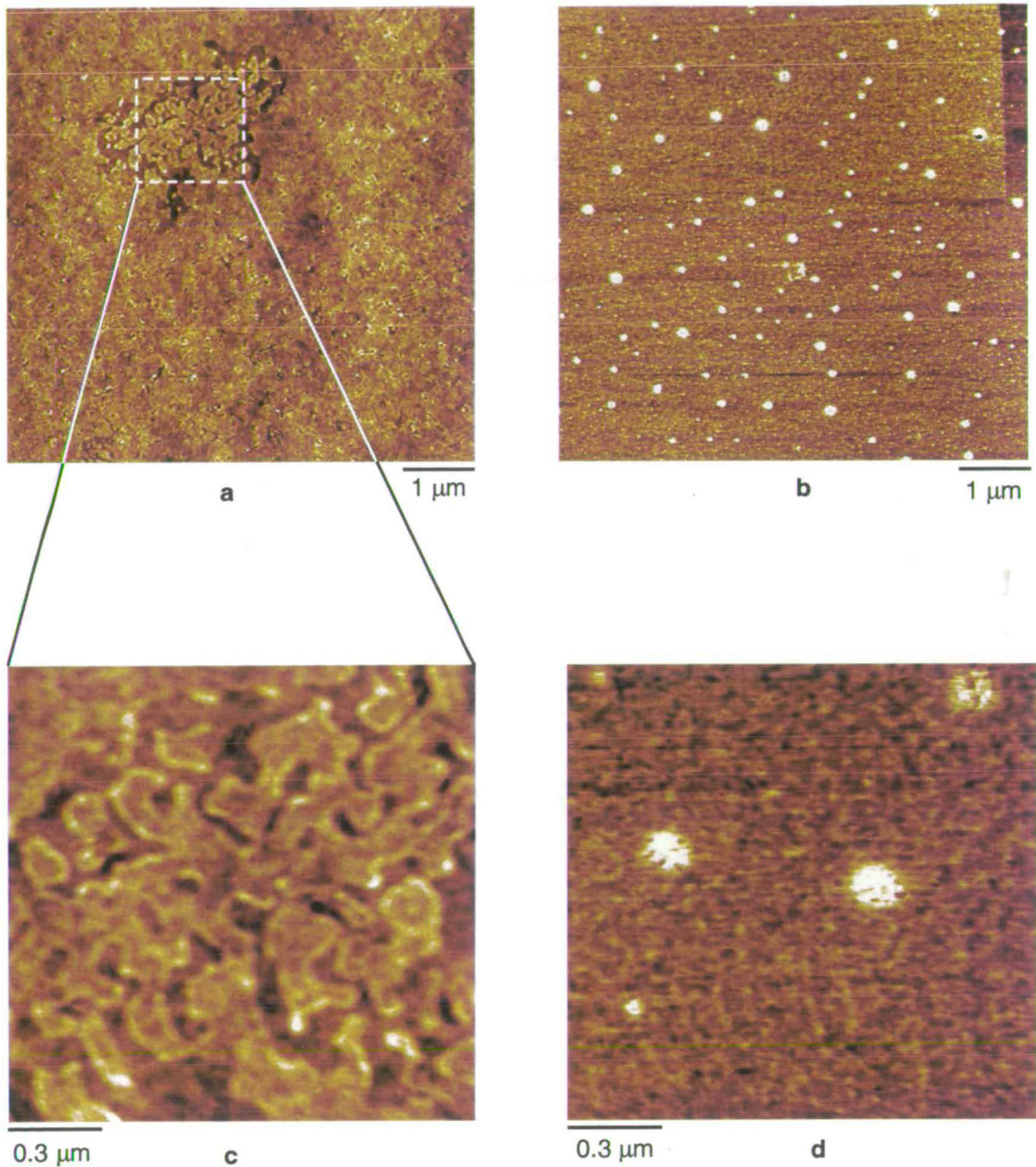[5] They are not to be confused with the loops of adsorbed chains that extend normal to the surface.

Fig. 5.14. IC-SFM topography and phase images of a PDMS film in octane (characteristics of the film identical to Fig. 5.12 b). a: Topography: z range = 10 nm. b: Phase: z range = 9V. c and d: zoom in on the white dashed square, z range = 2.7 nm (2.44 V).
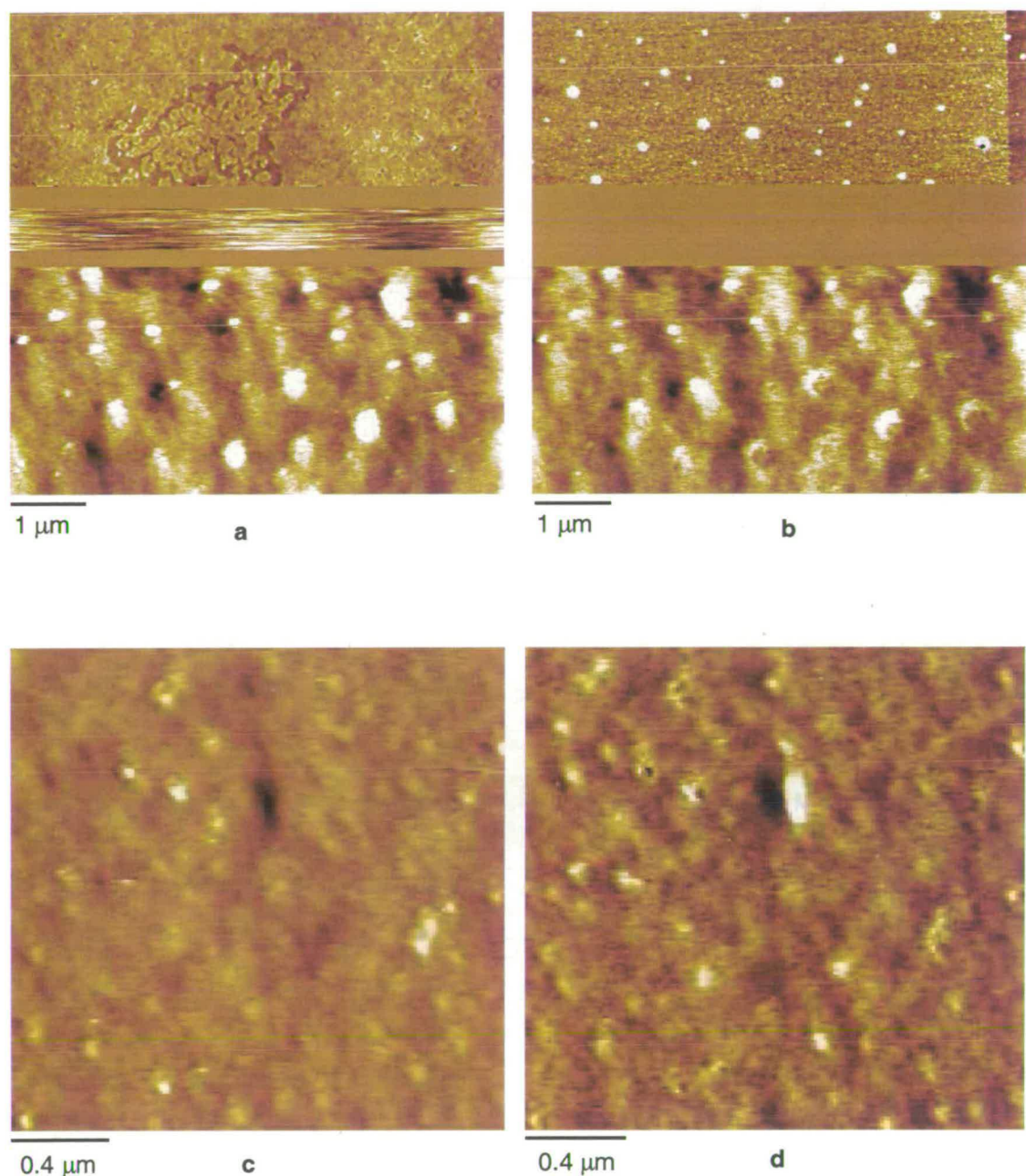
Fig. 5.15. IC-SFM topography and phase images of a PDMS film in octane. a and b: same as Fig. 5.14 a and b but change of tapping conditions on the fly (top, bottom), z range = 30 nm for the topography image (2.77 V for the phase image). c: (α, ω)-OH, 110 kg.mol^{-1}, PI >> 1, '$\phi_0 = 1$' (prepared from a solution of $\phi_0 = 0.1$), topography: z range = 5.7 nm. d: phase image corresponding to c: z range = 1.17V.
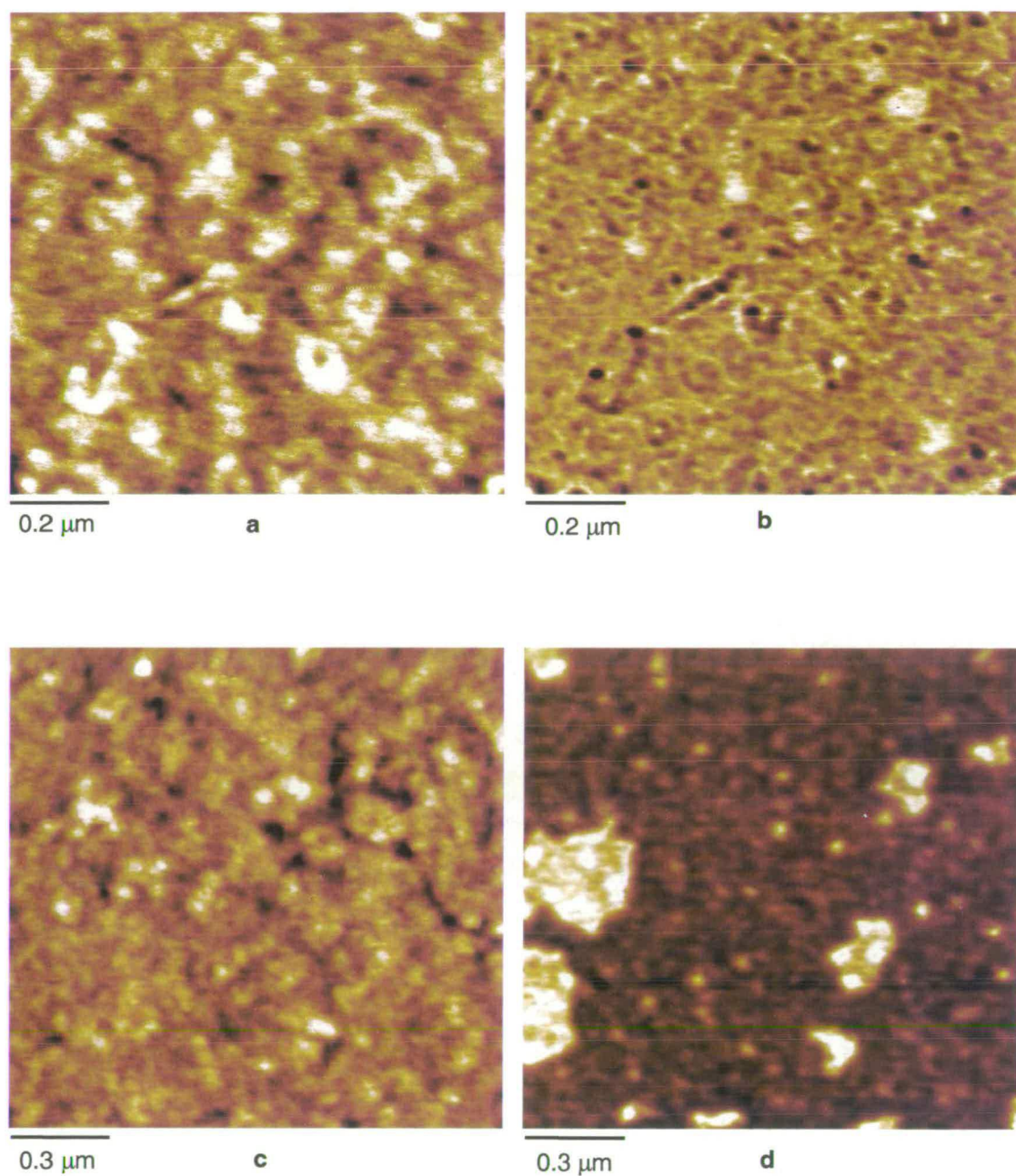
Fig. 5 16. a: (α, ω)-CH$_3$, 80.5 kg.mol^{-1}, PI $\approx$ 1.15, 'ϕ_0 = 1' (prepared from a solution of volume fraction ϕ_0 = 0.1), topography: z range = 1.8 nm. b: phase image corresponding to a, z range = 1.04 V. c: α-OH, 15.2 kg.mol^{-1}, PI $\approx$ 1.17, ϕ_0 = 1, topography: z range = 3.5 nm. d: phase image corresponding to c, z range = 2.5 V.

The extra features in the phase images are attributed to weakly adsorbed/entangled chains that are swollen because of the presence of molecules of good solvent and float around. Their mobility (think of see weed moved around by waves) prevents them from having a clear topographic signature, the SFM-tip sweeps them away as it taps the solid surface where there are only polymer trains and the substrate. On the contrary they do affect the phase signal because of their viscoelasticity/adherence to the tip in some occasions (this correlates well with random adhesion events in force distance curves in good solvent, see below). Therefore, we suggest that in Fig. 5.14, Fig. 5.16 and in the top half of Fig. 5.15 a and b, the tip taps the solid substrate, which results in a topographic map where the trains are being imaged. In Fig. 5.15 a and b (bottom half) and in Fig. 5.15 c and d, the tip does not penetrate the swollen layer and the topography/phase images are associated entirely with the structure and properties of the swollen polymer layer.

The complex nature of this type of adsorbed PDMS monolayers (bimodal) shows that only by imaging them both in bad and good-solvent conditions can their microstructure be determined. It is likely that used as a coating for a particular application, such a monolayer might behave differently depending on the solvent conditions it is subjected to.

5.3. First steps into nanoadhesive and nanofrictional properties

5.3.1. Adhesion between an SFM silicon probe and a PDMS monolayer

Introduction:

An SFM-tip coming into contact with a surface can be used to image it by means of a feedback loop that makes it follow the surface corrugation and prevents it from damaging the surface being imaged. If the feedback is cut off the z-pioezodrive can be used to drive the tip into the surface (soft matter for instance) and record the resulting vertical adhesion-related force. Nowadays dedicated instruments free of some of the most penalising artefacts like piezoscanner hysteresis and optical interferences have taken over from SFMs to carry out experiments of *Force Spectroscopy*. This is the case of the Molecular Force Probe (MFP-1D) by Asylum Research that we have used for all measurements being reported in this section. Details on this instrument can be found in § 3.1.3.

Force spectroscopy is being used to study static and dynamic properties of soft matter in general and polymer in particular, whether in the form of monolayers or isolated individual chains [Rief *et al.*, 1997] [Hugel *et al.*, 2001]. The force-distance (f-d) curves record events associated with a variety of possible scenarios: stretching individual or several polymer coils, bond(s) rupture, desorption processes, entanglements and aggregation effects. So far most of the measurements and published work have concentrated in good solvent conditions. Under these conditions polymer chains are very flexible and the entropic elasticity of single polymer chains dominates the force profiles. In poor or bad solvent conditions, although an interesting phenomenon such as the globule - stretched coil phase transition under an elongational force has been predicted [Halperin & Zhulina, 1991], experimental studies and evidence of the effect are scarce. Haupt *et al.* [2002] have recently presented evidence of this instability. They used polyelectrolyte chains in poor, aqueous solutions. The f-d curves exhibit the force plateaus predicted by the theory. We have focussed on PDMS chains adsorbed onto borosilicate glass slides. The chains were extracted from their monolayer in two different bad-solvent conditions: air and water. In addition to the predicted force plateaus, the force magnitude trend associated with the two different environments compares favourably with the theory. ·

Results and discussion:

We used rectangular-shaped oxidised silicon tips mounted on silicon cantilevers. An inverted 3D image of such a tip was obtained by IC-SFM, using a special tip-characterisation grating that consists of regularly spaced sharp spikes (see Fig. 5.17 a). The resulting images correspond to the convolution of the tip shape with that of the spikes but that of the SFM-tip surface is supposed to prevail. In Fig. 5.17 b we show an image of the tip prior to being used for force spectroscopy, while Fig. 5.17 c shows the same tip after a few thousand approach-retraction cycles.
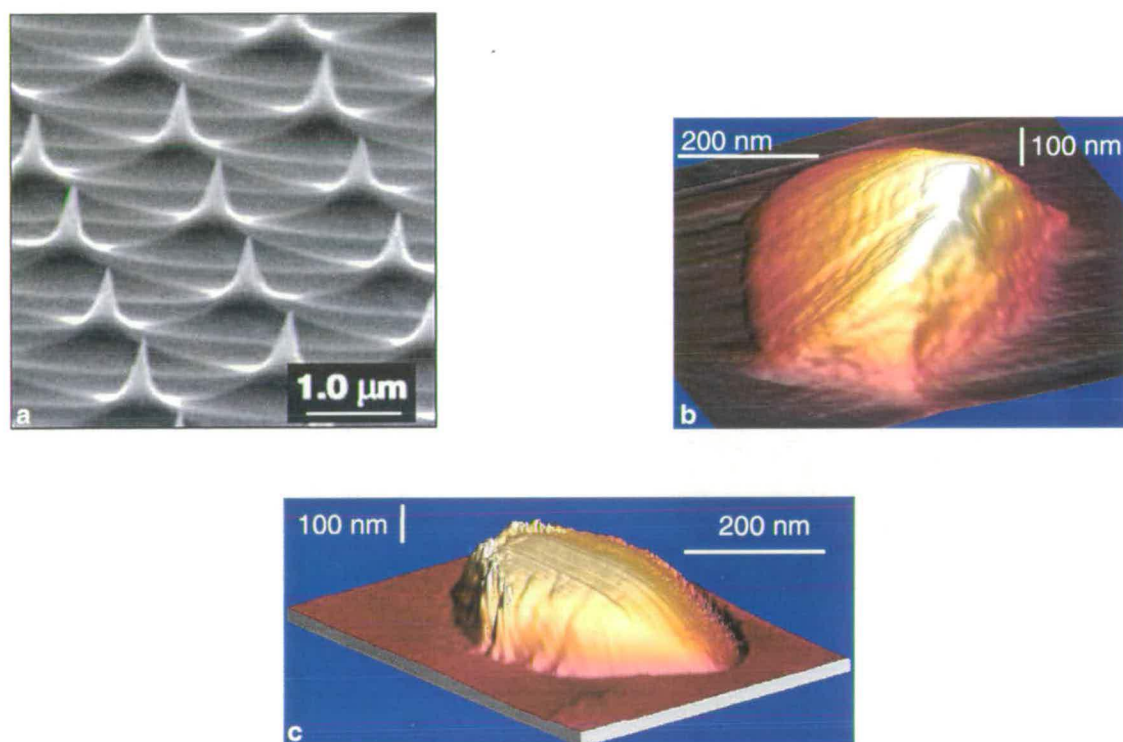

Fig. 5.17. a: Scanning electron micrograph of a silicon tip-characterisation grating (Mikromasch, www.spmtips.com). b: Reconstructed IC-SFM 3D image of an as-received tip (never used before). c: Reconstructed IC-SFM 3D image of the same tip after having been in contact with PDMS-coated glass a number of times. The tip is either worn out or is covered in PDMS chains.

The tip is first brought into contact with the sample and then retracts from the sample. The approach and retraction speed was chosen to be around 2 μm/s and the contact time was

varied from 0 to 5 s. During the cycle, the interaction force is measured via the deflection of the cantilever using the usual optical lever detection technique.

A monolayer was prepared according to the secondary melt route ((α, ω) OH-terminated chains of average molecular weight $M_W = 110$ kg.mol^{-1} and polydispersity PI $\gg$ 1). The excess of polymer was not washed away prior to immersing the sample in a toluene bath, which resulted in a very concentrated solution in the vicinity of the substrate surface. Some of the freed chains adsorbed onto the substrate, outside the homogeneous layer so as to produce incomplete coverage in the same way as CH_3-terminated chains do (see Fig. 5.9 c and d) but still irreversible adsorption despite the short incubation time (10 h at the most). Therefore we had on the same substrate a high grafting density region and a low grafting density one.

In Fig. 5.18, f-d curves obtained in air on the low grafting density area are shown. Characteristic plateau forces of about 50 pN (and multiples, mainly 100 pN) were measured (Fig. 5.18 b). We believe that we detect extraction of single polymer chains from their individual globules (or small aggregates).
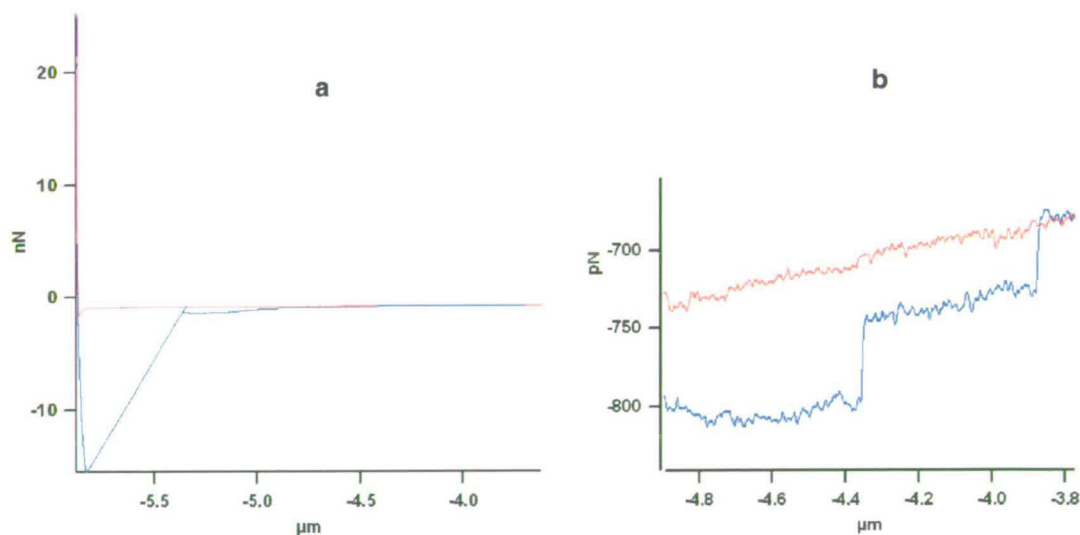

Fig. 5.18. F-d curves (red: approach, blue: retraction) on an incomplete monolayer in air. a: total curve. b: zoom in on the plateaus (-4.9 µm < x < -3.8 µm).

Although plateaus were also (less frequently) observed on the homogeneous monolayer (inside), they were easier to observe outside indicating that within the monolayer chains are strongly adsorbed and are restricted by entanglements with other chains.

In Fig. 5.19, we show some typical f-d curves in water. In the approach curve (red) the instability is attributed to the penetration of the tip into the monolayer. In the retraction curve the large adhesive peak is due to non-specific attractive interactions and capillary forces. A characteristic chain stretching event is seen and a long-range adhesive plateau follows before the tip disengage from the sample. The magnitude of the force-step of the plateau forces is in the region of 100 pN (and multiples, mainly 200 pN) in water.
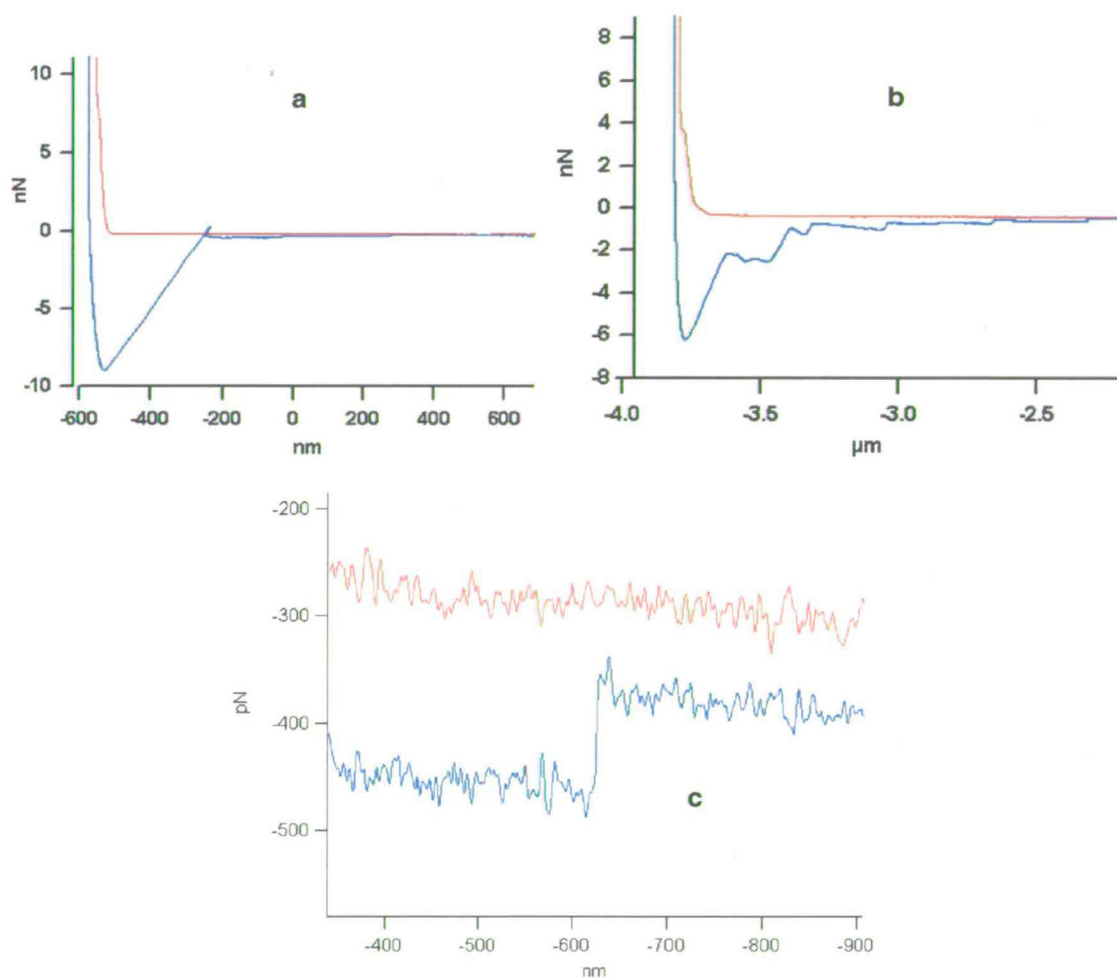

Fig. 5.19. Typical f-d curves (red: approach, blue: retraction) on an incomplete monolayer in deionised water. a, b: global curves showing a variety of events. c: typical plateaus obtained in water.

Even though the homogeneous monolayer did not give rise to many plateau-events in bad-solvent conditions, a feature that we believe to be characteristic of complete monolayers is shown in Fig. 5.20. The portion of the retraction curve situated before the pull-off event is non-linear. This can be interpreted as a collective behaviour of the chains acting as a compact piece of matter being deformed by the tip. The large adhesion peak compared to measurements in water is also due to capillary forces (oxidised silicon tip is hydrophilic) and increased van der Waals interactions (see § 2.1.1 and Fig. 2.1).
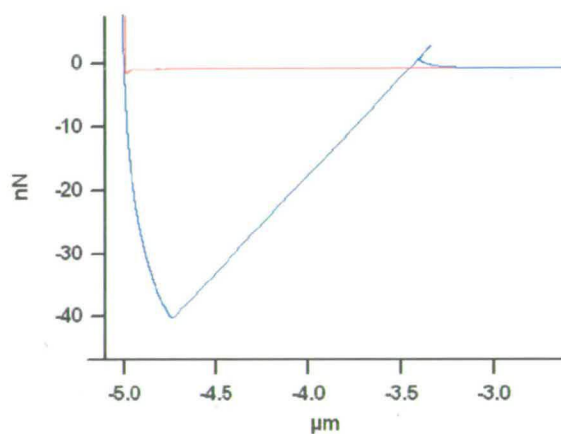

Fig. 5.20. Typical f-d curves (red: approach, blue: retraction) on a complete monolayer in air.

In a good solvent of PDMS like octane (see Fig. 5.21) the adhesive peak is eliminated and the tip-monolayer interactions are even repulsive. This is not exactly what we had predicted through calculating the Hamaker constant of the oxidised silicon/octane/PDMS system (see Fig. 2.1) even if we did predict a very low but attractive force. We feel that this is related to the data used for oxidised silicon. The well-known saw-tooth pattern in the retraction curve signifies entropic stretching of the polymer chains.
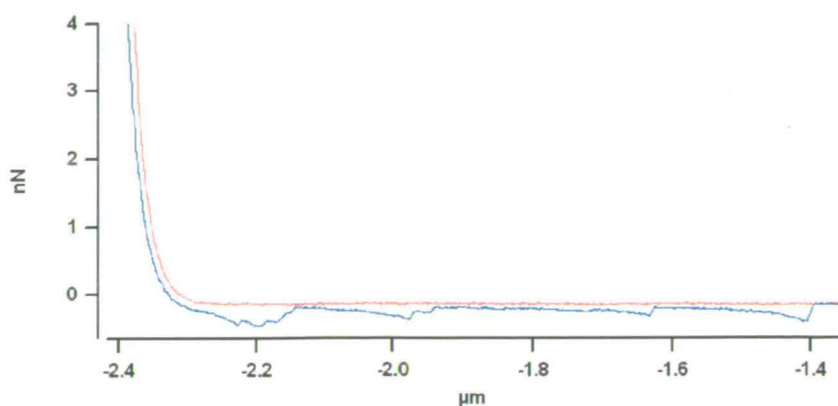

Fig. 5.21. Typical f-d curve obtained on a complete PDMS monolayer in octane.

The length of the plateaus compares favourably with the estimated length of the polymer chains. Control experiments with the lower molecular weight PDMS samples resulted in very few and very short plateau forces.

Halperin and Zhulina [1991] predicted that the elongation of a collapsed chain in poor solvent conditions under an external force results in a first order transition to a stretched coil. The energy difference between the collapsed globule and the extracted, elongated coil of length L and cylindrical shape is equal to the surface energy of the exposed chain:

$$U = 2\pi r L \gamma \qquad (5.19),$$

where r is the radius of the coil and should be of the order of some Angstroms, γ is the interfacial tension of the polymer with respect to the medium (in the case of air this is the surface tension). The force during the pull-out of the chain should be:

$$F_{Plateau} = 2\pi r \gamma \qquad (5.20).$$

We have estimated the intrinsic surface tension components of PDMS in § 5.1.3 using Lee's initial liquid surface tension components [2001], which is essentially the same as the air-PDMS interface tension: $\gamma^{LW}_{PDMS} \approx 22.2$ mJ m^{-2}, $\gamma^{-}_{PDMS} \approx 0.5$ mJ m^{-2}, $\gamma^{+}_{PDMS} \approx 0.006$ mJ m^{-2}. Equation (2.35) gives the total interface tension: $\gamma^{Total}_{PDMS} \approx 22.3$ mJ m^{-2}. If instead of air we take water as the surrounding medium, applying equation (2.34 bis) leads to: $\gamma^{Total}_{PDMS/Water} \approx 42$ mJ m^{-2}, which is somewhat different from the value we would have obtained neglecting the acid-base interactions (51 mJ m^{-2}). This increase in interfacial energy compares favourably with the increase of the plateau forces as predicted by equation (5.20). In both cases we can calculate r to be of the order of some Angstroms, which is in accordance with what is expected for the radius of the backbone of a single chain.

Halperin and Zhulina [1991] argue that finite-size effects can be neglected and the system can undergo a proper phase transition if the collapsed globule is surrounded by other chains, that is if the collapsed coils form a collapsed polymer monolayer; this condition is certainly compatible with our sample preparation procedure.

The theory is developed for a quasi-static elongation; it is to be expected that viscous forces could develop at finite speeds. The maximum viscous force should occur in the beginning of elongation and should be:

$$F = N \varsigma_0 v \qquad (5.21),$$

where N is the polymerization index, ζ_0 is the monomer-monomer friction coefficient and v is the elongation speed. For $N = 500$, $\zeta_0 = 1.2 \times 10^{-11}$ Ns/m (found by self-diffusion experiments [Léger *et al.*, 1996]) and $v = 2$ μm/s we obtain a maximum of viscous force of approximately 10 pN, which is smaller than the force associated with the interfacial energy difference. Furthermore, the initial stage of elongation is screened by the non-specific adhesion peak.

5.3.2. An example of friction between an SFM probe and a PDMS monolayer

In Fig. 5.22 we present a typical friction-load curve that shows three phenomena:

- at low loads the slope is low, corresponding to a low friction coefficient and indicating that the PDMS monolayer lubricates the surface;
- at intermediate loads there is an instability associated with the penetration of the tip into the monolayer;
- at higher loads the slope increases, which means that the friction coefficient is high. It is associated with the direct contact between tip and substrate. Subsequent scans at low load revealed high friction forces indicating that at high loads the PDMS monolayer was damaged.
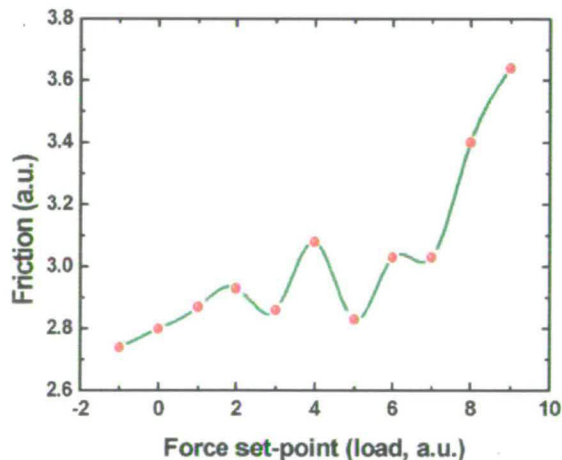

Fig. 5.22. Friction against load curve on a typical PDMS monolayer. This curve shows three regimes of friction.

5.4. Conclusion

Semi-empirical models of surface tension components such as vOCG and Lee's revision of vOCG make it possible to transform simple contact angles into energetic quantitites. Predictions of interface phenomena like adsorption, adhesion and others can be made in a more realistic way than the classic Hamaker constant that takes only van der Waals interactions into account. Careful choice of liquid triplets or doublets can lead to the method being applicable to low surface tension (polymers: films, bulk) as well as high surface tension materials like silica.

Intermittent Contact Mode Scanning force Microscopy is well suited to the study if the structure of soft matter, especially polymer monolayers. Hardened silicon tips through silicon nitride coatings can be used effectively to damage a polymer monolayer in a controlled way and thus study such a system in 3D and not only its surface topography. PDMS monolayers have a bimodal structure that only imaging in bad as well as good-solvent conditions can reveal: a mixture of monomers irreversibly attached to the surface and poorly adsorbed portions of chains constitutes an adsorbed (mainly physisorbed) PDMS monolayer.

Force profiles obtained by the retraction of an SFM tip from a polymer monolayer show long-range force plateaus. The magnitude and characteristics of the force profiles compare favourably with the theoretical predictions of a collapsed globule - stretched coil transition at poor/bad solvent conditions.

5.5. References

Adamson, A.W. (1990) *Physical chemistry of surfaces*, Wiley-Interscience, New York, p383-384.

Al-Maawali, S; Bemis, J.E; Akhremitchev, B.B; Leecharoen, R; Janesko, B.G; Walker, G.C. (2001) *Study of the polydispersity of grafted poly(dimethylsiloxane) surfaces using single-molecule atomic force microscopy*, Journal of Physical Chemistry B. **105**(18), 3965-3971.

Aplincourt, P; Bureau, C; Anthoine, J.L; Chong, D.P. (2001) *Accurate density functional calculations of core electron binding energies on hydrogen-bonded systems*, Journal of Physical Chemistry A. **105**(31), 7364-7370.

Bashforth, F; Adams, J.C. (1892) *An attempt to test the theory of capillary action*, Cambridge University Press and Deighton, Bell and Co.

Bellon-Fontaine, M.N; Cerf, O. (1990) *Experimental determination of spreading pressure in solid/liquid/vapour systems*, Journal of Adhesion Science and Technology. **4**(6), 475-480.

Bhushan, B; Qi, J. (2003) *Phase contrast imaging of nanocomposites and molecularly thick lubricant films in magnetic media*, Nanotechnology. **14**(8), 886-895.

Bright, I; Cheung, R; Koutsos, V. (2005) in preparation.

Busscher, H.J; Kip, G.A.M; van Silfhout, A; Arends, J. (1986) *Spreading pressures of water and n-propanol on polymer surfaces*, Journal of Colloid and Interface Science. **114**(2), 307-313.

Carré, A; Visovsky, N. (1998) *Adhesion and wetting hysteresis of a metal (mercury) on an oxide glass in air and nitrogen*, Journal of Adhesion. **68**(3-4), 301-313.

Cazabat, A.M; Fraysse, N; Heslot, F; Levinson, P; Marsh, J; Tiberg, F; Valignat, M.P. (1994) *"Pancakes"*, Advances in Colloid and Interface Science. 48, 1-17.

Cherry, B.W; El Muddaris, S. (1970) *Wetting, kinetics and strength of adhesive joints*, Journal of Adhesion. **2**, 42-48.

Chaudhury, M.K. (1996) *Interfacial interaction between low-energy surfaces*, Materials Science and Engineering R-Reports. **16**(3), 97-159.

Cole, R.J; MacDonald, B.F; Weightman, P. (2002) *Relative core level shifts in XPS: a theoretical study*, Journal of Electron Spectroscopy and Related Phenomena. **125**(2), 147-152.

De Gennes, P.G. *The dynamics of wetting*. In: *Fundamentals of adhesion,* Lee, L-H (1991), Plenum Press, New York, USA, p173-179.

Della Volpe, C; Siboni, S. (1997) *Some reflections on acid-base solid surface free energy theories*, Journal of Colloid and Interface Science. **195**(1), 121-136. The program for the calculation of acid-base solid surface free energy components referred to in the text is called SurfTen 4.3. It can be found and utilised at http://macsibo.ing.unitn.it:8080/.

Della Volpe, C; Deimichei, A; Ricco, T. (1998) *A multiliquid approach to the determination of flame-treated surfaces of rubber-toughened polypropylene*, Journal of Adhesion Science and Technology. **12**(11), 1141-1179.

Déruelle, M; Tirrell, M; Marciano, Y; Hervet, H; Léger, L. (1994) *Adhesion energy between polymer networks and solid surfaces modified by polymer attachment*, Faraday Discussions. **98**, 55-66.

Déruelle, M. (1995) *Les polymères aux interfaces, application à l'adhésion solide élastomère*, Thèse de doctorat, Université Paris VI, France.

Douillard, J.M; Zoungrana, T; Partyka, S. (1995) *Surface Gibbs free energy of minerals: some values*, Journal of Petroleum Science and Engineering. **14**(1-2), 51-57.

Fowkes, F.M. (1964) *Attractive forces at interfaces*, Industrial and Engineering Chemistry. **56**(12), 40-52.

Gindl, M; Sinn, G; Gindl, W; Reiterer, A; Tschegg, S. (2001) *A comparison of different methods to calculate the surface free energy of wood using contact angle measurements*, Colloids and Surfaces A: Physicochemical and Engineering Aspects. **181**(1-3), 279-287.

Glynos, E; Chremos, A; E. Theofanidou, E; Petekidis, G; Roovers, J; Camp, P; Koutsos, V. (2005) in preparation.

Good, R.J; Chaudhury, M.K; van Oss, C.J. *Theory of adhesive forces across interfaces. 2. Interfacial hydrogen bonds as acid-base phenomena and as factors enhancing adhesion*. In: *Fundamentals of adhesion,* Lee, L-H editor (1991), Plenum Press, New York, USA, 153-172.

Good, R.J. *Contact angle, wettability and adhesion: a critical review*. In: *Contact Angle, wettability and adhesion*, Mittal, K.L editor (1993), VSP, 3-36.

Granick, S. (2002) *Perspective: kinetic and mechanical properties of adsorbed polymer layers*, The European Physical Journal E - Soft Matter. **9**(5), 421-424.

Gutowski, W. *Thermodynamics of adhesion*. In: *Fundamentals of adhesion,* Lee, L-H editor (1991), Plenum Press, New York, USA, 87-135.

Halperin, A; Zhulina, E.B. (1991) *On the deformation-behavior of collapsed polymers*, Europhysics Letters. **15**(4), 417-421.

Haupt, B.J; Senden, T.J; Sevick, E.M. (2002) *AFM evidence of Rayleigh instability in single polymer chains*, Langmuir. **18**(6), 2174-2182.

Heck, P.H; van Horn, W. (1953) *The surface tension of liquid silicon and germanium*, Physical Review. **91**(3), 512-513.

Hetherington, G; Jack, K.H; Kennedy, J.C. (1964) *The viscosity of vitreous silica*, Physics and Chemistry of Glasses. **5**, 130-136.

Hugel, T; Grosholz, M; Clausen-Schaumann, H; Pfau, A; Gaub, H; Seitz, M. (2001) *Elasticity of single polyelectrolyte chains and their desorption from solid supports studied by AFM based single molecule force spectroscopy*, Macromolecules. **34**(4), 1039-1047.

Israelachvili, J.N. (1992) *Intermolecular & surface forces*, Academic Press, San Diego, USA.

Knoll, A; Magerle, R; Krausch, G. (2001) *Tapping mode atomic force microscopy on polymers: where is the true sample surface?* , Macromolecules. **34**(12), 4159-4165.

Koutsos, V; van der Vegte, E.W; Pelletier, E; Stamouli, A; Hadziioannou, G. (1997) *Structure of chemically end-grafted polymer chains studied by scanning force microscopy in bad-solvent conditions*, Macromolecules. **30**(16), 4719-4726.

Koutsos, V; van der Vegte, E.W; Hadziioannou, G. (1999) *Direct view of structural regimes of end-grafted polymer monolayers: a scanning force microscopy study*, Macromolecules. **32**(4), 1233-1236

Kwok, D.Y; Lam. C.N.C; Li, A; Leung, R; Wu, R; Mok, E; Neumann, A.W. (1998) *Measuring and interpreting contact angles: a complex issue*, Colloids and Surfaces A: Physicochemical and Engineering Aspects. **142**(2-3), 219-235.

Lam, C.N.C; Wu, R; Li, D; Hair, M.L; Neumann, A.W. (2002) *Study of the advancing and receding contact angles: liquid sorption as a cause of contact angle hysteresis*, Advances in Colloid and Interface Science. **96**(1-3), 169-191.

Layman, K.A; Hemminger, J.C. (2004) *Determination of surface OH acidity from the formation of acid/base complexes on ultrathin films of γ-Al_2O_3 on NiAl(100)*, Journal of Catalysis. **222**(1), 207-213.

Lee, L-H. (1996) *Correlations between Lewis acid-base surface interaction components and linear solvation energy relationship solvatochromic α and β parameters*, Langmuir. **12**(6), 1681-1687.

Lee, L-H. (2001) *The unified Lewis acid-base approach to adhesion and solvation at the liquid-polymer interface*, Journal of Adhesion. **76**(2), 163-183.

Léger, L; Hervet, H; Auroy, P; Boucher, E; Massey, G. (1996). *Slip at the wall*. In: Piau, J.M; Agassant, J.F. (eds) *Rheology for polymer melt processing*. Rheology series, **5**, Elsevier, Amsterdam, The Netherlands.

Lide, D.R. (1992) *CRC handbook of chemistry and physics 73nd edition*, CRC Press, New York, USA. (Available at the Darwin library).

Lide, D.R. (2001) *CRC handbook of chemistry and physics 82nd edition*, CRC Press, New York, USA.

Litvinov, V.M; Barthel, H; Weis, J. (2002) *Structure of a PDMS layer grafted onto a silica surface studied by means of DSC and solid-state NMR*, Macromolecules. **35**(11), 4356-4364.

Macdonald, B.F; Cole R.J; Koutsos, V. (2004) *The formation of dewetting structures after evaporation of n-dodecane on graphite studied by atomic force microscopy*, Surface Science. **548**(1-3), 41-50.

Malandrini, H; Sarraf, R, Faucompré, B; Partyka, S; Douillard, J.M. (1997) *Characterization of quartz particle surfaces by immersion calorimetry*, Langmuir. **13**(5), 1337-1341.

Mazurin, O.V; Strelsina, M.V; Shvaiko-Shvaikovskaya, T.P. (1983) *Handbook of glass data, Part A: Silica glass and binary silicate glasses*, Elsevier, Amsterdam, The Netherlands.

Médout-Marère, V; Malandrini, H; Zoungrana, T; Douillard, J.M; Partyka, S. (1998) *Thermodynamic investigation of surface of minerals*, Journal of Petroleum Science and Engineering. **20**(3-4), 223-231.

Meiron, T.S; Marmur, A; Saguy, I.S. (2004) *Contact angle measurement on rough surfaces*, Journal of Colloid and Interface Science. **274**(2), 637-644.

Meyer, E; Hug, H.J; Bennewitz, R. (2004) *Scanning probe microscopy. The lab on a tip*, Springer-Verlag, Berlin, Germany.

Mitchell, D.F; Clark, K.B; Bardwell, J.A; Lennard, W.N; Massoumi, G.R; Mitchell, I.V. (1994) *Film thickness measurements of SiO$_2$ by XPS*, Surface and Interface Analysis. **21**(1), 44-50.

Morita, M; Ohmi, T; Hasegawa, E; Kawakami, M; Ohwada, M. (1990) *Growth of native oxide on a silicon surface*, Journal of Applied Physics. **68**(3), 1272-1281.

Muto, A; Mine, T; Nakazawa, M. (1993) *Estimation of the thickness of ultrathin silicon nitride films by x-ray photoelectron spectroscopy*, Japanese Journal of Applied Physics. **32**(1), 3580-3583.

Nicholas, M.E; Joyner, P.A; Tessem, B.M; Olson, M.D. (1961) *Effects of various gases and vapors on surface tension of mercury*, Journal of Physical Chemistry. **65**(8), 1373-1375.

Panella, V; Chiarello, R; Krim, J. (1996) *Adequacy of the Lifshitz theory for certain thin adsorbed films*, Physical Review Letters. **76**(19), 3606-3609.

Rief, M; Gautel, M; Oesterhelt, F; Fernandez, J.M; Gaub, H.E. (1997) *Reversible unfolding of individual titin immunoglobulin domains by AFM*, Science. **276**(5315), 1109-1112.

Salvia, A.M; Castle, J.E. (1998) *The intrinsic asymmetry of photoelectron peaks: dependence on chemical state and role in curve fitting*, Journal of Electron Spectroscopy and Related Phenomena. **95**(1), 45-56.

Seah, M.P; Spencer, S.J. (2002) *Ultrathin SiO2 on Si II. Issues in quantification of the oxide thickness*, Surface and Interface Analysis. **33**(8), 640-652.

1 - Seah, M.P; Spencer, S.J. (2003) *Ultrathin SiO2 on Si IV. Intensity measurements in XPS and deduced thickness linearity*, Surface and Interface Analysis. **35**(6), 515-524.

Soga, I; Granick, S. (1998) *Infrared dichroism and surface conformational dynamics of adsorbed poly(dimethylsiloxane)*, Macromolecules. **31**(16), 5450-5455.

Staicopolus, D.N. (1962) *Computation of surface tension and contact angle by sessile-drop method I*, Journal of Colloid Science. **17**(5), 439-447.

Staicopolus, D.N. (1963) *Computation of surface tension and contact angle by sessile-drop method II*, Journal of Colloid Science. **18**(8), 793-794.

Staicopolus, D.N. (1967) *Computation of surface tension and contact angle by sessile-drop method III*, Journal of Colloid Science. **23**(3), 453-456.

Uilk, J.M; Mera, A.E; Fox, R.B; Wynne, K.J. (2003) *Hydrosilation-cured poly(dimethylsiloxane) networks: Intrinsic contact angles via dynamic contact angle analysis*, Macromolecules. **36**(10), 3689-3694.

Vallant, T; Brunner, H; Mayer, U; Hoffmann, H; Leitner, T; Resch, R; Friedbacher, G. (1998) *Formation of self-assembled octadecylsiloxane mobolayers on mica and silicon surfaces studied by atomic force microscopy and infrared spectrometry*, Journal of Physical Chemistry B. **102**(37), 7190-7197.

Van Oss, C.J; Ju, L; Chaudhury, M.K; Good, R.J. (1989), *Estimation of the polar parameters of the surface tension of liquids by contact angle measurements on gels*, Journal of Colloid and Interface Science. **128**(2), 313-319.

Villette, S; Valignat, M.P; Cazabat, A.M; Jullien, L; Tiberg, F. (1996) *Wetting on the molecular scale and the role of water. A case study of wetting of hydrophilic silica surfaces*, Langmuir. **12**(3), 825-830.

Wilkinson, G. (1982) *Comprehensive organometallic chemistry*, Pergamon Press, Oxford.

Xu, Z; Liu, Q; Ling, J. (1995) *An evaluation of the van Oss-Chaudhury-Good equation and Neumann's equation of state approach with mercury substrate*, Langmuir. **11**(3), 1044-1046.

Yaws, C.L. (1999) *Chemical properties handbook*, McGraw-Hill, New York, USA.

6. Conclusions and future work

6.1. Scanning White Light Interferometry

We have proved that SWLI is a technique capable of offering a solid alternative to imaging ellipsometry in the characterisation of thin and ultra-thin softer matter films, four aspects could be improved:

- Minimum thickness of metal overlayer necessary to eliminate transparent film thin effects. We feel that ultra-thin films could be imaged precisely even if the metal overlayer was much thinner than 80 nm, a systematic study on a test sample with a well-calibrated setup (see next bullet point) would provide this piece of information. Sputtering might be more effective than CVD especially with noble metals like gold that do not corrode and be a better solution than CVD coated aluminium.

- Precision of height measurements by the systematic calibration of the system using a step height standard in the nanometre range. VLSI proposes such a step height (height = 8 nm).

- Elimination of the substrate-induced roughness/waviness by mapping the substrate surface prior to coating it (a more advanced instrument than the New View 100 might have to be used). A cleaning method not as aggressive as Caro-cleaning is recommended: a combination of IPA and ultrasonic bath or UV-ozone cleaning.

- Promising measurements made on micro-patterned surfaces with short organic molecules (silanes) need to be carried on.

6.2. X-ray photoelectron spectroscopy

In this work we have used XPS to locate film boundaries, measure film thicknesses and detect chemical shifts due to two effects: oxidation, H-bond. The film thickness measurement aspect is particularly interesting as it offers a rather quick and non-destructive way to investigate with accuracy the 0 to 10 nm interval. It applies both to single-layered and multi-layered structures with the ability of distinguishing between chemical states. We are currently working on this aspect. The possibility of detecting weak H-bond related chemical shifts is certainly the most challenging and perhaps the most interesting in a future work perspective. Oxidation brings about large chemical shifts (> 1 to 2 eV) so that it is easy to distinguish between Si, $SiO_{x, x< 2}$, SiO_2 or PDMS (Si-O). H-bonds are much more challenging to detect, in particular for orbitals of atoms situated 'two atoms away' from the hydrogen atoms of interest (Si 2p). The corresponding shifts are of the same order of magnitude as the resolution in energy of the technique. Although we believe that not all the silanol sites were involved in H-Bonds as H-bond donors only, some more spectra need to be acquired. We propose to first verify that the resolution in energy of the spectrometer is good enough by using a test sample: PMMA on oxidised silicon[1]. A monolayer of short chains of PMMA ($\sim$ 6 kg.mol^{-1}) can be prepared either by spin coating or by the secondary melt route with CCl_4 as solvent. We have mentioned PMMA in § 2.1.2 and § 2.1.3 that PMMA is a base that H-bonds to acidic silica. The C1s component of the carbonyl group can be easily distinguished from aliphatic carbon, some of which comes from contamination. We would record high energy C1s photoelectron line with a pass energy of 10 or 5 eV along with the Si2s line (no spin doublet to worry about unlike Si2p). The carbonyl C1s binding energy is supposed to increase, while that of Si2s (oxide) is supposed to decrease. At the same time the change in surface area of aliphatic C1s with time would give us information about the speed with which adventitious contamination accumulates on the surface.

Supposing that the H-bond-related chemical shifts can be detected, we would apply the same procedure to PDMS-coated silicon wafers. The estimation of the relative amount of PDMS and substrate cannot be done precisely by recording the C1s photoelectron line as

---

[1] The p-doped silicon wafers that we currently use may have too thick an oxide layer to obtain information from the silanol Si atoms therefore less heavily doped silicon would be more suitable: p-doped $\approx 10^{15}$ cm^{-3} of carriers or less.

methyl carbon atoms are too similar to adventitious contamination. An auxiliary material is necessary to estimate the amount of contamination. An excellent candidate would be a piece of polytrifluoroehtylene (PtFE) with a surface state comparable to that of the PDMS-coated wafer to be analysed. The surface tension of this polymer is similar to that of PDMS therefore it is expected to attract just as much adventitious contamination as PDMS. Recording alternatively the C1s line of PtFE and that of PDMS plus Si2s would provide more information to set physically meaningful constraints to the curve-fitting program (in particular surface area ratios).

Obviously a more powerful x-ray source with the possibility of choosing an energy that matches the maximum of photoionization cross-section of a given core-level would be ideal. Such a piece of equipment exists: it is a synchrotron...

6.3. Contact angle goniometry

Surface Tension Component theories combined with contact angle measurements give access to the physical or physico-chemical properties of a surface. We have obtained sensible results for a slightly basic, low surface tension polymer (PDMS) and for an acidic high-surface tension oxide (oxidised silicon). Unfortunately this could only be achieved by making, some may say, daring assumptions regarding the surface tension components of a saturated sodium chloride solution. It is possible to estimate every single component of the surface tension of this polymer by using standard-surfaces:

- the LW component can be obtained by depositing a drop on a purely dispersive surface like PTFE[2] and measuring the contact angle (advancing),

- the acidic component can be estimated on a basic surface such PMMA,

- the basic component can be estimated on an acidic surface (PVC[3]).

- the solvation and electrostatic terms are the difference between the total surface tension and the LW plus the acid-base components.

---

[2] The purity of the PTFE standard surface must be ensured. SIMS with an electron flood gun (no metallization needed) is a technique that would certainly be of great value due to its high sensitivity.

[3] PVC is not bound to adsorb well on acidic surface like silica. Basic materials would make more suitable substrates: calcite (CaCO3) or magnesium oxide (MgO) would be much better candidates.

A basic liquid with a high enough surface tension not to wet clean oxidised silicon would be desirable. It would take the vacant position in our high-surface tension probe liquid triplet along with mercury and sodium chloride (in water). A saturated solution of sodium hydroxide is supposed to have a surface tension higher than 100 $mJ.m^{-2}$. Unfortunately it is obviously wrong to assume that OH^- ions will not affect the acid-base surface tension components as we did with Na^+ and Cl^- for sodium chloride. The procedure described above should be applied to this new probe liquid in order to estimate each surface tension component. Only surfaces with which an excess of OH^- ions is not going to react (chemically) could be investigated by this method.

In Chapter 5 we often stressed the importance of vapour adsorption on surface tension measurements. This quantity needs to be either measured or controlled. We recommend using ellipsometry in an environmental chamber with vacuum gauge and pressure gauge up to the saturation pressure of the probe liquid being used. Contact angle and surface tension measurements should be carried out in an environmental chamber (glove box) where the relative humidity could be kept at a controlled level or even eliminated. Dry nitrogen would be a better environment than air. Surface tension measurements are extremely sensitive to liquid density and correct calibration of the lens. The method employed in this work to estimate liquid density is too coarse so that a proper densitometer providing precise measurements with three decimal places is needed. Strange as it may seem, we have noticed that graticules are not necessarily effective in calibrating the lens. A better option would be to use syringe needles with certified diameters to a high tolerance and systematically compare them with graticule-calibrated measurements.

6.4. Scanning Force Microscopy, nanoadhesive and nanofrictional forces

6.4.1. IC-SFM

We have noticed (see § 5.2.2) that the topographic and phase maps obtained with the Pico SPM (Molecular Imaging) could be totally unrelated. Imaging in good-solvent

conditions partly mobile systems like an adsorbed PDMS monolayer on silica leads to the phase signal being sensitive to the diffuse layer above the substrate while the topopgraphic image correponds to chains well-adsorbed to the substrate. This behaviour changes depending on the cantilever vibration conditions so that both images show almost identical features. This illustrates the sensitivity of the technique to amplitude setpoint (hard tapping, soft tapping) as well as the free amplitude of oscillations when the SFM tip is far away from the surface. As every SFM has a specific way of acquiring and processing signals in this mode of operation, some work has to be done to be able to predict the form of image expected from a given surface in bad or good-solvent conditions. In particular a systematic study of the influence of the free amplitude and of the amplitude setpoint on the sign of the phase signal (positive or negative) when two different materials are present on the same surface, one being more viscoeleastic or softer than the other, would be invaluable.

For less dense monolayers (low grafting density) the use of sharper SFM tips might make it possible to resolve single chains in order to learn more about the adsorption energy. Microfabrication techniques have made progress and it is now possible to buy SFM tips the apex of which has a radius of curvature of order of 1 nm.

6.4.2. Adhesion and friction forces

We have only touched on adhesion and friction. The first results of adhesion experiments between a silicon probe and PDMS monolayers show that the Force Probe has a high enough force resolution to detect single events such as chains being stretched or force plateaus. The preliminary study of the nanofrictional properties of PDMS monolayers has shown that this type of films can be used as a lubricant as long as the load does not exceed a certain threshold. The intrinsic adhesive properties of PDMS could be probed if the SFM tip was covered in a PDMS monolayer. Because of the microscopic size of these probes, we recommend to clean the tip surface remotely by UV irradiation. As the probability that chain interdigitation happens is dependent upon the chain grafting density, we recommend to prepare solutions of volume fraction 0.1 and 0.5 as well as melts of PDMS of a given molecular weight to have monolayers with different characteristics. A thorough statistical analysis would require systematic processing of a great number of curves corresponding to each situation. Water would be a better choice than air as a bad-solvent since this decreases the magnitude of the non-specific van der Waals forces between tip and sample and

eliminates the capillary forces responsible for the large peaks observable in the retraction force-distance curves (see § 5.3.1).